The Pennsylvania State University
The Graduate School
Department of Bioengineering

QUANTITATIVE ANALYSIS OF IN VIVO PERISTALTIC AND SEGMENTAL MOTION IN THE RAT SMALL INTESTINE USING DYNAMIC MRI

A Dissertation in
Bioengineering
by
Amit Ailiani

Submitted in Partial Fulfillment
of the Requirements
for the Degree of

Doctor of Philosophy

May 2010

The dissertation of Amit Ailiani was reviewed and approved* by the following:

Andrew G. Webb
Professor of Bioengineering
Dissertation Co-Advisor, Co-Chair of Committee

James G. Brasseur
Professor of Mechanical Engineering, Bioengineering and Mathematics
Dissertation Co-Advisor, Co-Chair of Committee

Keefe Manning
Assistant Professor of Bioengineering

Steven J. Schiff
Professor of Engineering Science and Mechanics

Herbert Lipowsky
Professor of Bioengineering
Head of the Department of Bioengineering

*Signatures are on file in the Graduate School.

Abstract

Conventional methods of quantifying segmental and peristaltic motion in animal models are highly invasive; involving, for example, the external isolation of segments of the gastrointestinal (GI) tract either from dead or anesthetized animals. The present study was undertaken to determine the utility of magnetic resonance imaging (MRI) to quantitatively analyze these motions in the jejunum region of anesthetized rats (N = 6) non-invasively. Dynamic images of the GI tract after oral gavage with a gadolinium (Gd) contrast agent were acquired at a rate of six frames per second, followed by image segmentation based on a combination of three-dimensional live wire (3D LW) and directional dynamic gradient vector flow snakes (DDGVFS). Quantitative analysis of the variation in diameter at a fixed constricting location showed clear indications of both segmental and peristaltic motions. Quantitative analysis of the frequency response gave results in good agreement with those acquired in previous studies using invasive measurement techniques. The results of integrated and Fourier analysis of peristaltic and segmental motility suggest that the neurophysiology underlying the control of motility can be considered much simpler. For example the results of integrated analysis suggest segmental vs. peristaltic wave patterns must be represented primarily by the phase relationships among the principal components. Alternatively the results of Fourier analysis suggest peristalsis is represented by a single wave propagating in the aboral direction and a simple segmental pattern is a resultant of two waves propagating in opposite directions. A complex segmental motility requires a third high frequency segmental mode to complete the complex patterning. MRI results also show that inactin anesthesia does not have the same inhibitory effects on the gut motility as isoflurane, confirming indirect data in the literature acquired using invasive techniques, but also adding detailed knowledge of the changes in gastrointestinal motions produced by these anesthetics.

Table of Contents

List of Figures

List of Tables

List of Abbreviations

2D	Two Dimensional
3D	Three Dimensional
GI	Gastrointestinal
USL	Unstirred Layer
CFD	Computational Fluid Dynamic
MRI	Magnetic Resonance Imaging
FOV	Field of View
3DLW	Three-dimensional Live Wire
2DLW	Two-dimensional Live Wire
DDGVFS	Directional Dynamic Gradient Vector Flow Snakes
GVF	Gradient Vector Flow
Gd	Gadolinium
CD	Celiac Disease
IBS	Irritable Bowel Syndrome
PCA	Principal Component Analysis
EMG	Electromyography
ASM	Active Shape Model

NSF	National Science Foundation
MMC	Migrating Motor Complex
CNS	Central Nervous System
CNR	Contrast to Noise Ratio
SNR	Signal to Noise Ratio
NMR	Nuclear Magnetic Resonance
ACM	Active Contour Model
IACUC	Institutional Animal Care and Use Committee

List of Symbols

M_0	Magnetization Moment
B_0	Magnetic Field
E	Voltage
ω_0	Larmor Frequency
γ	Gyromagnetic Ratio
T_1	Spin-Lattice Relaxation Time Constant
T_2	Spin-Spin Relaxation Time Constant
G_{phase}	Phase Encoding Gradient
$I(x, y)$	Image Intensity
TR	Repetition Time
TE	Echo Time
F_Z	Laplacian Zero Crossing
F_G	Gradient magnitude
F_D	Gradient Direction
$l(a, b)$	Local Cost Function
G	Gradient
J_X	Partial Gradient in X
J_Y	Partial Gradient in Y

Acknowledgments

Firstly, I would like to thank my advisor Dr. Andrew Webb for his support in developing my understanding of magnetic resonance imaging along with his continual backing and financial support. I also appreciate the independence he gave me to pursue my own ideas. I would also like to thank my co-advisor Dr. James Brasseur for this collaboration along with the financial support. He also shared his enormous insight in mathematics which was extremely important for image analysis algorithms and modeling of the gut. I would also like to acknowledge Thomas Neuberger for his guidance in animal preparation and MR image acquisition, without him, this work would not have been accomplished. I would like to thank Dr. Nadine Smith for her help in preparation of animal protocols. I would also like to thank my committee members, Dr. Manning and Dr. Schiff for their time in reviewing and contributing ideas to this dissertation. Next, I would like to thank Dr. Higgins and his students Lav Rai and Kongkuo Lu for discussing live wire and its implementation in Matlab. Additionally, I acknowledge the help of Dr. Lipowsky and Anne for providing help in inactin study, Dr. Dodds in animal preparation for MRI experiments, Xiaofeng Liu and Dr. Prince (Johns Hopkins University, USA) and Jierong Cheng (Nanyang Technological University, Singapore) for sharing GVF software code. I would also like to thank my present and former colleagues Gino, Yanxing, Sung-Yup, Venu, Xiaofeng "Steve" Zhang, Jason, Kristina and Birjoo at Penn State University. This work was supported by NSF; Grant number: CTS 0506215.

I would also like to thank my wife Rachna for her utmost support, and encouragement when it was most required. Ruchi, your patience, love and support have made me stable and strong, especially in many such days where I spent almost 18 hours in the lab and not with you. Thank you so much for being a part of my life. Finally, I would like to dedicate this thesis to my beloved wife Rachna Sah, my grand parents, Ghanshyamdas Ailiani and Dadi, my parents, Varsha and Chandraprakash Ailiani, sister, Kripa, in-laws Mira and Anil Kumar Sah, Anita and Rajesh Bajaj, Sunita and Parmanand Bhatia, Raju and Renuka, Siddarth, Arpit and Shruti, my cousins, Divyansh, Anmol, Aditya, Vikram, Krishna and Vyom. Their support kept me going in last 8 years of my student life.

Chapter 1

Introduction

The gastrointestinal (GI) system plays an important role by participating in ingestion, digestion, transportation of food and evacuation of stool [1]. Food is mixed in the stomach and passed onto small intestine in the form of a viscous fluid termed "chyme". The GI tract (also known as gut) governs the process of absorption and transport nutrients to the bulk blood stream [1]. The process of digestion, mixing of chyme, absorption of nutrients and eventual evacuation of stool is highly complex and is linked via interdependent systems spanning the macro, micro and molecular scales. The macro-scale deformations ($1 - 2$ cm scale) of the lumen are induced by neurophysiological changes in the muscle tone. The transport and mixing of chyme at the macro-scale rely on contractions induced by muscle layers lining the gut wall. The motility of the gut is very complex and alters with caloric content of the food, different stages of digestion and emotional state of the person. Thus, it is challenging to accurately describe different motility patterns of the gut and in general, it can be categorized into two dominant patterns, peristalsis and segmental. These two

dominant motions essentially characterize the function of small intestine [2, 3]. Peristaltic motion represents a traveling wave that propagates chyme from the proximal (duodenum) to distal areas of the GI tract. In contrast, segmental motions represent radial constrictions at fixed locations along the GI tract and are essential to the macro-scale mixing of chyme.

The inner wall of the gut, also known as mucosa, is lined with columnar epithelial cells [4, 5]. The epithelial cells of mucosal surface are covered with small finger-like projections called villi ($\approx 100 - 200\mu m$ scale) [4, 5]. Thus, macro motions transport food material in both axial and radial directions, mix chyme, and nutrients in the lumen come in contact with villi and are then transported across epithelial cells. This project argues that something else (villi motion) is needed for micro-scale transport to the surface. We hypothesize that villi move under a controlled motion and improve the efficiency of absorption. The epithelial cells are covered with dense border of micro-villi ($\approx 1\mu m$ scale) that directly participate in the process of absorption. The nutrients are rapidly absorbed from the fluid near the mucosal surface creating a diffusion gradient across the lumen [6]. The nutrients are then transported radially from the center of the lumen either via slow diffusion process or advective fluid motions.

Few models have been proposed to understand the rate of nutrient absorption within an intestinal lumen [6]. The well-known "unstirred layer" (USL) model assumes that the center of the lumen is an active site for stirring and an unstirred layer is formed at the boundary of the lumen [6]. The macro flow motions of chyme result in the transport of nutrients to the surface where they can potentially interact with villi. Our hypothesis is villi movement causes micro-mixing within the USL and reduces the time scale required for nutrients to reach epithelial cells. We further hypothesize that the coupling of macro

and micro mixing leads to efficient mixing and absorption of nutrients. In order, to have a thorough understanding of the effects of macro motions on the transportation, mixing, and absorption of nutrients, we propose a computational model which focuses on multi-scale processes of the gut. Our aim is to couple *in vivo* experimental data with computational models of small intestine motion at the macro scale and villi movement at the micro-scale. The focus of this thesis is to non-invasively acquire time resolved *in vivo* macro motions of the small intestine in rats using dynamic MRI and quantitatively characterize data that will help in computational fluid dynamic (CFD) modeling of the macro motions. The motility acquired using dynamic MRI represents physiologically relevant, true *in vivo* details of gut motion.

The normal motility of the small intestine is disrupted in various GI diseases and pathological conditions such as type II diabetes, dyspepsia, irritable bowel syndrome (IBS), diarrhea, and celiac disease (CD) [7]. It is well established that peristalsis is reduced during anesthesia while segmental contractions still occur [8–10]. The processes responsible for these diseases are not fully understood but new ideas have been proposed to determine the link between the pathophysiology and dysfunction of the GI system [11]. The overall aim of thesis is to (1) quantify and characterize motility patterns of small intestine, (2) determine the underlying mechanism of the gut and (3) characterize the influence of general anesthesia on GI motility in rats. A brief description and applications of the current study is discussed in the following section.

1.1 Description of the current study

The foundation of this thesis is:

To develop an accurate geometry model of macro motions of small intestine under true in vivo conditions and couple experimental data with another study that uses computational fluid dynamic (CFD) model to predict fluid motions and nutrient absorption. The objective of the joint study is to understand mixing, transportation of nutrients, and absorption processes in the small intestine. A non-invasive contrast enhanced dynamic MRI was employed to measure motility of the small intestine in rats without extensive animal preparation. A unique combination of image processing algorithms have been applied to time resolved MRI data of small intestine to overcome breathing artifacts and improve several MRI imaging issues such as contrast and signal to noise ratio, which are not present in invasive methods. In order to understand the source of motility peaks in the frequency spectra and decompose the complex gut signal into independent modes, a principal component analysis (PCA) and Fourier decomposition was applied to time varying motility of GI data. The quantitative analysis, PCA, and Fourier decomposition can bring in new knowledge about the underlying motility of small intestine with implications to physiology. A dynamic MRI approach was also applied to evaluate effects of anesthesia on motility of small intestine. The results of the quantitative analysis, simplified geometry model, PCA, and Fourier modes can be coupled with the CFD model to better understand mixing and absorption processes at the macro-scale.

The current approach in solving this problem could also be applied to (1) assessing physiological parameters of the gut in diseased animal models such as diabetes, irritable

bowel syndrome, diarrhea, Celiac disease and Crohn's disease; (2) humans and clinical settings to determine the underlying physiology of human gut; (3) assessing the efficacy of drugs to treat motility of the small intestine; (4) simulations and building computer models for normal and diseased states of the gut; (5) understanding neurophysiology of the small intestine; (6) quantifying the motility of other parts of the gut such as the large intestine and colon; and (7) optimizing animal protocols of the study. A brief review of different methods to study gut motility, their limitations and acquisition of gut motility using our approach is discussed in the following section.

1.2 Methods to assess gut motility

The methods used to assess GI motility can be broadly divided in invasive, minimally invasive and non-invasive. Within the data acquired, the GI motility assessment methods can be further classified into *in vitro* or *in vivo* and imaging or non-imaging.

Various invasive techniques have been used for estimating the motility of the small bowels in animal studies. The *in vitro* technique known as the Trendelenburg method (see Figure 1.1a) has been extensively used to study segments of the intestine that have been exteriorized from animals postmortem [8, 12–16]. The motions are acquired using simultaneous video imaging and electromyography (EMG) to record pressure levels at different regions along the small intestine. *In vitro* techniques are lacking because they do not capture true physiological gut motions and the mucosa of the small intestine degrades within the few hours after the onset of experiments. The Trendelenburg method has also been modified

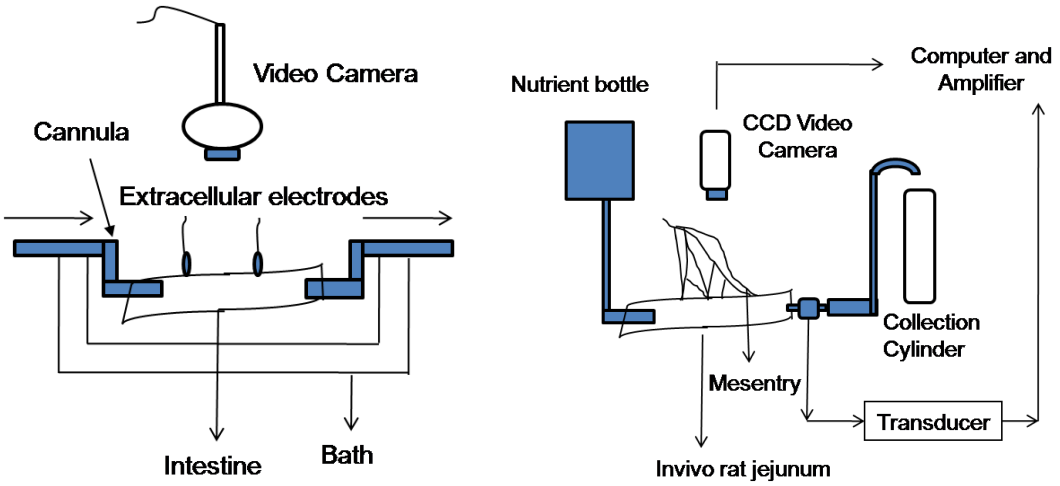

(a) *In vitro* Trendelenburg (b) *in vivo* Trendelenburg

Figure 1.1. Illustration of (a) *in vitro* Trendelenburg (adapted from [14]) and (b) *in vivo* Trendelenburg (adapted from [18]) method used to assess gut motility in dead and anaesthetized animals, respectively.

(see Figure 1.1b) to study *ex vivo* animal models in which a segment of the gut is exteriorized in an anesthetized animal while maintaining its nerve and vascular supply [17, 18]. These *ex vivo* conditions prevent the degradation of the mucosa but may not provide an accurate representation of *in vivo* gut motility. These experiments are mostly terminal, cumbersome for long-term monitoring, and can cause distress for the subjects. Another invasive approach is impedancometry, which uses electrodes and strain gauge transducers implanted within the serosa or smooth muscle of the gut to trace progress of food particles and quantify propagation velocity and muscular contraction frequencies [19]. A non-invasive approach can acquire gut motility under true *in vivo* conditions without extensive animal preparation and continuous monitoring for longer time intervals.

Non-invasive and minimally invasive methods have been applied to both human and animal studies. They can be further categorized into imaging and non-imaging. A non-imaging approach such as manometry is minimally invasive and records intraluminal pressure levels

using long catheters inserted into the lumen under anesthesia. These procedures provide indirect measurements of gut motility and are sparsely used as it can cause discomfort to the patients. Imaging-based methods such as radiography, ultrasound, and magnetic resonance imaging (MRI) are completely non-invasive and are used in clinical and pre-clinical fields. A non-invasive method to study gut motility in unanesthetized animals such as dogs, pigs and rats has been proposed by Ehrlein and colleagues [3, 20, 21]. This method uses radiography or video fluoroscopy while recording motility with previously implanted strain gauge transducers. Radiography can be used to obtain two-dimensional (2D) temporal images of the cross-section of the intestine. These experiments and other non-invasive techniques such as contrast enhanced X-ray radiography can be inappropriate in humans for long, repetitive data acquisition due to ionizing radiation. These techniques also require extensive tissue and animal preparation and monitoring throughout. As the radiography is being performed on unanesthetized rats, the temporal data of gut motility represents the undisturbed true physiological state of the gut. Ultrasound imaging is not preferred due to poor image quality and is highly user dependent. On the other hand, MRI has gained acceptance in clinical imaging of the small intestine due to its non-invasive, non-ionizing nature, excellent soft tissue contrast, 2D and 3D imaging in any plane, fast repetitive image acquisition, and longer time intervals [22, 23]. In MRI, the paramagnetic contrast agent gadolinium can be used to enhance the contrast of images and allow easier delineation of the boundary and lumen of the gut wall [23]. MRI has been used on humans for diagnosing early signs of Crohn's disease [24–26], quantifying peristaltic frequencies with and without drugs [23], acquiring functional information such as water flux and water content in the small intestine [27], and assessing contrast agents for small bowel disease [28–32].

The majority of MRI studies are employed on humans for qualitative evaluation of mucosal lesions and discoloration of the lumen and sometimes on time resolved motility of the small intestine. Few MRI studies have been carried out to study the small intestine of animal models [33] and none with quantitative analysis of segmental and peristaltic motions. The thesis presents the first quantitative, *in vivo* results of both peristalsis and segmentation in rat models. Rats were chosen since they easily fit within the bore of the magnet and are easier to gavage and anesthetize. Furthermore, several peristaltic studies have been conducted on rats using invasive approaches and can provide a good comparison and validation for measured MRI parameters. The utility of MRI is very high because it captures the true physiological gut motion and overcomes several limitations outlined earlier. However, MRI still faces several issues that are not seen in invasive techniques.

In comparison to invasive imaging modalities such as the Trendelenburg method, *in vivo* MRI faces several challenges such as motion, localization of the jejunum region, the tradeoff between temporal and spatial resolution, and much lower image contrast-to-noise and signal-to-noise ratios than in video techniques. In image acquisition using dynamic MRI, post processing and image analysis methods for analyzing motility of the small intestine should have the following requirements: (1) the positional information of the jejunum region of the small intestine should be obtained before acquiring dynamic motion; (2) as data is acquired from live animals, the dynamic image sequence should be free of breathing artifacts and animal movements; (3) the dynamic data should be acquired at a sufficient rate to reflect temporal changes, reasonable contrast, and spatial resolution to delineate the boundaries of the small intestine. In order to address these issues, administration of an oral contrast can improve visualization of the GI tract, and a combination of image and signal processing

techniques can improve the quality of data for analysis. This discussion leads to the overall goals and specific aims of this thesis. The overall goals of this thesis can be categorized into technical, physiological, and computer modeling. The specific aims to achieve these are discussed within each category.

1.3 Overall Aims

1. ***Technical.***

Specific Aim 1: Non-invasive acquisition of macro gut motions using dynamic MRI.

The aim of this step was to develop a 3D, dynamic MRI protocol for image acquisition of the jejunum region of the small intestine in rats. Dynamic and gadolinium based contrast enhanced MRI was performed on the rats to acquire the motions of the small intestine. A 3D spatial multi-slice data set covering the entire GI tract was acquired to aid in mapping the individual small intestine. Dynamic images of the localized small intestine were acquired at ≈ 6 frames per second using a gradient echo pulse sequence to capture the gut motion.

Specific Aim 2: Develop image analysis methods to produce data for local space time changes in geometry of the small intestine.

After image acquisition the next step was to develop a 3D image segmentation tool to delineate the small intestine boundary. The other post processing steps included: (1) registration to correct breathing artifacts, (2) linear interpolation to replace missing images, and (3) spatio-temporal maps for simplified and compact representation of the gut motility.

The first step in image analysis was to align all the images based on a standard 2D rigid registration procedure to correct artifacts induced by the animal's breathing and movement. In situations of large shifts, missing images were linearly interpolated in time. The next step in quantitative analysis of gut motion was to perform accurate 2D space + time image segmentation. We applied a novel hybrid of two segmentation algorithms: a 3D live wire (LW) and dynamic directional gradient vector flow snakes (DDGVFS). The segmentation step outputs a vector of data containing x and y coordinates of the small intestine boundary. In order to generate spatiotemporal maps, a 2D thinning algorithm based on the formulation by Saha et al. [34] was employed, followed by the application of a branch deletion algorithm as described by Kiraly et al. [35] to the segmented images to compute a smooth medial axis. The medial axis was computed for each image in time and a 2D function $D(x,t)$. Values representing the diameter at each point along the medial axis (x) and in time (t) was derived from the Euclidean distance maps of segmented binary images. $D(x,t)$ was represented as space-time iso-contour plot, in which one axis is the distance along the medial axis and the other axis is time. These maps were used together as a unit to represent complex gut motility patterns.

2. ***Physiological.***

Specific Aim 3: Quantitative analysis and characterization of dominant motions of small intestine.

The next step was to quantify the details of gut motility to learn which classes of gut motion are dominant in rats under true *in vivo* conditions. The motility patterns of the small intestine were identified using spatio-temporal maps. Various physiological parameters such

as maximum and minimum diameter of the gut, frequency of constriction, peristalsis speed, etc were derived from spatio-temporal maps. It was possible to view the spatio-temporal maps as 2D plots, which provided a simplified and compact representation of dynamic MRI movies of the small intestine. The complex patterns were easily identified in the maps that were otherwise difficult to distinguish in the original video sequence. The first motivation of this aim was to compare the physiological parameters acquired using MRI to the results of invasive procedures from the literature. Several invasive studies have been carried out to study peristalsis in rat jejunum and thus provided a good comparison for this thesis [17,18].

Specific Aim 4: Determine underlying mechanism of motility of small intestine with implications to physiology.

The spatio-temporal maps are a simple representation of motility patterns acquired using MRI and do not offer any perception about underlying mechanism of gut motility. Quantitative analysis and sophisticated modeling approaches such as principal components and Fourier modes were employed to determine underlying order and gain insight on the complex motility of the gut. The next aim was to discover an underlying mechanism within the intricacy of gut wall motions and their neurophysiological control. The first approach involved the integration of 3 analytical techniques applied to MRI data of the rat jejunum: principal component analysis (PCA) using active shape models (ASM), spatio-temporal maps, and frequency analysis. PCA computes dominant eigenvectors of the time-varying GI data and decomposes gut motion into a finite number of independent modes. The temporal nature of the lumen geometry was reconstructed using the first few principal components. The spatio-temporal maps and frequency analysis of decomposed modes was used to visualize

and quantify dominant modes of small intestine. The second approach was based on Fourier decomposition and was employed to determine the source of more than one frequency peak in segmental motility.

Specific Aim 5: Determine the effects of anesthesia on peristaltic and segmental gut motility.

The feasibility of our approach was tested by applying dynamic MRI to two groups: rats anaesthetized with either isoflurane or inactin. These are commonly used anesthetics in animal experiments and have differential effects on the gut motility. The purpose was to non-invasively determine, how the basic peristaltic and segmental gut motions were affected by specific types of anesthesia.

3. ***Computer modeling.***

As outlined earlier the central aim of this thesis was to couple experimental MRI data with computer simulations and CFD modeling. Various researchers have used information acquired from different imaging techniques to characterize mechanical and physiological functioning of different parts of the GI system such as the stomach [36–38]. Computer modeling can predict pressure gradients and fluid flow within the GI system. In a similar manner, with input from the quantitative analysis of dynamically acquired MRI data of the rat, such as diameter of the small bowel as a function of space and time, frequency of contractions, speed of propagation, etc, a lattice Boltzmann model showed how the wall movements affected the fluid flow in the small intestine. The basic modes of peristaltic and segmental motility decomposed with PCA and Fourier decomposition can be coupled

with CFD models to determine their physiological relevance and effects on absorption and transportation characteristics.

CFD modeling of the macro motions without villi and macro motions coupled with villi under the lattice Boltzmann framework is being carried out by Gino Banco and Yanxing Wang under the supervision of Dr. Brasseur in the mechanical engineering department. This interdisciplinary program was funded by National Science Foundation (NSF) via grant CTS-056215. The MRI experiments and development of image analysis algorithms to derive physiological parameters were carried out by Amit Ailiani under the supervision of Dr. Webb. Most of the MRI experiments were carried out under the supervision of Research Scientist, Thomas Neuberger, at Huck institute MRI center. Animal care and preparation of animal experiment protocols were carried out by Dr. Smith. A summary of quantitative and image analysis steps of the current study is reviewed in the following section.

1.4 Summary of image analysis

Even with the introduction of an MRI contrast agent, the dynamic images of the jejunum have relatively low signal-to-noise and contrast-to-noise ratios (compared to video images produced using Trendelenburg method) and exhibit rapid changes in morphology including deep indentations of the gut. The image registration tool can be used for automatic detection of images that are affected by the animal's breathing and movement. The image segmentation tool that combines 3D LW and DDGVFS can accurately segment registered 3D data of the small intestine with minimal user intervention. A thinning algorithm in combination with multi-stage branch deletion can be applied to the binary images of ac-

quired gut motility to produce a smooth medial axis. A highly curved and twisted medial axis was computed for every image in time. The medial axis was sampled with equidistant points and the diameter of the gut was calculated for each point along the length of the gut (x) and in time t ($D(x,t)$). All MRI data sets were processed with the aforementioned steps and the outputs were then used to construct spatio-temporal maps. The complex gut motility acquired over $\approx$ 1000 images was condensed onto a 2D image and distinct patterns of peristalsis and segmental motility were identified. The physiological parameters such as dominant frequency of motility, amplitude of constriction, speed of propagation were quantified from spatio-temporal maps. The image analysis algorithms for 3D image segmentation, 2D image registration, 2D active shape models, and frequency analysis were validated for simple cases and then applied to real MRI data.

The remainder of the thesis is organized as follows. Chapter 2 is an overview of the anatomy and physiology of small intestines in humans and rats and past work evaluating gut motility in humans and animal models. A summary of our approach, basics of MRI, MRI image acquisition, literature review, and the theory behind different image processing algorithms such as image segmentation, thinning and active shape models are discussed in Chapter 3. Along with detailed background material, Chapter 3 introduces dynamic MRI of the small intestine and image processing algorithms to analyze the motility of the small intestine. Chapters 4-6 then describe in detail the application of these methods on data collected from the small intestine in rats anesthetized with isoflurane and inactin drugs. Chapter 4 studies the effects of isoflurane anesthesia and compares measured data with values in the literature. Chapter 5 presents the detailed principal component analysis and

the physiological relevance of decomposed modes of isoflurane data using Specific Aim 4. Chapter 6 compares the effects of isoflurane and inactin drugs on the motility patterns and physiological parameters of the small intestine in rats. Finally, Chapter 7 summarizes the thesis contributions and discusses the future work.

Chapter 2

Background

In this chapter, the relevant background material for the project will be discussed. The discussion is meant to cover previous research in the field of GI motility and methods to evaluate GI motility. The chapter will outline the anatomy and physiology of small intestine in humans and rats, GI pathologies, various methods of assessing gut motility, limitations of previous work and the motivation for our approach.

2.1 Anatomy and function of small intestine

The gastrointestinal (GI) tract is a long hollow tube which runs from the mouth to the anus (see Figure 2.1) [4]. Swallowed food is pushed through the esophagus and into the stomach by peristaltic contractions of the esophageal wall [4]. The stomach is connected to the esophagus and releases chyme into the duodenum of the small intestine [4]. The functions of the stomach include temporary storage of food material to initiate processing food particles into chyme, and dispensing of chyme into small intestine [4]. The stomach is connected to small intestine via pylorus and the transport of chyme into small intestine is

controlled by a valve, pyloric sphincter, found at the end of pylorus. In a similar pattern, the small intestine is connected to large intestine via ileocecal valve. Its main function is to prevent the reflux of contents of large intestine into small intestine.

The small intestine is a segment of GI tract that is distal to the pyloric sphincter of stomach and proximal to the ileocecal valve of the large intestine [4]. It is the largest segment of GI tract ($\approx$ 6.8 m) in an adult human being and is divided into three parts: the duodenum ($\approx$ 25 cm), jejunum (2 m) and ileum (3 m) [4, 5]. The lumen diameter of the ileum ($\approx$ 2.5 cm) is comparatively smaller than that of the jejunum ($\approx$ 3.5 cm).

The internal structure of the three parts of the small intestine is almost identical and participates in complex motility patterns. The internal structure of the small intestine is composed of 5 layers: *mucosa*, *submucosa*, *circular muscularis*, *longitudinal muscularis* and *serosa* (see Figure 2.2) [5]. *Mucosa*, the innermost layer, lines the lumen of the small intestine and is both highly absorptive and secretory [5]. The *mucosa* is coated with loose connective tissue, *lamina propria*, and a thin layer of smooth muscle, *muscularis mucosae*, that separates it from the *submucosa*. The *submucosa* sandwiched between the mucosa and an outer muscle layer is thick and accommodates an affluent circuitry of blood vessels and enteric nerve plexus [4, 5]. Adjoining the *submucosa* is the *circular muscularis*, which is the innermost thick layer of circular muscle cells. The outer muscular layer, *longitudinal muscularis*, is made up of thin longitudinal smooth muscle cells [4, 5]. The circular and longitudinal muscles are adjacent to each other and connected via coiled fasicles. [4,5]. The *myentric plexus*, a network of nerve fibers and ganglion cells, is located between longitudinal and circular muscles. It provides innervation from both the sympathetic and parasympathetic autonomic nervous system [5] for the GI tract. The *serosa*, the outermost layer, is

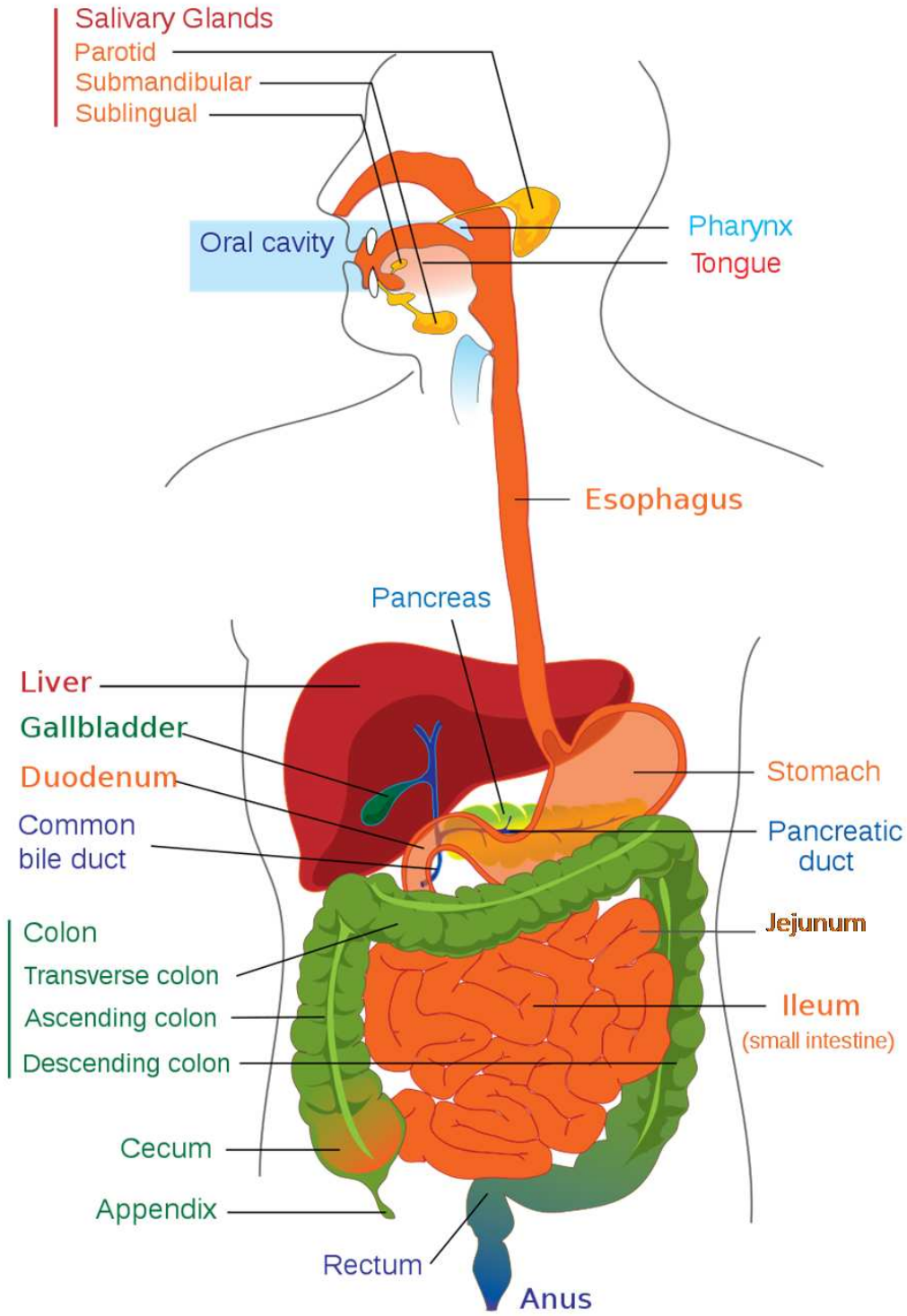

Figure 2.1. Illustration of human digestive system. The GI tract consists of the esophagus, stomach, small intestine, large intestine, colon and rectal canal. The small intestine is divided into duodenum, jejunum and ileum. The illustration is a public domain image from `http://commons.wikimedia.org/wiki/File:Digestive_system_diagram_en.svg` created by Mariana Ruiz and edited by Joaquim Alves Gaspar.

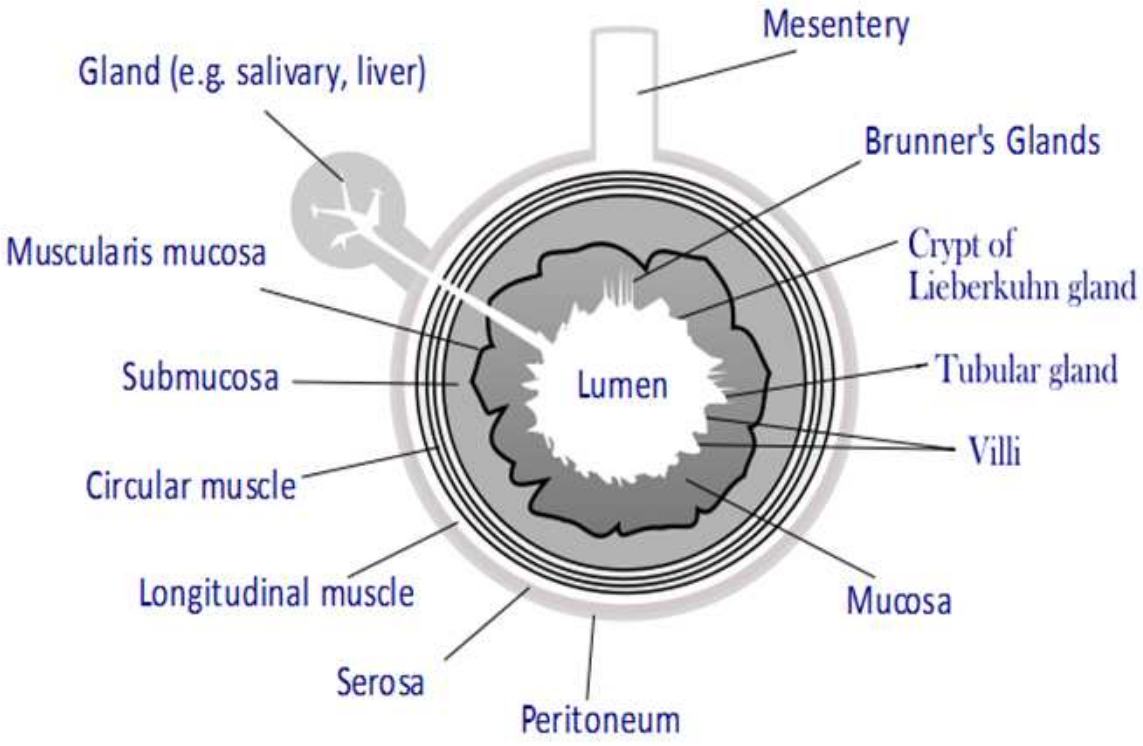

Figure 2.2. Illustration of GI tract cross section. The lumen of small bowel is composed of four well defined layers: the exterior *serosa*, *muscularis*, *sub mucosa* and the innermost *mucosa*. The *muscularis externa* is composed of longitudinal and circular smooth muscles. The illustration is a public domain image from `http://commons.wikimedia.org/wiki/File:Gut_wall.svg` created by Auawise.

composed of flat polygonal cells and loose connective tissue. The *serosa* encloses the entire intestinal lumen except a small region on the posterior wall where mesentery fastens it to the abdomen wall [4, 5].

The mucosa of small intestine harbors circular folds, depressions and projections that increase the surface area and create favorable conditions to move nutrients, and solutes from the lumen that are transferred to the vascular system [39]. The mucosal layer pleats into thick circular folds known as the folds of Keckring. The primary role of the folds is to augment absorptive surface area. The folds protrude into the lumen at different heights (3

to 10 mm) and internally circumvent either one half, or two-thirds, or entire circumference of the lumen depending on the location. The entire mucosal layer, surface of the folds, and the area between the folds are embedded with microscopic finger-like projections known as *villi* [40]. The height of villi varies from 0.1 to 0.2 mm [40]. The epithelial cells of the mucosal layer are backed by a layer of loose connective tissue, the *lamina propria*, which participates in the formation of villi (see Figure 2.5).

Thin strands of smooth muscle fibers, derived from the *muscularis mucosae* are present in the *lamina propria* and extend to the villi tips. The base of villi is part of the *lamina propria* and are served by mesh of capillaries, nerve fibers and a central lacteal, which runs along the longitudinal axis of villi to transport absorbed nutrients to the blood stream [4]. An extended row of epithelial cells cover the small intestine lumen and villi [40] (see Figure 2.5). The apical side of epithelial cells are further equipped with a striated dense border of 1 μ m microscopic rods known as microvilli [40] (see Figure 2.5). The microvilli increase the cellular surface area and directly participate in the process of absorption. Thus the epithelial cells along with villi and microvilli are considered principal contributors in the process of absorption [40].

The function of the small intestine can be compared to mixing and pumping equipment [5]. The products resulting from digestion are absorbed in the duodenum, jejunum and ileum regions across the epithelial lining of small intestine [5]. Once nutrients have been absorbed from chyme, chyme residue is depleted of nutrients, becomes insubstantial, and is emptied into the large intestine [5]. The large intestine absorbs water and some vitamins from the residual chyme and waste material is excreted out of body through the rectum and anal canal [4, 5]. The main function of the small intestine is to supply nutrients, vitamins,

minerals and electrolytes to the entire body.

The rats were chosen as animal subjects for the current study. The anatomy, physiology and functioning of GI tract in humans is in considerable agreement with rat species except for some distinct differences [39]. The differences in the anatomy of human and rat small intestine are discussed in the following section. The detailed physiology underlying the processes of transportation, mixing and absorption processes of small intestine are discussed in Section 2.3.

2.2 Differences in anatomy and motility of rat and human small intestine

Humans (75 Kg) weigh exceedingly more than rats (250 g), but the length the human GI tract is ≈ 5.5 times the length of the rat's intestinal tract. Like humans, the small intestine in rats can be divided into three sections: the duodenum (≈ 9.5) cm, the jejunum (≈ 90 to 135 cm) and the ileum (≈ 3.5 cm) [39, 41, 42]. An anatomy of rat's GI tract and an isolated straightened sections of GI tract are shown in Figures 2.3 and 2.4, respectively. The small intestine in rats constitute about 83% of the entire GI tract with the jejunum comprising $\approx 90\%$ of the length. The human small intestine constitutes about 81% of the entire GI tract, with the jejunum region comprising only $\approx 38\%$ of the length [39, 41, 42].

The rat and human small intestines possess different features that increase the surface area and enhance the process of absorption and mixing. The human small intestine houses many folds of Keckring, which are not found in rat small intestine. Both species have numerous villi that increase the surface area by a factor of 5 and 10 in rats and humans,

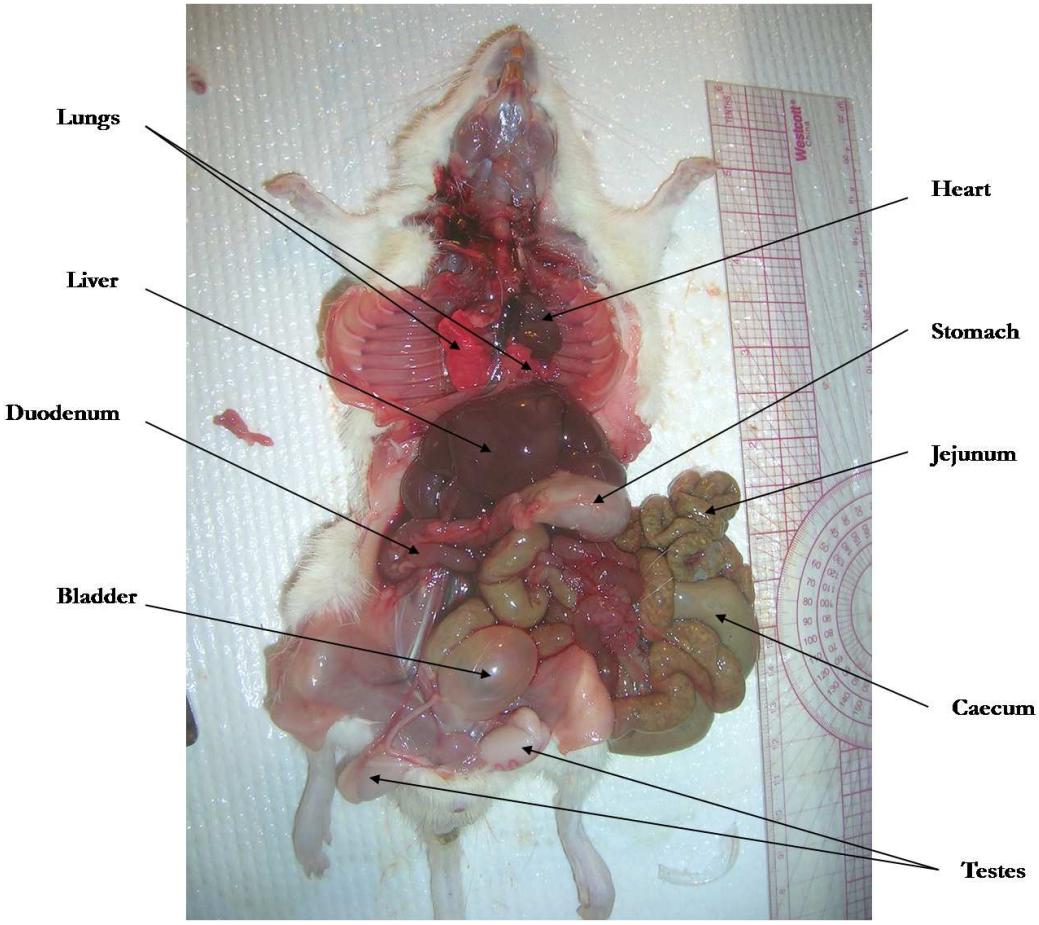

Figure 2.3. Picture of rat's GI tract. The GI tract is divided into the stomach, small intestine and large intestine. The small intestine is further divided into the duodenum, jejunum and ileum. The jejunum region consists of 90% of the entire GI tract. The aim of thesis was to acquire the motility of the mid jejunum region using dynamic MRI. The image was obtained from Gino Banco and the rat dissection was performed under the supervision of Dr. Nadine Smith.

respectively [39]. The human and rat small intestine both possess enterocytes (mainly found in duodenum and jejunum) lined with microvilli that increase the surface area by a factor of ≈ 20 [39, 41–43]. A large surface area exists in the jejunum region and is mainly due to the folds of Keckring in humans and comparative length of jejunum (90%) in rats.

The approximate values describing the gut motility and transit time are presented in the literature. The values are approximate, as such parameters can vary and depend on the

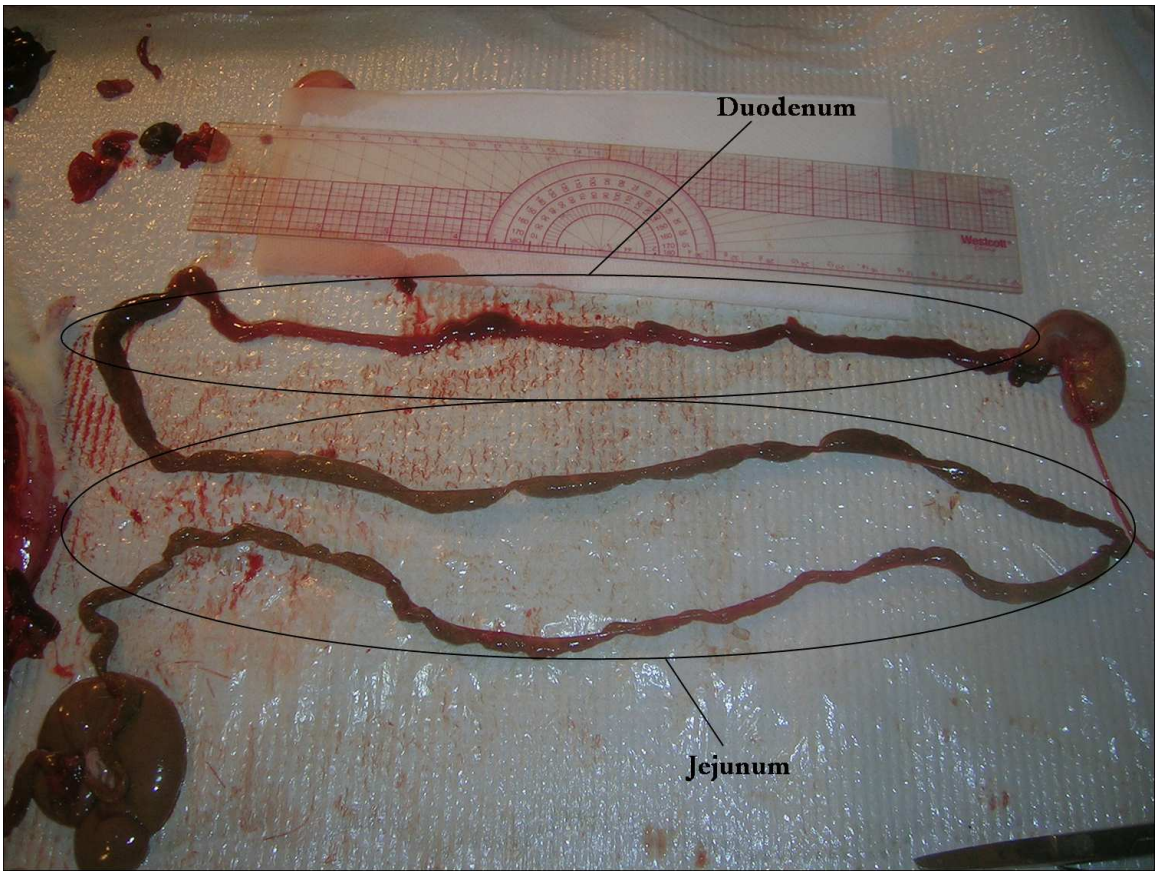

Figure 2.4. Picture of isolated rat small intestine. The small intestine is divided into the duodenum, jejunum and ileum. The jejunum region consists of 90% of the entire GI tract. The aim of thesis was to acquire the motility of themid jejunum region using dynamic MRI. The image was obtained from Gino Banco and the rat dissection was performed under the supervision of Dr. Nadine Smith.

nature of luminal contents and state of the gut (fasting vs. fed state) [39]. Transit time is defined as the total time taken for chyme to pass a section of GI tract [39]. Transit time in human small intestine is $\approx 3-4$ hrs and traverses at a speed of $1-4$ cm per min [43]. As in humans, the transit time in rat small intestine is also $\approx 3-4$ hrs but the speed of propagation is relatively slower. The speed of propagation gradually decreases from oral to caudal sections of small intestine [39, 44] in rats.

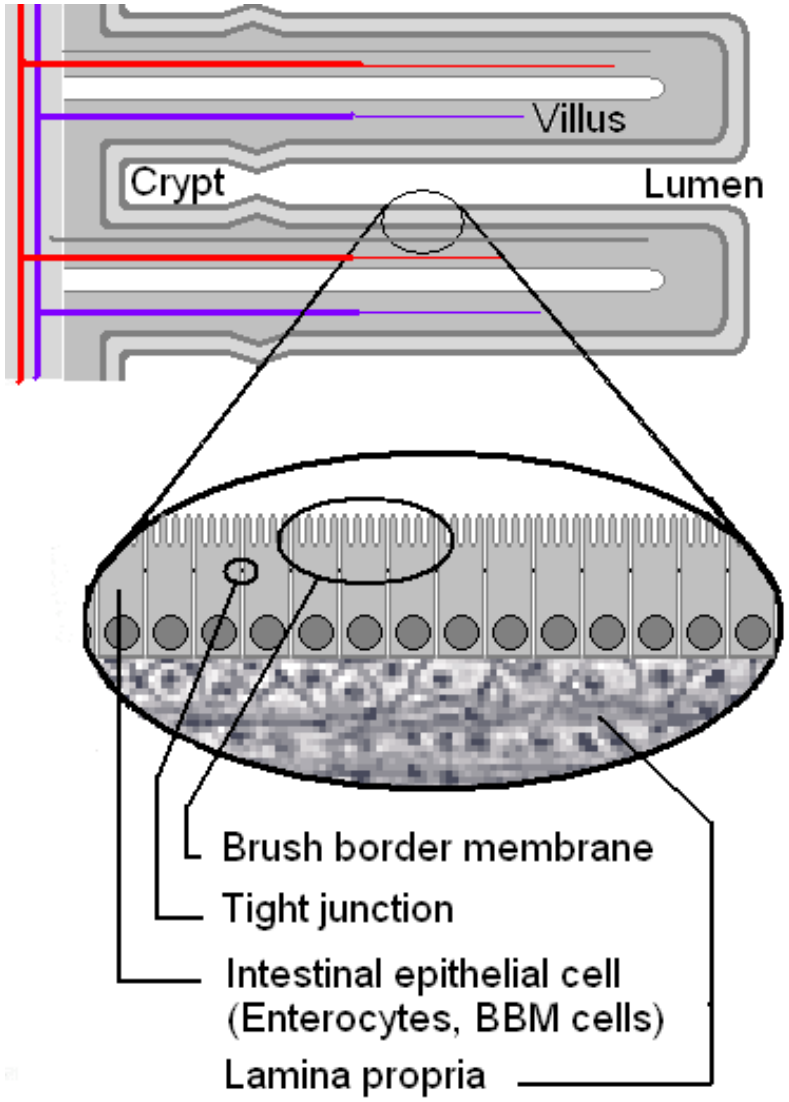

Figure 2.5. Illustration of the arrangement of villi and microvilli. The villi are small finger like projections protruding into the lumen of small intestine. The close proximity of villi and microvilli increases the surface area for better nutrient absorption. The illustration is a public domain image from `http://upload.wikimedia.org/wikipedia/commons/0/0f/Normal_Villus_Illustration.png` created by author Pdeitiker on wikimedia commons.

2.3 Physiology of the small intestine

The process of digestion, transport and mixing of chyme and absorption of nutrients is highly coupled bridging macro, micro and molecular scales. The lumen of the small intestine is

surrounded by the layers of circular and longitudinal smooth muscles. The macro scale deformations of the small intestine are induced by simultaneous contraction and relaxation of smooth muscles, controlled by neurophysiological changes in the muscle tone. Macro motions induce transport and mixing of chyme and transport nutrients to the mucosal surface lined with villi. Nutrients are then absorbed into the blood stream. Most nutrients are absorbed in the jejunum region and hence the central aim of this thesis is to evaluate and quantify the motility of jejunum region of the small intestine. The luminal contents are propagated and mixed by a variety of muscular contractions.

It is now known that the complex motility patterns of the small intestine are induced by the unified control of circular and longitudinal muscles either via chemical or hormonal changes in response to a meal or neuronal impulses from enteric and central nervous system [45]. The enteric nervous system, also known as "little brain," can function independently and induce contractions by local neuronal signals and activate the slow waves of smooth muscle cells [1, 45]. It is assumed that chains of motility patterns are a result of internal stimuli [45]. Different motility patterns arise with the type and caloric content of the meal. While significant advances have been made in understanding the complex mechanisms of gut function, many details remain unclear. Different motility patterns have been identified by researchers in clinical and pre clinical models. The two most important modes or motility patterns described in the literature are peristalsis and segmental.

Abbott and Pendergrass described short waves as segmental and long waves as peristaltic [46]. Peristaltic motility is depicted as a propagating wave initiated by contractions in circular muscles and travels only in the aboral direction [3, 47, 48]. Peristaltic motility is a dominant feature after the ingestion of a non-caloric meal and propagates chyme caudally [3].

Different types of peristaltic contractions described in the literature include: (1) weak and short distance and (2) strong and long distance waves. The latter form of peristaltic waves transport food from proximal to distal end of the gut [49]. Peristaltic gut motility is initiated by the enteric nervous system and the frequency and velocity of contractions are determined by the frequency and velocity of slow waves traveling distally.

In contrast to peristaltic motility, segmental motility appears at unique isolated locations along the gut, obstructing the lumen by pushing chyme in opposite directions and dividing the lumen into segments. Segmental contractions are often induced after the ingestion of a high caloric meal. In contrast to peristalsis, segmental contractions are stationary and instead mix chyme. Bayliss et al. were the first to describe segmental motility in response to different stimuli, which they referred to as pendular movements [47, 48]. Cannon later confirmed that segmental movements were stationary and did not appear as pendulum movements as observed by Bayliss and Starling [49]. The other variations of segmental contractions have been reported by Grivel and Ruckebusch. The recorded motility revealed segmental contractions with a propagating component in the fed state. Ehrlein et al. have done an exhaustive study on gut motility in dogs and reported different motility patterns in the fed state: short and long peristaltic waves, individual and clustered stationary segmental contractions [3]. Ehrlein et al. have also reported phase III motility pattern in the fasting state. They are also referred as the inter digestive "migrating motor complex" (MMC) and are characterized by peristaltic waves traveling large areas of intestine [3]. The aim of this thesis is to understand dominant motility patterns during the fed state and therefore motility patterns like MMC are not discussed in detail.

It has been proposed in the literature that segmental contractions induce advective

fluid motions that assist in the mixing of chyme. The nutrients are transported from the center of the gut to near surface region and the nutrients have to pass a region governed by diffusion process. The advective fluid motions are inhibited in this area and thus transport is dependent on slow diffusion process to reach absorptive surface area.

It is well known that even after thorough mixing in the center of the lumen, an USL is formed at the surface of the lumen [50]. Numerous studies have implied USL of 600μm for humans and 300 - 900μm for animals [50]. Dietschy *et al.* performed first studies on animal models and brought to light that the USL plays an important role in the process of intestinal absorption [51, 52]. Strocchi *et al.* have suggested that an USL of 300 - 900μm does not have any physiological relevance and would impede the normal absorption of nutrients. For example, if glucose molecules must diffuse across a thickness of 600μm, the absorption process will be very slow and only 1% of the luminal content will be absorbed [50, 53, 54]. Such low rates of absorption contrast studies that suggest 30% to 50% of total glucose taken into body is absorbed within a few minutes after the chyme has entered the small intestine [50, 53, 54]. Strocchi *et al.* have argued that *in vivo* estimations of the USL have been carried out on animals undergoing surgery and deep anesthesia [50]. These conditions cause the small intestine to have abnormal or no motility and thus do not represent true physiological conditions [50]. The *in vivo* studies performed on conscious animals with cannulas implanted before actual measurements revealed that an USL of much smaller size (100μm) than those in invasive studies (300 to 900 μm). Recent studies carried out by Levitt *et al.* used a different approach and have reported that USLs are physiologically relevant and are ($< 40\mu$m) [6, 55]. These results suggest that under true *in vivo* conditions the small intestine maintains a much narrower USL and contractions of longitudinal and

circular muscle induce efficient macro mixing. They have also postulated that a thin USL is induced via contractions of villi at the absorptive surface rather than the mixing of chyme at the center of the lumen. Along similar lines we speculate that the presence of smooth muscle fibers within villi control the pumping action of villi. The villi movements cause micro fluid mixing motions within the USL and thus enhance the process of absorption. The motivation and different aspects of the current study are highlighted in the next section.

2.4 Description and motivation of current study

The macroscopic contractions may play an important role in transporting nutrients from the center of the lumen (nutrient filled regions) towards the periphery of epithelium (nutrient depleted regions). These contractions may not be effective in transporting the nutrients across USL, where nutrients are mainly transported by slow diffusion process. The presence of smooth muscle fibers within villi, have prompted speculations on the role of villi at micro scales during nutrient absorption. We propose that that the contraction and relaxation of smooth muscle fibers control the pumping action of villi and sway within the unstirred liquid layer. The movements of the villi cause micro fluid mixing motions and thus enhance the process of absorption [39]. We hypothesize that the mixing and transportation are multi scale processes and highly coupled, resulting in an overall efficient absorption of the nutrients. We further hypothesize that the controlled movements of villi induce a micro mixing layer in the liquid layer adjacent to them. It results in an efficient absorption process and reduces the time scale for the nutrients to travel across USL.

Our hypothesis is that macro motions transport nutrients from the center of the lumen

towards the surface and movements of villi reduces the time scale for the nutrients to diffuse across USL and thus increase the efficiency of absorption. The transportation and mixing processes are multi scale and are highly coupled. The central aim of this interdisciplinary program is to evaluate the role of (1) macro motions and (2) macro motions coupled with micro motions, on transportation and mixing processes. The central point of this thesis is to acquire macro motions of small intestine using dynamic MRI to couple experimental data with another study that use computer simulations and CFD models. The *in vivo* experiments were performed on anesthetized rats in the fed state. The rats were chosen as animal subjects for this thesis and several groups have attempted to study macro motions in rat's jejunum using invasive methods. The key goal of this thesis is to acquire, identify and quantify macro motions of rat small intestine. A truly non-invasive approach that can acquire the true *in vivo* state of the gut should be a prerequisite for analyzing gut motility. In many cases the quantitative analysis of GI tract motility is an important indicator of disease and progress of remediation.

We have proposed a non-invasive approach such as MRI to acquire *in vivo* motion of the small intestine without disturbing the actual gut motion and altering any physiological conditions. We have used contrast enhanced dynamic MRI because of its excellent delineation of boundary, is fast enough to acquire the motility of bowels, has acceptable spatial resolution, and uses non-ionizing radiation, allowing for longer imaging time intervals and repeating experiments on the same subjects. We have further proposed combination of sophisticated image processing tools to overcome breathing artifacts, delineate boundaries using a novel 3D segmentation approach, and perform detailed quantitative analysis using spatio-temporal maps and frequency analysis. Quantitative analysis can produce new

insights in the complex motility patterns of small intestine with implications to physiology and underlying mechanisms. To facilitate a complete understanding and produce new knowledge of acquired gut motility, we have applied sophisticated modeling methods like principal components and Fourier analysis. Small intestine functions coupled at the macro and micro scale help in efficient transport of food material, chyme mixing and absorption of nutrients. These processes are affected in various GI diseases such as dyspepsia, irritable bowel syndrome (IBS) and Celiac disease (CD). These diseases can cause mucosal lesions that impair nutrient absorption and secretion [7]. Disorders of autonomic nervous system, such as diabetes mellitus and Hirschsprung's disease, are the leading causes of GI dysfunction [1]. The understanding and quantitative analysis of the processes responsible for these diseases can provide a link between neurophysiology, normal function and dysfunction of the GI system [11]. Various anesthetics such as gaseous isoflurane, halothane, ether and injectable anesthetics such as ketamine, xylazine, morphine and alpha-chloralose have been employed in both the clinical and pre clinical fields. Anesthetics can alter the physiology and can indirectly affect the motility of gut. Thus, our aim is to non-invasively understand the effects of anesthesia on peristalsis and segmental gut motility in rats using dynamic MRI and quantitative analysis.

This interdisciplinary program was funded by National Science Foundation (NSF) via grant CTS-056215. CFD modeling motions of small intestine under the lattice Boltzmann framework is being carried out by graduate student, Gino Banco and postdoctoral scholar, Yanxing Wang under the guidance of Dr. Brasseur in the mechanical engineering department. The MRI experiments and a thorough quantitative analysis of the experimental data were carried out by graduate student Amit Ailiani under the supervision of Dr. Webb

in bioengineering department. Most of the MRI experiments were carried out with the help of Research Scientist, Thomas Neuberger. The animal care and preparation of animal protocols during imaging experiments were carried out by Dr. Smith.

Various methods have been attempted to evaluate gut motility in the last hundred years on humans and animal models. The application of methods in the clinical field requires a minimally invasive approach that is sensitive enough to detect functional and structural changes. We begin in the next section with a detailed literature review of past methods to understand gut motility. This discussion was presented to highlight several issues on the physiological relevance of acquired data and how we can overcome them in our approach. In the coming sections, we present an overview of our approach in Chapter 3 as outlined in Figure 3.1. We have covered a detailed review on the basics of MRI, image acquisition using MRI and how dynamic MRI can be applied to acquire gut motility in rats is discussed in Chapter 3 in Section 3.2. Past work in image analysis algorithms and the combinations applied in this thesis are covered in Section 3.3.

2.5 Past methods to assess motility patterns of small intestine

The methods used to assess motility patterns of the small intestine can be classified as invasive, minimally invasive and non-invasive. These methods are sub-classified by their conditions (in vivo and in vitro) and type of data acquisition (imaging or non-imaging). The invasive methods have been mainly applied in preclinical research and minimally invasive and non-invasive methods are tailored for clinical studies. An overview of the methods used

to assess motility patterns are discussed in the following sections.

2.5.1 Invasive

The invasive methods are mainly applied to animals under *in vitro* conditions where segments of the gut are isolated to understand the relationship between the ENS and motility of the small intestine. In 1917 a classic paper was published by Trendelenburg on *in vitro* experiments of the gut (see Figure 1.1a). It has been cited more than 400 times and is still being used to understand the complex patterning of the gut [56]. The original paper described an approach that first distended the gut, then recorded its motility patterns and the effects of nutrients and solutions on motility [56]. Peristalsis is the most studied motility pattern using the Trendelenburg method and segmental motility has been recently attempted by Gwynne *et al.* [14,15] . The Trendelenburg experiment was adapted by other researchers to initiate peristalsis in isolated or exteriorized segments of the gut. These experiments have been improved in order to characterize motility patterns of greater complexity. Additional data such as pressure and volume of fluid passed were simultaneously acquired and later correlated to the motility recording using video imaging.

Improvements were made to the Trendelenburg method by adding video recording [57,58] and automated image analysis of the acquired motility using spatio-temporal maps [12,59]. The isolated segments are cannulated at both ends and perfused with physiological media, e.g., krebs solution, and kept under constant tension to maintain a fixed length throughout the experiment [8,12–15,17,18,59]. The tissue was kept either in saline solution to induce peristalsis [8, 12, 13, 17, 18, 59] or flushed with specific solutions such as decanoic acid or amino acids to induce segmental type contractions and develop an *in vitro* model of the fed

state [14, 15]. The changing morphology of the small intestine is typically acquired using a CCD video camera [8, 12–15, 17, 18, 59]. Other parameters, such as an electromyograph (EMG), expelled fluid volume, and pressure levels at different regions along the segment, were recorded simultaneously and correlated with the contractile activity of the small intestine [8, 12–15, 17, 18, 59]. The *in vitro* conditions were not ideal for measuring gut motility as the mucosa of the small intestine can degrade within the first few hours after the onset of the experiment. Thus *in vitro* experiments may not reflect accurate effects of anesthesia, drugs, or solutes on the motility of the small intestine. The Trendelenburg method has been recently revised to apply under *in vivo* conditions.

Recently, Bogeski *et al.* have adapted the Trendelenburg method to acquire gut motility under *in vivo* conditions. Bogeski *et al.* have applied the Trendelenburg method to quantify *in vivo* motility of the small intestine in rats [17, 18]. In contrast to *in vitro* experiments, animals were not killed and instead were kept under constant deep anesthesia. The small-intestine was dissected out and separated from the rest of the gut, blood vessels and mesentery of the gut wall, which were still intact (see Figure 1.1b). These experiments prevented the degradation of mucosa and thus motility was observed with video imaging for longer periods. Trendelenburg experiments demanded extensive animal or tissue preparation and continuous monitoring during experiments. In addition, the modified Trendelenburg experiments were mostly terminal since animals were under deep anesthesia and underwent a major surgical procedure. Despite great efforts, the motility acquired in the modified Trendelenburg experiments may still have not represented the true physiological state of the gut. However, these drawbacks can be overcomed in non-invasive experiments, where the small intestine is not altered. A detailed literature review and type of motility

acquired using non-invasive methods is discussed in the following section.

2.5.2 Minimally invasive and Non-invasive

The minimally invasive and non-invasive experiments can be categorized into non-imaging and imaging and are mostly applied in humans and less in animals. Non-imaging experiments involve manometry and record motility in conscious animals using extraluminal transducers implanted at different areas along the length of the gut. The imaging experiments involve radiography, X-ray fluoroscopy, ultrasound and MRI.

2.5.2.1 Non-imaging

Bayliss and Starling published the first results on the motility of the small intestine in anesthetized dogs using minimally invasive non-imaging approach, water manometry [47, 48]. Connections between the small intestine and central nervous system (CNS) were disconnected and the gut was placed in a warm saline bath. The measurements were done via an instrument termed the *"enterograph"* [47]. It measured contractions of longitudinal and circular muscles as a function of pressure change. Peristaltic contractions were induced spontaneously, mechanically, or via distension of the gut by administering a bolus. A series of similar experiments were carried out in anesthetized animal models (dog, rabbit and cat) [47, 48]. In 1902, Cannon presented the first results on the use of non-invasive radiography imaging to monitor the transport of bismuth in the small intestine of anesthetized cats in a fed state [49]. Cannon described different properties of segmental and peristaltic contractions and confirmed the existence of similar motility patterns across different animal species such as rats and dogs. Simren et al. have used manometry to record motility

in humans suffering from IBS, where a diagnosis has been related to an abnormal propagation pattern of individual duodenal pressure waves. In animal studies, Schnoor et al. have shown the feasibility of long-term monitoring by acquiring measurements of GI motility from conscious and sedated porcine models using an intraluminal impedance technique with real time measurements of pressure and gut motility [19]. Manometry is sparsely used in clinical studies as it requires an insertion of a long catheter under anesthesia, which can cause distress in patients. It is also difficult to identify propagating and non-propagating contractions solely based on the analysis of pressure data.

In the later years of non-invasive technique development, imaging and non imaging methods were combined to better understand and identify complex motility patterns. Ingelfinger and Abbott combined balloon recordings with X-rays and were thus able to distinguish peristalsis from segmental contractions [60]. Grivel and Ruckebusch acquired bowel motility by measuring the electrical activity of chronically implanted electrodes in a conscious dog, sheep and rabbit. A comprehensive computer based analysis of the recorded signals was introduced by Ehrlein *et al.* who measured gut motility in unanesthetized dogs using extraluminal strain gauge transducers [61]. Before the actual recording, the transducers were surgically implanted into the axes of circular muscle at different locations along the entire GI tract. The pyloric sphincter was monitored by implanting induction coils within serosal layers of the gut. The analog circuitry was connected to digital computers and a plethora of physiological parameters such as frequency and period of contractions and time difference between contractions at adjacent sites were recorded. In 1983, Ehrlein et al. studied effects of stimulants such as 5-hydroxytryptophane and insulin on gut motility in unanesthetized dogs with simultaneous radiography and motility recordings using strain gauge transducers.

Later, Ehrlein and colleagues studied gut motility in a similar fashion and employed video fluoroscopy instead of radiography [3].

2.5.2.2 Imaging

In the following section, the applications, advantages and drawbacks of imaging modalities: radiography, ultrasound, and MRI and prior work in the field of gut motility is reviewed. The studies exclusively based on imaging do not require extensive animal preparation. The imaging based methods are commonly used in clinical studies and the motility acquired accounts for undisturbed state of the gut. The use of imaging modalities like radiography and video fluoroscopy is limited due to the amount of radiation being deposited in the subjects [23, 62]. Other imaging methods such as ultrasound and MRI use non-ionizing radiation and are useful in the GI field for detecting early signs of disease and diagnosing pathologies.

X-ray radiography:

Non-invasive procedures using radiopaque markers have been used to assess gut motility in humans suffering from type II diabetes [63]. Motility was evaluated by tracing food particles mixed with ring-shaped markers made of barium sulphate and polyvinyl chloride with abdominal radiographs acquired at different time intervals until the rings disappeared [63]. The results have shown that patients suffering from type II diabetes show a significant elongation of transit times in the lower GI tract, suggesting that the lower GI tract deteriorates prior to the upper GI tract. Ehrlein et al. have used X-ray radiography and video fluoroscopy along with implanted electrodes and strain gauge transducers in animal mod-

els [3,21,61]. These studies characterized peristaltic, segmental and complex wave patterns during the fed and fasting state in awake animals. As the imaging was performed on animal models the effects of radiation dose were not highlighted and a high radiation dose can be a limiting factor in clinical studies.

Ultrasound imaging:

Duplex Doppler has been used in clinical studies to comprehend and image peristalsis of the gut in patients with bowel obstruction [64]. The strength and frequency shift of the doppler signal was used to characterize different degrees of peristaltic contractions and localize blocked regions. In 1999, Yong-joo *et al.* performed a similar ultrasound study on canine animal models to identify small intestinal peristaltic movements [65]. The number of peristaltic waves were quantified over a 24 h period at 3 frames per second. The signals above a certain amplitude and duration threshold were considered as peristaltic contractions. On the other hand the smaller stationary contractions were not detected by this technique. As the ultrasound imaging is sensitive to pressures and respiration during imaging, it is sparsely used for GI studies.

Magnetic resonance imaging:

MRI has gained acceptance in human clinical imaging of the small intestine due to its non-invasive, non-ionizing nature, excellent soft tissue contrast, ability to obtain images in any desired plane and the prospects of acquiring functional information [23,66,67]. In GI studies, a paramagnetic contrast agent, such as gadolinium diethylenetriamine pentacetic acid (Gd-DTPA), can be used to enhance the delineation of the lumen of the gut wall

on T_1 weighted images [23, 66, 67]. The main application of MRI in humans is imaging patients with inflammatory bowel disease such as Crohn's disease [24–26, 29, 68]. Patients suffering from Crohn's disease show increased wall thickness on MR images (4 to 5 mm). MR imaging after intravenous application of contrast medium can also detect early signs of Crohn's disease such as 1) a stricture within the lumen of the small bowel, 2) the presence of deep ulcers penetrating the small bowel and 3) a pseudo mass with fibrous or fatty components [68].

MRI has been utilized in gauging gastric emptying and motility of the stomach in humans after a liquid meal [67]. Schwizer *et al.* acquired dynamic series, 60 axial images with turbo spin echo, at a time interval of 1.2 s between each image, repeated every 15 mins for total of 2 h. The propagation of individual contractions were captured on the images [67]. MR enterolysis is a minimally invasive technique to evaluate small intestine. A nasoduodenal tube is incorporated to enlarge the bowels. Patak *et al.* [62] have published a technique that distends the lumen with isapghula fibers mixed in an aqueous solution, and thus avoids the insertion of a tube. The quality of MR images was satisfactory enough to distinguish the bowels from surrounding tissues. The first experiments to evaluate the efficacy of contrast agents in imaging the small bowels were carried out by Wesbey *et al.* [33]. The paramagnetic agents, made up iron salts in the ferrous Fe^{+2} or ferric Fe^{+3} form, illuminated the stomach and gut wall in rats and humans. These paramagnetic agents are non lethal, have a powerful magnetic field around their vicinity and in turn enhances T_1 and T_2 relaxation coefficients. The intensity of the spin echo MRI signal is given as:

$$I = \rho(x, y) \exp^{\frac{-TE}{T_2}} \times [1 - \exp^{\frac{-TR}{T_1}}] \tag{2.1}$$

where I = MRI signal intensity, $\rho(x, y)$ is spatially dependent proton density, TE is echo time and TR is the repetition time. It is evident from equation 2.1 that the shortening of T_1 and elongation of T_2 enhances image intensity, I [33]. Lauenstein *et al.* have evaluated an exhaustive list of contrast agents to distend small bowel and recommended adding substances that can retain the water content of the bowels [66]. In addition to gastric emptying, MRI can be employed to evaluate peristaltic contractions, repeated diameter measurements of the bowels and effects of pro-kinetic and anti-motility drugs [23]. Froehlich *et al.* performed a feasible study, which was an extension of their previous work [62]. The subjects were given an oral drink of Ispaghula and paramagnetic contrast agent Gd-DOTA. They quantified frequencies and amplitude of peristaltic contractions before and after the injection of drugs. The images were acquired using a breath hold, 2D GE pulse sequence, acquisition time = 0.5 s, TE = 1.5 ms, TR = 4 ms, slice thickness = 10 mm, matrix size 192×256 and FOV = 500 mm. The cross-sectional diameter of the lumen over time was measured to quantify peristaltic frequencies (10.96 ± 2.51 cycles per minute) and amplitude (6.65 ± 1.15 mm) of the small bowel [23]. The intravenous application of anti-motility drug, scopolamine, resulted in the stoppage of peristalsis in 21.3 ± 2.8 s while the pro-kinetic drug, metoclopramide, enhanced amplitude contractions [23]. MRI has also replaced invasive intubation techniques to measure water fluxes in small intestine in humans. Hoad et al. have demonstrated a non-invasive way of measuring small bowel water content validated against naso-dudodenal infusion of mannitol saline solution [27]. The other applications of MRI include evaluation of the effects of prokinetic drugs, such as cisapride on gastric emptying, and gut motility in diabetic patients [69].

Thus, MRI has been mainly applied in the clinical field and very few studies have been

performed on animal models. MRI *in vivo* imaging has been applied in rats for simultaneous delineation of the gut lumen and quantifying the positional information of solid food particles. The lumen was visualized by Gd contrast agent and the food particles were localized by fluorine labeled mini capsules [33]. Thus far we have reviewed various invasive and non-invasive methods to evaluate the motility of small bowels in humans and animal models. There are distinct limitations of each method and how to overcome them is the motivation of this thesis. The limitations of past methods and big picture of this thesis is discussed in next section.

2.6 Limitations of past methods

Despite improvements, the conventional Trendelenburg method still requires extensive tissue preparation or animal surgery, and it is challenging to maintain a true physiological state throughout the experiments. A truly non-invasive method of obtaining quantitative information on GI tract mobility would be highly desirable. Manometric procedures are site dependent and are an indirect way of quantifying GI motion [23]. In addition these procedures are not straightforward and an insertion of a long catheter under anaesthesia can cause significant amounts of distress for the subjects. Thus manometric procedures are sparsely used in clinical studies [23, 62].

Conventional x-ray techniques such as fluoroscopy and radiography use ionizing radiation and thus are not preferred for frequent and elongated scans [70]. A non-invasive imaging modality like ultrasound has narrow spans while scans are highly user dependent

and difficult to replicate [70]. The extra pressure induced by the ultrasound transducer during imaging can also invoke gut movements. The application of ultrasound imaging to small bowel motility is limited as it is user dependent, indirectly interpreted, restricted by intestinal gas and inconsistent reproducibility [23]. The invasive and ultrasound imaging methods can upset *in vivo* gut motion. Despite extensive MRI work in humans, very few studies have been performed in animals, and no quantitative analysis of GI tract motions has been published. The central use of MRI of small bowels is in the evaluation of mucosal lesions and discoloration of the lumen. Few studies on the motility of small intestine exist while none contain detailed quantitative analysis.

Quantitative analysis of small intestine motility in rats have been published using either *in vitro* and *in vivo* Trendelenburg experiments or manometric procedures or implanting electrodes on the small intestine. These experiments are either invasive or minimally invasive and require extensive tissue and animal preparation and monitoring throughout. The Trendelenburg animal experiments are mostly terminal and a similar set of experiments cannot be applied on the same animal. The mucosa of the gut wall deteriorates much faster under *in vitro* conditions and remains intact under *in vivo* conditions. The recorded motility acquired may still not represent true *in vivo* gut motility. The effects of nutrients, drugs and macro molecules injected into the lumen or serosa under *in vitro* conditions may not reflect true physiological state of the gut [17, 18]. Another unifying theme of previous quantitative analysis done on the small intestine motility in rats is none used MRI.

We begin in the next chapter with an introduction to our approach covering each aspect of project starting data acquisition, animal handling and final quantitative analysis of the acquired data. We have also summarized basics of MRI and our approach in non-invasive

dynamic imaging of small intestine in rats. We then discuss a thorough literature review and theory of different image processing algorithms and their application in the current study.

Chapter 3

Overview

Figure 3.1 summarizes dynamic MRI approach and image processing algorithms applied to MRI data to analyze gut motility. The rectangular blocks denote processes and their application in the field of gut motility signify thesis contribution. The interim data is labeled between two consecutive blocks and shown via a sample image. The direction of arrow represents the order in which the processes are executed. The block-diagram has three parts, (1) simplified (solid blue), (2) integrated (solid red) and (3) Fourier analysis (solid green). A simplified analysis is used to quantify physiological parameters and visualize motility patterns of MRI data. The motility of the small intestine was further analyzed using integrated and Fourier analysis approach. The Sections 3.2 to 3.4 describe each process block in detail along with their relationship with data. Chapters 4-6 further elaborate on dynamic MRI, applications of image processing algorithms to GI motility and knowledge on physiology of small intestine, which form the thesis contribution. A detailed review on the basics of MRI and image formation, how dynamic MRI can be applied to motility of small intestine and past work in image processing algorithms is covered in Sections 3.2 to

3.3.

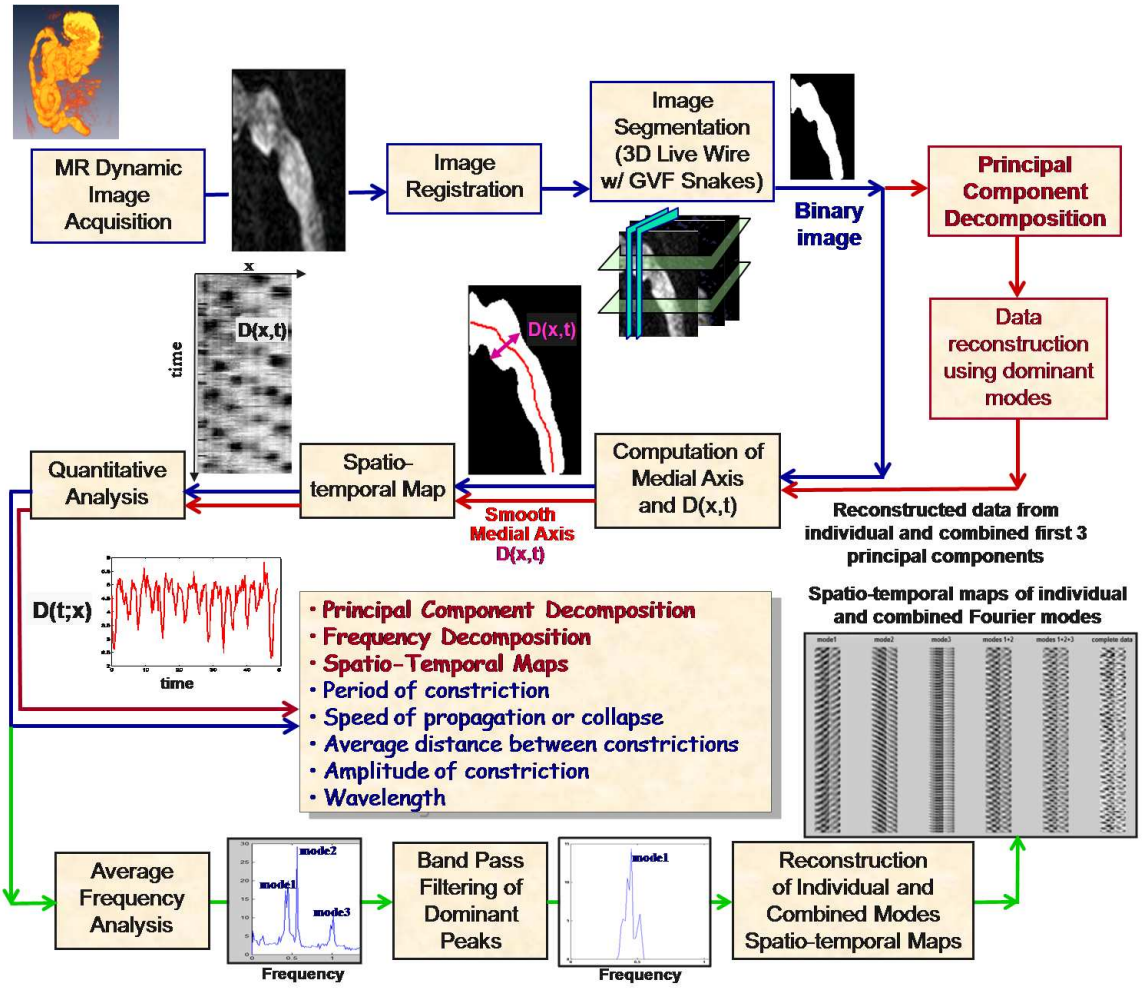

Figure 3.1. Summary of our approach. The block diagram can be divided into three parts, simplified analysis (blue line) , integrated analysis (red line) and Fourier analysis (green line). These paths connects different elements of the block diagram in a particular sequence. The simplified analysis starts from MR image acquisition and follows image registration, image segmentation, medial axis, spatio-temporal maps and quantitative analysis. The integrated analysis approach takes on a slightly different route between image segmentation and computation of medial axis blocks. The integrated analysis approach involves three analytical methods Principal component decomposition using ASM, frequency decomposition and spatio-temporal maps. Finally Fourier analysis, uses simple average frequency analysis, band pass filtering of dominant peaks and reconstruction of spatio-temporal maps to visualize individual and combined Fourier modes.

3.1 Summary of our approach

A block diagram presented in Figure 3.1, outlines the summary of our approach. We have applied non-invasive dynamic MRI to overcome the limitations of past methods, outlined in Section 2.6. The block diagram is a compact and simplified representation of quantitative analysis of MRI data. The analysis can be broadly divided into three parts, simplified analysis (solid blue line), integrated analysis (solid red line) and Fourier analysis (solid green line). These paths connects different elements of the block diagram in a particular sequence and are explained further.

A simplified analysis (blue path) starts from MRI image acquisition block and ends with quantitative analysis block. Dynamic MRI can be applied without extensive animal preparation and can acquire true *in vivo* physiological motion of the small intestine. The experiments were performed on rats anesthetized using isoflurane gas. The rats were given an oral gavage of Gd contrast agent to improve the contrast to noise ratio (CNR) and signal to noise ratio (SNR) of the data. The positional information of the jejunum region was determined using 3D imaging of entire GI tract and 3D imaging was performed before every dynamic imaging. The dynamic data was acquired at 6 frames per second and was high enough to acquire the motility of small intestine in rats. As the imaging is performed on live animals significant image processing is required to correct breathing artifacts and animal movements and some images are significantly affected, thus do not represent a genuine section of small intestine. The breathing artifacts are corrected using image registration.

The dynamic nature of the small intestine can induce deep contractions in the lumen and shape of small intestine can rapidly change between consecutive images. A semi-

automated 3D image segmentation tool is applied to objectively compute the boundary of small intestine which is used in later stages to determine the diameter of the small intestine as a function of space and time. The requirement of this step was to automatically segment ≈ 1000 images in per data set of the small intestine with minimal user intervention.

The dynamic movie of the small intestine shows presence and absence of constricting regions as a function of time. The complex spatial and temporal patterns can be represented in a simplified way by computing diameter of small intestine. The boundary of the small intestine computed using 3D image segmentation can now be used as an input for skeletonization algorithm to compute medial axis of every image of small intestine in time. The medial axis can now be used to compute diameter of the bowels as function of x, along medial axis and time 't'. This 2D function can be mathematically represented as $D(x,t)$.

A simplified representation of gut motility can be achieved by a 2D iso-contour plot of $D(x,t)$. The constricted regions of the lumen appear dark and dilated regions of the lumen appear bright on a spatio-temporal map. The analysis of motility patterns and physiological parameters measured using MRI were derived from spatio-temporal maps of each data set. A plot of diameter variation vs. time can be derived from the constricting region of a spatio-temporal map and physiological parameters such as average diameter, amplitude and frequency of constriction, speed of propagation, etc. We have seen how dynamic MRI combined with post processing and image analysis approach can be used to assess motility of the small intestine in rats. This approach was applied to characterize complex gut motility and evaluate effects of different anesthetics, isoflurane and inactin, on the motility of small intestine. The results of isoflurane and inactin are presented in Chapters 4 and 6, respectively. A simplified analysis was combined with PCA using ASM

to determine the underlying order of gut motility and decompose complex gut motility into simple modes. For example, the frequency analysis of segmental gut motility resulted in three frequency modes and with PCA and Fourier analysis, we can decompose it into simple modes and associate their relevance with the underlying mechanism of gut.

The integrated analysis approach (red path) presented in Figure 3.1 follows a different route than a simplified analysis (blue path) and is explained in detail in Chapter 5. The integrated analysis approach share some modules (MRI image acquisition, image registration, image segmentation, computation of medial axis and spatio-temporal maps) with the simplified analysis. In the later stages after image segmentation, integrated analysis follows a slightly different approach. The segmented binary data can be decomposed into simple orthogonal modes using principal component analysis.

The 2D space + time segmented boundary of the small intestine can be used as a database of binary images for ASM. The Principal components are determined using eigenvector eigenvalue decomposition and the temporal nature of the lumen is reconstructed using individual and combined dominant eigenmodes or eigenvectors. The visualization of spatio-temporal patterns and a detailed analysis of the decomposed modes can be achieved via spatio-temporal maps and frequency analysis. The complete technical details of ASM and Fourier modes are presented respectively in Sections 3.4.1 and 3.4.2. The complete results and physiological relevance of decomposed modes are presented in Chapter 5.

The decomposed modes of principal components of segmental motility had similar frequency components as the complete data. To determine the source of additional frequency peaks, a third analysis (green path) was devised and it followed: average frequency analysis, Fourier decomposition, band pass filtering and visualization of Fourier modes using

spatio-temporal maps. The average frequency analysis was automatically obtained from the spatio-temporal map of acquired gut motility and averaged over all the locations in "x". The dominant peaks in frequency spectrum were computed and a band pass filter was applied to each dominant mode for every location in "x". A new spatio-temporal map was reconstructed for individual and combined Fourier modes. Fourier analysis was applied to peristaltic and segmental motility of isoflurane and inactin groups. The corresponding results of Fourier modes are shown in Chapters 4 and 6. The complete data analysis of MRI data using simplified, integrated and Fourier analysis can throw light on the underlying mechanism of complex gut motility and can lead to realistic and physiologically relevant models of gut motion.

A detailed literature review of the use of MRI in the field of GI was discussed in Chapter 2 in Section 2.5.2.2. In the coming sections, the basics of MRI and image formation and the dynamic MRI approach for GI motility are explained in this chapter in Section 3.2. The relevant past work in the field of image processing and the complete technical details of image analysis tools like image segmentation, image registration and skeletonization algorithm are introduced in Section 3.3. The image processing tools presented in Figure 3.1 were combined and applied for the analysis of gut motility in rats. The results of each step are presented in Chapter 4.

3.2 Basics of Magnetic resonance imaging

The basics of MRI are reviewed for the readers who are not familiar with MRI. The dynamic MRI approach used in this thesis is presented in Section 3.2.3.

MRI has gained overall acceptance in medical imaging due to its non-invasive, non-ionizing nature, excellent soft tissue contrast, high resolution, and 2D and 3D imaging in any plane [22,23,33,62]. The fundamental MRI signal originates from protons mainly from water and secondary from fat tissues. The sample or patient is lodged within center of superconducting magnet which delivers a constant magnetic field B_0. In MRI, radio frequency (RF) coils are used to transmit time-dependent magnetic fields that excite the nuclei and receive the energy from them [71]. In the absence of B_0 all the protons are arbitrarily oriented and in the presence of B_0, as per quanto-mechanical nuclear magnetic resonance (NMR) theory the protons acquire two energy levels which relates to the z component of the gross NMR signal proportional to magnetization moment M_0. M_0 results from the difference in magnetic moment of protons line up either in parallel or anti parallel to B_0. Figure 3.2 shows M_0 is along $+z$ axis and does not have any transverse magnetization and in order to create a transverse magnetization a time-dependent magnetic field B_1 is applied. It will excite the water protons and the magnetic fields produced by water protons in turn induce another oscillating current in the receiver coil [71].

As per Faraday's law the voltage E is induced in the receiver coil by time varying magnetic field and is given by

$$E = \frac{-d\phi}{dt} \tag{3.1}$$

RF coils are tuned to the Larmor frequency $\omega_0 = \gamma \times B_0$ which is the angular frequency at which the protons are revolving about the main magnetic field. The different magnetization components return to thermal equilibrium over time and their relaxation over time is dictated by Bloch equations. The relaxation of longitudinal M_x and M_y and transverse

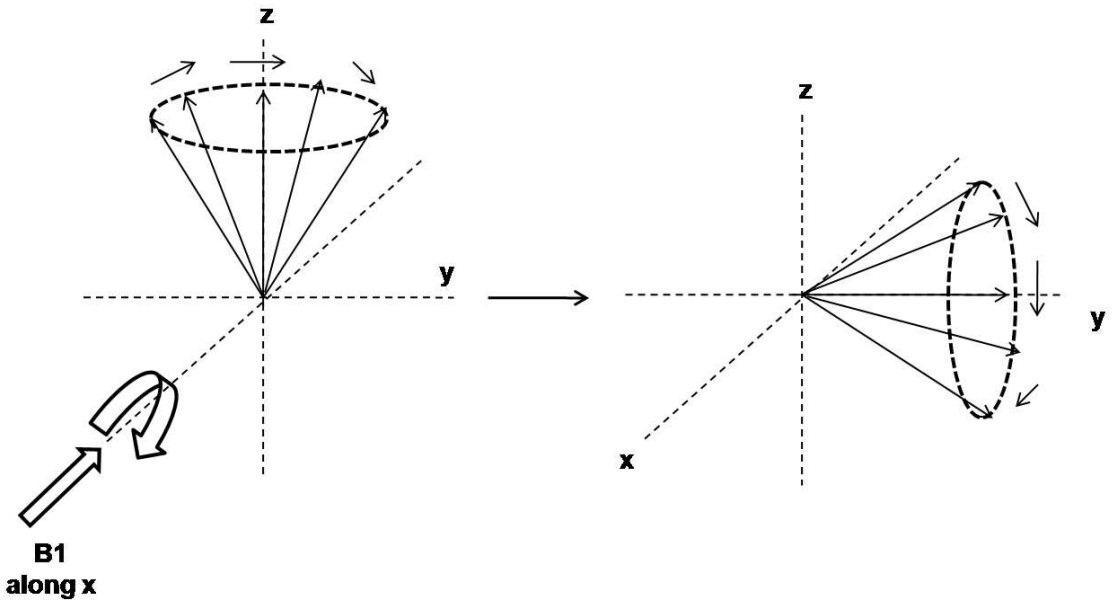

Figure 3.2. Illustration of application of B_1 field along the x axis. The figure has been adapted from [22]. The figure on the left shows, before application of B_1 field all the protons are aligned along z axis. The figure on the right shows, immediately after the application of B_1 field water protons are rotated in the transverse plane.

M_z components of magnetization can be derived from Bloch equations and represented in a simplified form as:

$$M_z(t) = M_z(t=0) + [M_0 - M_z(t=0)](1 - e^{-t/T_1}) \tag{3.2}$$

$$M_y(t) = M_y(t=0)(e^{-t/T_2}) \tag{3.3}$$

$$M_x(t) = M_x(t=0)(e^{-t/T_2}) \tag{3.4}$$

The time constant T_1 is spin-lattice relaxation time constant and describes relaxation of longitudinal magnetization and on the other hand T_2 is spin-spin relaxation time constant

regulating transverse magnetization. The signal received from water protons does not give any spatial information about the object. The image formation from this NMR signal is done by spatially localizing the signal by applying magnetic field gradients G_x, G_y and G_z along the x, y and z axes along with RF pulse, a work created and developed by Dr. Lauterbur [72]. All the gradients are assumed to be linear, spatially varying over the region of interest and can be represented as:

$$\frac{\delta B_z}{\delta z} = G_z, \quad \frac{\delta B_y}{\delta y} = G_y, \quad \frac{\delta B_x}{\delta x} = G_x \tag{3.5}$$

The gradients are designed so that there is no contribution from them and only external magnetic field exists at the isocenter ($x = 0, y = 0, z = 0$). For example, the relationship between magnetic field B_z, B_0, ω_z is given as:

$$B_z = B_0 + zG_z \tag{3.6}$$

$$\omega_z = \gamma B_z = \gamma(B_0 + zG_z) = \omega_z = \gamma z G_z \tag{3.7}$$

A similar set of equations can also be extended to other spatially dependent field gradients along x and y. A simple acquisition and reconstruction of 2D MRI image is outlined in the next section.

3.2.1 MR image formation

The image formation can be described into three steps: (1) slice selection, (2) phase encoding and (3) frequency encoding. We have used gradient echo pulse (GE) sequence for dynamic

imaging of the small intestine (see Figure 3.3). In a simple GE pulse sequence, a frequency selective pulse 90^0 and the slice gradient tips all the protons within a thickness $\Delta\omega/\gamma G_{slice}$ in the transverse plane. The protons outside this region are not tipped and do not see any RF pulse. In the second step, a phase encoding gradient G_{phase} is applied along y axis and induces spatially dependent phase shift into the signal. At the time of signal acquisition frequency encoding gradient is switched on along z axis and it imparts spatially dependent frequency information in acquired signal. The signal which is being recorded by the receiver RF coil has all the frequency and phase information that is necessary to spatially localize it. The received signal $S(t)$ can be mathematically expressed as in the equation 3.8; where $\rho(x, y)$ is the proton density and equation 3.8 can be rewritten in the form of k-space as in the equation 3.9.

$$s(G_y, \tau_p e, G_x, t) \propto \int_{slice}\int_{slice} \rho(x, y) e^{-j\gamma G_x x t} e^{-j\gamma G_y y \tau_{pe}} dxdy \tag{3.8}$$

$$s(k_x, k_y) \propto \int_{slice}\int_{slice} \rho(x, y) e^{-j2\pi k_x x} e^{-j2\pi k_y y} dxdy \tag{3.9}$$

The variables k_x and k_y in equation 3.9 are defined as:

$$k_x = \frac{\gamma}{2\pi} G_x t, \quad \text{and} \quad k_y = \frac{\gamma}{2\pi} G_y \tau_p e \tag{3.10}$$

The representation of MRI signal in the form of equation 3.9 gives a direct analogy to two dimensional inverse Fourier transform. As a consequence, the data acquisition is in the Fourier Domain or the K-space and a 2D image can be reconstructed by a simple 2D inverse

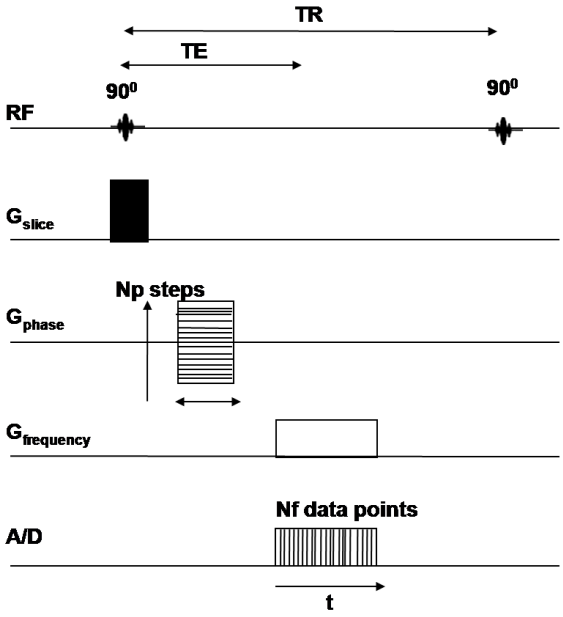

Figure 3.3. Illustration of gradient echo pulse sequence. This figure has been adapted from [22]. The pulse sequence was used in acquiring dynamic images of the small intestine. A modified version of the pulse sequence, where RF pulse was less than 90^0 and 3/4 partial Fourier imaging was used in our application.

Fourier transform of the acquired data and can be represented as:

$$\rho(x,y) = \int_{-\infty}^{+\infty} \int_{-\infty}^{+\infty} S(k_x,k_y) e^{+j2\pi(k_x x + k_y y)} dk_x dk_y \tag{3.11}$$

The signal obtained for each value of phase encoding gradient is sampled N_f number of times and this forms one line of the k-space. The entire k-space is filled by varying the value of G_y at an interval of repetition time TR. Hence the total scan time is $N_p \times TR$. The phase encoding gradient is incremented in steps and during each of these steps, the frequency-encoding or readout gradient is used to acquire one line of K-space.

3.2.2 Contrast in MR imaging

The image intensity $I(x, y)$ in GE pulse sequence is given by:

$$I(x,y) \propto \frac{\rho(x,y)(1 - e^{\frac{-TR}{T1}})e^{\frac{-TR}{T2^*}} \sin\alpha}{(1 - e^{\frac{-TR}{T1}})\cos\alpha} \tag{3.12}$$

The effects of relaxation time constants T_1 and T_2 on image intensity $I(x, y)$ can be controlled by imaging parameters repetition time TR and echo time TE from MRI console. After obtaining the entire information, the data matrix is 2D Fourier transformed to obtain the image.

3.2.3 MR imaging of small intestine

The spin echo (SE) pulse sequence is most commonly used in MRI imaging and has excellent contrast to noise ratio (CNR) and signal to noise ratio (SNR). In addition to 90^0 RF pulse a second 180^0 RF pulse is used to flip the phase of dephasing protons and the signal acquired is independent of $T2^*$ effects. For example, an image with matrix size 128×128 and $TR = 2s$, the total time for image acquisition will be > 4 mins. So in our application we have to image as fast as possible and simultaneously have a reasonable CNR and SNR. In order to localize the jejunum region of the GI tract for dynamic imaging, a rapid T_1-weighted spin-echo sequence was run. Once the jejunum region was identified, a GE partial Fourier imaging pulse sequence was applied to acquire three fourth of the original K-space. The missing K-space data was zero filled before taking inverse Fourier transform. The experimental MRI protocol and the results of dynamic imaging are presented in Chapter 4. The need for advanced imaging processing algorithms is required to automatically process

the data with minimal user intervention. In comparison to invasive mehtods, non-invasive MRI approach suffers in terms of CNR and SNR. The dynamic imaging performed on live animals can induce breathing artifacts and distort the shape of intestine. Thus image processing approach is required to improve the quality of acquired data. The past work in the field of medical image processing, relevant to this thesis, is discussed in the following section.

3.3 Past work in image analysis algorithms

This section covers past work in the field of medical image processing. A detailed literature review of image segmentation, skeletonization and PCA using ASM are presented in this section. The combination of sophisticated image analysis algorithms were applied to MRI data of small intestine and are further discussed in the following sections. Once the MRI data is acquired and corrected for breathing artifacts, the next step is to compute the boundary of small intestine using 3D image segmentation tool (see Figure 3.1). The technical details of different segmentation algorithms are presented in Section 3.3.1.

3.3.1 Development of semi-automated 3D image segmentation tool

Image segmentation, in general is applied to imaging data to delineate and extract objects of interest [73]. Image segmentation can be divided into three categories: a) manual, b) fully-automated and c) semi automated. Manual methods are time consuming and have biased results depending on the user's interpretation. Because of these downfalls, it would be a daunting task to segment a large volumetric data set [74, 75]. Fully-automated image segmentation are application-specific to structures such as the brain and lungs [76, 77].

Semi-automated image segmentation algorithms are generally applicable to various situations and have more robust results. They involve user intervention for steps where the probability of errors is likely to be higher, while the repetitive job is carried out by the computer. In comparison to fully-automated categories, semi-automated algorithms take somewhat longer to process the images but often provide more accurate edge detection. The results of the image segmentation algorithm should be repeatable, accurate and efficient [78].

Semi-automated image segmentation algorithms can be further classified as: a) model-based such as snakes Kass et al. [79] and active shape models based on Cootes et al. [80], b) image-based such as 2D live-wire based on Mortensen and Barrett et al. [81], or (c) a hybrid of image- and model-based such as iterative live-wire and live-snakes based on Souza et al. [78]. We have implemented the following image segmentation algorithms 1) 2D live-wire or intelligent scissors [81], 2) 3D live-wire [82–84], 3) active contour models or snakes [79], 4) gradient vector Flow snakes (GVF) [85] [86]. For our application we have combined 3D live wire and directional dynamic gradient vector flow snakes [87](DDGVFS) to accurately determine the edges of 2D spatial + time of dynamically acquired images.

Our aim was to develop a semi-automated 3D image segmentation tool to segment dynamically acquired MRI images of small intestine. The goal is to develop a flexible semi-automated image segmentation tool that can accurately detect boundary of 3D (2D spatial + time) data set of the small intestine within reasonable amount of time. The list of algorithms presented in the following sections was experimented to implement a robust semi-automated 3D image segmentation tool.

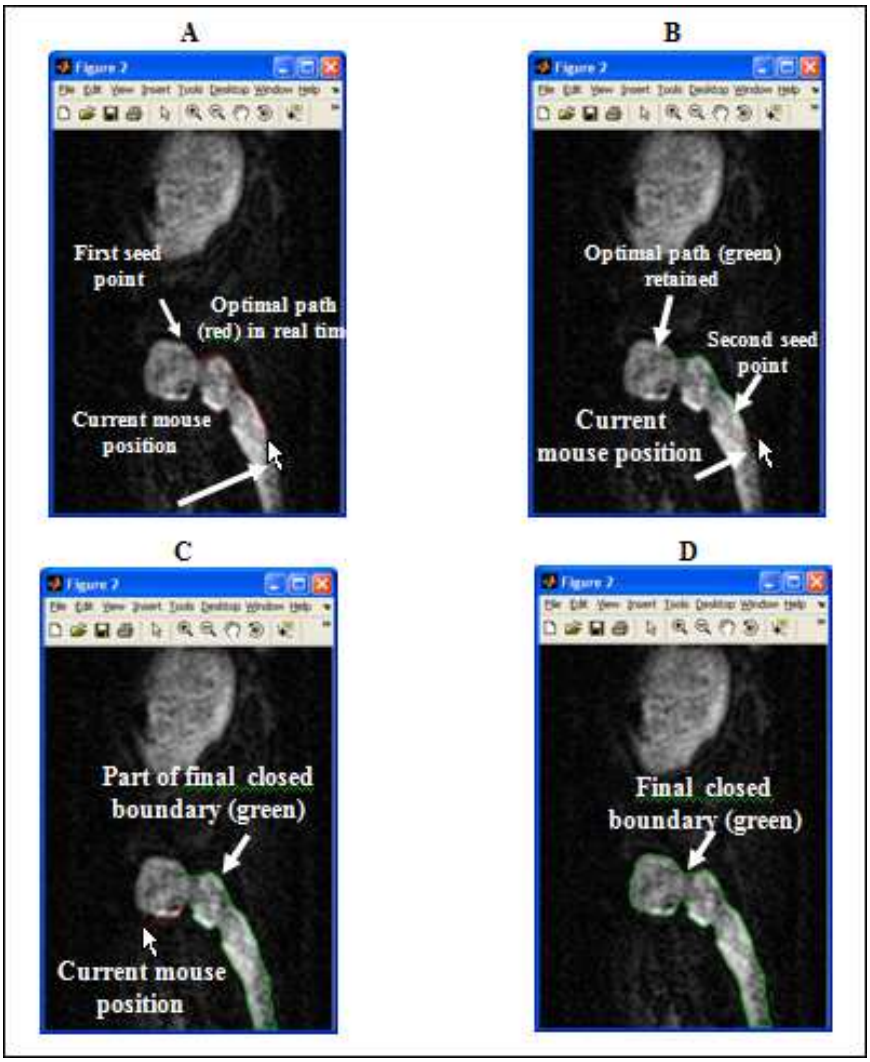

Figure 3.4. Demonstration of 2D live wire algorithm. (A) After the placement of the seed point on the boundary local cost function is computed and optimal path (red) is displayed in real time. (B) Once the user is satisfied with the displayed path a second seed point is clicked, the previously computed path (green) is retained and once again the optimal path between second seed point and the current mouse position (red) is displayed in real time. (C) A similar process is repeated by placing seed points on the boundary. (D) Final closed boundary of the object.

3.3.1.1 2D Live Wire

"2D Live-Wire" also known as "Intelligent Scissors" is an interactive tool used for image segmentation [81]. The entire algorithm, based on the formulation by Barrett and Mortensen, was implemented in C and MATLAB. The boundary is extracted by automatically adhering

to the edge of an object while guided by simple move-and-click mouse motions [81]. The boundary is extracted between a pair of points lying on the boundary by calculating an optimal path between them using Dijkstra's algorithm [81]. After the placement of first seed point on the boundary, an optimal path computed between the initial seed point and the current position of the mouse is displayed in real time. The optimal path automatically snaps on to the boundary of the object. If the user is satisfied, the optimal path is stored in an array and the user selects a new seed point. The whole process is repeated until a desired closed boundary is obtained. The 2D live wire algorithm minimizes a cost function for computing the boundary of small intestine. The different features of cost function are presented in the following section.

3.3.1.2 Cost function for 2D live wire

The optimal path between a pair of points "a" and "b" which belongs to 8 neighborhood of a, is based on the minimization of the weighted sum of component cost function dependent on the following: 1) Laplacian zero crossing F_Z, 2) Gradient magnitude F_G and 3) Gradient direction F_D. The local cost function can be defined as:

$$l(a,b) = w_Z * F_Z(b) + w_G * F_G(b) + w_D * F_D(a,b) \tag{3.13}$$

where w_Z, w_G and w_D are the weights of the corresponding features. The gradient G of input image J is defined as $G = \sqrt{J_X^2 + J_Y^2}$ where J_X and J_Y are the corresponding partial gradients. The cost feature associated with the gradient magnitude for a pixel b, is

normalized between 0 and 1 and then minimized.

$$F_G(b) = 1 - \frac{G^{'}(b)}{max(G^{'}(b))} \qquad \text{where} \qquad G^{'}(b) = G(b) - min(G(b)) \tag{3.14}$$

Thus the pixels located on the edges have a larger gradient magnitude and a minimum gradient cost and vice versa for the pixels not lying on the edge. The normalized Laplacian zero crossing for a pixel b, $J_L(b)$ is defined as:

$$J_L(b) = 0 \qquad \text{for all the pixels that lie on the edge} \tag{3.15}$$

$$J_L(b) \neq 0 \qquad \text{for all the pixels that do not lie on the edge} \tag{3.16}$$

The cost F_Z associated with Laplacian zero crossing is defined as:

$$F_Z(b) = 0 \quad \text{if} \quad J_L(b) = 0 \quad \text{and} \tag{3.17}$$

$$F_Z(b) = 1 \quad \text{if} \quad J_L(b) \neq 0 \tag{3.18}$$

$F_Z(b)$ and $F_G(b)$ are dependent on the gradient of an image and the gradient direction $F_D(b)$ provides a smoothness constraint to the boundary by assigning a low cost if pixels a and b have similar gradient direction and a high cost if they do not have similar gradient direction. The gradient direction is a simple representation of the direction of the unit vector defined by partial gradients in x (J_x) and y (J_y) directions. For a pixel a let D_a be a unit vector in the gradient direction and $D_a^{'}$ be a unit vector perpendicular to D_a in the clockwise direction. The unit and unit normal vectors can be represented in terms of

partial derivatives as:

$$\mathbf{D}_a = [J_x, J_y] \qquad \text{and} \qquad \mathbf{D}_a^{'} = [-J_y, J_x] \tag{3.19}$$

The cost associated with the gradient direction, F_D is minimized and can be computed as:

$$F_D(a,b) = \frac{2}{2\pi}\{\arccos[d_a(a,b)] + \arccos[d_b(a,b)]\} \tag{3.20}$$

$$\text{where} \qquad d_a(a,b) = \mathbf{D}^{'}(a) \cdot L(a,b) \qquad \text{and} \tag{3.21}$$

$$d_b(a,b) = \mathbf{D}^{'}(b) \cdot L(a,b) \tag{3.22}$$

$$\mathbf{L}(a,b) = \frac{1}{\|a-b\|}\{b-a, \quad \text{if} \quad \mathbf{D}^{'}(a) \cdot (a-b) \geq 0\} \quad \text{OR} \tag{3.23}$$

$$\mathbf{L}(a,b) = \frac{1}{\|a-b\|}\{a-b, \quad \text{if} \quad \mathbf{D}^{'}(a) \cdot (a-b) \leq 0\} \tag{3.24}$$

The manual 2D live wire algorithm was implemented in C and Matlab and the details and results of implementation are reviewed in the following section.

3.3.1.3 Implementation of 2D live wire

After the selection of an initial seed point on the boundary, a local cost function is calculated between the initial seed point and the current position of the mouse. An optimal path is computed between the points and it is displayed in real time based on Dijkstra's algorithm [81]. Dijkstra's algorithm computes the shortest path between the two points by minimizing the integrated cost between two points. As the algorithm has to calculate an optimal path in real time, Dijkstra's algorithm was implemented as Matlab executable file (MEX) to

improve the speed of processing. The steps involved in 2D live wire are shown in Figure 3.4.

The 2D live wire algorithm is the basis for 3D live wire algorithm and can be easily extended to automatically segment a 3D volume. The literature review and implementation of 3D live wire is discussed in Section 3.3.1.4.

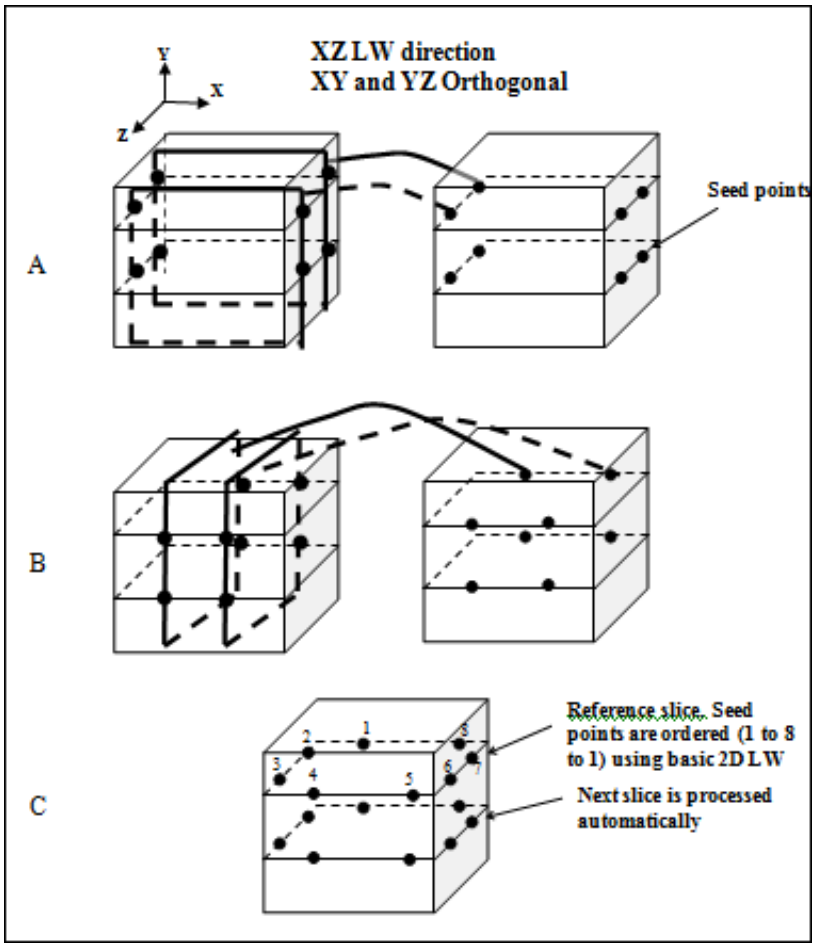

Figure 3.5. Demonstration of 3D live wire (Lu and Higgins *et al.* [88]. 2D images are stacked into 3D dataset. XZ is chosen as live wire direction and XY and YZ are chosen as orthogonal directions. (A) The basic 2D live wire is run on 2 slices in the XY plane and corresponding seed points are projected on to the XZ plane. (B) The basic 2D live wire is run on 2 slices in the YZ plane and the corresponding seed points are projected on to the XZ plane. (C) Reference slice is picked in the XZ plane and all the seed points are ordered clockwise or counter clockwise to compute a closed boundary. The order of the seed points is now used for the next slice and the whole process is repeated until all the slices are processed.

3.3.1.4 3D Live Wire

Various researchers have proposed 3D live wire to segment volumetric regions of interest [82–84, 88, 89]. The user is involved in segmenting few planes and other planes are segmented via shape based interpolation [89]. Falcao *et al.* proposed segmenting few planes, orthogonal to the live wire plane and then automatically computing closed boundaries of the volumetric data set [83]. This method was further improved by Hamarneh *et al.* by adding a point ordering step [84]. Kongkuo *et al.* improved basic 2D live wire by improvising the cost function over past work by adding an additional gradient direction cost. They also introduced a new improved 3D live wire that allows faster delineation of 3D volumes [88].

It is a semi-automated algorithm in which "seed points" are generated through the use of 2D live wire segmentation planes orthogonal to the stack of images. A simplified point ordering algorithm is used to order the seed points to define start and end points. The points are then used in order, much like the manual mouse movements in the 2D technique to generate a connected boundary in each image. The algorithm was implemented in MATLAB. 3D live wire can be applied in the transverse, coronal or sagittal plane [88]. The 2D live wire algorithm is used on few orthogonal planes to segment desired region of interest and the segmented boundary is projected back on to the live-wire plane as the seed points on the boundary of the object. A point ordering algorithm is used to connect (clockwise or anticlockwise) the seed points on every slice. A reference slice is picked up from 3D stack of images and 2D live wire algorithm is used to manually order the seed points on the reference slice [88]. This order of seed points is used to order the points on to the next slice in the

live wire direction [88]. Similarly, the order of the next slice can be used for the following slice in live wire direction until all the slices have been processed. Due to the irregularities in complex 3D shapes, at times 2 seed points are generated in the same region. 3D live wire is not completely automated and the extra processing time improves the accuracy of the 3D region of interest [88]. The basic idea of 3D live wire is shown in Figure 3.5 and is implemented from the paper published by Kongkuo *et al.* [88]. For simplicity only 2 orthogonal planes are shown in each direction in Figure 3.5.

The 2D and 3D live wire algorithms are classified as image based methods and were discussed in Sections 3.3.1.1 to 3.3.1.4. The image segmentation algorithms can be further categorized as model based. A model based method, termed as "Snakes", was first presented in 1987 by Kass *et al.* and have been improved a lot since then. The different variations of Snakes algorithm are presented in Sections 3.3.1.5 to 3.3.1.7. The hybrid combination of 3D live wire and DDGVFS was applied to the MRI data of small intestine. The complete details are presented in the following section.

3.3.1.5 Active contour model

Active contour model (ACM) or Snakes algorithm was first proposed by Kass *et al.* and used energy minimization framework to achieve the goal of edge detection [79]. Snakes are deformable curves generated within an image domain and are moved under the influence of internal forces from within the model itself and external forces computed from the image data [79, 85, 86]. Deformable models have been used in edge detection, image segmentation, and track moving objects [79, 85, 86]. The models are drawn toward the edges by potential

forces, which are defined to be the negative gradient of a potential function [79,85,86]. The role of internal forces is to prevent the model from bending too much (bending forces) and to hold the model together (elasticity forces) [79,85,86]. There are several issues associated with the basic snakes algorithm: an initial estimate of the model a) must be very close to the boundary and b) cannot traverse into the concavities of the boundary [85, 86]. Prince *et al.* have proposed Gradient Vector Flow (GVF) Snakes to increase the capture range of the initial estimate of ACM. The method corrects the problem of snakes by calculating "field of forces, called the GVF forces, over the image domain" [85, 86]. The GVF forces are computed by applying diffusion equations to the gradient of an image edge map, and to "extend capture range so that snakes can find objects that are quite far away from the initial guess" [79, 85, 86].

A 2D deformable ACM can be represented in parametric form as:

$$\mathbf{x}(s) = [x(s), y(s)], s \in [0, 1] \tag{3.25}$$

The parametric curve moves within an image domain to minimize the energy functional:

$$\mathbf{E} = \int_0^1 \frac{1}{2}(\alpha|x^{'}(s)|^2 + \beta|x^{''}(s)|^2) + E_{ext}(x(s))ds \tag{3.26}$$

where α and β are the weights associated with tension and rigidness of the model. $x^{'}(s)$ and $x^{''}(s)$ are the first and second order derivatives of $x(s)$ with respect to s. They also correspond to tension and rigidness of the model that moves around in the image domain.

E_{ext} is computed from the image itself and is defined in such a way that it has lower values on the edges and boundary of the object. The contour that minimizes E must satisfy the Euler equation:

$$\alpha x^{"}(s) - \beta x^{""}(s) - \Delta E_{ext} = 0 \tag{3.27}$$

Euler's equation in terms of internal and external energy can be represented as:

$$F_{int} = \alpha x^{"}(s) - \beta x^{""}(s) \quad F_{ext} = -\Delta E_{ext} = 0 \quad \text{and} \quad F_{int} + F_{ext} = 0 \tag{3.28}$$

The internal forces restrict bending and stretching of the contour and the external force attracts the contour toward desired features such as edges, lines and boundary of the object [79]. Equation 3.30 is solved by considering $\mathbf{x}(s)$ as dynamic i.e. function of time $\mathbf{x}(s,t)$. A partial derivative of $\mathbf{x}(s,t)$ w.r.t t, $x_t(s,t)$, is computed and is set equal to equation 3.30. The term on the right hand side of the equation is minimized once the snake reaches a stable state.

$$\alpha x^{"}(s) - \beta x^{""}(s) - \Delta E_{ext} = x_t(s,t) \tag{3.29}$$

The basics snakes were further improved on by Xu *et al.* [85, 86]. The external force used in Snakes algorithm was replaced by GVF field computed by applying a set of diffusion equations and thus extending the span of boundary information over relatively larger area. The basic Snakes algorithm suffered from adhering to local minima and not able to get out from such regions. The GVF overcomes this problem and is being widely used in medical imaging. The technical details of GVF are introduced in the next section.

3.3.1.6 Gradient vector flow snakes

Gradient Vector Flow (GVF) Snakes was proposed by Xu *et al.* [85,86] to improve the basic Snakes algorithm. A Gaussian filtered image or gradient of Gaussian filtered image can be used as an external force in the snakes algorithm in equation 3.30. In GVF algorithm a modified and a new external force termed as GVF was incorporated. GVF is computed by applying diffusion equations to the gradient of gray scale or binary edge maps and it replaces external force in snakes algorithm with GVF field represented as $\mathbf{v}(x, y)$. The GVF field is an equilibrium solution for a set of partial differential equations given as:

$$\mathbf{v}_t = \mu\Delta^2\mathbf{v} - (\mathbf{v} - \Delta f)|\Delta f|^2 \tag{3.30}$$

where $\mathbf{v}_t$ is the partial derivative of $\mathbf{v}(x, y, t)$ with respect to t. The edge map f is similar to gradient magnitude of the original image and has higher value for the pixels on the edge and lower values for the pixels which do not lie on the edge. GVF code was available online (`http://iacl.ece.jhu.edu/projects/gvf/`) and was used with the basic snakes algorithm implemented in Matlab.

The GVF algorithm was further improved upon by Cheng and Foo [87] by replacing the magnitude of an image with the actual gradient information. The algorithm can improve edge detection by incorporating the sign of gradient and does not depend on just the strength of magnitude. The technical details of DDGVFS are presented in the following section.

3.3.1.7 Dynamic Directional Gradient vector flow snakes algorithm

Cheng and Foo [87] have introduced a further improvement termed Dynamic Directional Gradient vector flow snakes algorithm (DDGVFS), which incorporates the sign of the gradient and improves image segmentation in the presence of two opposite edges very close together, as is often the case when considering the dynamic motion of the GI tract.

The different segmentation algorithms outlined in Sections 3.3.1 and 3.3.1.5 were implemented and combined for segmenting the boundary of small intestine. We have applied hybrid combination of 3D live wire and DDGVFS for MRI data of small intestine. The details of 3D segmentation are introduced in the following section. The complete results of small intestine are presented in Chapter 4 in Section 4.3.4.

3.3.1.8 3D image segmentation of small intestine

Iterative live wire and live snakes proposed by Souza *et al.* is a hybrid combination of live wire and snakes [78]. Liang *et al.* [90] have presented a hybrid approach which combine live wire and Snakes, termed as "United Snakes". They have applied in different applications ranging from segmentation of: neuronal dendrites in EM images, dynamic chest images using X-ray fluoroscopy and breast images in mammogram. They have shown United Snakes perform better than individual snakes and live wire algorithm. We have incorporated a slight variation over iterative live wire and live snakes [78] and united snakes [90]. In our approach we have used a hybrid combination of 3D live wire and DDGVFS to segment MRI images of the small bowel. 3D live wire is a powerful image-based semi-automated technique used for segmenting 3D data sets and is driven by the user during the segmentation process. On the other hand DDGVFS is an efficient model-based method; an initial estimate of

the boundary is driven to object's boundary even if it is quite far away from the desired boundary. Hybrid combination methods try to combine the strengths of each method to overcome their individual limitations [78]. In our approach 3D live wire is run on a stack of slices to compute an approximate boundary, an approximate boundary is then used as an initial estimate for DDGVFS and final boundary is the output of DDGVFS. A simple illustration of such approach is shown in Figure 3.6.

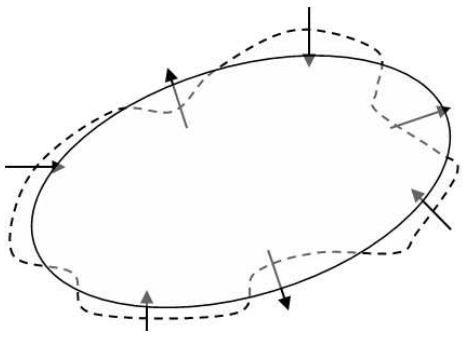

Figure 3.6. Hybrid combination of 3D live wire and GVF snakes. The dotted line is an approximate closed boundary computed by 3D live wire. The solid line is a final boundary computed using GVF snakes.

Until now we have reviewed the technical details of image segmentation and the next step in image analysis is to determine the medial axis of small intestine (see Figure 3.1). The medial axis was determined to compute the diameter of small intestine as a function of x along the medial axis and time t. The medial axis was computed for every image in time and it can be represented as a 2D function, $D(x, t)$. The medial axis was determined by applying 2D thinning algorithm on the binary images of small intestine. The complete technical details of thinning algorithm are presented in the following sections and the results of thinning algorithm are presented in Chapter 4 in Section 4.3.4.1.

3.3.2 Computation of medial axis

The next step in image analysis is to compute the medial axis of small intestine for every image in time. The medial axis can be computed using a skeletonization algorithm such as 2D thinning algorithm and in turn it can be used to used to compute 2D function $D(x,t)$, diameter as a function of space and time. The space time iso-contour plots can now be used to represent motility patterns of small intestine. A 2D thinning algorithm based on Saha *et al.* was implemented in Matlab and the technical details are explained in the following section.

3.3.2.1 2D Thinning

A 2D thinning algorithm based on the formulation by Saha *et al.* [34] was implemented to find medial axis of the images of the small bowel acquired using MRI. Thinning is an iterative process and with each iteration it deletes the boundary pixels based on certain criteria until we get a connected one pixel thick skeleton [34]. Each iteration is also known as pass and this process is repeated until no boundary pixel is deleted [34]. In this algorithm all the foreground pixels are considered black and background pixels white. A black pixel is considered as a boundary pixel if at the start of the iteration it has at least 1 white pixel. A boundary pixel is termed as a "significant point" if at least two opposite four neighbors of the pixel are white at the beginning of the pass. A boundary pixel is termed as "break point" if it is black and deletion of a boundary pixel creates two or more back regions in an image. A boundary pixel is removed if it is not a significant or a break point. The algorithm is very similar to process of iterative erosion of boundary points and conserves the shape and topology of an image. During thinning process an algorithm looks for a boundary point,

labels it either for removal or final point of the skeleton. Once a black pixel is labeled as a final point it is not touched in the following passes. The next step in thinning is to store tree structure of the skeleton to traverse along the skeleton and delete short false branches. This step is explained in the following section.

3.3.2.2 Tree structure of the skeleton

In comparison to earlier generations of thinning algorithm, the results based on Saha *et al.* have less number of short false branches. Kiraly *et al.* have proposed different geometric techniques to remove false branches in 3D skeleton of tubular structures [35]. The multi-stage cleaning of 3D skeleton leads to a tree structure which has ordered set of branches and each branch has an ordered set of points [35]. The main application of their work was to improve in directional planning and real time navigation during virtual bronchoscopy [35]. A skeleton of an image is stored as a tree data structure (D) and helps in navigation from one end to the other end of the skeleton [35]. A tree structure is made up of 3 fields, points of a skeleton (p_i, $i = 1$ to a), branches made up of ordered and connected points (B_j, $j = 1$ to b) and all paths that start from the root point are made up of ordered and connected branches (P_k, $k = 1$ to c). The branch starting from the root point is termed as a root branch. If a particular point p_i of the computed skeleton has two neighbors in its 8-neighborhood it is added as point to branch, else if it has two or more neighbors, it stems in to two or more new branches [35]. This procedure is iterated for the new branches until the whole skeleton has been processed. All possible paths start with a root branch and end with a terminal branch which does not bifurcate further into new branches [35]. If a particular branch stems into 2 or more branches, it is stored as a parent branch and the

new branches are stored as child branches. A parent-child relationship of all the branches is stored and it helps later in traversing through the skeleton. A simplified skeleton in a tree structure form is shown in Figure 3.7. The different components of the skeleton are stored

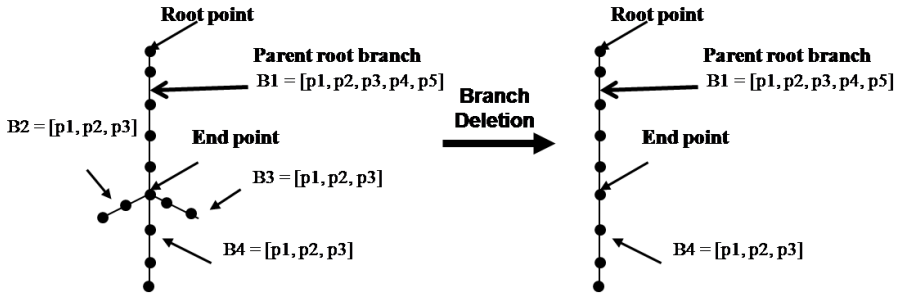

Figure 3.7. Tree structure of a simplified skeleton.

to traverse through the central medial path of the binary image. Some of the important components in relation to 3.7 are: (1) a branch which has an ordered set of connected points $B_1 = [p1, p2, p3, p4, p5]$, $B2 = [p1, p2, p3], B3 = [p1, p2, p3]$ and $B4 = [p1, p2, p3]$, (2) a path has an ordered set of connected branches $P1 = [B1, B2], P2 = [B1, B3]$ and $P3 = [B1, B4]$ and (3) a parent child relationship of all the branches is stored. For example parent branch B_1 has child branches: $B2$, $B3$ and $B4$ The thinning algorithm results in short false branches and a multi-stage process is applied to delete them. The false branches can vary in length from one pixel to several pixels. A length based criteria as described by Kiraly *et al.* [35] was used to clean the skeleton of an image. A simple centering of the medial axis was applied based on Chamfer Distance map of binary images. The details are presented in Section 3.3.2.3.

3.3.2.3 Deletion of false branches

Once a tree structure of a skeleton is obtained, the next aim is to delete short terminal false branches (e.g. B_2 and B_3 in Figure 3.7) of a computed skeleton. At the end only one of the paths (e.g. P3 in Figure 3.7) is retained and other paths are eliminated. The two criteria based on the paper published by Kiraly *et al.* , were used to delete the short terminal branches of the skeleton [35]:

(1) Length based elimination [35]: Any terminal branch B that falls under the conditions in equations 3.3.2.3 and 3.3.2.3 is deleted and a tree structure is updated.

$$l_B - CD_R(l_{BP}) \leq 1 \tag{3.31}$$

$$\frac{l_B - CD_R(l_{BP})}{CD_R(l_{BP}} < 1 \tag{3.32}$$

The variables used in equations 3.3.2.3 and 3.3.2.3 are defined as follows: l_B is the length of branch B, B_p is parent branch of branch B, l_{Bp} is the end point of the parent branch B_p and $CD_R(l_{BP})$ is maximum radius of a circle centered at l_{B_p} that can completely fit within region of a binary shape. The first criteria in equation delete short branches that do not extend 1 pixel beyond the end point of its parent branch. The second criteria in equation focuses on deleting branches that do not extend at least 1 radius beyond its parent's end point region.

(2) Simple centering [35]: Thinning algorithm focuses on generating centered branches

but some of the points of the output skeleton may not be centered and shifted by few pixels [35]. This step ensures all the points of the skeleton are as far as possible from the boundary within the local neighborhood [35]. A point p of the skeleton is iteratively moved from its 2D location p to 2D location q (q belongs to 8-neighborhood of p) until the following conditions fails [35]:

$$CD_R(q) > CD_R(p) \tag{3.33}$$

The final step is a mathematical fitting of the medial axis with a cubic spline function to make it smooth and continuous.

We have reviewed MRI image acquisition, image segmentation and computation of medial axis (see Figure 3.1). Once the medial axis is computed, the next step in image analysis was to determine the spatio-temporal map of dynamic gut motility. The complex spatio temporal patterning of dynamic gut motility is difficult to comprehend by a naked eye. The dynamic motility acquired over 1000 images can be compactly represented in a simple 2D spatio-temporal plot. A brief introduction on spatio-temporal maps is presented in the following section. The results of spatio-temporal maps of peristalsis and segmental gut motility acquired using dynamic MRI are presented in Chapter 4 in Section 4.4.4.

3.3.3 Spatio-temporal maps

The conventional way of computing the diameter at each point along the medial axis is by drawing lines perpendicular to the medial axis and finding an intersection with the bound-

ary. The contractile nature of the small intestine can induce high curvature regions and a conventional method can fail in locating an intersection on the boundary of the small intestine. We have computed medial axis using thinning algorithms and Euclidean distance maps were used to derive diameter of the small intestine at different points along the medial axis. The diameter was computed along the length of the small intestine (x), for every image in time t. The complex gut motility can now be represented as a 2D function $D(x,t)$, in a simple 2D plot. The physiological parameters of gut motility can be derived from spatio-temporal maps.

Until now we have reviewed complete details of simplified analysis of gut motility involving modules from MRI image acquisition to quantitative analysis of physiological parameters (see Figure 3.1). The combination of image processing algorithms were applied to overcome several issues in MRI imaging: correction of breathing artifacts, interpolate missing images, accurate segmentation of dynamic boundary of small intestine, computation of curvilinear and crooked medial axis and simplified representation of complex gut motility via spatio-temporal map. The dynamic MRI approach, 3D image segmentation tool, unique combination of image processing algorithms applied to MRI data and detailed quantitative analysis are the contributions of this thesis. A simplified analysis was used to characterize the physiology of gut motility under *in vivo* conditions. In order to determine the underlying mechanism of gut motility, an integrated analysis approach involved, PCA using ASM, frequency decomposition and spatio-temporal maps was applied to the segmented data of small intestine. The different modules of integrated analysis (blue path) are shown in Figure 3.1. The motivation of integrated analysis, past work in ASM and

complete technical details of ASM are presented in Sections 3.4.1 to 3.4.2. The results of integrated analysis are presented in Chapters 5 and 6.

3.4 Motivation of Principal Components

The spatio-temporal maps have been extensively used in the GI studies to visualize complex motility patterns. It is otherwise difficult to comprehend a motility pattern by just browsing through dynamic series of images. However, the spatio-temporal maps do not offer any underlying physiological information about the gut motion. A simple Fourier analysis of the diameter variation vs. time of segmental motility resulted in at least three dominant peaks and were found consistent in all the animals. A sophisticated approach such as PCA was applied to determine the underlying mechanism of gut motility and to decompose complex motility into simple principal components. The unique integrated analysis involved PCA along with spatio-temporal maps and frequency analysis can produce clarity about the functioning of gut. 2D Active shape models based on the method published by Cootes *et al.* [80, 91] was used to determine the dominant eigenvectors of time varying motility of small intestine. The technical details of ASM and integrated analysis are presented in Sections 3.4.1 to 3.4.2.

3.4.1 Past work in active shape models

Active shape models (ASM) is a technique used to determine the dominant variations with in a process and represent it by finite set of eigenvectors or modes [80, 91]. The ASM was introduced to aid in image segmentation [80, 91] and is described in a two step process. At first a point distribution model is computed by selecting landmark points within a training

data set. A training data set comprises of different possible shapes sampled from a large database. The PCA is applied to decompose the data into finite dominant eigenvectors. In a second stage different shapes (similar to those in the training data) are generated by varying the eigenvectors with in statistically allowable shape domain. The search for an object within an image starts off with a previously computed mean shape and an external force is applied on each point of a mean shape. A mean shape is deformed and each model moves to a new location near the edges. A new deformed shape is registered to a mean shape and the same process is repeated until a cost function is minimized until a new shape is automatically segmented. The definition of cost function can vary from application to application and in most cases an external force such as image intensity, gradient of an image, intensity difference, image entropy, etc. are used.

ASM cannot be applied for segmenting the boundary of the small intestine as the geometry model of the small intestine is animal specific. The shape of the intestine can even vary within the same animal and it depends on how the gut is being imaged. Thus, we have used ASM as an approach to decompose complex gut motion into simple modes and spatio-temporal maps and frequency analysis were used to visualize and analyze spatial and temporal patterns of the decomposed and combined modes. The detailed mathematical theory of how ASM can be applied to motility of the small intestine is discussed in the following section.

3.4.1.1 Point distribution model

The First step in ASM is to create a database of training images, label a set of landmark points on all the images and derive a point distribution model [91]. We are dealing with

images that deform as a function of time. Let $\mathbf{x}_t$ be a "vector" of $2n$ landmark points on a sample shape at time t ($t = 1$ to N).

$$\mathbf{x}_t = [x_{t0}, y_{t0}, x_{t1}, y_{t1}, \cdots\cdots x_{tk}, y_{tk} \cdots, x_{tn-1}, y_{tn-1}] \tag{3.34}$$

3.4.1.2 Alignment of shapes

The training shapes are aligned using linear least squares approach and a mean shape is obtained from N aligned samples. Let us consider two shapes from the training database x_a and x_b. We have to apply a transformation matrix M on x_a that will result in an alignment of by minimizing the sum S_a (see equation 3.40). The transformation matrix M is a function of three parameters, translation t_b, rotation θ_b and scaling s_b and can be represented in the equation form as:

$$M(s_b, \theta_b)[x_a] + t_b \tag{3.35}$$

The terms $M(s, \theta)$, t and $\mathbf{x}_{ak}$ can be defined as:

$$M(s, \theta) = \begin{bmatrix} s\cos\theta & -s\sin\theta \\ s\cos\theta & -s\sin\theta \end{bmatrix} \tag{3.36}$$

$$t = (tx, ty)\text{and} \tag{3.37}$$

$$\mathbf{x}_{ak} = \begin{bmatrix} x_{ak} \\ y_{ak} \end{bmatrix} \tag{3.38}$$

The combined equation of applying the transformation matrix M on shape x_ak can be written in the equation form as:

$$M(s_b, \theta_b)[x_{ak}] + t_{bk} = \begin{bmatrix} (s\cos\theta)x_{ak} - (s\sin\theta)y_ak + t_{xk} \\ (s\cos\theta)x_{ak} + (s\sin\theta)y_ak + t_{yk} \end{bmatrix} \tag{3.39}$$

$$S_a = ((x_a - M(s_b, \theta_b))[x_b] - t_b)^T((x_a - M(s_b, \theta_b))[x_b] - t_b) \tag{3.40}$$

Once the shapes are aligned using least squares approach, the next step is to compute a mean shape of the aligned samples.

3.4.1.3 Mean shape

An iterative approach is used to align all N shapes. At first a transformation matrix is applied on all the shapes $t = 2$ to N to align them with the first shape. A mean shape is computed from the aligned shapes and now all the shapes $t = 1$ to N are aligned with a mean shape. A new mean shape is computed and the process is repeated until mean shape converges. The mean shape can be calculated as:

$$\bar{x} = \frac{1}{N}\sum_{t=1}^{N} x_t \tag{3.41}$$

3.4.1.4 Deviations from mean shape and co-variance matrix

A set of N time samples, with each sample containing $2n$ elements (x and y coordinates), are represented as a "cloud" of N points in 2n dimensional space. It is assumed that the spread of N points is uncorrelated and lies in an ellipsoidal region around the mean. Different

modes of variation of land-mark points are found by calculating the deviation, dx_t, of each sample from the mean shape, and then calculating a $2n \times 2n$ co-variance matrix represented by S. The co-variance matrix S and deviation dx_t can be written in the equation form as:

$$\mathbf{dx}_t = \mathbf{x}_t - \bar{x} \tag{3.42}$$

$$S = \frac{1}{N}\sum_{t=1}^{N} dx_t {dx_t}^T \tag{3.43}$$

The mean shape and co-variance matrix are computed from aligned samples and the next step is to perform PCA.

3.4.1.5 Eigenvector eigenvalue problem

The covariance matrix S is used as the kernel to an eigenvalue problem to derive the principal component eigenvectors, also known as eigenmodes. The principal modes are the eigenvectors (p_k) of S, and the variance of each eigenvector is represented by its corresponding eigenvalue (λ_k). The decomposed modes are orthogonal to each other and they can be represented in an equation form as:

$$Sp_k = \lambda_k p_k \qquad \text{and} \qquad {p_k}^T p_k = 1 \tag{3.44}$$

A $2n \times 2n$ co-variance matrix leads to $2n$ eigenvectors and their corresponding $2n$ eigenvalues. A $2n$ dimensional ellipsoid can be approximated by the first k eigenvectors which represents a large portion ($> 95\%$) of the total variance The sum of 2n eigenvalues can be calculated

as:

$$\lambda_T = \sum_{k=1}^{2n} \lambda_k \tag{3.45}$$

The eigenvalue of mode k can be represented as the percentage in terms of total variance λ_T as:

$$\frac{\lambda_k}{\lambda_T} \times 100 \tag{3.46}$$

The PCA results in dominant set of eigenvectors or eigenmodes. The different variation of shapes lying in a higher dimensional space can be be reconstructed by scaling the eigenvectors within allowable region around the mean shape. This leads into the discussion on allowable shape domain and the coefficients of eigenvectors termed as "b-values".

3.4.1.6 Allowable shape domain

Any point lying within an "allowable shape domain" (-3 to $+3$ standard deviations (SD) around the mean), within the cloud represents a shape similar to the shapes in the training database. The standard deviation (SD) for a particular mode k is $\sqrt{\lambda_k}$. Any shape x within the cloud can be represented using a linear combination of first k eigenmodes $P = [P_1, P_2, \cdots\cdots\cdots, P_k]$ and a mean shape $\bar{x}$. It can be represented in the equation form as:

$$x = \bar{x} + Pb \tag{3.47}$$

The b-values can be computed by projecting all the samples on the eigenvectors. The mathematical representation of b-values is discussed further.

3.4.1.7 b-values

The matrix b is a set of coefficients of the corresponding eigenvectors. The coefficients of the corresponding eigenvectors can be computed by projecting all the samples on the corresponding eigenevectors. Mathematically it can be represented as:

$$b = (x - \bar{x})P^{-1} \quad = \quad (x - \bar{x})P^{T} \tag{3.48}$$

The scatter plot of the b-values of the corresponding eigenvectors can verify if the decomposed modes are independent or dependent of each other and the independent modes will result in an uncorrelated b-plot. The PCA modes had similar frequency components as that of the original data and thus a third analysis based on Fourier decomposition was an appropriate choice to determine the source of additional peaks in the segmental motility. Additionally the results of Fourier analysis can provide an analytical geometry model of the small intestine that can be easily incorporated with computational fluid dynamics model. The details of Fourier analysis are presented in the following section.

3.4.2 Fourier analysis

The third analysis based on simple Fourier decomposition (green path) decomposes complex gut motility into simple orthogonal Fourier modes. The analysis was applied to the peristaltic and the segmental motility acquired using isoflurane and inactin anesthesia. The average frequency analysis of peristaltic motility revealed a single dominant peak among all animals and the segmental motility resulted in three dominant modes among majority of animals. A band pass filter was then applied to dominant peaks for each spatial location

in "x" and a new spatio-temporal maps were reconstructed for corresponding modes. The results of Fourier analysis are presented in Chapters 5 and 6.

We have reviewed complete technical details of MRI, image segmentation, simplified, integrated and Fourier analysis, and is summarized via different modules presented in Figure 3.1. The summary of our approach to analyze the gut motility and contributions of thesis are reviewed here. We have proposed dynamic MRI protocol along with advanced image analysis methods to quantify the motion of small intestine. The image processing algorithms discussed in Section 3.3 were reviewed, combined and tailored for our application to analyze the motility of the small intestine acquired using dynamic MRI. We have developed novel segmentation algorithm by combining 3D live wire and DDGVFS to accurately segment dynamic motion of the small intestine with minimal user intervention. We have introduced an objective way of correcting breathing artifacts and missing images. We have then employed a combination of thinning algorithm and Euclidean distance maps to compute $D(x,t)$. The importance of sophisticated image analysis algorithms lies in overcoming several imaging issues such as breathing artifacts, interpolation of missing images and accurate delineation of the boundary of the small intestine. These steps form the basis for the simplified analysis of complex gut motility and an accurate determination of physiological parameters. The integrated and Fourier analysis was applied to determine the underlying mechanism of the complex gut motility. The results of unique analysis can produce new knowledge about the physiology of gut. This thesis being interdisciplinary will contribute in different areas: (a) better understanding about the physiology of small intestine, (b) technological advances in the application of MRI of gut motility and (c) application of image analysis algorithms for

better interpretation of the GI data.

The detailed steps and in turn the results of each step starting from MRI image acquisition, post processing of the data and final quantitative analysis are described and discussed in Chapter 4. Chapter 4 present results of simplified analysis on *in vivo* motility in rats anesthetized using isoflurane. Chapter 5 presents a integrated analysis approach and its analysis of isoflurane data. In a separate study, a similar approach was used in acquiring and analyzing the motility of rats anesthetized using inactin. Chapter 6 compares different motility patterns, physiological parameters and the results of simplified, integrated and Fourier analysis of the two studies.

Chapter 4

Characterization of motility of small intestine

Our approach was briefly introduced in 3. The implementation details and the results of Specific Aims 1 and 2 will be discussed in this chapter. The dynamic motion of the small intestine was acquired in rats treated with isoflurane anesthesia. In the coming sections, the technical details of image analysis algorithms and MRI image acquisition and complete results on application of image-analysis tools and detailed quantitative analysis of isoflurane data will be presented. We will focus on the modules of simplified analysis presented in Chapter 3. A general block diagram of simplified analysis include MRI image acquisition, registration, segmentation, computation of $D(x,t)$ and final quantitative analysis of the gut motion. This block-diagram can be derived from the summary diagram presented in Chapter 3 in Figure 3.1.

4.1 Abstract

Conventional methods of quantifying segmental and peristaltic motion in animal models are highly invasive; involving, for example, the external isolation of segments of the GI tract either from dead or anesthetized animals. The present study was undertaken to determine the utility of MRI to quantitatively analyze these motions in the jejunum region of anesthetized rats ($N = 6$) non-invasively. Dynamic images of the GI tract after oral gavage with a Gd contrast agent were acquired at a rate of six frames per second, followed by image segmentation based on a combination of three-dimensional live wire (3D LW) and directional dynamic gradient vector flow snakes (DDGVFS). The isoflurane data was analyzed using three approaches, (1) simplified analysis, (2) integrated analysis and (3) Fourier analysis presented in Chapter 3. A simplified analysis of the variation in diameter at a fixed constricting location showed clear indications of both segmental and peristaltic motions. Quantitative analysis of the frequency response gave results in good agreement with those acquired in previous studies using invasive measurement techniques.

4.2 Introduction

Peristalsis and segmental are two dominant motions that characterize the motility and function of small intestine [2, 3]. The peristaltic contractions are propagating and in contrast segmental contractions are stationary. Peristaltic motion represents a traveling wave that propagates the chyme from the oral to aboral ends of the GI tract. In contrast, segmental motions represent radial constrictions at fixed locations along the GI tract and are essential to the macro and micro-scale mixing of the food chyme. Both peristaltic and segmental

motions are essential for the absorption of nutrients that takes place within the small intestine. The normal processes of the small intestine are known to be affected in various pathological conditions such as type II diabetes, dyspepsia, irritable bowel syndrome (IBS), and celiac disease [7]. The goal of this study was to non-invasively acquire motion of the small intestine using MRI and compare physiological parameters with invasive procedures such as *in vitro* and *in vivo* Trendelenburg methods [8, 12–18]. These invasive techniques provide only approximate measurements of gut motility as the gut is not under true physiological conditions, requires extensive sample and animal preparation, are inconvenient for long-term monitoring, and can cause distress for the subjects. Researchers have employed MRI in clinical studies to diagnose early signs of Crohn's diseases [24–26], effects of drugs on the motility [23] and functional information such as water content and water flux [28–32]. As per our knowledge and literature review few MRI studies have been carried out in animal models and none with quantitative analysis of peristaltic and segmental contractions.

The main aim of the present work was to non-invasively determine the motion of the small intestine under true physiological conditions in a rat model. At the time of imaging we faced several challenges such as accurate localization of the jejunum region, the tradeoff between temporal and spatial resolution, and much lower image CNR and SNR than in video techniques. We have addressed these issues by improving the visualization of GI tract using contrast enhanced partial Fourier dynamic MRI and combined sophisticated post processing and image analysis tools to analyze the motility of small intestine.

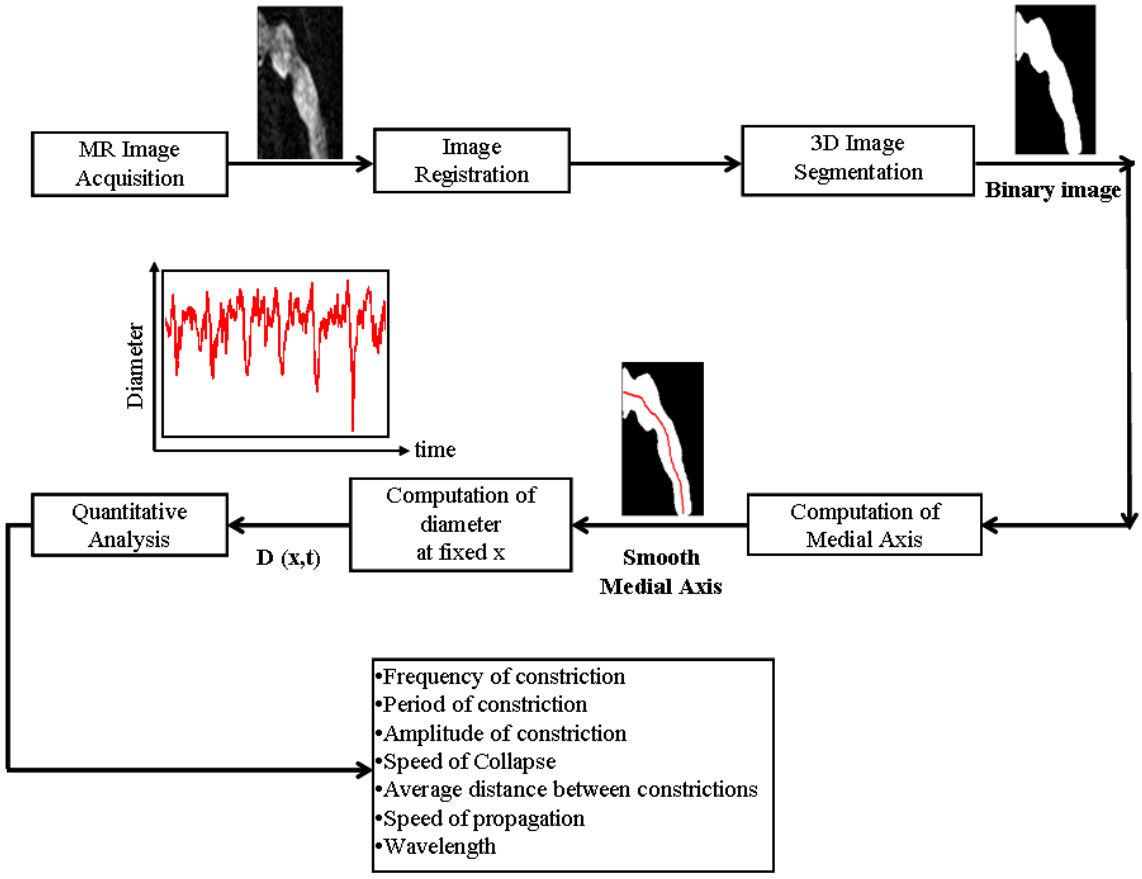

Figure 4.1. Block diagram of simplified analysis of MRI data. A simplified analysis describe Specific Aims 2 and 3, the different image analysis and postprocessing steps to quantify physiological parameters of the peristaltic and segmental motility. The direction of the arrow between process blocks represents the order in which the processes are executed.

4.3 Materials and Methods

Figure 4.1 shows the general block diagram of MRI data acquisition and image processing used to quantify gut motion. Each component is explained in detail in the following sections.

4.3.1 MRI data acquisition of gut motility

All experimental protocols were approved by Penn State Universitys Institutional Animal Care and Use Committee (IACUC). The detailed experiment MRI procedure and the time

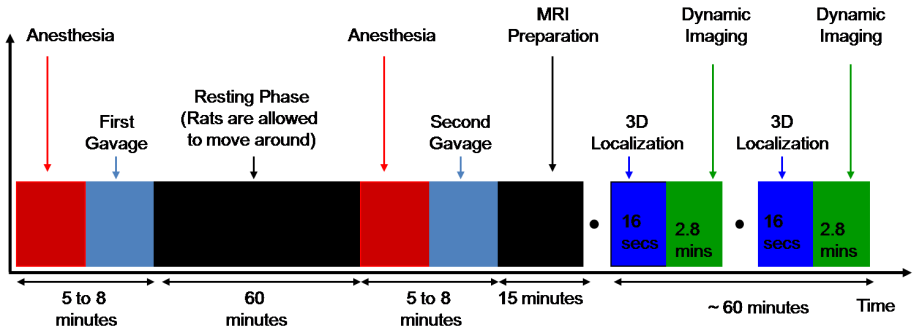

Figure 4.2. Experimental MRI procedure and time line. The rats were anaesthetized using isoflurane and given a double oral gavage of Gd contrast agent before MRI imaging. A 3D imaging of the entire GI tract was performed before every dynamic imaging to aid in the localization of jejunum region.

line of anaesthesia, oral gavage and MRI imaging is shown in Figure 4.2. Rats were given access to laboratory chow and water ad libitum. Animals weighing 200 to 300 g were anesthetized using a mixture of isoflurane (4%) and oxygen gas (flow $\approx 1\frac{\text{liter}}{\text{min}}$). An oral gavage of an 1% gadolinium diethylenetriamine pentaacetic acid (Gd- DTPA) saline solution ($0.75\frac{\text{ml}}{\text{kg}}$ volume) was administered $\approx$ 1h before imaging. The rats were anesthetized again immediately prior to imaging and a second gavage of $0.75\frac{\text{ml}}{\text{kg}}$ was given. During the experiment the isoflurane level was reduced to 2% and oxygen gas flow was regulated to $0.5\frac{\text{liter}}{\text{min}}$. During scanning, the animals temperature and respiration rates were monitored (SAI Model II, Brooklyn, NY, USA) using a rectal probe and pressure transducer, respectively, to ensure that they remained constant. Six animals in total were studied, with segmental motion detected in all six, and peristaltic motion in two. The respiration rate averaged for all data sets for all animals was 0.75 ± 0.12 Hz. The average temperature was 34.42 ± 0.9C. MRI experiments were performed using a horizontal bore 7T magnet with a 12-cm diameter gradient set and a Varian Direct Drive console. In order to identify suitable segments of the GI tract for dynamic imaging, a rapid T_1-weighted spin-echo localizer sequence was run with

16 slices of 1-mm thickness and in-plane resolution of 0.6mm $\times$ 0.4mm. During the total experimental time of $\approx$ 1 h it was found that the position of the GI tract can change by several millimeters, and therefore a separate localizer scan was acquired before each series of dynamic images. For dynamic imaging, a single slice spoiled gradient echo sequence was run with the following parameters: $TE = 1.12$ ms, $TR = 3.12$ ms, data matrix = 96 $\times$ 54 (3/4 Fourier), zero-filled data matrix = 96 $\times$ 72, slice thickness = 2 mm, field-of-view = 3 cm $\times$ 2.5 cm , in-plane resolution 312 μm $\times$ 347 μm, and time per image = 168 ms. A quadrature transmit/receive coil with an inner diameter of 6.3 cm was used. Series of up to 1000 consecutive images were acquired at the same location to capture the gut motion. The location of the slice was chosen to include a length of jejunum as long and straight as possible.

4.3.2 Simplified analysis of gut motility

The dynamic MRI data was analyzed using simplified analysis that include image processing and quantitative analysis modules. The modules are covered in Sections 4.3.3 to 4.3.4.3.

4.3.3 Image registration: breathing artifacts

The first step in image analysis was to align all the images based on a standard procedure involving computing the 2D correlation function between each image and the first one acquired in a dynamic series. The shifts in the x- and y-directions that maximized the value of the 2D correlation function were computed, and then used to realign all of the images. Typical values of translation were = 1 to 2 mm. At the point of maximal respiration, a completely different section of the GI tract lies within the imaging slice; therefore, these

(a)Image without significant shift

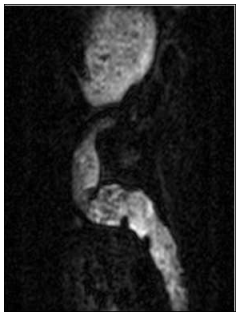

(b)Image with significant shift

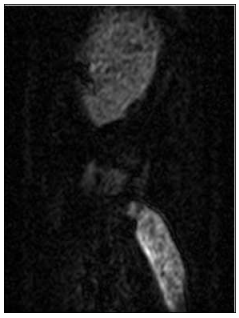

(c) Correlation Plot

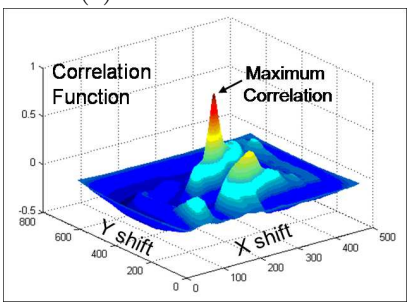

Figure 4.3. Illustration of 2D rigid registration. Animal's breathing induces large shifts and the section of the small intestine being imaged is completely off from the imaging plane and does not have any meaningful shape. An example is shown in (b) and such images are deleted and missing images are linearly interpolated. A 2D correlation function is computed between the first image in time series and the remaining images to determine the translation in x and y.

data cannot be used for analysis see Figure 4.3. Since these images are very different in shape and position, they result in very small values of the correlation coefficient, and large apparent y shifts, typically in the range of 5 to 15 mm (see Figure 4.4). These criteria were used in order to objectively and automatically remove these images from the

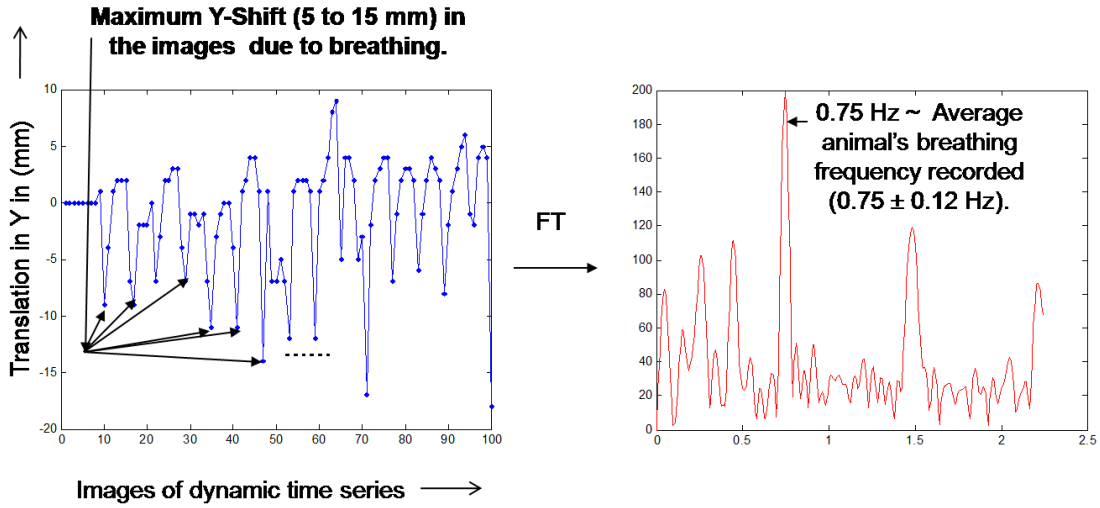

Figure 4.4. Quantitative way of discarding images due to animal's breathing. The figure on the left side shows Animal's breathing induces large shifts in Y ranging from 5 to 15 mm. The plot shows that large shifts are periodic and Fourier transform reveals a dominant frequency that matches with average animal's breathing measured by pressure transducer.

analysis stream. The plot in Figure 4.4 shows that large shifts are periodic and its frequency analysis results in a dominant frequency that matches with animal's average breathing (0.75 ± 0.12 Hz) as measured by pressure transducer. Although image acquisition can be gated to the respiratory cycle, this would introduce an uncertainty in the timing of each image acquisition, which complicates quantitative analysis of the data; therefore, no respiratory gating was applied. Images showing a significant degree of out-of-plane motion were discarded and replaced by a linear interpolation of the images acquired prior to and immediately after the discarded one. In practice, the respiration rate was very consistent throughout the experiment and approximately every sixth image was discarded.

4.3.4 3D Image Segmentation

Even with the introduction of an MRI contrast agent, the dynamic images of the jejunum have relatively low SNR and CNR (compared to, for example, the video images produced using the Trendelenburg method) and exhibit rapid changes in morphology including deep indentations of the gut. The first step in quantitative analysis of gut motion is therefore to perform 2D space + time image segmentation. Two segmentation algorithms, 3D LW and DDGVFS, were run sequentially. 3D LW was performed on the time-series images to compute an initial (approximate) boundary. This boundary was used as an input to the DDGVFS algorithm, which then iterated to the final solution. This combined approach represents a variation on that of Liang *et al.* [90], which they termed united snakes. Image segmentation was developed using an interactive Matlab graphical user interface (version 7.3; Mathworks, Natick, MA, USA) and Matlab executable (MEX) programs. 3D LW [88], also known as intelligent scissors, is an extension of 2D LW based on the formulation of Mortensen *et al.* [81] and represents an interactive manual tool used for image segmentation. The boundary is extracted between a pair of chosen points by calculating an optimal path between them using Dijkstras algorithm [81]. After the placement of first seed point on the boundary, an optimal path computed between this point and the current position of the mouse is displayed in real time. The optimal path between a pair of points a and b is based on the minimization of the weighted sum of component cost function given by equation 3.13. The features Laplacian zero crossing (F_Z), gradient magnitude (F_G), gradient direction (F_D) were used in the cost function and and the weights of the corresponding features are $w_Z = 0.3$, $w_G = 0.3$, and $w_D = 0.1$. In the extension to 3D LW, seed points in the third

dimension are generated using 2D LW on planes orthogonal to the stack of images [88]. In most applications the third dimension is spatial, but in this particular application the data represent 2D spatial + 1D time. As mentioned previously, the segments of the gut contract and expand and the shape of the small bowel varies rapidly from one image to another image (t = 168 ms). In highly contractile areas the seed points generated by the semiautomated 3D LW do not lie exactly on the boundary of the gut and the algorithm was found to fail to compute a good boundary in the images with deep indentations; therefore, a second algorithm was used to fine-tune the image segmentation using the results from the 3D LW as an initial approximation to the boundary. Snakes are deformable curves generated within an image domain and are moved under the influence of internal forces from within the model itself and external forces computed from the image data [79, 86]. The central idea is an iterative global energy minimization framework to achieve edge detection [79, 86]. For an initial approximation to the desired contour, the snake finds the minimum energy contour by iteratively solving an energy function (see equation 3.26) by joining internal forces to keep the contour smooth. External forces are used to attract the snake to image features and constraint forces keep the overall shape of the contour [79, 86]. The external force used in Snakes and GVF is the magnitude of the gradient of the image and it does not consider the sign of the gradient and thus is unable to distinguish between positive and negative edges. The results published by Cheng *et al.* [87] have shown that DDGVF does a better job of image segmentation in the presence of two opposite edges very close by and an initial estimate of the boundary can be directed to stick to a particular edge of interest [87]. In case of GVF snakes the information of near by edges can diffuse and depending on gradient values it can snap on to both edges. The definition of positive and

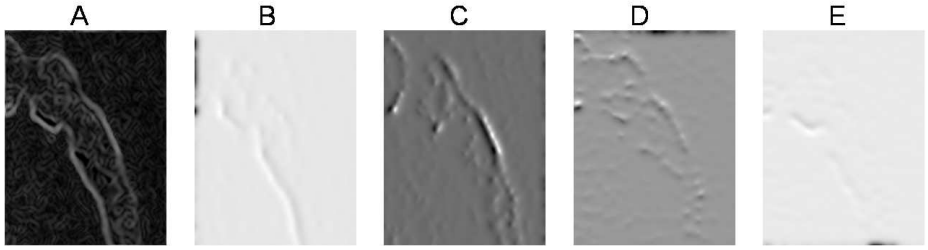

Figure 4.5. DDGVF field of an edge map. (A) The edge map of a gray scale image of small intestine. Dynamic Directional Gradient Vector Flow Field in (B) $+x$, (c) x, (D) $+y$ and (E) y directions for positive step edges.

negative step edges depends on the direction of the normal at each point along the contour. The location of the initial contour is unknown and DDGVF is dependent on the location and shape of the contour. In the case of Snakes and GVF, external force is static but in DDGVF it uses gradient directional information dynamically and does a better job in segmenting complicated shapes. The DDGVF field is computed from the edge map of the gray scale image (Figure 4.5A) and DDGVF field for all possible directions for a positive step edge is shown in Figures 4.5B to 4.5E. The technical details of snakes, GVF snakes and DDGVF snakes are presented in Chapter 3 in section 3.3.1.5.

The following parameters and weights were used for the second stage DDGVFS algorithm: $\alpha = 0.1$, $\beta = 0.1$, $\mu = 0.15$, GVF iterations = 50, snake iterations = 80, and snake step size = 0.2. The evaluation criteria, a ratio of intersection over union of binary 3D volumes, outlined in [82, 83, 88] was used to compute % accuracy and % repeatability of 3D segmentation tool. Overall, the combination of the two techniques, gave good segmentation results in $\approx 97\%$ of all of the images analyzed. The algorithm was found to fail in cases where the gradient strength of the edges was not high enough to attract the initial boundary. In such cases, manual 2D LW was applied to the remaining images.

On average it took ≈ 15 s to process each image or ≈ 4 h per data set (1000 images) on a computer with the following specifications: Intel Pentium 4 processor, 3.2 GHz, $3GB$ of random access memory (RAM). The majority of functions such as cost computation in LW, Windows based mouse-tracking, iterative snakes, etc. were implemented in Matlab Version 7.3, but Dijkstras algorithm was implemented in C to improve the processing speed.

4.3.4.1 Computation of medial axis

In order to compute the medial axis of the GI tract, a 2D thinning algorithm based on the formulation by Saha *et al.* [34] was applied to the segmented images to compute the medial axis. The technical details of thinning algorithm and multistage false branch deletion is presented in Chapter 3 in section 3.3.2. Thinning represents an iterative process and with each iteration it deletes the boundary pixels based on certain criteria until a connected 1-pixel-thick skeleton is achieved. The algorithm is very similar to the process of iterative erosion of boundary points and conserves the shape and topology of an image. Simple application of this thinning algorithm was found to result in small false branches in addition to the medial axis. Kiraly *et al.* [35] have proposed geometric techniques to remove false branches in the 3D skeleton of tubular structures via determination of a tree structure for the skeleton that has ordered sets of branches, with each branch having an ordered sets of points. The latter method was implemented to remove the small branches. The final step is mathematical fitting of the medial axis with a cubic spline function to make it smooth and continuous. The technical details of thinning, false branch deletion are explained in Chapter 3 in Sections 3.3.2.1 to 3.3.2.3.

The conventional way of computing the diameter at each point along the medial axis, by drawing lines perpendicular to the medial axis and finding their intersection with the upper and lower boundaries of the small intestine, is known to fail in regions of high curvature such as those encountered in images of the jejunum. A more sophisticated and robust method is to use distance transform maps, which describe the circle of maximal radius that can fit within a particular region of binary shape with its center lying on the medial axis.

4.3.4.2 Computation of spatio-temporal maps

Euclidean distance maps were calculated from binary segmented images and these were used to compute $D(x,t)$, the diameter at a fixed constricting location in x, along the medial axis of every image in time. Spatio-temporal maps of occlusion vs time can be produced by computing the values of the minimum (D_{min}) and maximum (D_{max}) diameters at each point along x and scaling by a factor $\frac{(D(x,t)-D_{min})}{(D_{max}-D_{min})}$: this results in the minimum diameter being represented as dark and maximum diameter being bright. A 1D signal that described the variation of the diameter as a function of time was obtained from a fixed location at x by computing the average diameter of the gut in the regions of constriction, and the characteristic frequency (F) of the constriction was computed using Fourier transformation.

4.3.4.3 Quantitative analysis: physiological parameters

From the spatiotemporal maps, the characteristic frequency (F) of the constriction was computed by applying a discrete Fourier transform, the amplitude of constriction (A) is given by $\frac{1}{2}(D_{max} - D_{min})$, the speed of the collapse or speed of constriction (S) is given by A/T. The velocity (v) of the propagation of the peristalsis wave was determined from the

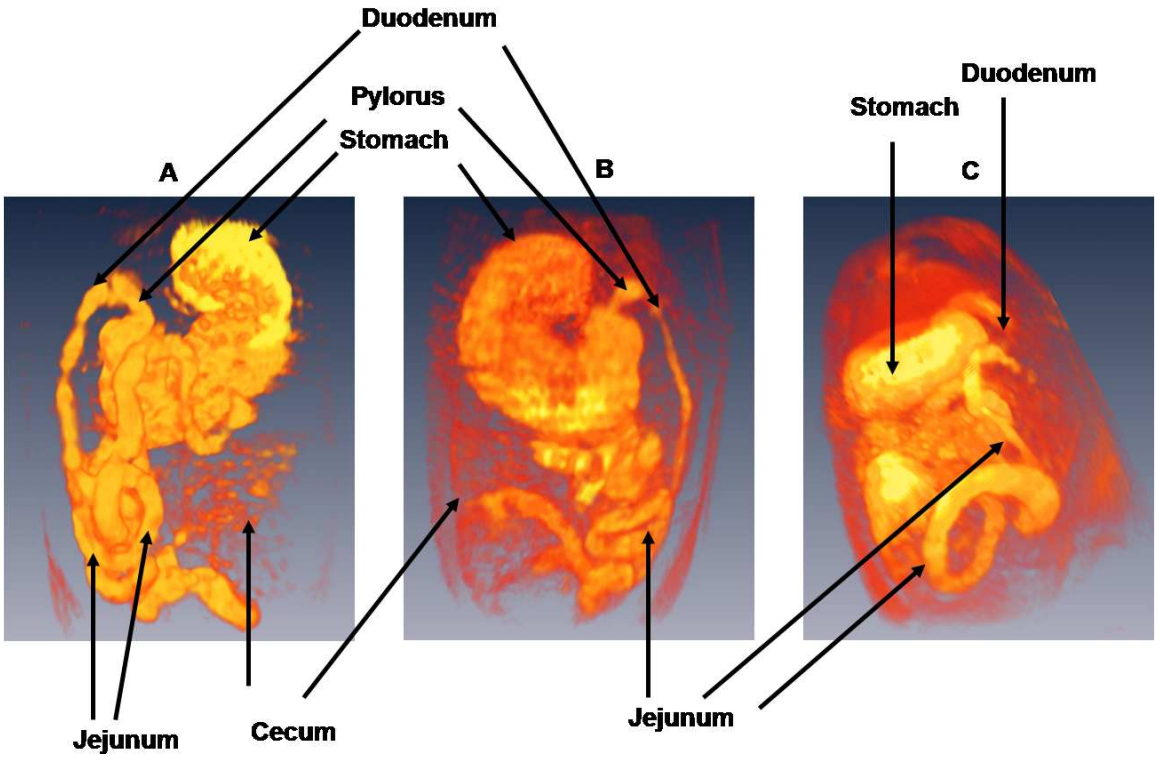

Figure 4.6. Reconstruction of the GI tract from a 16-slice T_1-weighted spin-echo sequence. Data acquisition parameters: field-of-view = $6cm \times 4cm$, data matrix = 100×100, TR = 10 ms, TE = $4ms$, slices = 16, thickness = 1 mm.

slope of the diagonal streaks in the spatio-temporal maps, and finally the wavelength (λ) calculated from v/F.

4.3.5 Statistical analysis

The inter animal dependency for different physiological parameters of peristalsis and segmented motions were computed using one way Anova with multiple comparisons using the Holm-Sidak method: a p-value of 0.05 was used for significance.

4.4 Results

4.4.1 Localization and motility of small intestine

An example of a reconstructed multi-slice data set used to localize the jejunum is shown in Figure 4.6. The distinction between duodenum and jejunum is clear, and the pylorus and cecum can also be identified. Figure 4.7A depicts the time-series of dynamic MRI scans, used for the input to the image segmentation algorithm.

4.4.2 3D image segmentation of gut motility

Figure 4.7 provides results on the intermediate steps (in sequential order from A to H labeled on top of each figure) of 2D spatial + time image segmentation algorithm on dynamic motility of the small intestine. Figure 4.7A provide, 3D time-series of dynamic MRI scans, used for the input to the image segmentation algorithm. Figure 4.7B provides a spatial-temporal plot at four positions through the jejunum, demonstrating the rapid spatial changes of the time-series of 2D (x,y) images stacked into a 3D (x,y,$time$) data set. Manual 2D LW is used to segment the boundary of the small intestine in corresponding orthogonal planes. Figure 4.7C shows each orthogonal plane generates 2 seed points and they get accumulated with successive orthogonal planes. Figure 4.7D shows desired number of seed points are generated on all the images. A approximate closed boundary is computed using automated LW algoithm is shown in Figure 4.7E. An approximate boundary computed by LW (solid red) can be used as an initialization for DDGVF snakes and the final boundary (solid green) computed is shown in Figure 4.7H.

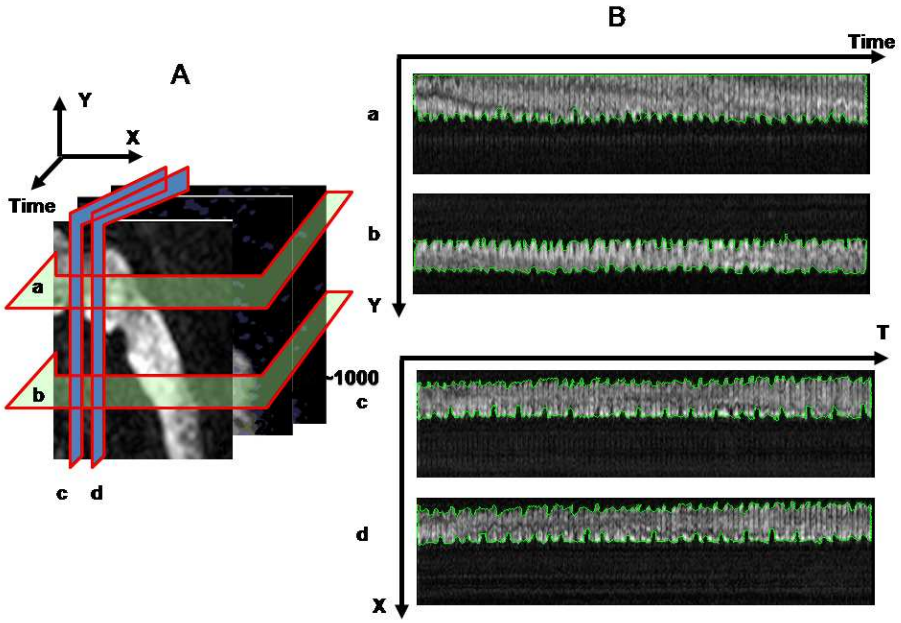

(a)Applying 2D Live Wire in orthogonal planes

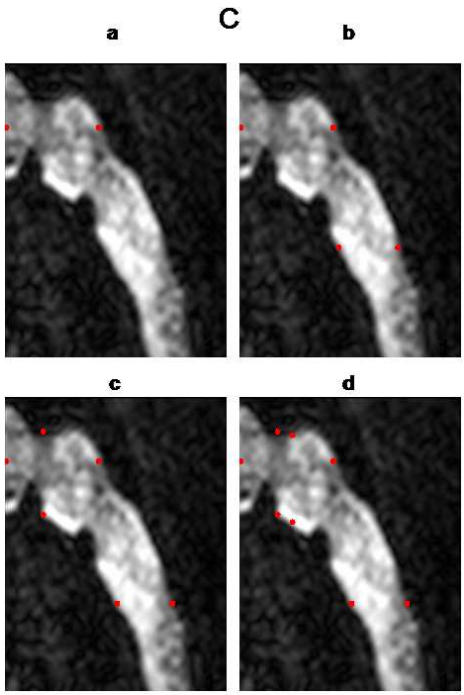

(b)Each orthogonal plane generates two seed points on the boundary

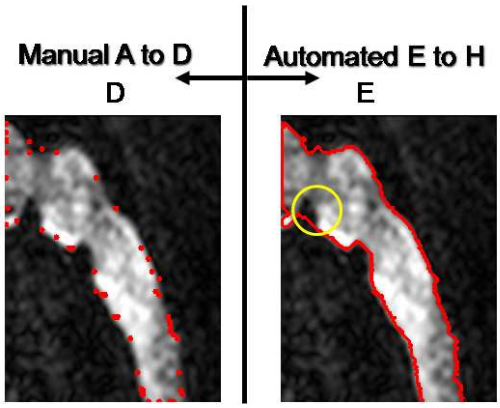

(c) Approximate boundary using Live Wire

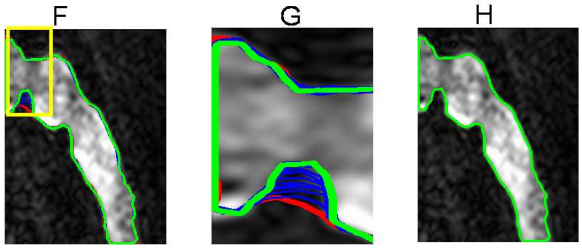

(d) Final boundary using DDGVF Snakes

Figure 4.7. Steps involved in 2D Spatial + time image segmentation algorithm of MRI data of small intestine. (A) 2D images are stacked in time. XY is chosen as LW plane and for understanding purpose only 2 orthogonal planes (a to d) are shown in each direction XT and YT. (B) Manual 2D LW is used to segment the boundary of the small intestine in corresponding orthogonal planes. The segmented boundary is projected to generate seed points on the boundary in LW plane. (C) Each orthogonal plane generates 2 seed points and they get accumulated with successive orthogonal planes. (D) Desired number of seed points are generated on all the images to compute approximated closed boundary using automated 2D LW. (E) An approximate boundary is computed using automated 2D LW. It fails in the regions of high concavities where it is difficult to generate seed points (as shown by solid yellow circle). (F, G and H) An approximate boundary computed by LW (solid red) can be used as an initialization for DDGVF snakes. The intermediate steps from the approximate boundary to final boundary are shown by blue lines. The zoomed in rectangular region of the small intestine (in F) is shown in G and the final boundary (sold green) computed is shown in H.

Figure 4.8 shows successive images from the jejunum region of a rat during segmental motility (row 1), the approximate boundary produced from 3D LW algorithm (row 2), and the final boundary computed using DDGVFS (row 3). The accuracy and repeatability of

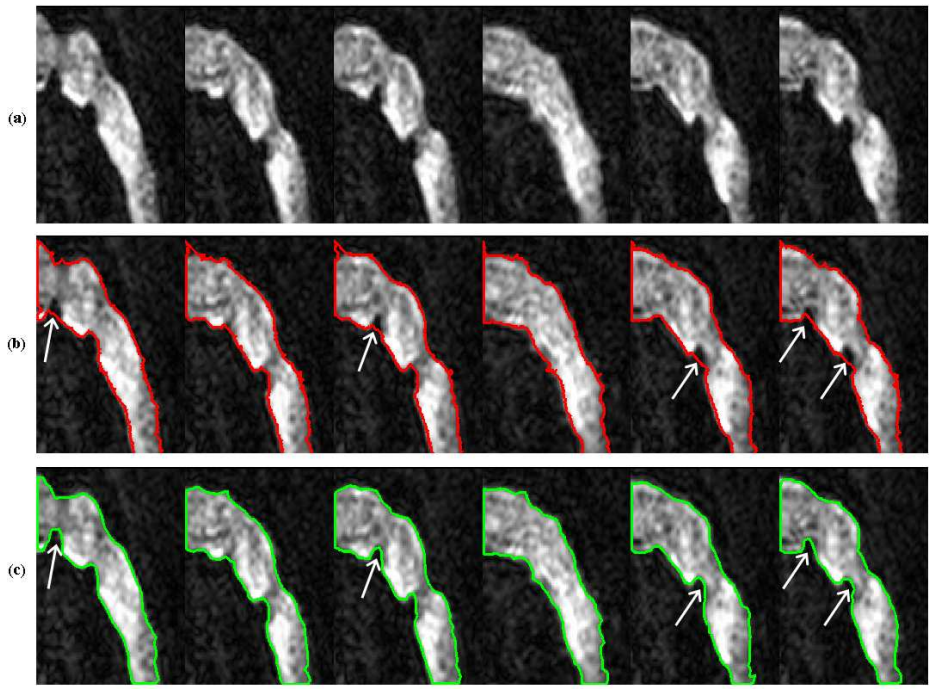

Figure 4.8. Illustration of dynamic time series and results of 3D segmentation. (Row 1) Successive images from the jejunum region of a rat, (Row2) approximate boundary computed using 3D LW, and (Row3) final boundary using DDGVFS. The 3D LW algorithm failed to compute a good boundary in the regions of deep indentations, as shown by an arrow in the images in Row 2. The corrected boundary for the corresponding indentations is shown by the arrows in Row 3.

the segmentation algorithm was evaluated for one of the cases, by comparing 3D (2D space + time) binary masks of the segmented jejunum region with a gold standard, where the boundary is segmented with purely manual 2D LW, using the criteria described in Lu [88], Falcao and Udupa [82,83]. The accuracy was 97.1% and the repeatability (with three trials) was 98%.

Illustration of successive steps in 2D thinning algorithm on small intestine.

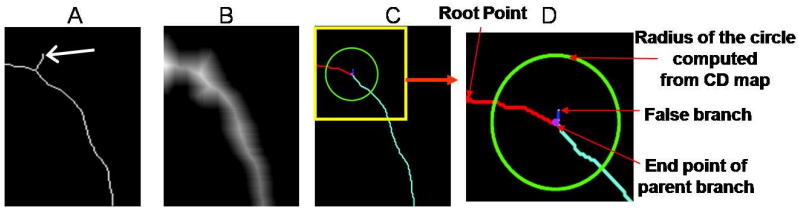

(A) Skeleton with false branch, (B) Chamfer distance map,
(C and D) Tree structure and length based elimination of false branch

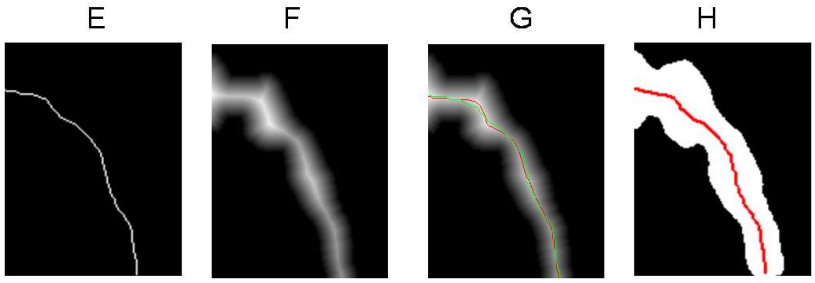

(E)Skeleton after branch deletion, (F)Euclidean distance map,
(G) Simple centering of skeleton and (H) Final smooth medial axis.

Figure 4.9. Compute medial axis of small intestine. Binary image was reconstructed after image segmentation. A 2D thinning algorithm was applied on the binary images to compute a skeleton. (A) The thinning algorithm outputs skeleton with central medial axis and short false branches. (B) The next step is to use Chamfer distance map in false branch deletion algorithm. (C and D) The first step in false branch deletion algorithm is to compute a tree structure of the skeleton and possible paths to traverse along the skeleton. The different branches are shown in red, blue and green colors. Short branch (blue) was deleted based on length based criteria explained in methods section. A zoomed in rectangular region of short branch is shown in D. (E) A skeleton without short branches is now used in next stages to compute a final medial axis. (F) A Euclidean distance map is used to center the skeleton as per the criteria explained in methods section. (G) The skeleton before centering is shown in green and after centering is shown in red. (H) finally centered skeleton was interpolated with cubic spline to generate a smooth and continuous medial axis.

4.4.3 Medial axis of the small intestine

Figure 4.9 shows successive steps involved in producing the medial axis, using thinning algorithm, multistage false branch deletion and final smoothing. The technical details of intermediate steps are described in 3.3.2.

4.4.4 Characterization of motility patterns

The quantitative analysis of small intestine revealed two types of motions, peristalsis and segmental, shown in Figures 4.10 and 4.11, respectively. Although it is well known that anesthesia reduces peristaltic activity [8, 92], the data in this study showed both clear peristaltic and segmental activity using a mixture of isoflurane and oxygen gas. However, periods of peristalsis were found to be much shorter-lived than those of segmental motion, which occurred essentially continuously in all animals studied.

4.4.4.1 Peristalsis

Peristaltic motility was detected by its characteristic pattern, as shown in Figure 4.10, corresponding to a single constriction, which travels along the length of the gut from right to left (the location of constriction is marked by an arrow in images 2 to 10) in a single peristalsis wave, in contrast to segmental contractions, which are stationary. The spatio-temporal map of peristalsis wave is represented by continuous dark diagonal streaks 4.10b. The variation of the diameter of the gut at a given anatomic location during a single peristalsis wave is shown in images 1 to 10 in Figure 4.10a by a circle corresponding to the changes in the diameter of the GI tract. For peristaltic motility, a 1D signal of the variation of diameter vs. time at a fixed location in x from a spatio-temporal map, is

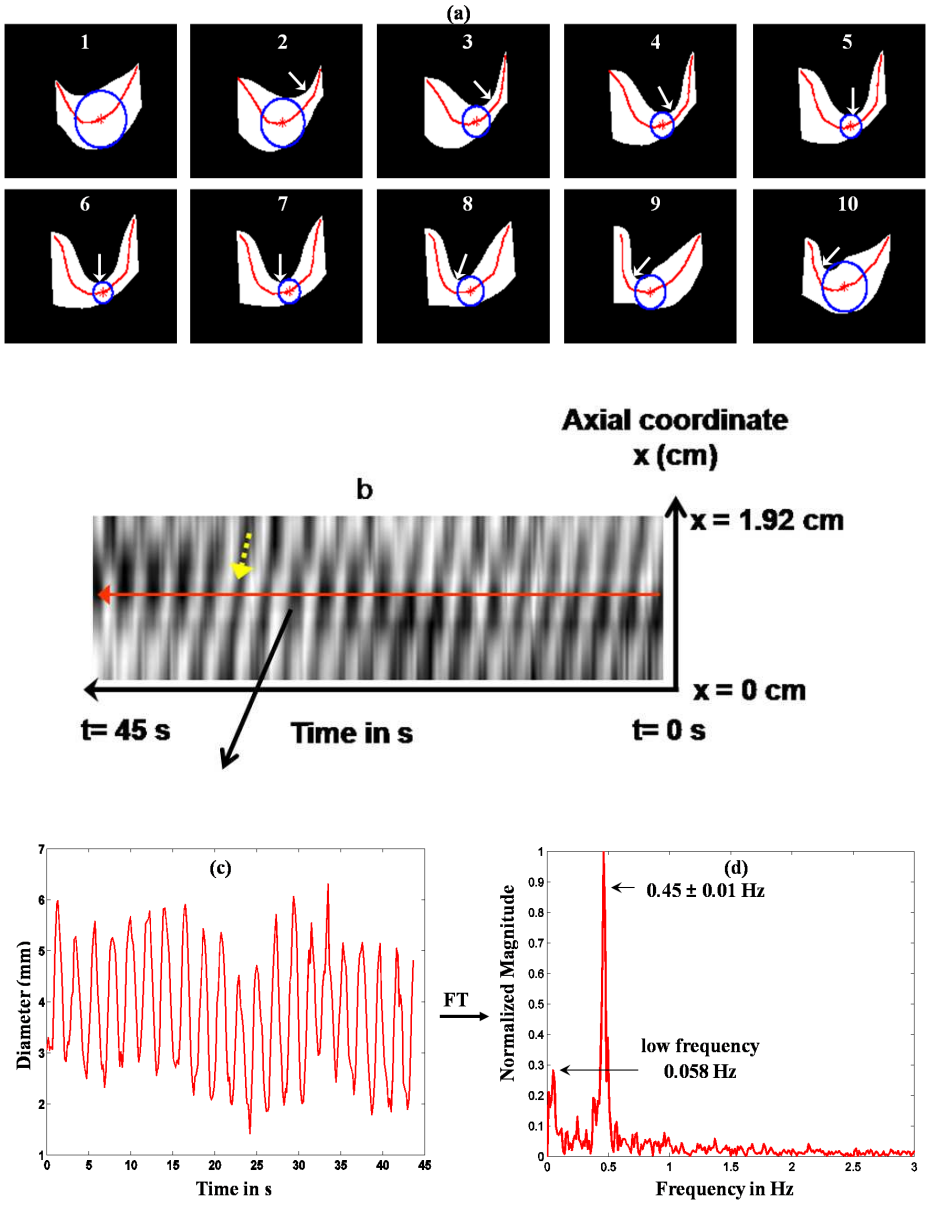

Figure 4.10. Analysis of peristaltic motility of the rat jejunum acquired using dynamic MRI. (a): The binary images show how a single constriction (marked by the arrow) travels along the length of the gut during a single peristalsis wave. The diameter of the gut at a fixed location (marked by $*$) is shown by a solid circle in images 1 to 10; (b) spatio-temporal map of peristaltic motility is represented by dark continuous diagonal streaks. The peristaltic motility represents a propagating wave; (c and d) plot of diameter vs. time, $D(x,t)$, derived from Euclidean distance map at a fixed constricting location in x; and corresponding frequency plot obtained by simple Fourier transformation.

shown in 4.10c. The characteristic frequency (F) of the constriction was computed using Fourier transformation; it resulted in a single frequency (0.45 ± 0.01 Hz) that characterizes $81.5 \pm 4.7\%$ of the total power of the frequency spectrum, as shown in 4.10d. The peak situated at very low frequency (0.058 Hz, 6% of the total power), which can be seen as a slow variation in the baseline in 4.10b, is consistent with very slow changes in the position of the GI tract that are not completely removed by the image registration step.

4.4.4.2 Segmental

In contrast to peristalsis, segmental motions appear as constrictions at a fixed spatial location, as shown in Figure 4.11a. The spatio-temporal map of segmental motility is represented by discontinuous dark vertical bands representing locations of constriction 4.11b. The location of the constriction is marked by an arrow in the images 1 to 8 and the constriction occurs at a fixed location and does not travel along the length of the gut. Frequency analysis of the plot of diameter vs. time from the spatio-temporal map in Figure 4.11c, gave two major peaks (0.27 ± 0.04 Hz and 0.42 ± 0.07 Hz), with the contribution of the peaks representing $> 65 \pm 18\%$ of the total power of the frequency spectrum (see Figure 4.11d). Similar to the peristalsis case, the lower frequencies (0.034 and 0.13 Hz, 8% of the total power each) are also seen in the spectrum of segmental motility.

4.4.5 Physiological parameters of gut motility measured using MRI

From the data shown in Figures 4.10 and 4.11, parameters such as the period, amplitude, speed of constriction, and velocity of propagation can be estimated: the results are shown in Table 4.1. The average frequency response (see Figure 4.12) among all animals revealed con-

sistent frequencies among all animals for peristalsis and segmental motility. An important aim of the analysis was to determine the degree of inter-animal variability in the numbers obtained. The differences between different data sets were computed using one way Anova with multiple comparisons. A p value of < 0.05 was used to indicate any significant differences among the data sets. No significant difference ($p < 0.05$) was found in segmental for: frequency, the derived period of constriction, and the average distance between constrictions. A variety of other measurements are also reported in Table 4.1. Although these latter measures were consistent with respect to repeated measurements within the same animal, there was significant difference between animals at the $p = 0.05$ level. The reason for this is relatively straightforward: measures such as the maximum and minimum diameter of the jejunum, the speed of collapse, and amplitude of the constriction are highly dependent upon the exact position of the MRI slice within the jejunum (since the slice thickness is much less than the average diameter of the jejunum). In contrast, the frequency of segmental motion, and the average distance between constrictions do not depend upon the exact location of the slice within the jejunum. No significant difference ($p < 0.05$) was found in the parameters for peristaltic motility.

4.4.6 Source of low frequency components

In order to confirm that the low-frequency components were indeed unrelated to motility, and that any residual effects of respiration could not result in apparent motility, a full analysis was performed on a section of the jejunum which was not undergoing either peristaltic or segmental motion. The results are shown in Figure 4.13, which replicates the very low frequencies seen in Figures 4.10 and 4.11 segmental motility. The analysis revealed peaks

Parameter	Segmental	Peristalsis
% Motility	97%	3%
Maximum diameter*(mm)	$4.6 \pm 1.35^*$	5.42 ± 0.53
Minimum diameter*(mm)	$2.28 \pm 0.8^*$	1.45 ± 0.52
Amplitude of constriction*(mm)	$1.16 \pm 0.38^*$	1.98 ± 0.33
Frequency of constriction (Hz)	0.26 ± 0.022 0.42 ± 0.021 0.72 ± 0.089	0.47 ± 0.028
Period of constriction (s)	3.5 ± 0.53	2.18 ± 0.02
Average distance between constrictions (mm)	4.56 ± 1.21	N/A
Mean speed of propagation (mm/s)	N/A	4.34 ± 0.35
Speed of collapse*(mm/s)	$0.33 \pm 0.1^*$	0.91 ± 0.15
Wavelength*(mm)	$9.08 \pm 2.74^*$	9.4 ± 0.78

Table 4.1. Measured parameters for segmental and peristalsis motions. The values are given as Mean ± SD and N/A = not applicable. The parameters marked with $*$ represents significant inter-animal differences at $p = 0.05$ level for peristalsis and/or segmental motility.

in the same low-frequency range as seen in Figures 4.10 and 4.11.

4.5 Discussion

A number of groups who have used the in vitro Trendelenburg experiments have reported that the frequency of peristalsis in the jejunum region of rat small intestine was approximately 26 to 28 $cycles/min$ (0.43 to 0.47 Hz) [12, 13, 93–96], which is in good agreement with the results presented here. The speed of propagation (4.34 ± 1.03 mm/s) of peristalsis wave as measured here by MRI lies within the range reported [17, 18] using the in situ Trendelenburg method (2 to 5 mm/s). The frequency and period of these peristaltic waves correlates well with the frequency of the short length propagating slow wave activity of the interstitial cells of Cajal. A number of studies have pointed out that the maximum frequency

of the peristaltic motility is determined by the frequency of electrical spikes generated by interstitial cells of Cajal and have reported the maximum frequency in the jejunum regions of different animal models, such as dogs (17 $cycles/min$) [97] and pigs (15 $cycles/min$) [98]. It should also be noted that the in vivo experiments carried out by Ferens *et al.* [17] have described propagating contractions occurring in clusters at very low frequencies of $2.28 \pm 0.04\ min^1$. These very low frequencies were not detected from the MRI data in the current study and are probably masked by low-frequency modulations in the data; caused by, for example, uncorrected respiration effects and inaccuracies in the segmentation. The role of the anesthesia is also probably important here: Torjman *et al.* [99] have shown that GI transit of charcoal was reduced by $\approx 50\%$ at 2 h after brief administration of isoflurane. In terms of segmental motion, Gwynne and Bornstein [14] and Gwynne *et al.* [15] have shown that segmental contractions can be evoked in vitro in isolated guinea pig small intestine by intraluminal infusion of fatty acids and amino acids. They have reported that the frequencies of segmental constrictions are independent of the slow waves [14] and had consistent frequencies in jejunum of $9.6 \pm 6.0\ cycles/min$, adjusted in the later report to $7.8 \pm 5.8\ cycles/min$, in guinea pigs. The MRI data shown in Table 4.1 give a frequency in the jejunum that lies at the upper end of that reported by Gwynne and Bornstein [14] and Gwynne *et al.* [15], but considerable care should obviously be taken in comparing the results from different animals under very different measuring conditions.

4.6 Conclusions

This study represents the first quantitative analysis of motion of the GI tract in vivo in animal models using MRI. In contrast to invasive procedures, MRI does not require extensive tissue preparation, and captures a much truer physiological state of the gut. Due to the low CNR and rapid temporal change in morphology in the dynamic images, significant image processing is required for accurate segmentation of the GI tract. The image segmentation algorithm based on the combination of 3D LW and DDGVFS accurately segmented $\approx 97\%$ of the motility of the small intestine. Quantitative analysis of the segmented data showed that both peristalsis and segmental motions are present in anesthetized animals, and could be readily identified by propagating and stationary type constrictions, respectively. Peristaltic motility was reduced in the rats, as expected, due to the use of isoflurane.

4.7 Summary

Chapter 4 focussed on dynamic MRI data acquisition of small intestine in rats anaesthetized using isoflurane, combination of sophisticated image analysis algorithms to analyze the gut motility and comparison of physiological parameters measured using MRI with the data in the literature. In addition to simplified analysis the motility of small intestine was analyzed using integrated and Fourier analysis. The frequency analysis of segmental motility revealed three dominant peaks among majority of animals. Integrated PCA was applied to decompose the complex gut motility into independent modes. We have used ASM as a technique to compute principal components and employed spatio-temporal maps and frequency analysis to visualize and analyze space time geometry of decomposed modes.

The motivation of PCA was to determine the underlying mechanism and its implications to physiology of gut motility. In addition to PCA, Fourier analysis was applied to determine source of additional frequency peaks in segmental motility. The technical details and results of integrated and Fourier analysis are presented in Chapter 5.

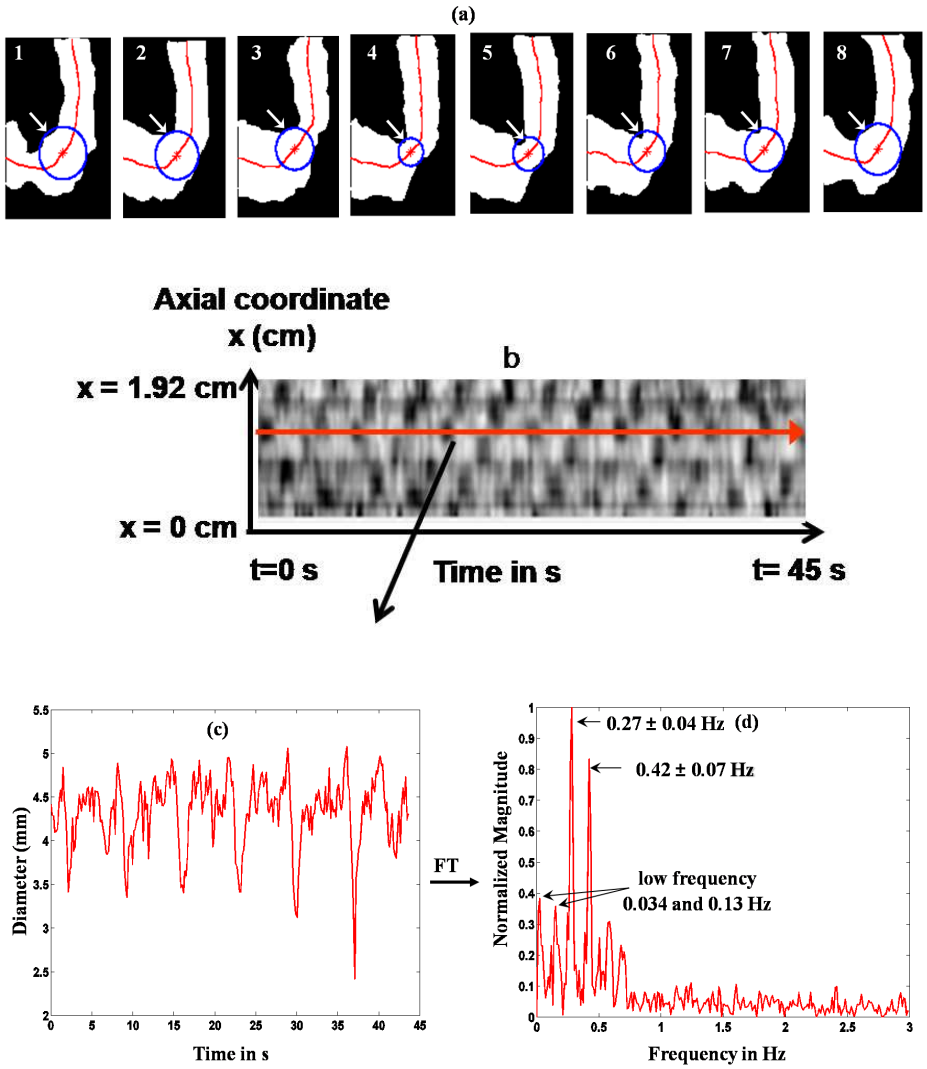

Figure 4.11. Analysis of segmental motility of the rat jejunum acquired using dynamic MRI. (a) Binary images show the variation of diameter vs. time at a fixed location in x on the medial axis during segmental motility. In contrast to peristaltic motility, the constrictions of segmental motility are stationary and occur approximately at the same location. The diameter of the gut at a fixed location ($*$) is shown by a solid circle in images 1 to 8; (c) spatio-temporal map of segmental motility represents dark discontinuous vertical bands. Unlike in peristalsis, these constrictions are stationary and do not propagate; (c and d) plot of diameter vs. time, $D(x,t)$, derived from a fixed constricting location; and corresponding frequency plot obtained by simple Fourier transformation.

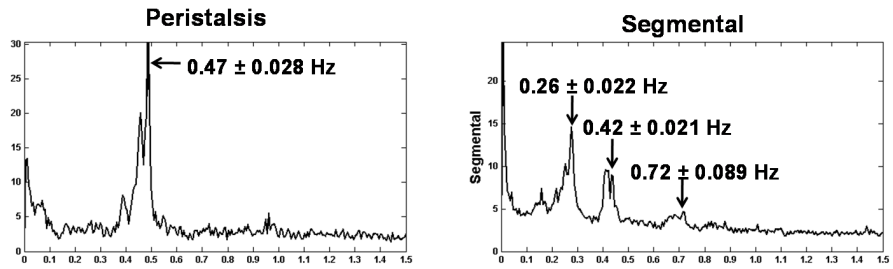

Figure 4.12. Average frequency response of peristalsis and segmental motility.

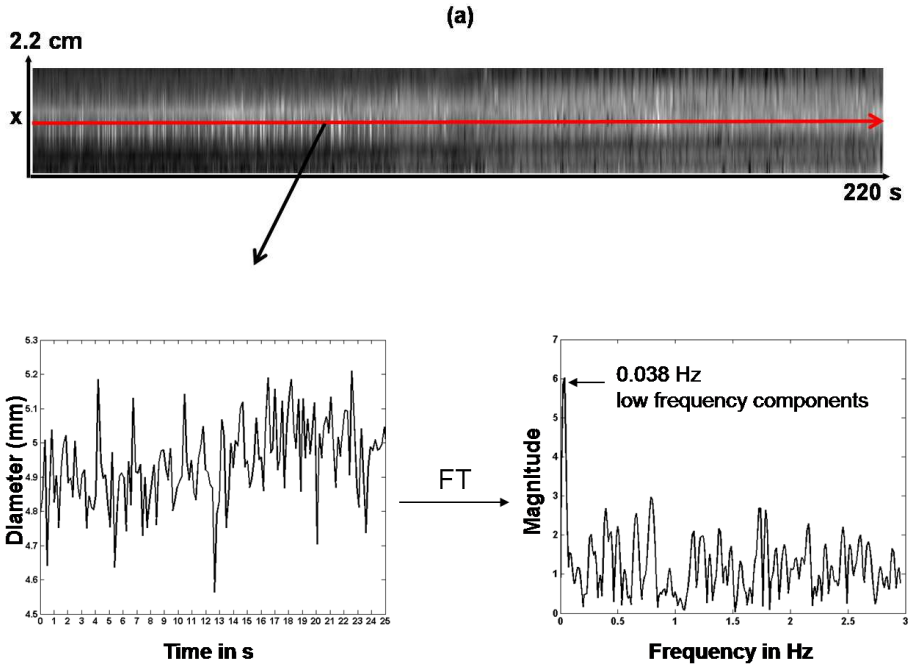

Figure 4.13. Presence of low frequency components in actual gut motility. A frequency analysis was performed on the section of gut which did go under any type of gut motility. (a) Spatio-temporal map of a section of gut with long period of inactivity; (b) The plot of diameter variation vs. time was derived at a fixed location in x, from a spatio-temporal map; (c) The frequency analysis revealed peaks in the same low-frequency range as seen in Figures 4.10 and 4.11

.

Chapter 5

Determine the underlying mechanism of gut motility

We have shown a non-invasive way of quantifying in-vivo motion of the small intestine using dynamic MRI, representing in-vivo peristaltic and segmental motion of rat jejunum. Consistent inter-animal data were acquired allowing quantification of a number of physiologically important parameters. In our experimental setup the small intestine is under true physiological condition and is unaltered. The physiological parameters of gut motility in rats obtained using the current MRI study were used to parameterize the geometry model for computational fluid dynamic model. This model can help us to understand several processes such as transport of nutrients, absorption and pressure gradients, which are difficult to measure experimentally.

We have added another dimension in the quantitative analysis of gut motility by decomposing complex gut motility into few dominant modes using integrated and Fourier analysis. The results of the analysis can help us to interpret an underlying mechanism of the neu-

rophysiology of the gut. In integrated analysis ASM was used to determine the principal components and the technical details of ASM were presented in Chapter 3 in Section 3.4. In the coming sections, the results of integrated and Fourier analysis and the physiological relevance of the decomposed modes are discussed.

5.1 Introduction

Gut motility plays an intrinsic role in mixing, transport and absorption of the nutrients, particularly in the jejunum region of small intestine. Various researchers employing conventional method like Trendelenburg recording have availed spatio-temporal maps and are extremely useful to quantify and understand the motility of the small bowels. The prevalent state of the macro scale gut motility, either peristaltic, segmental, combination of both or even more complex can be visualized by iso-contour spatio-temporal plots but often with an unclear understanding and functionality.

In our early study we have shown that dynamic MRI in combination with image analysis and spatio-temporal maps can non-invasively analyze and quantify the motions in the jejunum region of anesthetized rats (see Figure 4.1). The quantitative physiological measurements such as amplitude and dominant frequency of constriction, distance between constrictions for segmental motion, and wave propagation speed in peristalsis were derived from the spatio-temporal maps. In context to our previous isoflurane study clear evidence of the segmental, standing wave pattern with three dominant frequencies (0.25 ± 0.022 Hz, 0.42 ± 0.021 Hz and 0.72 ± 0.089 Hz) and peristaltic, a traveling wave pattern at a single frequency (0.47 ± 0.028 Hz).

The objective of the present study is to discover an underlying order within the intricacy of gut wall motions and their neurophysiological control through integrated analysis, Fourier analysis and spatio-temporal maps. The overall aim of the study is to perform quantitative analysis with physiological interpretation of the principal components and Fourier modes of peristaltic and segmental motilities. It is well known that PCA reduces the dimensionality of the data and points out few dominant modes that essentially represent larger variation of the data. The motivation for PCA is to break the complex dynamics of the system into smaller number of simple components and we approached PCA in the hope that each component has something unique about it. The current chapter describes the results and their physiological relevance associated with individual modes of peristalsis and segmental motilities. On the other hand the motivation of Fourier analysis is to determine the source of individual frequency peaks in peristaltic and segmental motility.

Integrated analysis combine three analytical techniques: principal component analysis (PCA) using active shape models (ASM), spatio-temporal maps, and frequency analysis. Dynamic MR images of the GI tract were acquired at six frames per second, segmented by in house developed semi automated 2D spatial + time image segmentation software, decomposed into simple modes using active shape models and computation of the medial axis to create spatio-temporal map of the combined and individual modes (for details refer Chapter 4). The temporal nature of the lumen geometry were reconstructed using the first 3 principal components ($56 - 75\%$ total signal variance), either individually or summed. The 2D function, lumen diameter vs. axial coordinate and time, spatio-temporal map of occlusion vs. space-time and frequency spectra of the constricting locations were derived from the original and decomposed geometries. In integrated analysis all quantifications were

done for the principal components and the full deformations.

The spatio-temporal map of the decomposed modes and their frequency response revealed unique simple spatial patterns operating at the same frequencies as observed in the original gut motion. The unique integrated analysis demonstrates complex peristaltic and segmental motilities a) can be represented by the linear combination of first three modes, b) have a simpler underlying checker board modal structure and c) their principal components have similar frequency and spatial patterns except for the spatial scale. The individual modes revealed unique simplified spatial patterns for peristaltic and segmental motility. However PCA was not able to separate out the frequency modes of segmental motility. Thus Fourier analysis based on band pass filtering and spatio-temporal maps was applied to the data to gain further insight into the source of dominant frequency peaks of gut motility.

The average frequency analysis resulted in a single dominant peak for peristalsis and three dominant peaks for segmental data. Fourier analysis based on band pass filtering and spatio-temporal maps was applied to determine the physiological relevance of frequency peaks in gut motility. The results suggest a single dominant mode of peristaltic motility represents a traveling wave in the aboral direction. In contrast to peristaltic motility, segmental motility is much more complex and is a resultant of three frequency modes. In general the results of Fourier analysis of segmental motility suggest, first two frequency modes depict waves propagating in opposite directions and a third frequency mode represents a stationary pattern. The sum of simple frequency modes leads to complex stationary patterns which were otherwise difficult to interpret.

The results of integrated and Fourier analysis have led to a much better interpreta-

tion and understanding about the underlying mechanism of gut motility. The different approaches suggest that the neurophysiology underlying the control of motility can be considered much simpler; for example segmental vs. peristaltic wave patterns must be represented primarily by the phase relationships among the principal components or the summation of propagating waves at different frequencies and wave speeds. The results of the complex analysis can be coupled with CFD models to build physiologically relevant models and better predict fluid motions and nutrient absorption. In the coming sections a complete technical review, results and physiological implications of the integrated and Fourier analysis are discussed.

5.2 Methods

A centralized block diagram describing integrated and Fourier analysis approach was discussed in Chapter 3 (see Figure 3.1). The technical details of PCA using ASM were presented in Chapter 3 in Section 3.4.1 and are briefly reviewed in this section. The results of intermediate steps in integrated analysis and pre-processing of the data are demonstrated in Section 5.2.1. The results of integrated analysis and physiological relevance of the decomposed modes using PCA are discussed in Section 5.4. Towards the end the results and physiological interpretation of Fourier analysis using band pass filtering and spatio-temporal maps are presented in Section 5.5.

5.2.1 Integrated analysis using principal components

The First step in ASM is to create a database of training images, label a set of landmark points on all the images and derive a point distribution model. The acquired gut motion

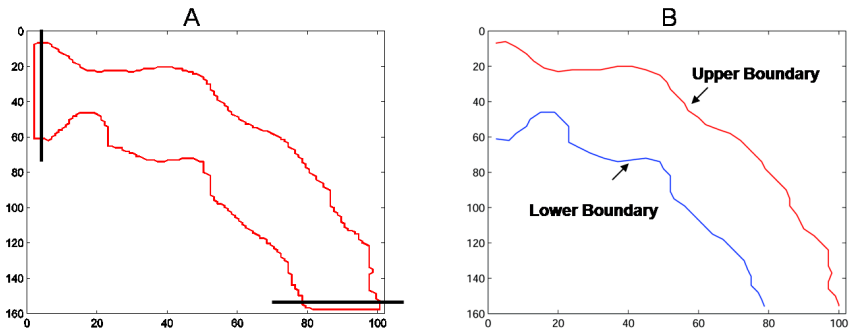

Figure 5.1. Processing of the data before applying ASM. The ends of the small intestine are not considered as they do not contribute to the actual gut motion. The closed boundary is divided in to upper and lower boundaries.

is dependent on time and thus the training images were arranged as a function of time. To build an accurate point distribution model, correct correspondences between landmark points of the training images are required. It is very laborious to manually place landmark points on all the training shapes. To automate this process and get a reasonable correspondences between the points of each image, the extreme ends of the small intestine were curtailed and the closed boundary was divided into upper and lower boundaries (see Figure 5.1). The ends of the closed boundary were chopped as they do not contribute to the actual gut motion and can induce errors in the decomposed modes. For each image equidistant points were marked on the upper and lower boundaries and grouped together to build a point distribution model. All the samples are iteratively aligned using least squares approach to compute a mean shape as shown in Figure 5.3. Let x_t be a "vector" of $2n$ landmark points on a sample shape at time t ($t = 1$ to N). The points in vector form starting 1 to $\frac{n}{2}$ correspond to the upper boundary and the points from $\frac{n}{2}+1$ to n correspond to the lower boundary. A single sample in time t can be represented in the equation form

as (see Figure 5.2):

$$\mathbf{x}_t = [x_{t1}, y_{t1}, x_{t2}, y_{t2}, \cdots, x_{tk}, y_{tk} \cdots, x_{t\frac{n}{2}}, y_{t\frac{n}{2}}, x_{t\frac{n}{2}+1}, y_{t\frac{n}{2}+1}, x_{tn-1}, y_{tn-1}, x_{tn}, y_{tn}] \quad (5.1)$$

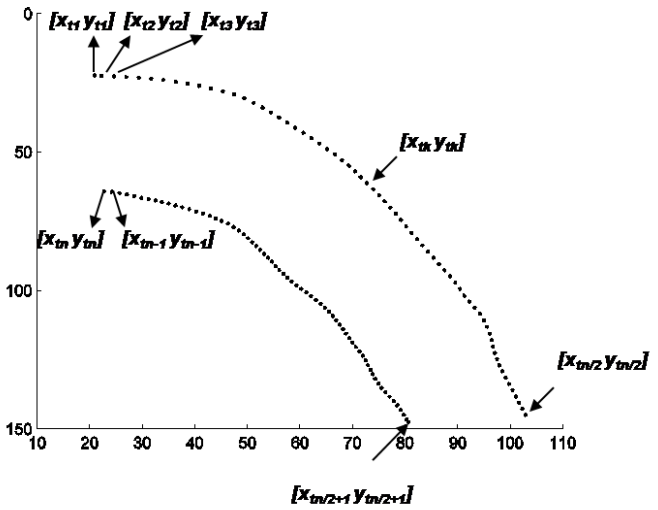

$$\boldsymbol{x_t} = [x_{t1}, y_{t1}, x_{t2}, y_{t2}, \ldots, x_{tk}, y_{tk}, \ldots x_{t\frac{n}{2}}, y_{t\frac{n}{2}}, x_{t\frac{n}{2}+1}, y_{t\frac{n}{2}+1} \ldots\ldots, x_{tn-1}, y_{tn-1}, x_{tn}, y_{tn}]$$

Figure 5.2. Selection of landmark points for an accurate PDM. The ends of the small intestine are not considered as they do not contribute to the actual gut motion. The closed boundary is divided in to upper and lower boundaries.

The training shapes are aligned using linear least squares approach and a mean shape is obtained from N aligned samples (See Figure 5.3a). An iterative approach is used to align N shapes. At first a transformation matrix is applied on all the shapes $t = 2$ to N to align with the first shape (see Figure 5.3b). A mean shape is computed from the aligned shapes and now all the shapes $t = 1$ to N are aligned with a mean shape. A new mean shape is computed and the process is repeated until mean shape converges (see Figure 5.3c).

A set of N time samples, with each sample containing $2n$ elements (x and y coordinates),

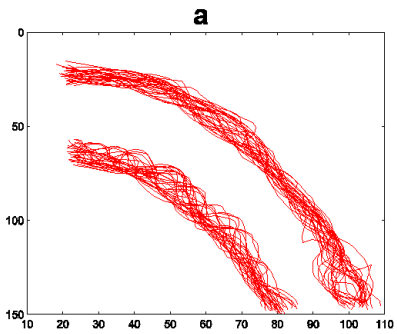

All Samples aligned with first shape using least squares approach

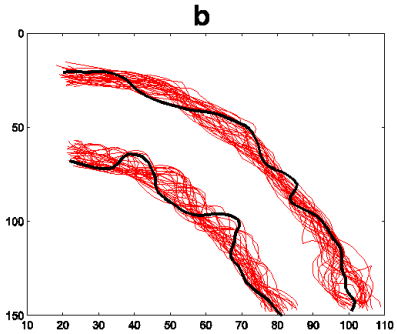

First mean shape

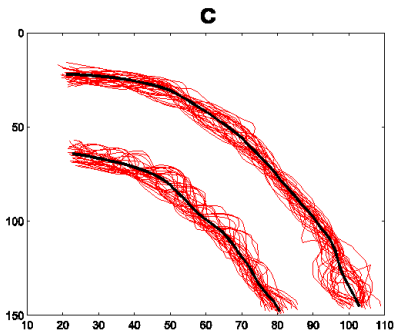

Final mean shape

Figure 5.3. Mean shape of the small intestine. (a) All the samples are aligned with first shape using iterative least squares approach; (b) First mean shape; All the samples are realigned with first mean shape. The process is repeated until the mean shape converges; (c) Final mean shape.

are represented as a "cloud" of N points in $2n$ dimensional space (see Figure 5.4). It is assumed that the spread of N points is correlated and lies in an ellipsoidal region around the mean. Different modes of variation of land-mark points are found by calculating the deviation, d_{xt}, of each sample from the mean shape, then calculating a $2n \times 2n$ covariance matrix S, the covariance matrix S is used as the kernel to an eigenvalue problem to derive eigenvectors or eigenmodes. The results of integrated analysis are presented in Section 5.4. An alternative approach based on Fourier analysis and band pass filtering is discussed in the following section.

5.3 Fourier analysis

The complete technical details of Fourier analysis were presented in Chapter 3 (refer Figure 3.1) and briefly reviewed in this section. An automated frequency analysis was applied to the spatio-temporal maps of acquired peristaltic and segmental motility data. A signal of diameter variation vs. time was derived from every location in 'x' and a simple Fourier transform was applied to compute frequency components. The average frequency spectrum was then computed by averaging frequency spectrum over all the spatial locations. The average frequency analysis among different animals resulted in three dominant modes for segmental motility and a single dominant mode for peristaltic motility. The average frequency response of each motility sequence was used to apply band pass filters around dominant frequency peaks for every location in 'x' and then reconstruct a filtered spatio-temporal map. The spatio-temporal maps were reconstructed after filtering each dominant peak, combining first two and all the peaks. The results of Fourier analysis for peristaltic

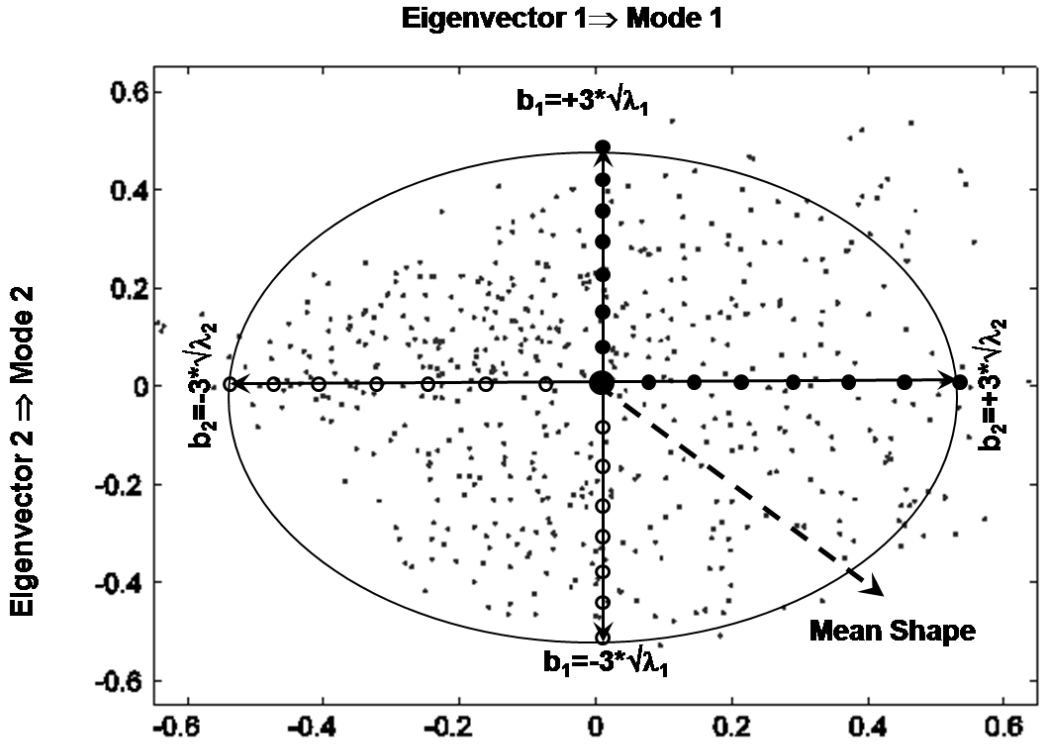

Figure 5.4. Variation of eigenvector 1 vs. 2 of segmental motion. The majority of the samples lie within an ellipsoidal "allowable shape domain", defined from −3SD to +3SD. The primary axes of the ellipsoidal region are defined by the eigenvectors 1 and 2. The shapes are reconstructed by scaling corresponding eigenvectors at the locations from $b = -3$SD (small light circles) to $b = 0$ (large dark circle 3 mean shape) to $b = +3$SD (small dark circles), and zeroing out the coefficients of other eigenvectors. The plot is highly uncorrelated and thus it shows that the decomposed modes are independent of each other.

and segmental motility of isoflurane study are presented in Section 5.5.

5.4 Results of Integrated analysis

5.4.1 Spatio-temporal patterns of principal components

The PCA analysis using active shape models resulted in, for both peristalsis and segmental motions, three principal components containing the majority (up to 75%) of the total signal

variance. Figure 5.4 shows a plot of the b-coefficients, Eq. [10], of the first two modes corresponding to peristalsis. The correlation coefficient for the plot was calculated to be -2.35×10^{-16}, confirming that the two modes are indeed independent. Similar results were found for all mode combinations for both peristalsis and segmental motions. In Figure 5.4, one can consider the samples as lying within a 2D ellipsoid ("allowable shape domain" ranging from −3SD to +3SD) with its primary axes defined by eigenvectors 1 and 2. A variation of an individual eigenvector or mode can be visualized by reconstructing shapes by using the equation, $x = \bar{x} + Pb$, noting that the mean shape corresponds to the origin in the b-plot, and scaling its corresponding eigenvector m from $b_m = -3\sqrt{\lambda}_m$ to $b_m = +3\sqrt{\lambda}_m$ and zeroing out the coefficients of other modes. For simplicity we have sampled at some locations along the eigenvector (see Figure 5.4) and the corresponding reconstructed shapes of segmental and peristaltic motility for eigenvectors 1, 2, and 3 are shown in Figure 5.5. The first three individual modes of segmental (top row) and peristaltic motility (bottom row) are shown in Figure 5.5, and reveal different spatial patterns, which correspond with the patterns observed in the actual gut motion. For example, the length scale of peristalsis can be seen to be much longer than that of segmental motion, as shown in Figure 5.5.

5.4.2 Analysis of decomposed modes

In the next step we have analyzed peristalsis and segmental data by integrating three methods: PCA using active shape models, frequency analysis and spatio-temporal map. The importance of applying PCA to the gut data is to reduce the complexity of the gut data into smaller number of simple components and the results show that each component has something unique about it. The results of individual modes of segmental and peristalsis data

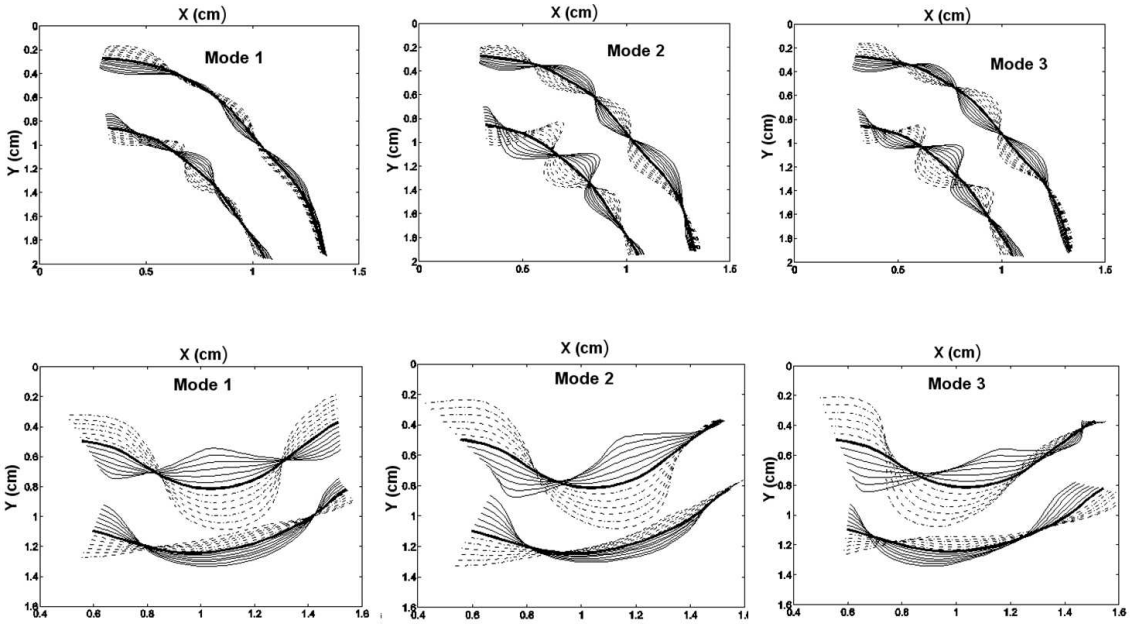

Figure 5.5. Spatial patterns of peristalsis and segmental motility. The spatial patterns associated with a particular eigenmode m, was reconstructed by scaling its corresponding eigenvector, from $-3\sqrt{\lambda_m}$ (light dotted) to 0 (dark solid mean shape) to $+3\sqrt{\lambda_m}$ (light solid).

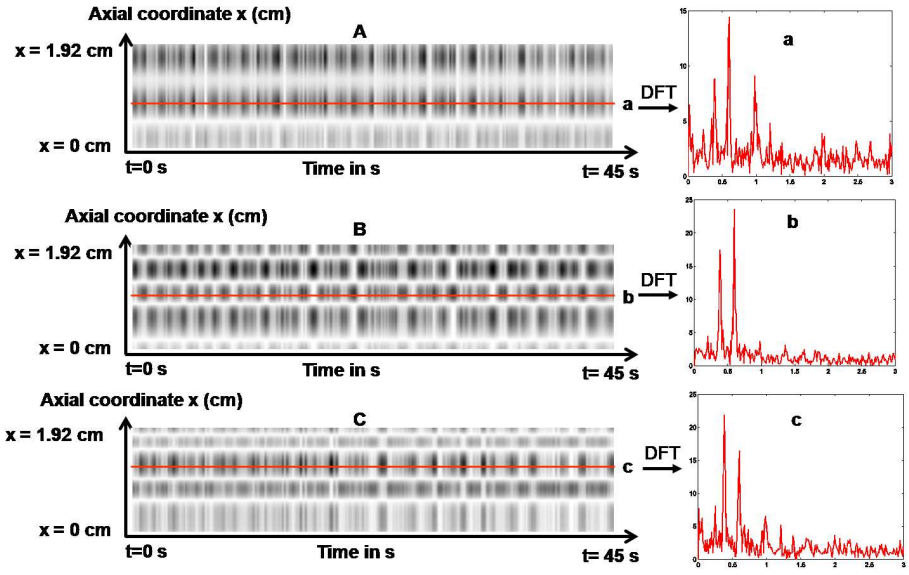

Figure 5.6. The shapes of the first three dominant modes of segmental motion were reconstructed by arranging the coefficients of a particular Eigen vector in time. Spatio-temporal maps of first three dominant modes of segmental motion. are shown in Figures (A) mode 1, (B) mode 2 and (C) mode 3. A 1 dimensional signal of diameter variation vs. time was derived from the constricting regions of the spatio-temporal map of each (solid red lines, a ,b and c) mode. The results of FT of the derived signal are shown in the corresponding figures on the right a to c.

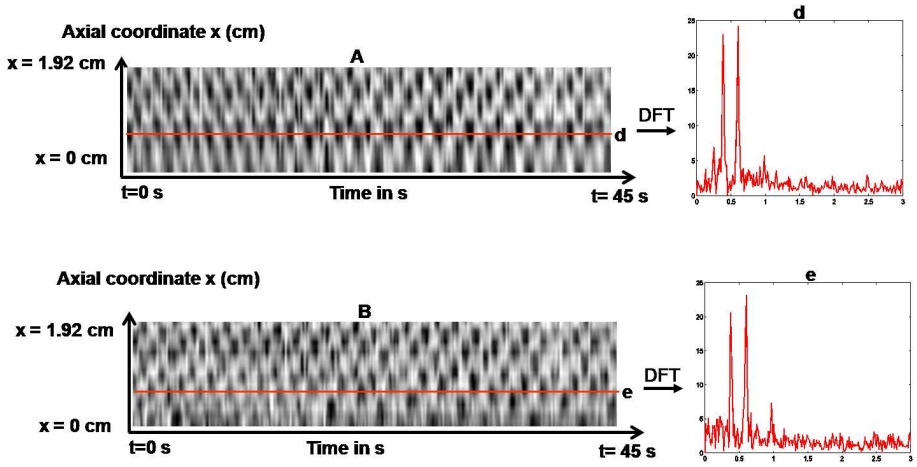

Figure 5.7. Comparison of the contractile activity of the first 3 modes of segmental pattern (A), (generally represent 56% to 75% of the original gut motion) with actual segmental motion (B). The spatio-temporal maps were used for the comparison and it is evident that (A) first 3 modes show most of the activity as is seen in (B) all the modes. Similar results were obtained for all the peristalsis and segmental datasets and for our analysis we have considered only first 3 modes. A 1 dimensional signal of diameter variation vs. time was derived from the constricting region of the corresponding spatio-temporal maps (solid red lines, d and e). The corresponding results of DFT of the 1d signal are shown in the figures d and e.

visualized using spatio-temporal map reveal individual modes are simpler to understand (see Figures 5.6 and 5.8) and become complex when combined together (see Figures 5.7 and 5.9). It is easier to quantify the scales of the segments of the gut in each individual mode than in the spatio-temporal map of original gut motion or even in combined three modes.

The frequency spectra of the actual gut motion were compared with the frequency spectra of reconstructed data using individual and combined first 3 modes. For simplicity we have considered a one dimensional signal (diameter variation vs. time) from a single constricting region (as shown by a solid red line) in the spatio-temporal maps of individual, combined first 3 modes and actual gut motion (for segmental see Figures 5.6, 5.7 and for peristalsis see Figure 5.8 and 5.9). The frequency spectra are shown besides their corresponding spatio-temporal maps (see Figures 5.6, 5.7, 5.8, and 5.9). The results show that in all

the cases each individual mode has a unique and simple checker board pattern, and their frequency response match well with the frequency response of data reconstructed using first three modes and actual gut motion. We have compared spatio-temporal maps and frequency analysis of segmental and peristalsis data sets reconstructed using only first three modes vs. all the modes (for segmental see Figure 5.7 and for peristalsis see Figure 5.9). The qualitative comparison show spatio-temporal map of the combined three modes and original gut data are very similar. On the other hand quantitatively, frequency analysis of a one dimensional signal (diameter variation vs. time) derived from the same anatomic location (as shown by a solid red line) of spatio-temporal map of the data reconstructed using first three modes and original data matched well.

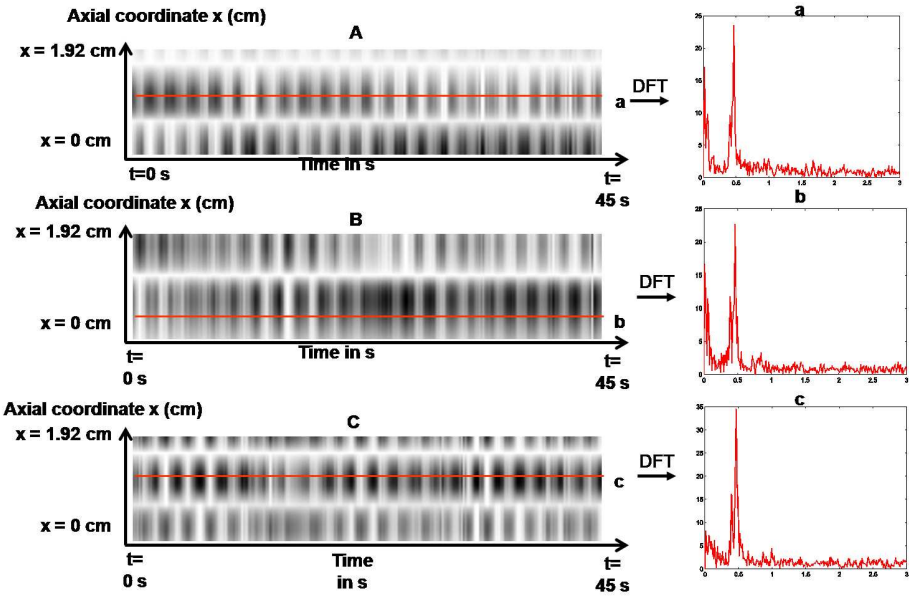

Figure 5.8. The shapes of the first three dominant modes of peristalsis motion were reconstructed by arranging the coefficients of a particular eigen vector in time. Spatio-temporal maps of each mode were computed and are shown in Figures (A) mode 1, (B) mode 2 and (C) mode 3. A 1 dimensional signal of diameter variation vs. time was derived from the constricting regions of the spatio-temporal map of each (solid red lines, a to c) mode. The results of FT of the derived signal are shown in the corresponding figures a to c.

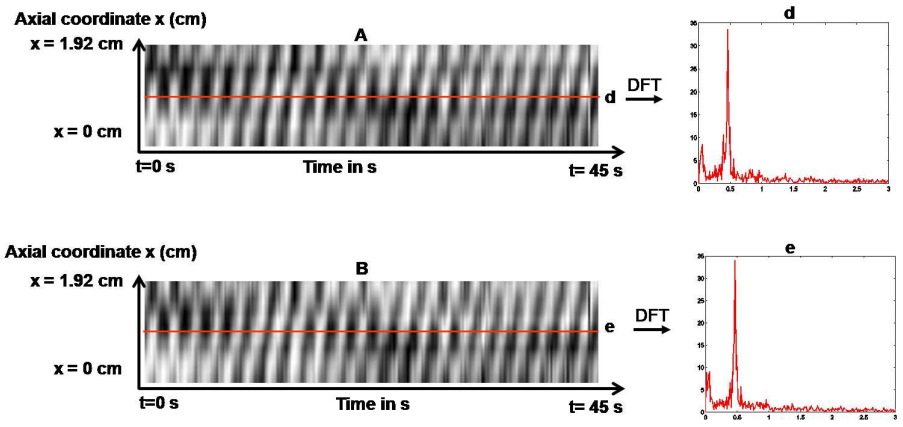

Figure 5.9. Comparison of the contractile activity of the first 3 modes of peristalsis pattern (A), (generally represent 75% of the original gut motion) with actual peristaltic motion (B). The spatio-temporal maps were used for the comparison and it is evident that (A) first 3 modes show most of the activity as is seen in (B) all the modes. Similar results were obtained for all the peristalsis data sets and for our analysis we have considered only first 3 modes. A 1 dimensional signal of diameter variation vs. time was derived from the constricting region of the corresponding spatio-temporal maps (solid red lines, d and e). The corresponding results of FT of the 1d signal are shown in the figures d and e.

5.4.3 Summary of integrated analysis

In order to summarize the results the spatio-temporal maps and frequency analysis of individual modes (3), combined modes (3) and actual peristaltic and segmental data are shown in Figure 5.10. The results show that:

1. The plots of average frequency analysis shows the decomposed and combined modes have inherited the same frequency from the original data.

2. The majority of peristaltic and segmental data of the small intestine of each animal can be represented by combining just first 3 modes. The dimensionality of data reduced from 268 to just 3 modes.

3. Individual modes of peristalsis and segmental data have a unique and simple checker board pattern.

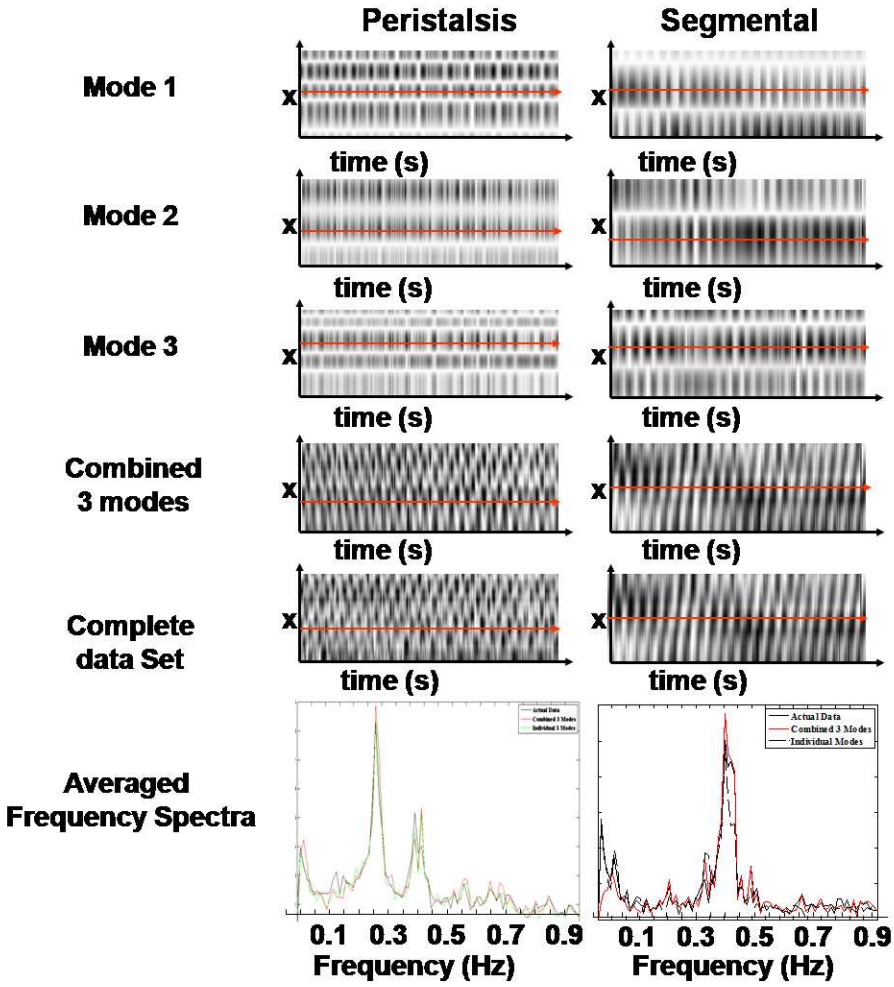

Figure 5.10. Summary of integrated analysis of peristalsis and segmental motion.

5.4.4 Physiological implications of principal components

The last part of integrated analysis deals with physiological interpretation of first three principal components of peristaltic and segmental motilities. It is well known that PCA reduces the dimensionality of the data and points out few dominant modes that essentially represent larger variation of the data. The results imply first three modes are sufficient to represent the complex gut motion. At the basic level the modes have identical checker board patterns of different length scales which are speculated to be activated by the neuronal

signals operating with similar frequency components.

The results of integrated analysis can be compared with another motility study on the esophagus by Ghosh *et al.* [100, 101]. The chief function of esophagus is to transport the chewed food from the oral cavity into stomach and is dominantly peristaltic. The results suggest underlying peristaltic contractions of esophagus require segmental contractions to completely free it from the remnants of the food bolus. A similar behavior of segmental type checkerboard patterning was also found within the spatio-temporal maps of the principal components of peristaltic motility of the small intestine.

Since the principal components were similar except for the spatial scale within each class, segmental vs. peristaltic wave patterns must be primarily represented by the phase relationships among principal components. Thus, the complexity of patterning in gut motility has a simpler and similar underlying modal structure in both classes of motion. The integrated analysis have led us to speculate that the underlying order of the neurophysiology of the GI muscles is elementary. We further hypothesize that the neurophysiological control of complex motility patterns in the gut may be centered on a few hard-wired patterns embedded within the ganglionic structure of the gut wall stimulated in phase and frequency to produce local peristaltic or segmental motility, or more complex mixtures of motions.

5.5 Results of Fourier analysis

The results of Fourier analysis for a single case of peristaltic and segmental motility case using isoflurane anesthesia are shown in Figures 5.11 and 5.12, respectively. In general the results of Fourier analysis suggest peristaltic motility is represented by a single dominant

mode and segmental motility is much more complex represented by summation of three orthogonal modes. The physiological interpretation of Fourier modes were derived from the corresponding spatio-temporal maps of decomposed modes that were filtered out from the complete data.

A single dominant mode of peristaltic motility imply a propagating wave in the aboral direction (see Figure 5.11). The low frequency components do not add value towards the resultant patterning and a single dominant mode represents most of the peristaltic motion. Animal movements and some breathing artifacts that were not corrected during image registration result into low frequency components. The dominant frequency peak was situated at (0.47 ± 0.028 Hz).

The segmental motility varied from simple to complex patterning. Simple segmental patterning corresponded to just one or two constricting regions and complex segmental patterning had four to five constricting regions. The three dominant frequency modes were situated at 0.25 ± 0.022 Hz, 0.42 ± 0.021 Hz and 0.72 ± 0.089 Hz. The dominant modes of segmental motility suggest first two modes are propagating waves in opposite directions and their summation creates a standing wave pattern as seen during segmental motion. Although the combination of first two modes create a stationary pattern but it does require an additional high frequency stationary mode to complete the patterning as seen in the complete data (see Figure 5.12). The simple segmental patterning was observed in just two datasets and a high frequency mode was absent in those cases. The results are shown in Appendix-B.

Similar characteristics of peristaltic and segmental motility were observed among all the animals. The results of Fourier analysis of all the cases of peristalsis and segmental motility

are shown in Appendix-B.

5.5.1 Physiological implications of Fourier analysis

Lammers et al. have exclusively published on high resolution mapping of slow waves in the small intestine in animal models to determine their origin and propagation [102–104]. It is suggested in the literature that propagating slow waves provide an input signal to the muscle layers surrounding the gut wall to contract. The recent literature points out that the slow waves are initiated by a network of cells known as interstitial cells of Cajal [105, 106]. The results of Fourier analysis can be compared to propagating slow waves and suggest gut motility is initiated by propagating waves and their summation can lead to complex segmental and simple peristaltic gut motility. The decomposed Fourier modes may correspond to the slow waves that originate from the neighboring areas of small intestine. Thus the results of Fourier analysis can provide an insight to the underlying mechanisms of different types of gut motion.

Chapter 5 presented results on PCA using ASM and the physiological relevance of decomposed modes of peristalsis and segmental motility using integrated and Fourier analysis. In the coming sections Chapter 6 present results on different motility patterns and comparison of physiological parameters for isoflurane and inactin groups. The results of Fourier analysis on inactin data are also discussed in Chapter 6.

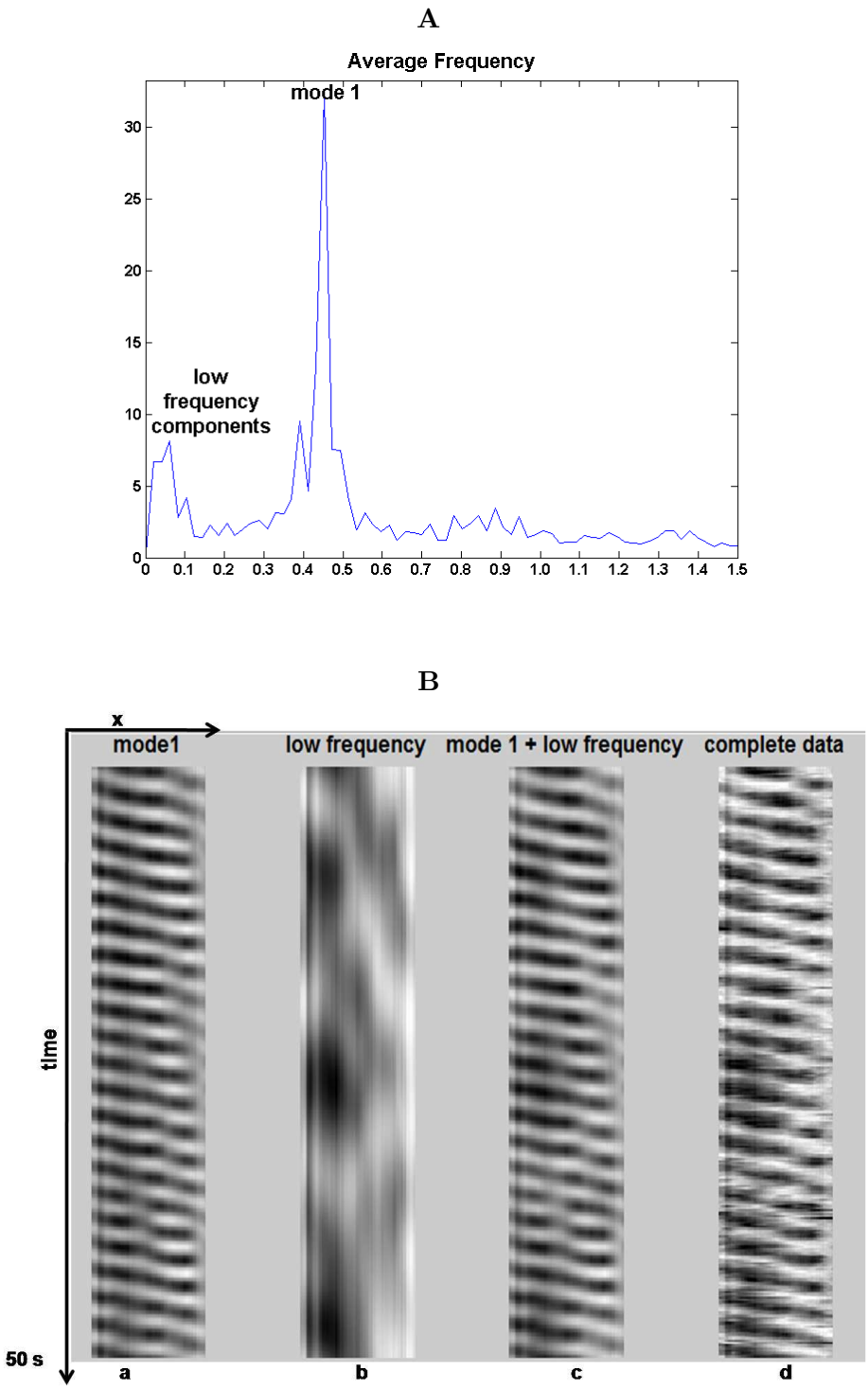

Figure 5.11. Fourier analysis of peristaltic motility: Isoflurane. (A) Average frequency analysis of peristaltic motion. An automated frequency analysis was computed for every location in 'x' from spatio-temporal map and then averaged over all the locations. The dominant and low frequency peaks were used to filter the original signal and spatio-temporal maps were reconstructed to visualize their contribution. (B) The reconstructed spatio-temporal maps represented following cases: (a) individual dominant peak (mode1); (b) low frequency components (low frequency); (c) summation of low frequency and mode1 and (d) unaltered complete data. The frequency centers were obtained from the average frequency analysis of the dataset.

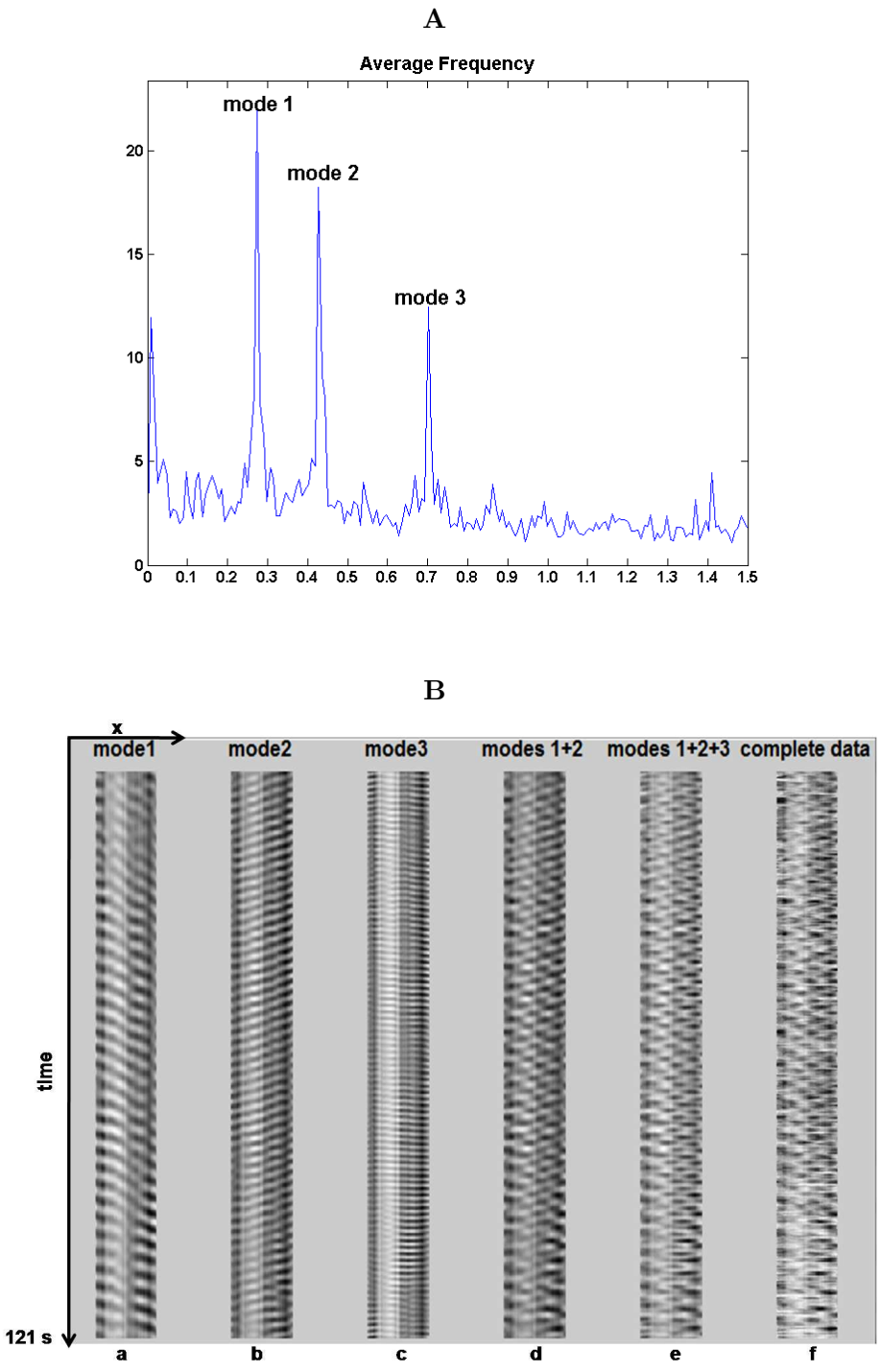

Figure 5.12. Fourier analysis of segmental motility: Isoflurane. (A) Average frequency analysis of segmental motion. An automated frequency analysis was computed for every location in 'x' from spatio-temporal map and then averaged over all the locations. The dominant peaks were used to filter the original signal and spatio-temporal maps were reconstructed to visualize the contribution of each peak. The reconstructed spatio-temporal maps represented following cases: (a to c) individual dominant peaks (mode1, mode2 and mode3); (d) summation of first two peaks (modes 1+2); (e) summation of all three peaks (modes 1+2+3) and (f) unaltered complete data. The frequency centers were obtained from the average frequency analysis of the corresponding dataset.

Chapter 6

Quantify effects of isoflurane and inactin on gut motility

Chapter 6 compares different motility patterns and measured physiological parameters for peristalsis and segmental in two groups, rats anaesthetized using isoflurane and inactin. The centralized image analysis and data acquisition steps are similar to those described in Chapter 4. The gut motility was visualized using spatio-temporal maps and the physiological parameters were derived from the maps.

6.1 Abstract

The aim of this study was to quantify and compare motility patterns of rats anesthetized with either inactin or isoflurane using noninvasive dynamic magnetic resonance imaging. Rats were initially given an oral gavage of contrast agent, in order to visualize the gastrointestinal tract more clearly, and then two-dimensional images were acquired every 168

ms through the jejunum of the anesthetized rat. Image registration, segmentation, and automated processing was used to produce spatio-temporal maps and average frequency plots, which formed the basis to quantify motions such as peristalsis, segmental, as well as periods of inactivity. Inactin data was also analyzed using Fourier analysis and the results are compared with isoflurane data. Results showed that the gut was inactive for longer periods in rats treated with isoflurane than in those with inaction. The speed of propagation and the wavelength of peristaltic motility as well as the frequency and speed of collapse of segmental motility were significantly higher in rats treated with inactin. The results show that inactin anaesthesia does not have the same inhibitory effects on the gut motility as isoflurane, confirming indirect data in the literature acquired using invasive techniques, but also adding detailed knowledge of the changes in gastrointestinal motions produced by these anesthetics. The results of Fourier analysis further reinforces our earlier hypothesis on the underlying mechanisms of peristaltic and segmental motilities.

6.2 Introduction

The vast majority of animal experiments require some form of anesthesia for physical restraint, pain mitigation, or long-term monitoring. There are a large number of both gaseous and injectable anesthetic agents, each of which has advantages and disadvantages for specific applications. Continuous application of gaseous anesthetics such as isoflurane, halothane and ether is relatively easy to administer, and results in relatively light anesthesia and rapid recovery [107]. Injected agents such as inactin [108–110] can last for many hours, or may require frequent redosing as is the case for ketamine/xylazine. Some agents can be used

for repeated, serial experiments, but others such as alpha-chloralose are more suited for terminal use. Irrespective of whichever agent is used, it is important to understand the changes in physiology which are produced by the particular agent. For example, there can be significant global or local systematic changes in blood flow, blood oxygenation, pH, heart rate and respiratory rate.

Our particular interest is the effects of anesthesia on GI motility via alterations in peristalsis and segmental motions. Isoflurane, for example, has been reported to affect gut motility and intestinal absorption [107]. In terms of the effects on GI motility the studies conducted by Torjman *et al.*, [99] suggest that isoflurane affects the physiological circuitry that initiates the propagating waves. In a group of rats which were exposed briefly to isoflurane, and then were awake for 120 mins after anaesthesia, the GI transit of charcoal was reduced by approximately 50% compared to that of control animals. A second group of rats, treated with a prokinetic drug (metachlopramide) prior to the same brief exposure to isoflurane showed an identical reduced GI motility. In contrast, inactin which is an injectable anesthetic has been shown to provide sustained anesthesia for long periods, and maintain stable physiological parameters [108–110]. Sababi *et al.* [109] have evaluated the effect of intestinal motility on the absorption via various GI markers that play an important role in the absorption process in the duodenum. The data showed that rats treated with inactin showed little signs of post operative ileus, had stable blood pressure and exhibited gut motility even after the surgical procedure. It has also been reported that inactin does not interfere with brainstem autonomic reflexes and produces stable physiological parameters [108]. Sababi *et al.* also performed a comparative study of nitric oxide synthase and inhibitory action of cyclo-oxygenase on duodenal functions in rats

anesthetized using inactin, alpha-chloralose and urethane [110]. They have reported that inactin and alpha-chloralose behaved similarly in terms of studied basal values. Several groups have conducted in-situ Trendelenburg experiments on the motility of small intestine in rats anesthetized using alpha-chloralose and ketamine [17, 18]. The anesthetic alpha-chloralose was reported not to interfere with GI reflexes.

Although these types of invasive measurements on post-mortem animals provide strong evidence of the differential effect of different anesthetics on GI motility, they do not elucidate the specific effects on peristaltic and segmental motions, which can only be studied under true in vivo conditions using a non-invasive technique. We have shown previously the first results from dynamic magnetic resonance imaging (MRI), followed by image registration, segmentation and processing, which enabled non-invasive and quantitative measurements of GI motility to be performed in rats anesthetized using isoflurane [111]. In this current study we compare results (some of which have been reported previously [111]), from animals anesthetized with isoflurane anesthesia with new data acquired using inactin in order to elucidate the differential physiological effects of these two different anesthetics.

6.3 Methods

All experimental protocols were approved by Penn State University's IACUC. Rats (Sprague-Dawley, $200 - 300$ grams) were used for all experiments. Animals were given access to laboratory chow and water ad libitum. All MRI experiments were performed using a Varian Direct Drive Console and Magnex 7 tesla, 33 cm bore horizontal magnet. A 12 cm diameter gradient insert, with maximum gradient strength 400 $\frac{\mathrm{mT}}{\mathrm{m}}$ and a quadrature birdcage

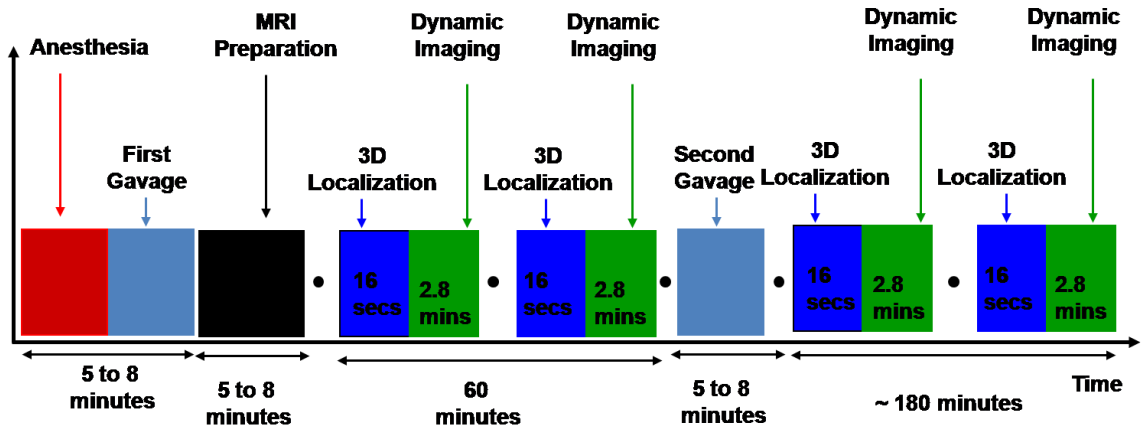

Figure 6.1. MRI procedure and time line for Inactin study. The rats were anaesthetized using inactin and given a double oral gavage of Gd contrast agent during MRI imaging. 3D imaging of the entire GI tract was performed before every dynamic imaging to aid in localization of jejnum region.

coil with 6 cm inner diameter were used for all studies.

6.3.1 Isoflurane-anesthetized rats

The protocol for isoflurane-anesthetized animals has been detailed previously [111] in Figure 4.2 and is summarized here. Rats ($n = 6$) were initially anesthetized using a mixture of isoflurane (4%) and oxygen gas (flow ≈ 1 $liter/minute$). An oral gavage of a 1% Gd-DPTA solution ($0.75\frac{\text{ml}}{\text{kg}}$ volume) was administered approximately 1 hour before imaging. The rats were anesthetized again immediately prior to imaging using the same mixture of isoflurane and oxygen, and a second gavage of 0.75 ml/kg Gd-DPTA solution was given. During the MRI scanning, continuous anesthesia was maintained with the isoflurane level reduced to 2% and oxygen gas flow regulated to 0.5 l/min. During scanning, the animal's temperature and respiration rates were monitored (SAI Model II, Brooklyn, NY) using a rectal probe and pressure transducer, respectively, to ensure that they remained constant. The average respiration rate, 0.75 ± 0.12 Hz and the average temperature, 34.4 ± 0.9^oC

was computed from different animals.

6.3.2 Inactin-anesthetized rats

The experimental protocol is shown in Figure 6.1. One gram of inactin (Thiobutabarbital sodium salt hydrate, Sigma-Aldrich) was dissolved in 10 ml of a 0.9% saline solution. Rats ($n = 6$) were anesthetized using a single i.p. injection of this inactin solution at a dose of $80mg/kg$, and approximately ten minutes post-injection were given the first oral gavage of a 1% Gd-DPTA solution ($0.75ml/kgvolume$). The rats were immediately placed in the scanner for imaging: a second gavage was administered approximately 1 hour after the first, the animal repositioned and imaging continued. The average respiration rate, 1.26 ± 0.31 Hz and average temperature, 34.2 ± 2^oC was derived from different animals. The experimental protocol is shown in Figure 6.1.

6.3.3 MRI data acquisition

MRI data acquisition has been described in detail in Chapter 3 and in the publication by Ailiani *et al.* [111]. In summary, a rapid T_1-weighted spin-echo "localizer" sequence to determine as long and straight a length of the jejunum as possible. For dynamic imaging, a single slice gradient-spoiled gradient echo sequence was run with the following parameters: echo time (TE) 1.12 ms, repetition time (TR) 3.12 ms, data matrix 96×54 (3/4 Fourier), zero-filled data reconstruction matrix 96×72, 2 mm slice thickness, field-of-view $3 \times 2.5\text{cm}^2$, in-plane resolution $312\mu m \times 347\mu m$ and acquisition time per image $\approx$ 168ms. Approximately 1000 sequential images are acquired during each dynamic run. Due to motion of the entire GI tract over time a separate localizer scan was acquired before each series of dynamic

images.

6.3.4 3D image segmentation and image processing algorithms

The spatio-temporal maps have been employed by several researchers in the past to identify peristalsis [17, 18] and segmental motilities [14, 15]. The overall aim of the data processing steps is to produce a series of spatio-temporal maps, from which various parameters of interest can be derived. The image series was first co-registered to remove the effects of small inter-image translational motions, and segmented using custom-designed software employing 3D live wire (3D LW) and directional dynamic gradient vector flow snakes (DDGVFS) algorithms [111]. In order to generate spatiotemporal maps a 2D thinning algorithm based on the formulation of Saha *et al.* [34] and followed by branch deletion algorithm [35] was applied to the segmented images to compute a smooth medial axis. The medial axis was computed for each image in time (see Figure 6.2)and a 2D function $D(x,t)$, describing the diameter at each point along the medial axis (x) and in time (t), was derived from the Euclidean distance maps of segmented binary images. Spatio-temporal maps of occlusion vs time can be produced by computing the values of the minimum (D_{min}) and maximum (D_{max}) diameters at each point along x and scaling by a factor $\frac{(D(x,t)-D_{min})}{(D_{max}-D_{min})}$: this results in the minimum diameter being represented as dark and maximum diameter being bright.

6.3.5 Average frequency and Fourier analysis

An automated frequency analysis (as described in Chapter 4) was performed for every location of spatio-temporal map and then averaged over the entire map. The results of inactin data were compared with isoflurane and are presented in Section 6.4. Fourier analysis

(A) Raw MRI images of segmental motility in inactin data

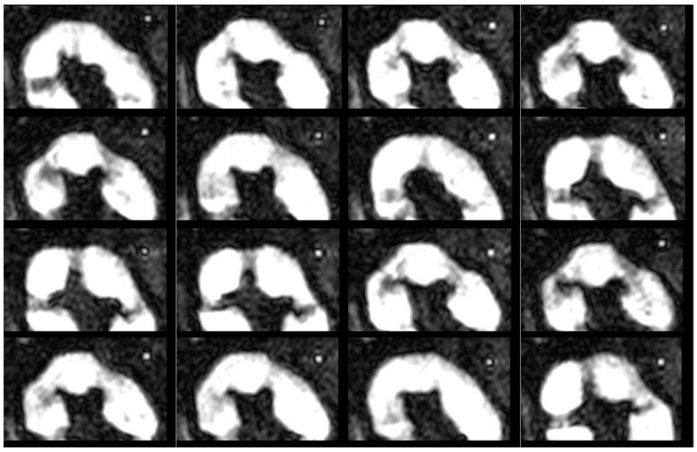

(B) Corresponding segmented images of small intestine.

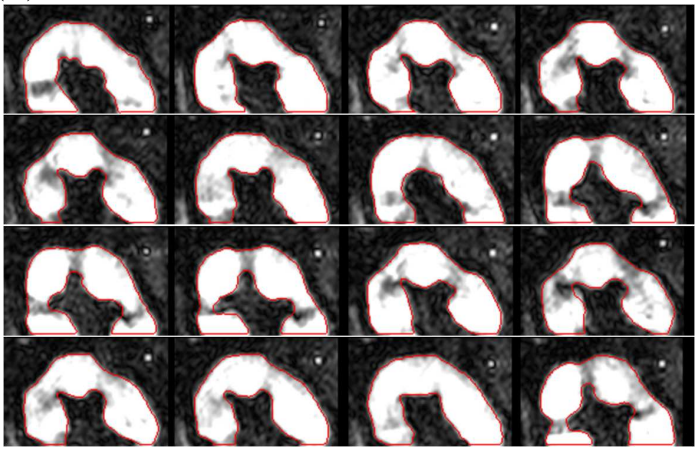

(C) Corresponding binary and medial axes of small intestine.

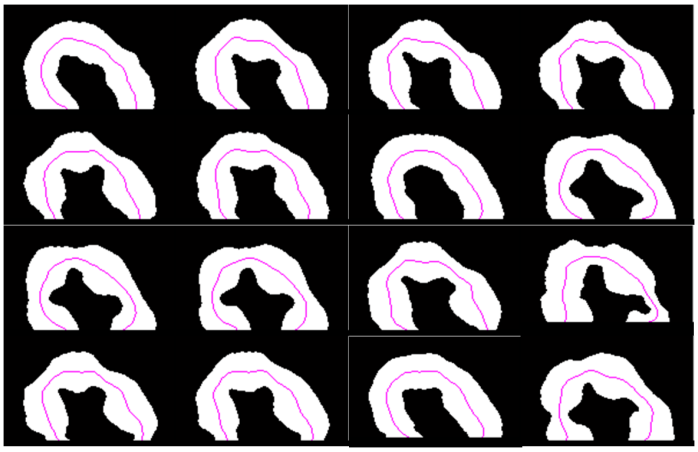

Figure 6.2. Raw and processed MRI images of inactin data. The sucessive images of segmental motility of inactin group are shown in (A) were segmented using 3D image segmentation tool (B) and binary segmented images were used to compute medial axis (C). The medial axis was then used to compute $D(x,t)$ and in turn spatio-temporal maps.

along with band pass filtering and spatio-temporal maps (as described in Chapter 5) was performed on inactin data and compared with isoflurane data. The results are presented in Section 6.4.3.

6.3.6 Physiological parameters from spatio-temporal maps

From the spatiotemporal maps, the characteristic frequency (F) of the constriction was computed by applying a discrete Fourier transform, the amplitude of constriction (A) is given by $\frac{1}{2}(D_{max} - D_{min})$, the speed of the collapse or speed of constriction (S) is given by A/T. The velocity (v) of the propagation of the peristalsis wave was determined from the slope of the diagonal streaks in the spatio-temporal maps, and finally the wavelength (λ) calculated from v/F.

6.3.7 Statistical analysis

The differences between physiological parameters for each anesthetic and between anesthetics were computed using one way Anova with multiple comparisons using the Holm-Sidak method: a p-value of 0.05 was used for significance.

6.4 Results: comparison of isoflurane vs. inactin data

A similar set of physiological parameters, spatio-temporal maps to visualize motility patterns, average frequency analysis and Fourier analysis were computed for inactin data and compared with that of isoflurane. The results are presented and summarized in the following sections.

6.4.1 Motility patterns

Overall, 118 data sets were analyzed for inactin anesthetized animals, representing 4.7 hours of data acquisition, and 110 data sets for isoflurane, representing 5.4 hours. Based upon the spatio-temporal maps, periods of peristalsis, segmental motion and inactivity were analyzed. Periodic peristalsis waves, in which a single constriction travels along the length of the gut, were represented by periodic dark diagonal streaks in the spatio-temporal map. Segmental motions appeared as stationary constrictions occurring at a fixed location, and at several locations along the length of the gut, and were detected as short dark vertical bands in the spatio-temporal map. Figure 6.2 shows both raw and processed images, which represent segmental motion. The median line drawn in Figure 6.2B is then used to calculate the spatiotemporal maps. The row 1 in Figure 6.3 shows illustrations of spatio-temporal maps, corresponding to peristalsis (left) and segmental (right) motions, respectively. The corresponding one dimensional plots of diameter vs. time are shown in row 2, along with the Fourier transform of these plots to produce the frequency spectrum in row 3 (see Figure 6.3). Peristalsis is represented by a single frequency, although it should be noted that the peak at very low frequency in row 3, Figure 6.3, arises from very small inter-image motion that are not fully corrected by the image registration [111]. An example of the source of low frequency components in gut motility is shown in Figure 4.13 in Chapter 4. Segmental motion is represented by three different frequencies, and this feature was seen in most of the animals studied. Peristalsis was seen much less frequently than segmental motion: for inactin it was detected in only $\approx 7\%$ of the data sets, and for isoflurane in $\approx 3\%$ of the data sets. The complete results, frequency analysis and spatio-temporal maps of peristaltic

Parameters	**Peristalsis**		**Segmental**	
	Mean ± SD		**Mean ± SD**	
Anaesthetic	**Isoflurane**	**Inactin**	**Isoflurane**	**Inactin**
% Motility	3%	7%	97%	93%
Freq*(Hz)	0.47 ± 0.028	0.463 ± 0.076	$0.26 \pm 0.022^*$ $0.42 \pm 0.021^*$ $0.72 \pm 0.089^*$	$0.32 \pm 0.095^*$ $0.495 \pm 0.096^*$ $0.853 \pm 0.179^*$
Wavelength*(mm)	$9.4 \pm 0.78^*$	$18.81 \pm 7.35^*$	9.08 ± 2.74	8.06 ± 0.7
Max diameter(mm)	5.42 ± 0.53	5.57 ± 1.17	4.6 ± 1.35	6.66 ± 1.89
Min diameter (mm)	1.45 ± 0.52	2.45 ± 0.8	2.28 ± 0.80	3.48 ± 1.31
Amp (mm)	1.98 ± 0.33	1.57 ± 0.39	1.16 ± 0.38	1.59 ± 0.61
Speed of collapse (mm/s)	0.91 ± 0.15	0.73 ± 0.17	0.33 ± 0.1	0.63 ± 0.33
Propagation velocity*(mm/s)	$4.34 \pm 0.35^*$	$8.99 \pm 4.04^*$	N/A	N/A
Avg distance between constrictions(mm)	N/A	N/A	4.56 ± 1.21	5.68 ± 1.9

Table 6.1. Comparison of measured parameters for segmental and peristalsis motions in isoflurane and inactin groups. The values given as mean± SD and N/A = not applicable. The parameters marked with $*$ showed significant differences at $p = 0.05$ between two anesthetics for peristalsis and/or segmental motility. The statistical analysis was computed using one way Anova with multiple comparisons using the Holm-Sidak method.

and segmental motility observed under isoflurane and inactin anesthesia are presented in Appendix-A. The analysis and results of a single case of peristaltic and segmental motility is shown in Figure 6.3.

6.4.2 Physiological parameters measured using MRI

Table 6.1 shows quantitative results calculated from the data sets for isoflurane and inactin (a subset of the values for isoflurane have been reported previously [111]) and in Table 4.1 in Chapter 4. Frequency analysis averaged over all the animals revealed a single peristaltic frequency for both isoflurane and inactin, with the same value at a $p = 0.05$ statistical level, and a very low inter-animal standard deviation.

The majority of the other measures shown in Table 6.1 are also very similar, with the notable exception of the propagation velocity and wavelength. An illustration on how to

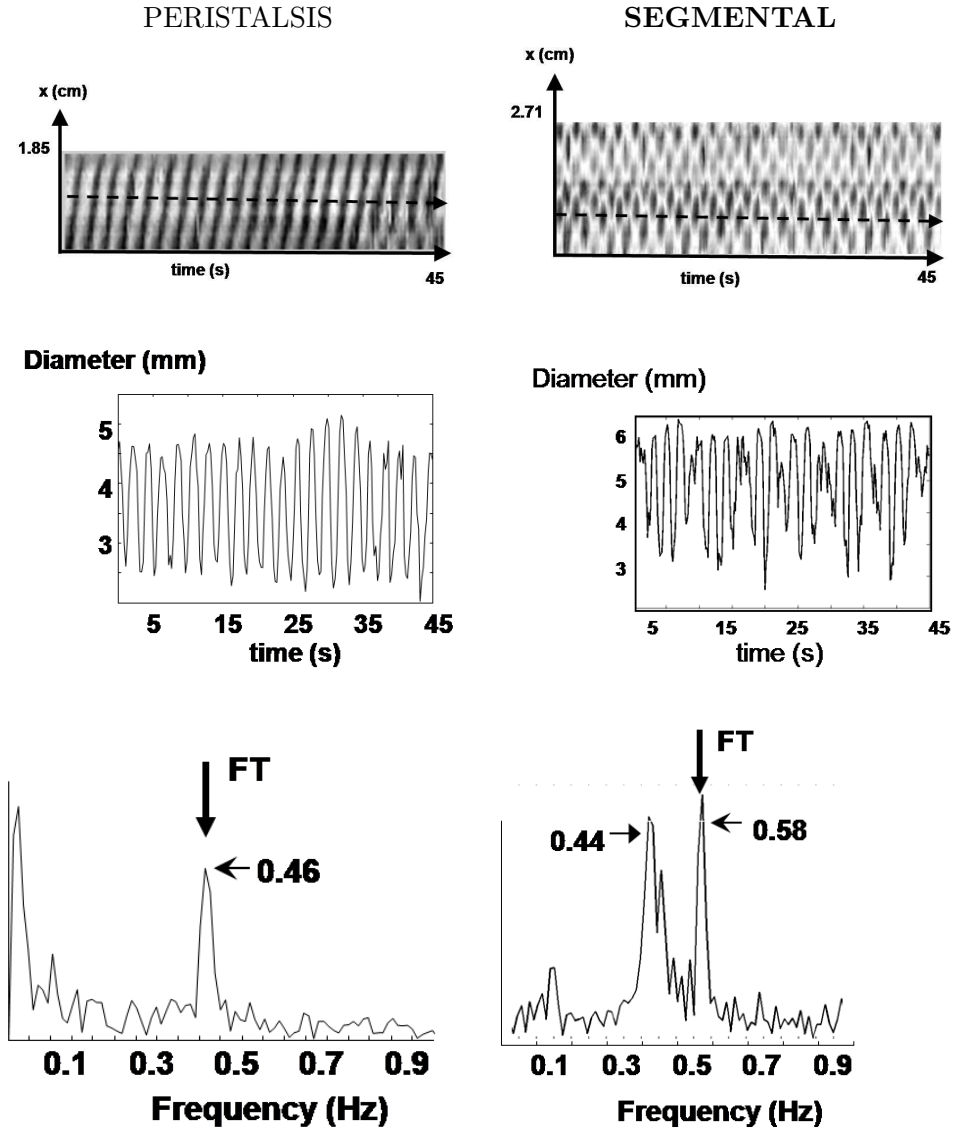

Figure 6.3. Illustration of peristalsis (left) and segmental (right) motilities using a spatio-temporal map with data derived from the dynamic MRI scans of a segment of the rat jejunum with inactin used for anesthesia. One-dimensional plots (along the dotted lines at fixed x location indicated in row 1), of the variation in diameter variation as a function of time. The frequency response of the corresponding signal reveals a single characteristic frequency for peristalsis, but two frequencies for segmental motion (as shown in row3). The analysis was done via computing (row 1) spatiotemporal maps, (row 2) deriving diameter at fixed location in x from the maps and (row 3)determination of the dominant frequency using FT. The analysis revealed: (1) peristalsis as propagating, diagonal streaks in a spatiotemporal map and single dominant frequency and segmental motilities as stationary, dark vertical bands in a spatiotemporal map and two dominant frequencies.

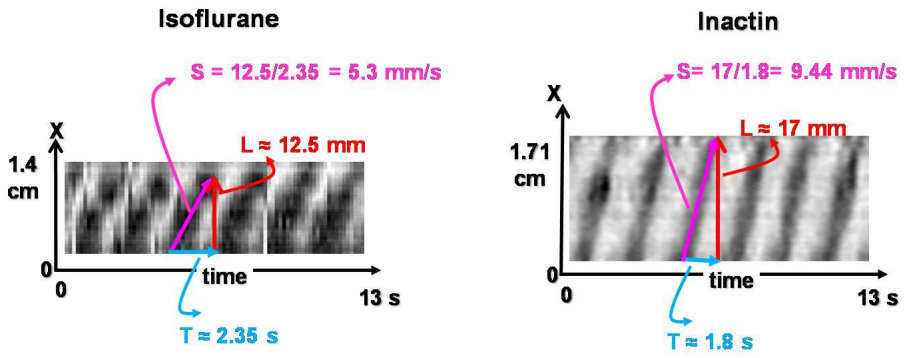

Figure 6.4. Peristalsis: isoflurane vs. inactin. The speed of propagation of peristalsis wave was derived from the corresponding spatio-temporal maps of isoflurane and inactin groups. The figure illustrates that speed of propagation can be derived by measuring the distance (L) traveled by a peristaltic wave within a time period (T). The speed of propagation can be computed from the ratio L/T and the wavelength (λ) can be derived from the ratio S/f, where f corresponds to the dominant frequency of peristaltic motility.

derive speed of propagation of peristaltic motility and comparison for isoflurane and inactin groups is shown in Figure 6.4. The speed of propagation (S) can be computed from the slope of diagonal streaks in corresponding spatio-temporal maps. The slope can be derived from the ratio L/T, where L = distance traveled by a peristaltic wave within time period (T). The speed of propagation computed among different animals suggest the speed of propagation is approximately twice as high in the animals anesthetized using inactin. Similarly the wavelength (λ) of peristaltic wave can be derived from the ratio S/f, where f = frequency of peristalsis wave. The results in Table 6.1 show that the average frequency of peristalsis (f) for both isoflurane (0.47 ± 0.028 Hz) and inactin (0.463 ± 0.076 Hz) is approximately same and in turn derived wavelength (λ) is also twice higher in animal anesthetized using inactin.

In terms of segmental motion, both isoflurane and inactin gave three distinct frequencies, with inactin showing significantly higher frequencies with a great degree of variability. There

is a greater standard deviation in these frequencies than those associated with peristalsis. In case of isoflurane Figure 4.12 revealed consistent frequencies among all animals for peristalsis and segmental motility. The results of average frequency and Fourier analysis for isoflurane and inactin groups are presented in the following sections. The detailed results of individual cases of peristaltic and segmental motility observed in animals anesthetized using isfolurane and inactin are presented in Appendix-A.

6.4.3 Average frequency and Fourier analysis

The results of average frequency analysis for each peristaltic and segmental dataset observed under inactin anesthesia are shown in Appendix-A in Section A.2. Summary of results of average frequency for isoflurane and inactin data are shown in Figure 6.5. The results of isoflurane data are also shown here for comparison with inactin data. The results suggest frequency peaks of inactin data are broader and have a great degree of variability than isoflurane. The results also support our earlier hypothesis that peristaltic motility can be characterized by a single dominant frequency peak and segmental motility being complex is characterized by three dominant peaks. To determine the underlying mechanism of dominant peaks a Fourier analysis based on band pass filtering and spatio-temporal maps was applied to inactin data. The results of a single peristaltic and segmental dataset are shown in Figures 6.6 and 6.7, respectively. The results of Fourier analysis of all the datasets are shown in Appendix-B in Section B.2. Fourier analysis of inactin data have similar results as that of isoflurane data and it further reinforces our earlier hypothesis. Thus suggests that in general the underlying mechanism of segmental motility can be considered as waves propagating in opposite directions create a stationary pattern. A third high frequency

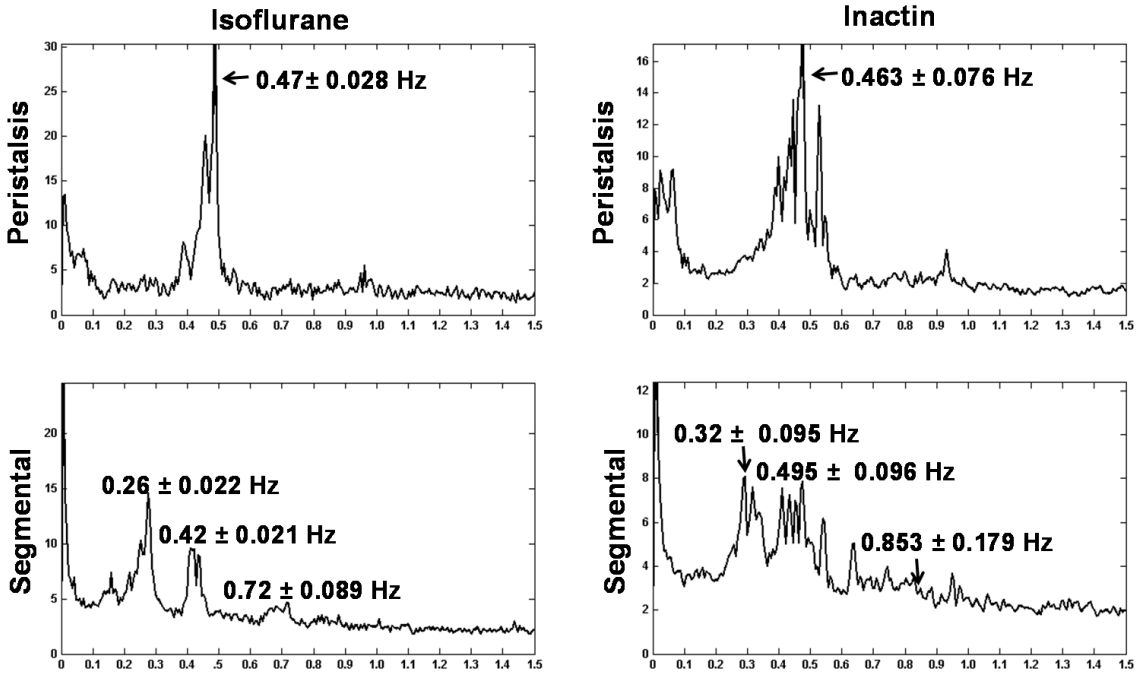

Figure 6.5. Average frequency analysis of peristaltic and segmental motility: isoflurane vs. inactin.

Anaesthetic	**datasets**	**%Inactivity**	**Inactive period(s) Mean ± SD**	**Max. inactive period(s)**
Isoflurane	110	10%	179.9 ± 22.4	504
Inactin	118	16%	17.7 ± 10.3	48.5

Table 6.2. Comparison of inactive periods in isoflurane and inactin groups. Isoflurane group has longer periods of inactivity than in inactin. These results indirectly prove that isoflurane has inhibitory effects on the motility of small intestine.

segmental mode is also required to complete the complex segmental patterning. On the other hand peristalsis is a single wave propagating in the aboral direction.

6.4.4 Physiological implication of inactive periods of gut

Interspersed between periods of segmental motion and (infrequent) peristalsis are periods of "inactivity" in which neither motion is present. An example of a spatiotemporal map

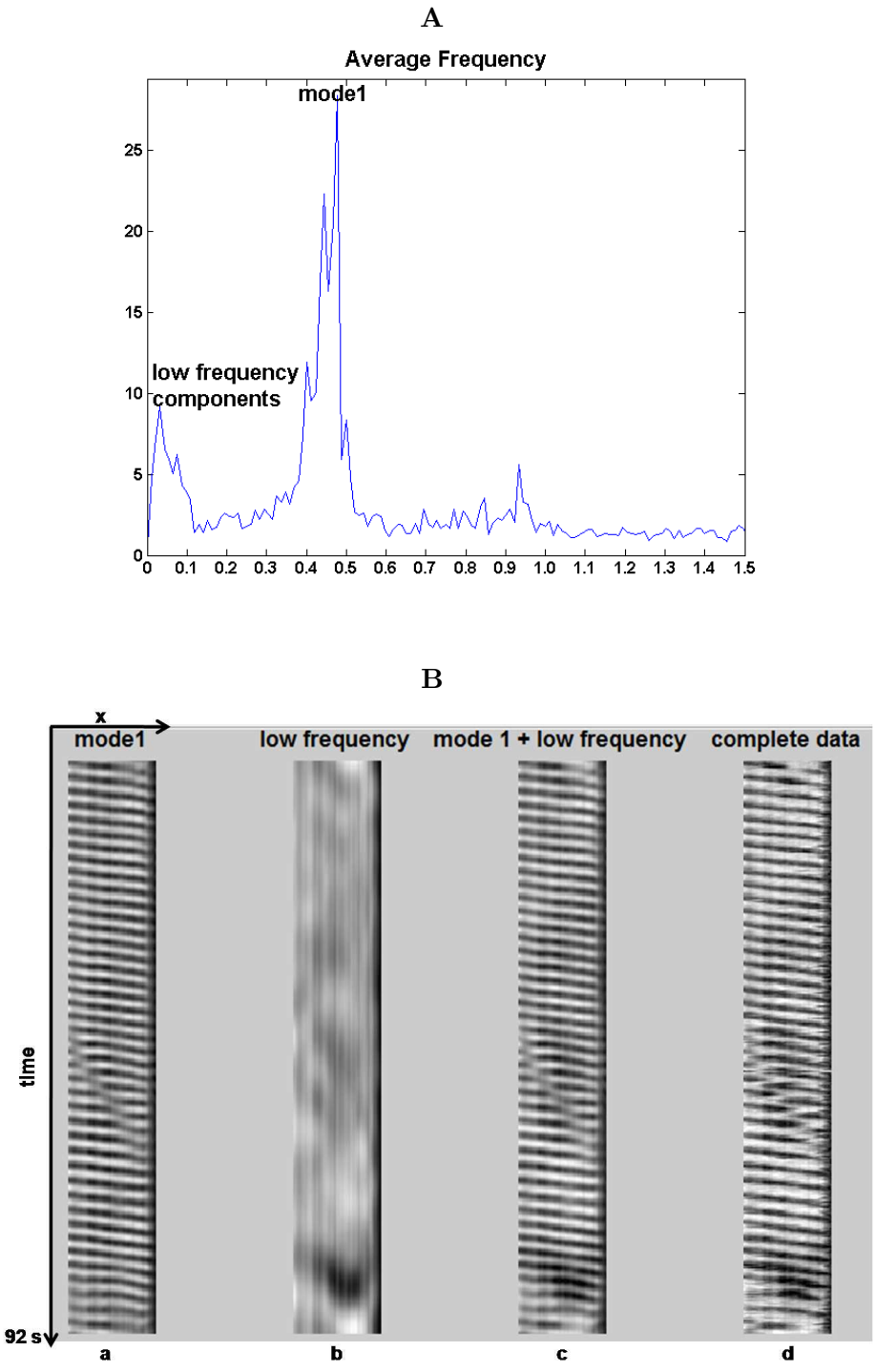

Figure 6.6. Fourier analysis of peristaltic motility

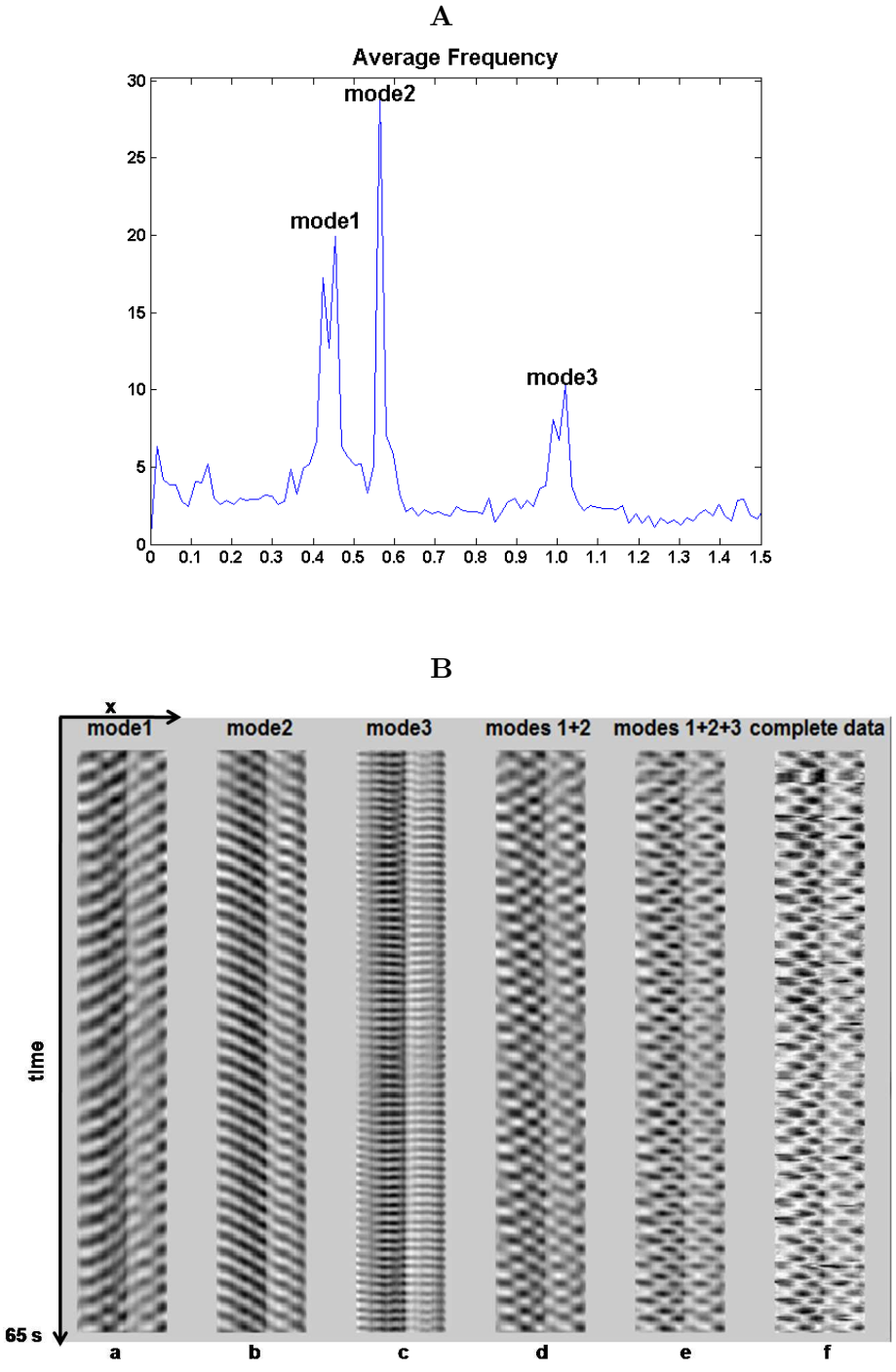

Figure 6.7. Fourier analysis of segmental motility

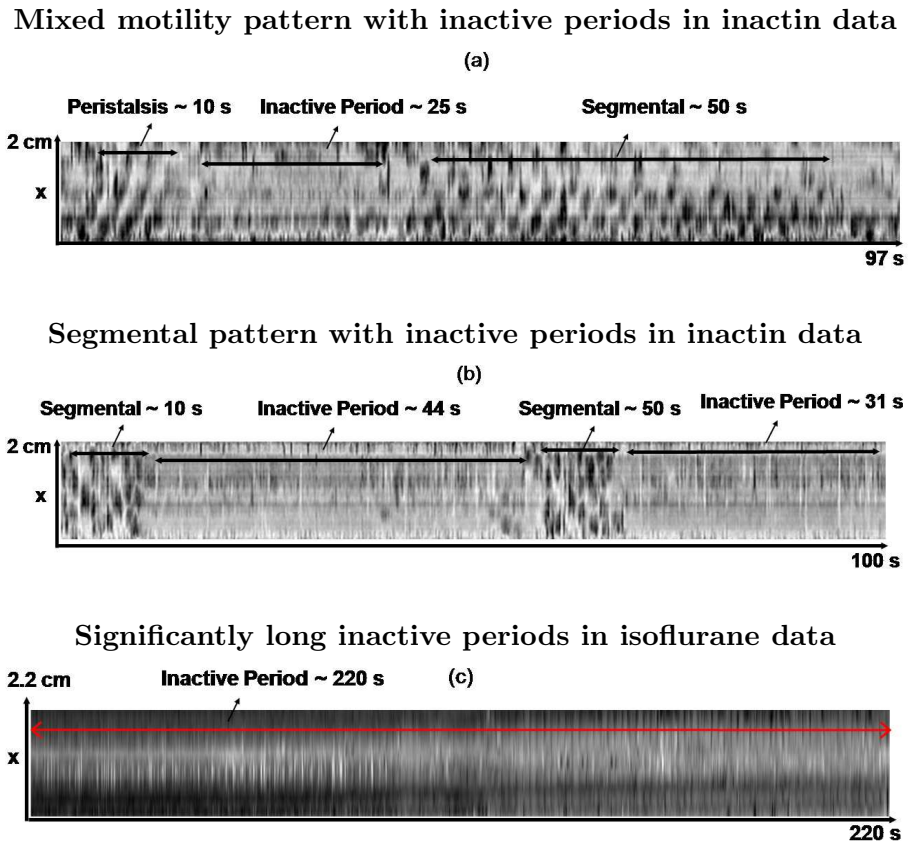

Figure 6.8. Physiological implication of inactive periods of gut for isoflurane and inactin data. (a) Mixed motility patterns with smaller inactive periods of gut. The illustration of mixed motility patterns of inactin data, such as peristalsis followed by segmental with small periods ($\approx$ 26 to 40 s) of quiescent between them The mixed patterns were absent in isoflurane data; (b) illustration segmental motility pattern with smaller periods of inactivity between them; (c) significantly longer periods of inactivity ($\approx$ 220 to 500 s) were observed in isoflurane data.

corresponding to such a period, interspersed between peristaltic and segmental motions, is shown in Figure 6.8a and two segmental motions, is shown in Figure 6.8b. An extended period of inactivity in a rat anesthetized with isoflurane is shown in Figure 6.8c. In terms of the relative length of periods of activity and inactivity, for isoflurane out of 110 total data sets, 11 (10%) showed significant periods of inactivity. The maximum single period of recorded inactivity was 504 s. The average inactive period was 179.9 ± 22.4 seconds. For inactin, out of 118 data sets, 19 (16%) showed periods of inactivity with a maximum period

of 48.5 seconds. The average inactive period was 17.7 ± 10.3 seconds. The results of inactive periods for isoflurane and inactin data are summarized in Table 6.2.

6.5 Discussion

The results presented here show that: (*i*) the inactive state of the gut was relatively higher in the rats treated with isoflurane than with inactin, (*ii*) the speed of propagation and wavelength of peristaltic motility and the frequency and speed of collapse of segmental motility were higher in the rats treated with inactin, and (*iii*) in comparison to isoflurane the inactin data revealed more segmental and peristaltic motions.

A literature review did not find any study which compared directly the effects of isoflurane and inactin anaesthesia on GI motility in rats. In terms of studies of one or the other anesthetic using invasive measurement techniques, Torjman *et al.* [99] have evaluated motility in rats divided into one control and four treatment groups exposed to isoflurane. The rats were fasted for 24 hours, allowed to drink water and were given an oral gavage of gelatin capsule containing charcoal powder which was used as a GI marker. Animals in the first treatment group were continuously exposed to 3% isoflurane for 2 hours, in the second group to 1.5% isoflurane for 6 mins and were awake for 1 hour after anesthesia, in the third group, anesthesia was administered similar to second group except they were awake for 2 hours, and in the fourth group anesthesia and time after anesthesia was similar third group, but in addition they had prior treatment with the prokinetic drug metochlopramide. All the animals were sacrificed post anesthesia, and the entire GI tract was separated. Parameters such as the physical distance traveled by the GI marker in the small intestine from

the pylorus, GI transit time and mean stomach volume were then computed. The first experimental group had the lowest GI rate of propulsion, with the rate of propulsion being three times higher for the animals in the second than third groups, but the propulsion rate even after 2 hours represented a 57% decrease relative to animals that had undergone no anesthesia. The animals treated with metochlopramide showed increased gastric emptying, but this did not translate to increased propulsion rate.

Sababi *et al.* [109] have evaluated the effect of intestinal motility on the absorption via various GI markers that play an important role in the absorption process in the duodenum. The data showed that rats treated with inactin showed no signs of post operative ileus, had stable blood pressure and exhibited gut motility even after the surgical procedure. The GI marker polyethylene glycol revealed that intestinal and mucosal integrity was completely intact. It has also been reported that inactin does not interfere with brainstem autonomic reflexes and produces stable physiological parameters [108]. Sababi *et al.* also performed a comparative study of nitric oxide synthase and inhibitory action of cyclo-oxygenase on duodenal functions in rats anesthetized using inactin, alpha-chloralose and urethane [110]. They have reported that inactin and alpha-chloralose behaved similarly in terms of studied basal values. Several groups have conducted in-situ Trendelenburg experiments on the motility of small intestine in rats anesthetized using alpha-chloralose and ketamine [17, 18]. The anesthetic alpha-chloralose does not interfere with GI reflexes. We can indirectly conclude that inactin which behaves similar to alpha-chloralose can also be used for GI studies. Sababi *et al.* [109] reported that rats treated with inactin did not show any postoperative ileus and exhibited normal gut motility after surgery.

The other aspect of the quantitative analysis was to derive the underlying mechanisms

of peristaltic and segmental motility. The results of Fourier analysis of inactin data were similar to that of isoflurane and further strengthen our earlier hypothesis outlined in Chapter 5. In future the motility of small intestine acquired using different anesthetics and analyzed using detailed quantitative approach can be compared with the control group (under no anesthesia) to find out which is more closer to the normal physiology of the gut.

6.6 Conclusions

Consistent with these data from the literature, our current study showed that isoflurane affects the gut motility to a much larger extent than inactin. For example, in inactin the inactive state of the gut is relatively short ($\approx$ 26 to 45 s) as compared to isoflurane ($\approx$ 220 to 500 s), and the speed of propagation (8.99 ± 4.04 mm/s) is two-fold higher for inactin than isoflurane (4.34 ± 0.35 mm/s). Segmental motility was dominant in both isoflurane and inactin treated rats. Frequency analysis of segmental motility showed the presence of three peaks in the two groups and the dominant frequency and speed of collapse of segmental motility were higher in the rats treated with inactin. The results also suggest that the basic patterning of motility is similar between inactin and isoflurane, but the two different drugs affect both the frequency of motility and the variability in the frequency. We can speculate that whereas isoflurane suppresses motility to a greater extent than inactin, the motility that is not suppressed is more specific with isoflurane than with inactin.

Chapter 7

Summary

7.1 Contributions

This thesis presented methods and tools to perform non-invasive contrast enhanced dynamic MR imaging of the small intestine in rats and quantify true physiological parameters. It also presented image analysis tools to analyze the acquired data and visualize complex motility patterns. The thesis contributions are summarized as follows:

1. Technical advances in MRI of small bowels.

2. A non-invasive way to acquire true physiological gut motion.

3. A novel 3D image segmentation tool to determine the boundary of small intestine.

4. New insights into underlying mechanism of gut and implications to physiology.

The technical details of thesis contributions are listed below:

1. The dynamic MRI, 3D image segmentation tool and a combination of image processing methods are proposed in Chapter 4. This study represents the first quantitative

analysis of motion of the GI tract in vivo in animal models using MRI. In previously proposed methods, it is easier to identify the exact location of the small intestine for invasive procedures and the two ends of the small intestine are fixed. Thus, the section of the gut being evaluated more or less is in the same imaging plane. Lastly, the CNR and SNR of the acquired data is far superior than any non-invasive way of data acquisition. But on the other hand, the invasive procedures are time consuming and are mostly terminal. In contrast to invasive procedures, MRI does not require extensive tissue preparation, and captures a much truer representative physiological state of the gut. A 3D imaging of the entire GI tract was performed before every dynamic imaging to identify the jejunum region of the small intestine. The frequency of the peristaltic and segmental contractions were found in the range from 0.23 to 0.63 Hz and MRI data acquired at 6 frames per second was sufficient enough to capture the physiological state of the gut. Due to the low CNR and rapid temporal change in morphology in the dynamic images, significant image processing is required for accurate segmentation of the GI tract.

2. The thesis proposed combination of sophisticated image analysis and mathematical methods for image segmentation, computation of a skeleton, shape modeling, Fourier analysis, spatio-temporal maps and image registration to quantify and analyze complex gut motion. These methods have been applied independently to other medical applications like virtual bronchoscopy, CT imaging of the chest, neuronal dendrites in EM images, dynamic chest images using X-ray fluoroscopy and breast images in mammogram. The dynamic nature of the small intestine and convoluted GI tract

often leads to deep indentations and high curvature segments. The combination of image processing methods listed below have been applied for the first time in quantitative analysis of the small intestine. We have proposed the combination of following algorithms:

(a) *2D Image registration*: As the imaging is being performed on live animal, animal's breathing induces shifts in x, y and z planes. The plot shown in Figure 4.3 demonstrates the variability in shifts from $1-2$ or $5-15$ mm. The large shifts in the range $5-15$ mm correlate well with breathing frequency and at this time a section of the gut being imaged is completely outside the imaging plane (see Figure 4.3). The registration step can be automatically used to find such images that do not have a meaningful shape and can be linearly interpolated in time to replace missing images.

(b) *3D Image segmentation*: Hybrid combination of 3D LW and DDGVFS for accurate segmentation of GI tract. 3D LW generates an approximate 3D boundary of 2D space+time MRI data of the small intestine by segmenting few orthogonal planes. The approximate boundary often fails in the area of deep indentations and is further refined by second algorithm, DDGVFS. DDGVFS iteratively attracts the approximate boundary within deep indentations. The proposed algorithm accurately segments $\approx 97\%$ of 3D volume and the remaining images were segmented using manual 2D LW.

(c) Medial axis: The conventional method of computing the diameter is done by drawing perpendicular lines to medial axis and finding an intersection with the

boundary on both sides of medial axis. Our approach included a combination of 2D thinning algorithm, false branch deletion, and Euclidean distance maps to quantify the diameter of the small intestine as a function of x, along the length of the gut and time,t. Our approach overcome errors in computing diameter in high curvature regions of the small intestine.

(d) *Spatio-temporal maps*: The spatio-temporal maps have been used in the past to visualize complex motility of the GI tract. The novel way of computing medial axis of the small intestine resulted in an accurate estimation of 2D function $D(x,t)$ (along the length of the gut for every image in time). The iso-contour plots of $D(x,t)$ can now be used for accurate representation of complex gut motions.

3. In two separate studies, the rats were anesthetized with inactin and isoflurane anaesthesia. As per our approach discussed in Chapter 3 we were able to characterize peristalsis and segmental motility patterns in anesthetized rats. The peristalsis was characterized as propagating constriction with single dominant frequency (≈ 0.46 Hz) and represented as diagonal streaks in a spatio-temporal map. In contrast, the segmental was characterized as stationary constrictions with three dominant frequencies (in the range 0.21 to 1.1 Hz) and represented as dark vertical bands in a spatio-temporal map. The percentage of segmental motility was dominant in both groups and percentage of peristaltic motility was higher for the inactin group. We were able to identify and visualize complex mixed motility patterns using spatio-temporal maps, such as peristalsis followed by segmental and inactive periods of the gut between peri-

stalsis and segmental motility. The physiological parameters such as frequency and speed of peristalsis measured using MRI were in good agreement with the results using previously proposed invasive studies. There are no published results on the segmental contractions in rats and so we were not able to directly compare measured frequency of segmental contractions. The measured frequency of segmental contractions in the jejunum region lies at the upper end of that reported in *in vitro* studies in isolated guinea pig small intestine [14, 15].

4. The results of integrated analysis presented in Chapter 5 indicate that the underlying mechanism of complex peristaltic and segmental motilities is simple and qualitatively similar, except for the spatial scale. The results also suggest that complex motility patterns may be generated internally by changing the frequency and phase of the principal components. On the other hand the results of Fourier analysis suggest that underlying mechanism of the gut is generated by waves propagating initiated by different sections of the gut. The spatio-temporal maps of decomposed modes bring forth that a peristaltic motility can be originated by a single wave propagating in the aboral direction. In contrast a segmental motility is much more complex and at least two waves propagating in opposite directions are needed to create a simple stationary pattern. In complex segmental patterns a third high frequency segmental mode is also required to complete the complex patterning. We further propose that underlying mechanism of the gut is simple and combination of finite order of principal components or Fourier modes. Different motility patterns of the gut can be generated by varying the frequency and phase of principal components or combining Fourier

modes. These patterns can be combined with CFD models to better predict fluid flow during absorption and transportation processes.

5. Inactin and isoflurane are commonly used anesthetics in animal imaging and experiments. Researchers have employed invasive techniques to quantify the effects of such anesthetics from post mortem animals on gut motility, intestinal absorption, post-operative ileus, blood pressure. As per our knowledge and literature review, inactin anaesthesia does not have inhibitory effects on the gut motility as isoflurane anaesthesia. We found, with inactin, the inactive state of the gut is relatively short ($\approx$ 26 to 45 s) as compared to isoflurane ($\approx$ 220 to 500 s), and the speed of peristaltic propagation (8.99 ± 4.04 mm/s) is two-fold higher for inactin than isoflurane (4.34 ± 0.35 mm/s). Although segmental motility was dominant in both isoflurane and inactin treated rats, analysis showed dominant frequencies and speed of collapse of segmental motility were higher in the rats treated with inactin. These are the first quantitative *in vivo* results comparing effects of inactin and isoflurane on the GI motility using dynamic MRI. The results presented here are consistent with the data in the literature and suggest isoflurane affects the gut motility to a much larger extent than inactin.

7.2 Future Work

The length of GI tract in humans is 5.5 times the length of GI tract in rats. The time for chyme to travel down a small intestine is on the same order in humans and rats, $\approx 3 - 4$ h. Thus, the frequency of small intestine is much slower compared to rats. The dynamic MRI and image analysis approach of this thesis can be easily applied to humans to better

understand gut physiology and determine the underlying order of complex motility.

The pro-kinetic agents cisapride and metoclopramade, enhance gut motility [112,113]. In contrast, anti-motility drugs loperamide (Imodium) and diphenoxylate have been employed to treat chronic diarrhea [114]. A set of experiments should be carried out to test different drugs that support or inhibit gut motility and compare them with inactin results, which represents normal gut motility. A similar set of experiments can be designed to quantify the effects of diabetic and other diseased models on the peristaltic and segmental motility of the small intestine.

The gut motility significantly depends on the amount of food in the gut before the experiment. In the current MRI protocol the rats were allowed to have a normal diet and water and were given a oral gavage of Gd contrast agent before dynamic imaging. Some of the segments of the small intestine which did not have enough food and water content were found collapsed and thus difficult to image. In future experiments, the rats should be fed with a mixture of jelly like material just before the experiments that can distend the small bowels. This will make sure the bowels of the rat are not collapsed and moreover gadolinium mixed with liquid can easily diffuse into all the parts of the small intestine.

The proposed segmentation algorithm took ≈ 4 h to process each data set (1000 images) on a computer with the following specifications: Intel Pentium 4 processor, 3.2 GHz, $3GB$ of random access memory (RAM). The majority of functions cost computation in LW, Windows based mouse-tracking, iterative snakes, etc. were implemented in Matlab but Dijkstras algorithm was implemented in C language to improve the processing speed. The processing time of the segmentation algorithm can be further improved by converting the MATLAB code to C++ and MFC based graphical user interface.

A simplified geometry model was developed for CFD from MRI data based on a set of physiological parameters such as maximum and minimum diameter, occlusion ratio, amplitude, frequency and speed of contraction, speed of propagation, etc. averaged over all the animals. Actual geometry can be derived from a spatio-temporal map of each data set and integrated with CFD model. The results of integrated analysis and Fourier analysis can be integrated to build sophisticated and physiologically relevant CFD models. The next step would be to compare and correlate the results of integrated and Fourier analysis to gain more insight into underlying mechanisms of the small intestine.

Finally, the role of the proposed quantitative analysis methods, should be investigated more in imaging of colon, and large intestines. The proposed image segmentation algorithm can also be applied to other applications like colonoscopy and any part of GI tract.

Appendix A

Spatio-temporal maps and average frequency analysis

The results of average frequency analysis and spatio-temporal maps of each peristaltic and segmental case observed under isoflurane and inactin anesthesia are presented in Sections A.1 and A.2.

A.1 Isoflurane

The dynamic MRI was performed on six animals and an individual peristaltic and segmental case was analyzed from each animal. However the peristaltic motility was not dominant and was observed in just two animals.

A.1.1 Peristalsis

The results of each animal (also termed here as dataset) are shown in Figure A.1.

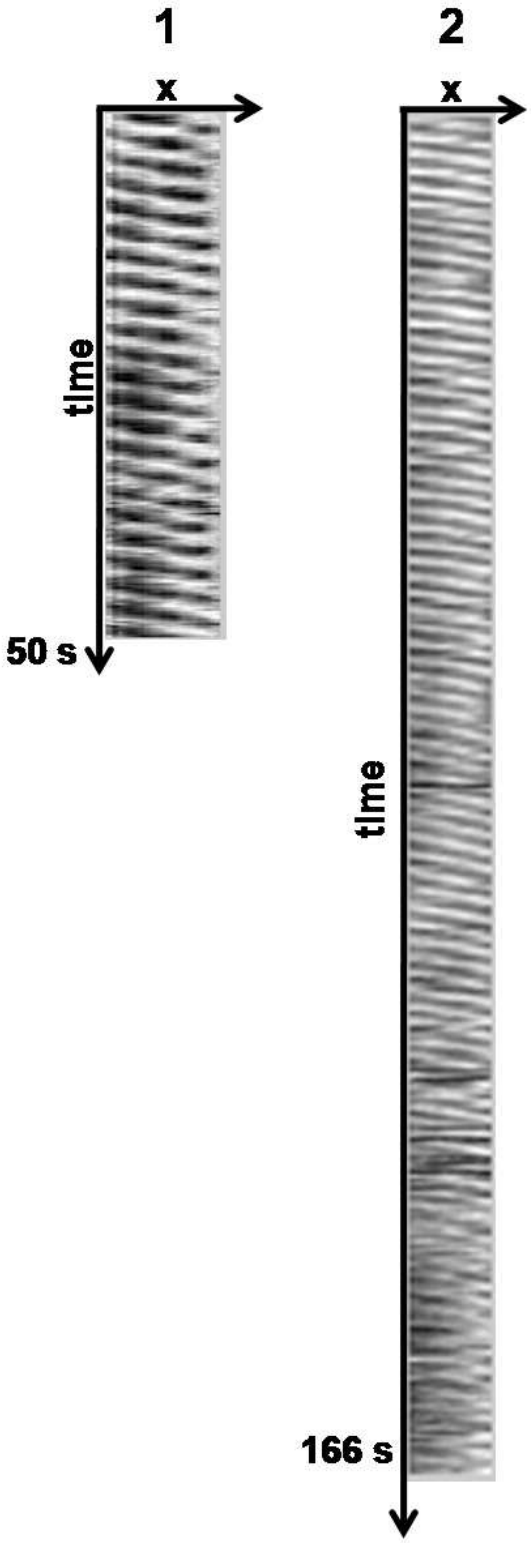

Figure A.1. Spatio-temporal maps of peristaltic motility: Isoflurane (2 cases). The dataset number is labeled on top of corresponding map.

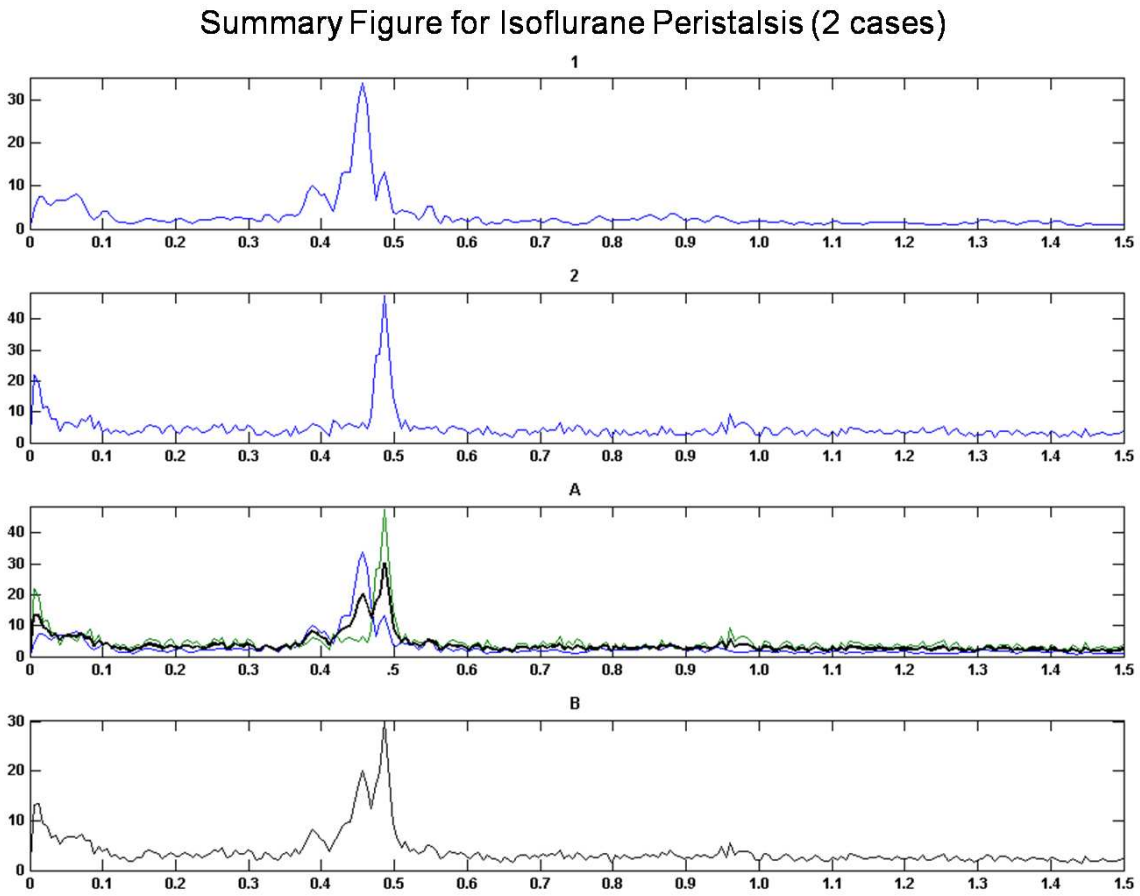

Figure A.2. Individual and average frequency analysis of peristaltic motility: Isoflurane (2 cases). The dataset number is labeled on top of corresponding individual frequency plot. The individual plots were used to compute an average frequency response. (A) The average frequency plot (solid black) is shown along with individual cases. (B) An average frequency plot on its own.

A.1.2 Segmental

The spatio-temporal maps of segmental motion observed under each animal are shown in Figure A.3.

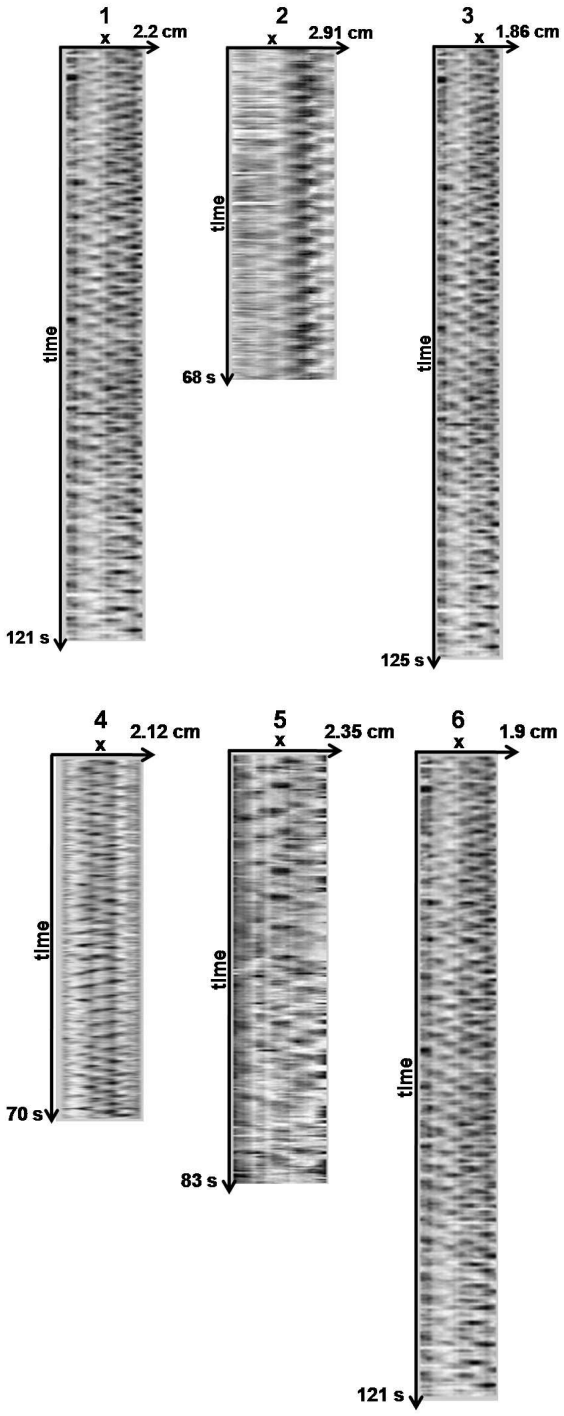

Figure A.3. Spatio-temporal maps of segmental motility: Isoflurane (6 cases). The dataset number is labeled on the top of each spatio-temporal map.

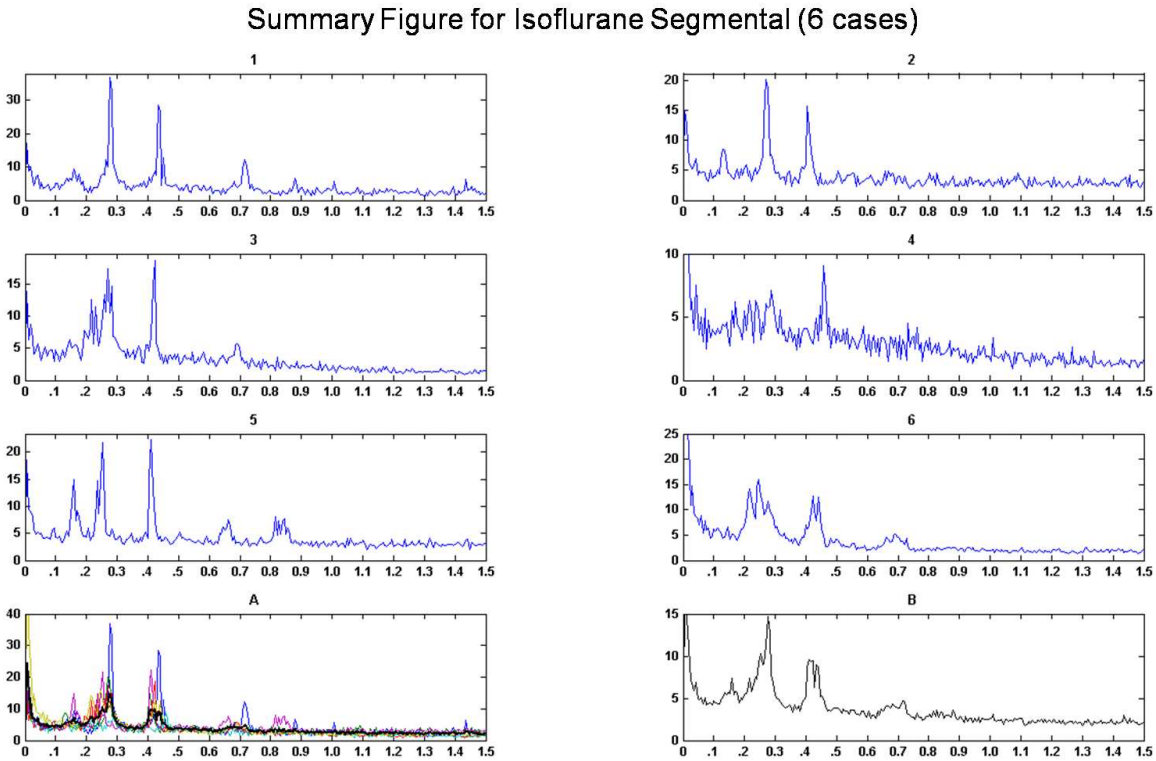

Figure A.4. Individual and average frequency analysis of segmental motility: Isoflurane (6 cases). The dataset number is labeled on top of corresponding individual frequency plot. The individual plots were used to compute an average frequency response. (A) The average frequency plot (solid black) is shown along with individual cases. (B) An average frequency plot on its own.

A.2 Inactin

The dynamic MRI was performed on six animals and an individual peristaltic and segmental case was analyzed from each animal. However the peristaltic motility was not dominant and was observed in just three animals.

A.2.1 Peristalsis

The results of each animal (also termed here as dataset) are shown in Figure A.5.

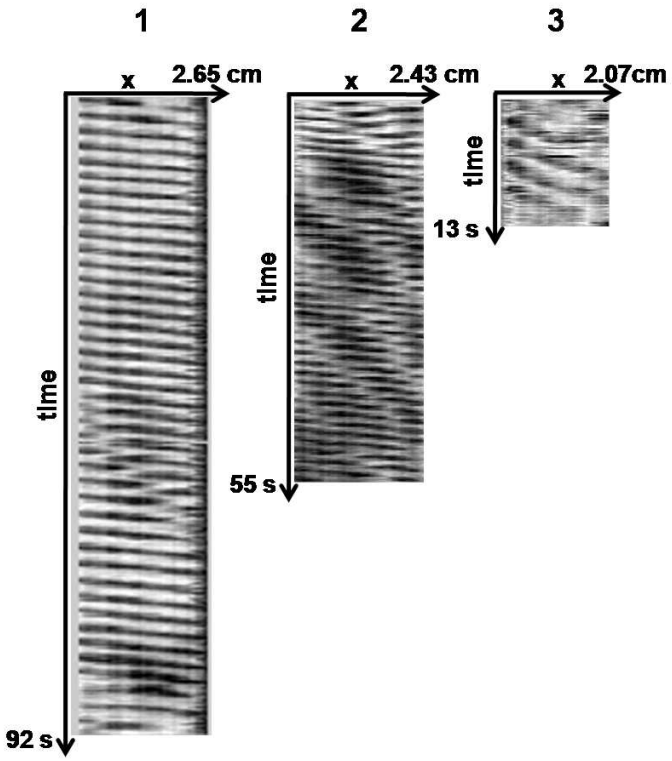

Figure A.5. Spatio-temporal maps of peristaltic motility: Inactin (3 cases). The dataset number is labeled on the top of each spatio-temporal map.

A.2.2 Segmental

The spatio-temporal maps of segmental motion observed under each animal are shown in Figure A.7.

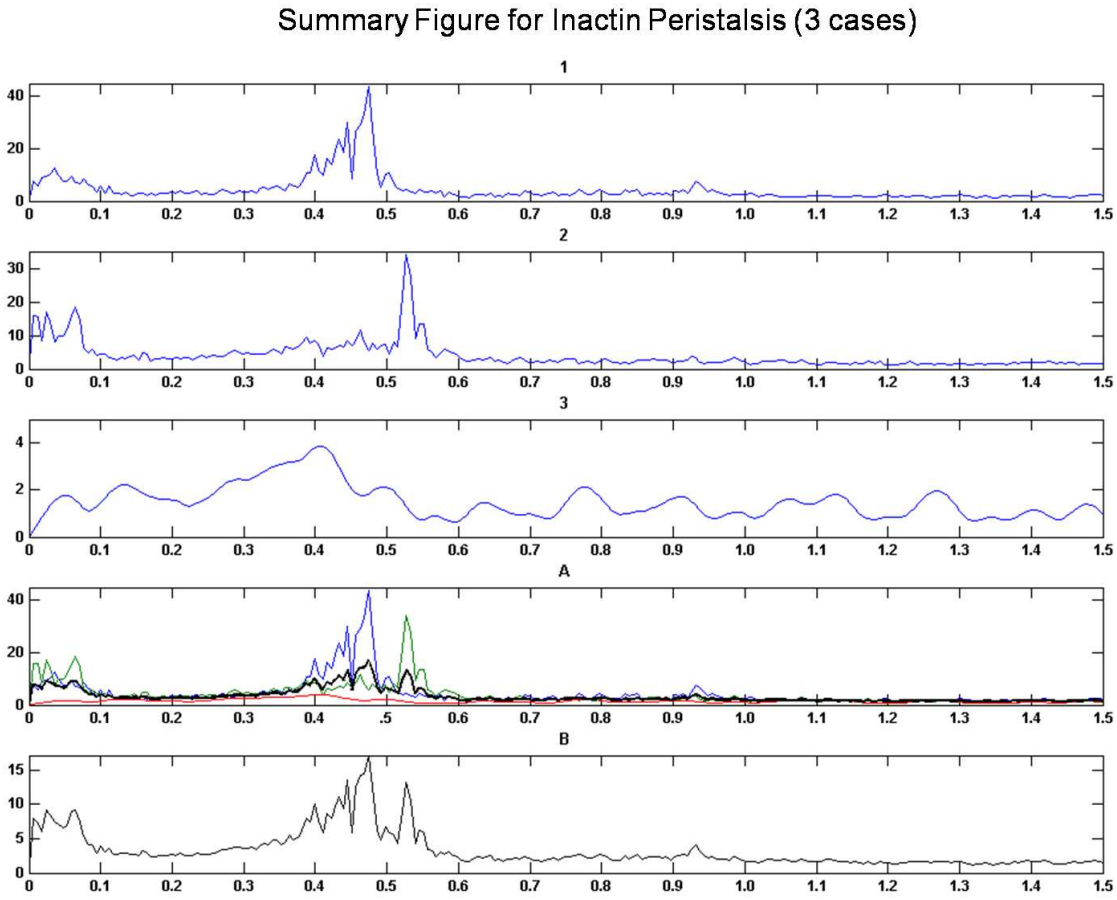

Figure A.6. Individual and average frequency analysis of peristaltic motility: Inactin (3 cases). The dataset number is labeled on top of corresponding individual frequency plot. The individual plots were used to compute an average frequency response. (A) The average frequency plot (solid black) is shown along with individual cases. (B) An average frequency plot on its own.

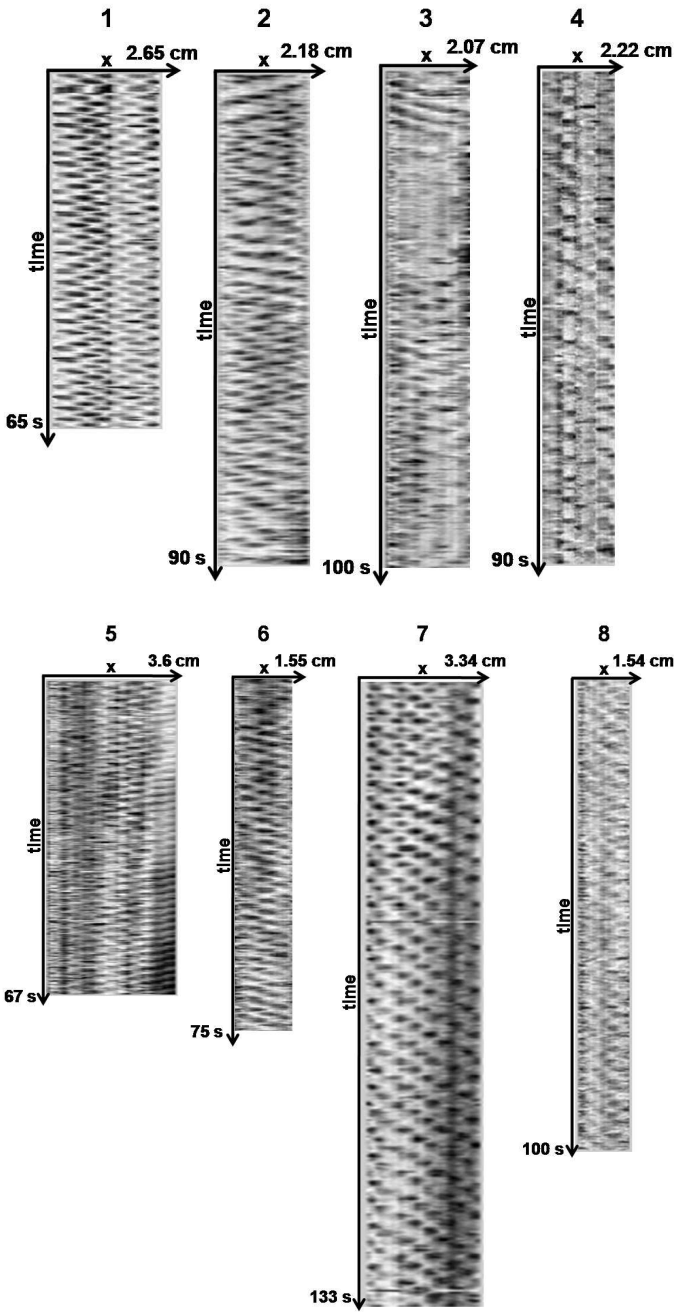

Figure A.7. Spatio-temporal maps of segmental motility: Inactin (8 cases). The dataset number is labeled on the top of each spatio-temporal map.

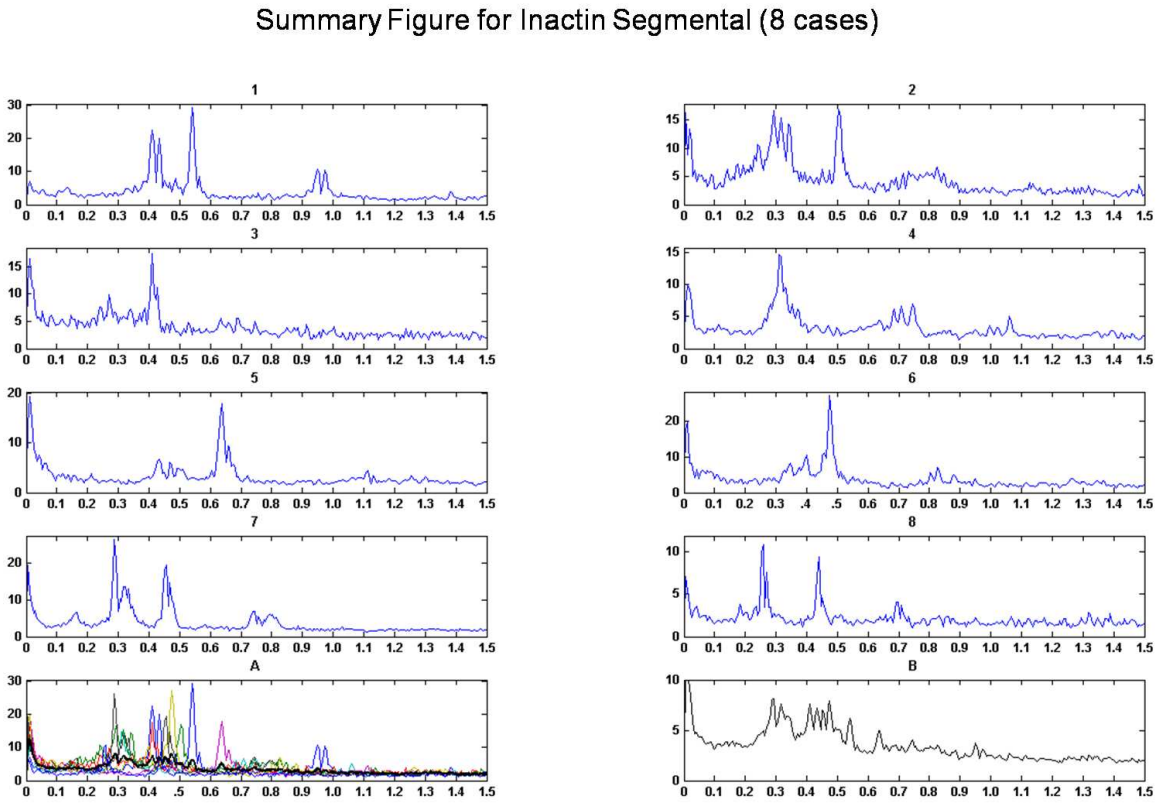

Figure A.8. Individual and average frequency analysis of segmental motility: Inactin (8 cases). The dataset number is labeled on top of corresponding individual frequency plot. The individual plots were used to compute an average frequency response. (A) The average frequency plot (solid black) is shown along with individual cases. (B) An average frequency plot on its own.

Appendix B

Fourier analysis results

The results of Fourier analysis and band pass filtering of all the cases of isoflurane and inactin are presented in Sections B.1 and B.2.

B.1 Isoflurane

The dynamic MRI was performed on six animals and an individual peristaltic and segmental case was analyzed from each animal. However the peristaltic motility was not dominant and was observed in just two animals. The results of Fourier analysis of peristaltic and segmental motilities observed under isoflurane anesthesia are presented in the following sections.

B.1.1 Peristalsis

The results of each animal (also termed here as dataset) are shown in Figures B.1 to B.2. The average frequency response for the corresponding dataset is shown in the top row (A) and spatio-temporal maps of decomposed modes and other combination of modes

Datasets	Mode1 (Hz)
1	0.45
2	0.49
Mean ± SD	0.47 ± 0.028

Table B.1. Frequency modes for peristaltic motion under isoflurane anesthesia. The values were derived from average frequency response of individual dataset from each animal and then averaged over all the animals (Mean ± SD).

are shown in the bottom row (B). The reconstructed spatio-temporal maps represented following cases: (a) individual dominant peak (mode1); (b) low frequency components; (c) summation of mode1 and low frequency components (mode1 + low frequency components); and (d) unaltered complete data. The frequency centers were obtained from the average frequency analysis of the corresponding dataset. The quantitative results of each peristaltic dataset and the average frequency analysis of all the datasets are summarized in Table B.1.

B.1.2 Segmental

The results of each animal (also termed here as dataset) are shown in Figures B.3 to B.8. The average frequency response for the corresponding dataset is shown in the top row (A) and spatio-temporal maps of decomposed modes and other combination of modes are shown in the bottom row (B). For datasets 1, 3, 5 and 6 (see Figures B.3, B.5, B.7 and B.8), the reconstructed spatio-temporal maps represented following cases: (a to c) individual dominant peaks (mode1, mode2 and mode3); (d) summation of first two peaks (modes 1+2); (e) summation of all three peaks (modes 1+2+3) and (f) unaltered complete data. The frequency centers were obtained from the average frequency analysis of the corresponding dataset. Similarly for datasets 2 and 4 (see Figures B.4 and B.6), the reconstructed spatio-temporal maps represented following cases: (a to b) individual dominant peaks (mode1

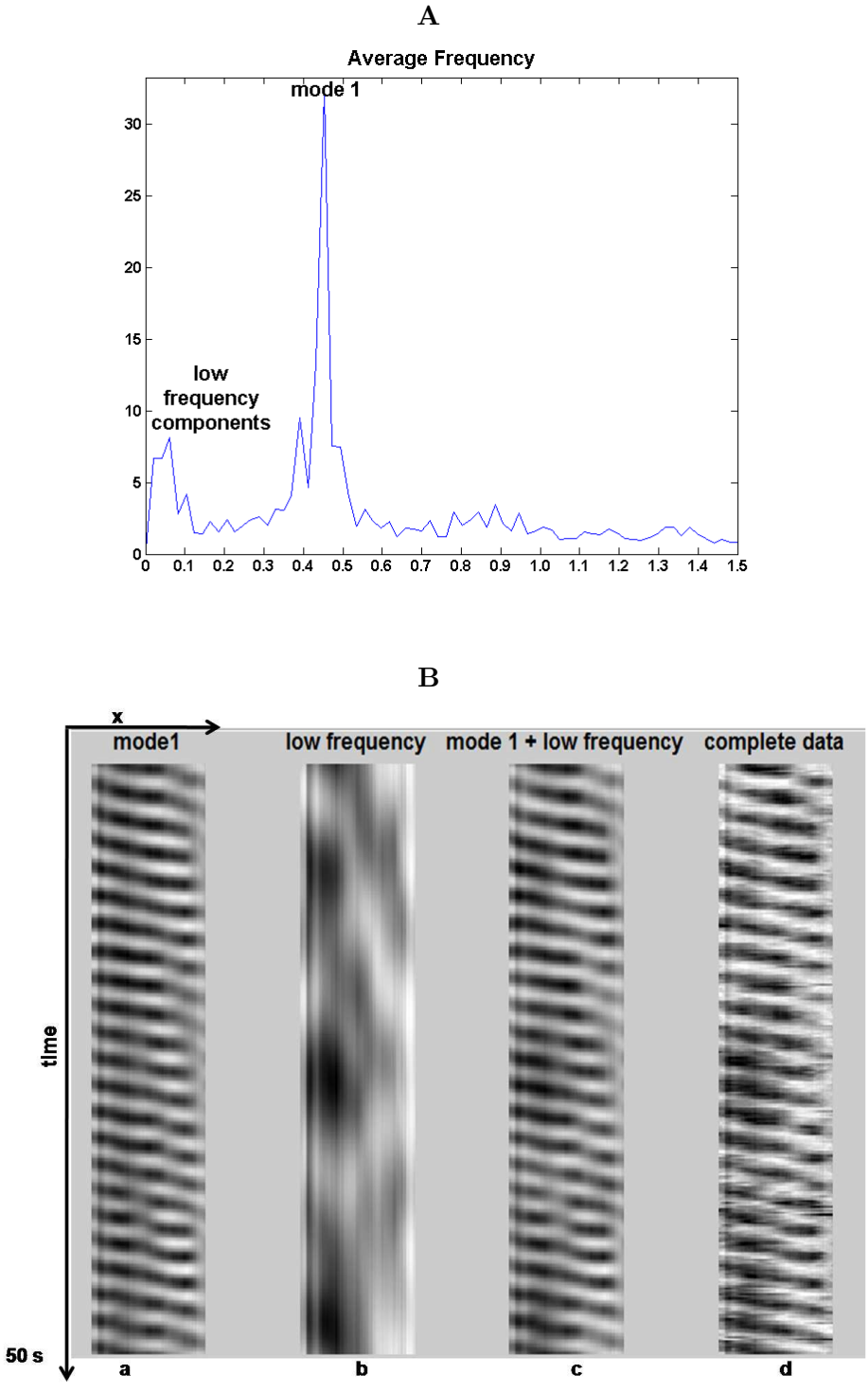

Figure B.1. Fourier analysis of peristaltic motility: Isoflurane Dataset 1.

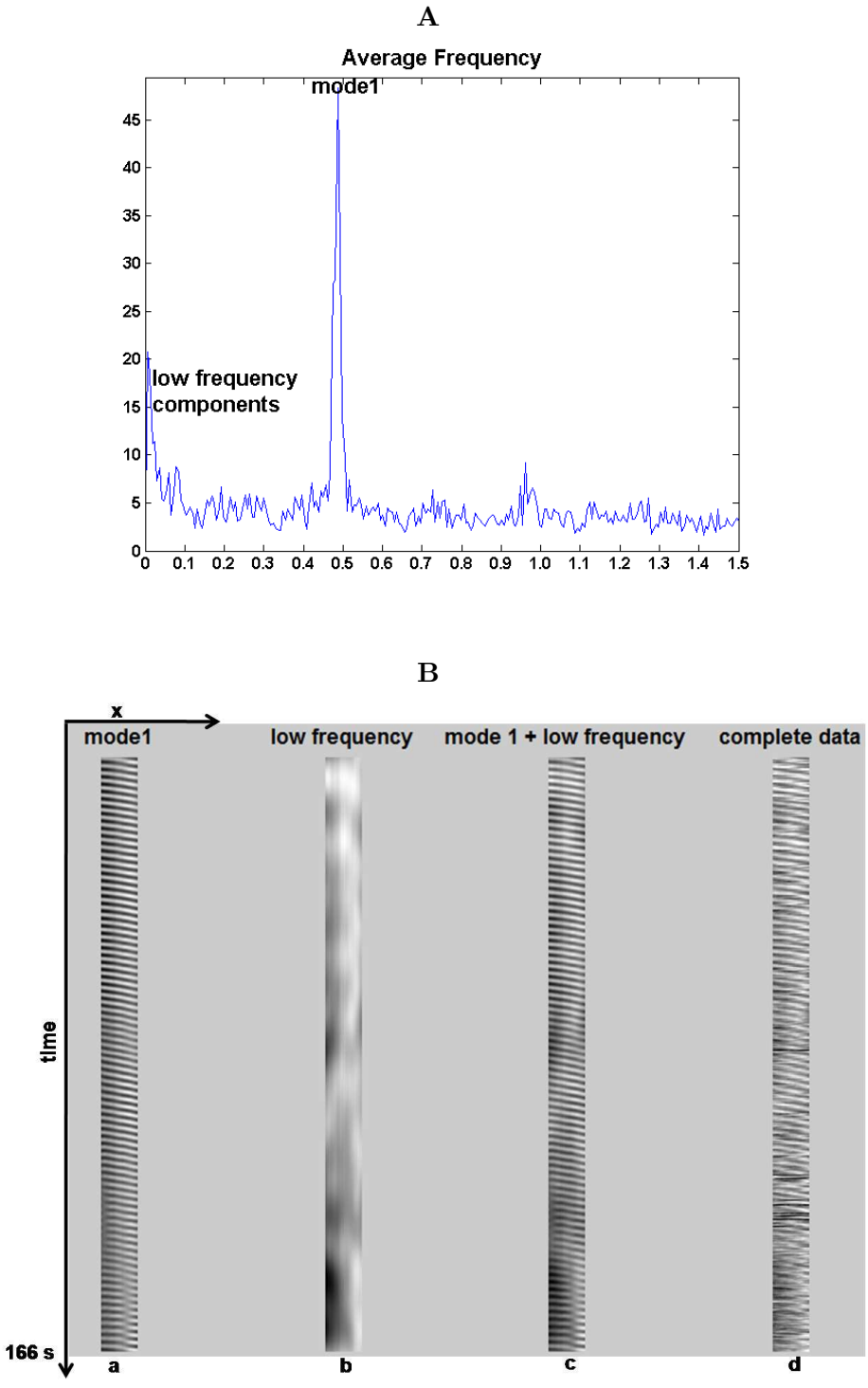

Figure B.2. Fourier analysis of peristaltic motility: Isoflurane Dataset 2.

Datasets	Mode1 (Hz)	Mode2 (Hz)	Mode3 (Hz)
1	0.27	0.43	0.7
2	0.28	0.4	*absent*
3	0.26	0.46	0.68
4	0.27	0.46	*absent*
5	0.24	0.41	0.85
6	0.22	0.42	0.65
Mean ± SD	0.26 ± 0.022	0.423 ± 0.021	0.72 ± 0.089

Table B.2. Frequency modes for segmental motion under isoflurane anesthesia. The values were derived from average frequency response of individual dataset from each animal and then averaged over all the animals (Mean ± SD).

and mode2); (c) summation of first two peaks (modes 1+2); and (d) unaltered complete data. The frequency centers were obtained from the average frequency analysis of the corresponding dataset. The quantitative results of each segmental dataset and the average frequency analysis of all the datasets are summarized in Table B.2.

B.2 Inactin

The dynamic MRI was performed on six animals and an individual peristaltic and segmental case was analyzed from each animal. Similar to isoflurane the peristaltic motility was not dominant and was observed in just three animals. The results of Fourier analysis of peristaltic and segmental motilities acquired using inactin anesthesia are presented in the following sections.

B.2.1 Peristalsis

The results of each animal (also termed here as dataset) are shown in Figures B.9 to B.11. The average frequency response for the corresponding dataset is shown in the top row (A) and spatio-temporal maps of decomposed modes and other combination of modes

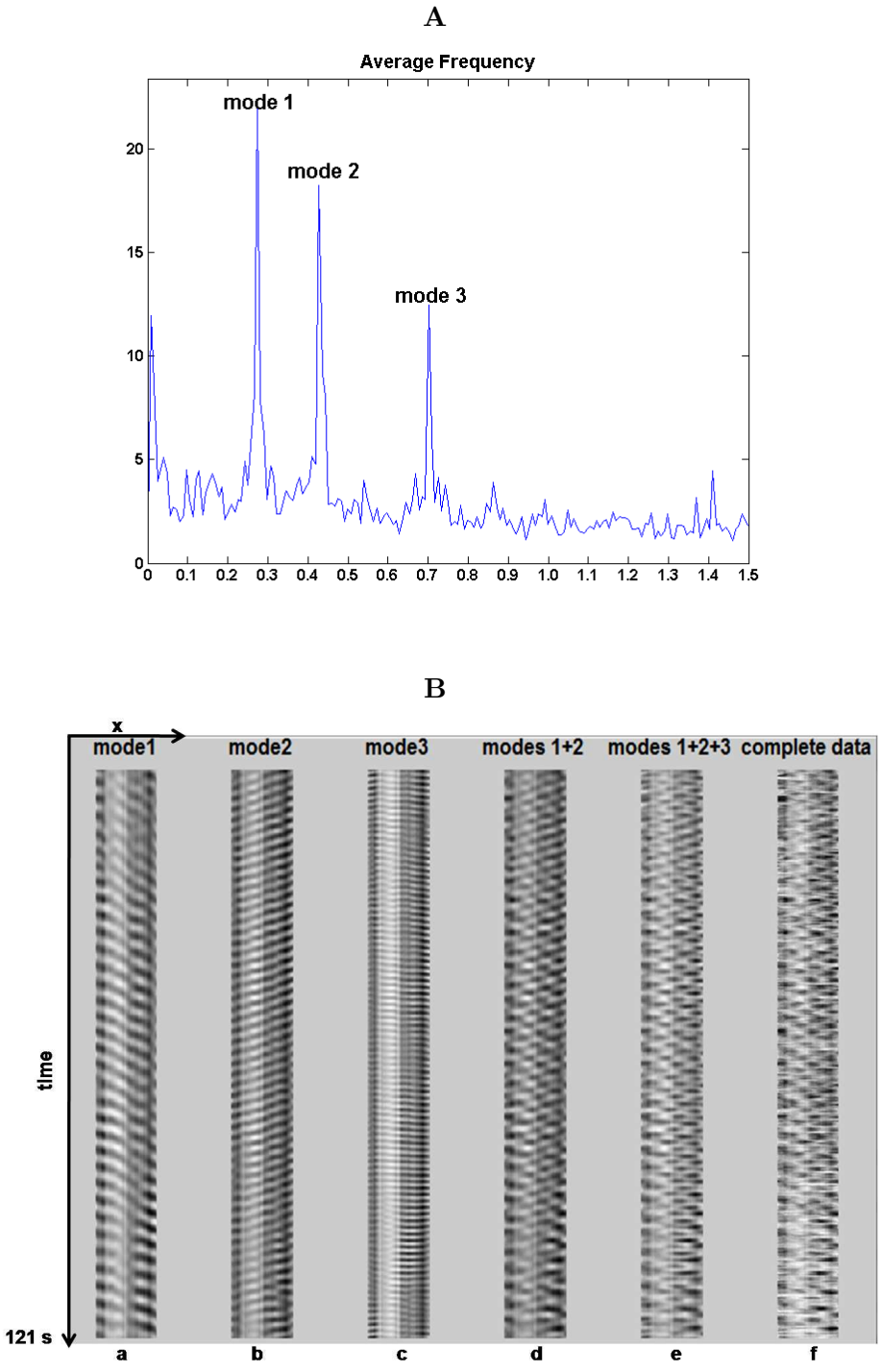

Figure B.3. Fourier analysis of segmental motility: Isoflurane Dataset 1.

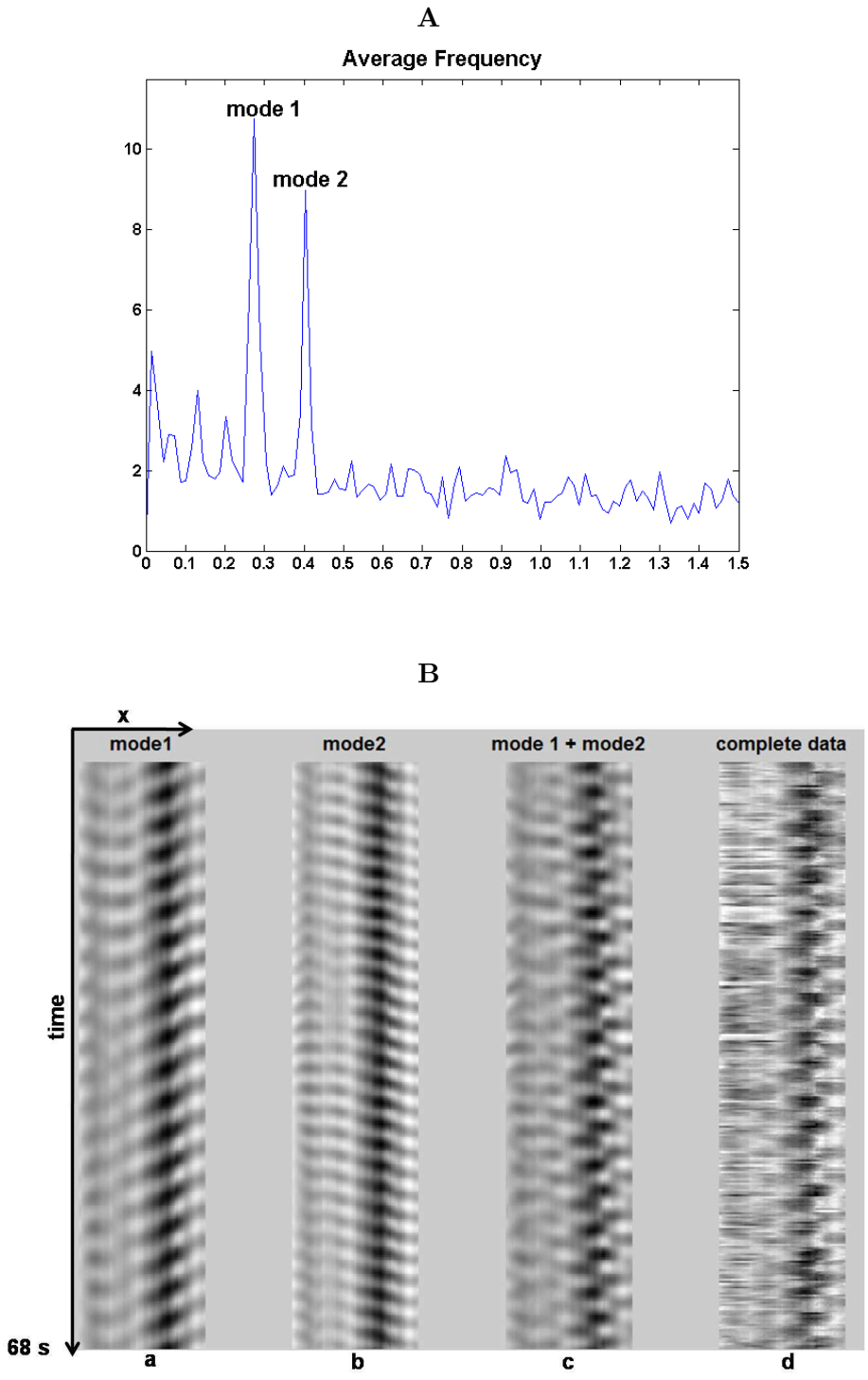

Figure B.4. Fourier analysis of segmental motility: Isoflurane Dataset 2.

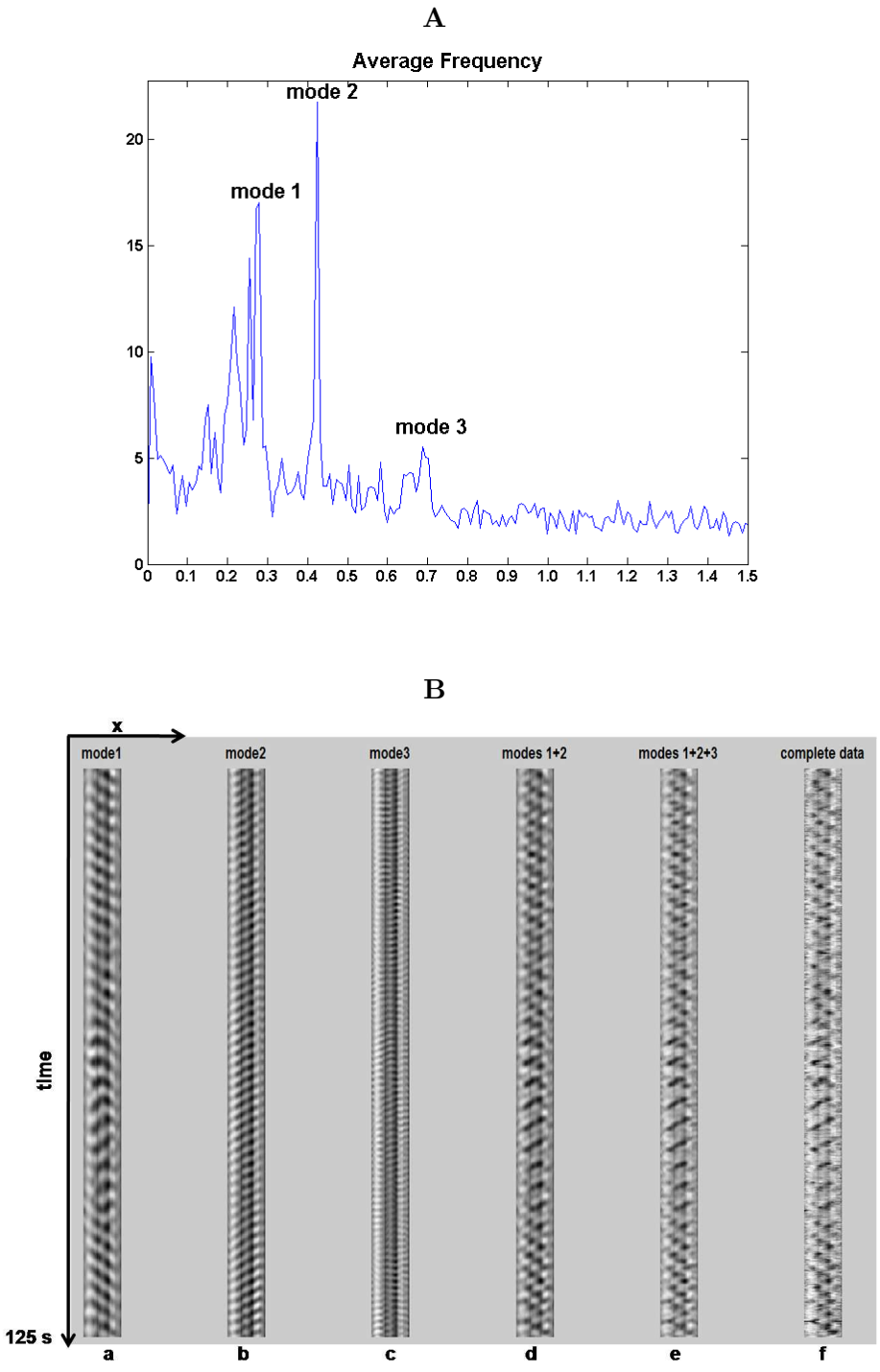

Figure B.5. Fourier analysis of segmental motility: Isoflurane Dataset 3.

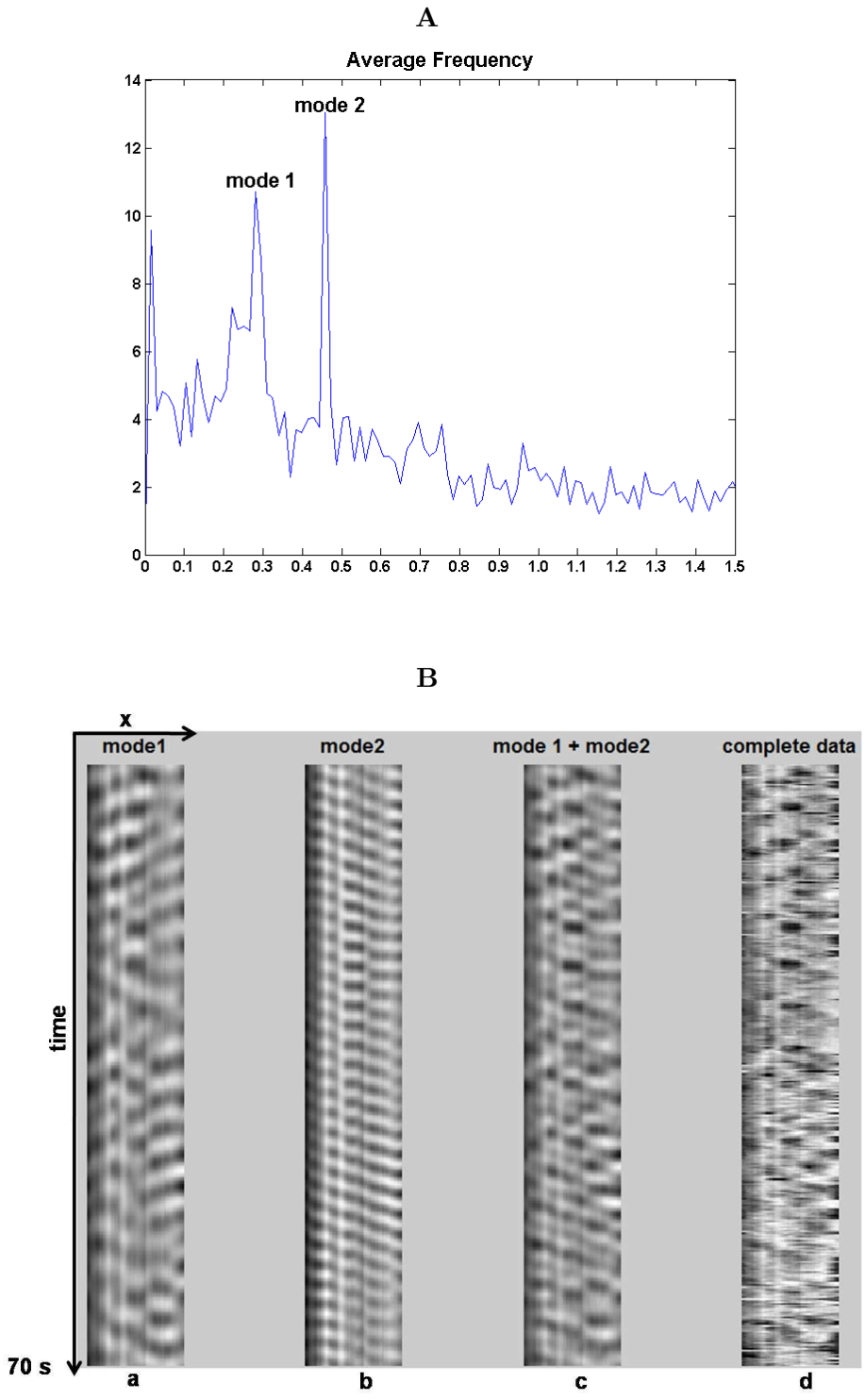

Figure B.6. Fourier analysis of segmental motility: Isoflurane Dataset 4.

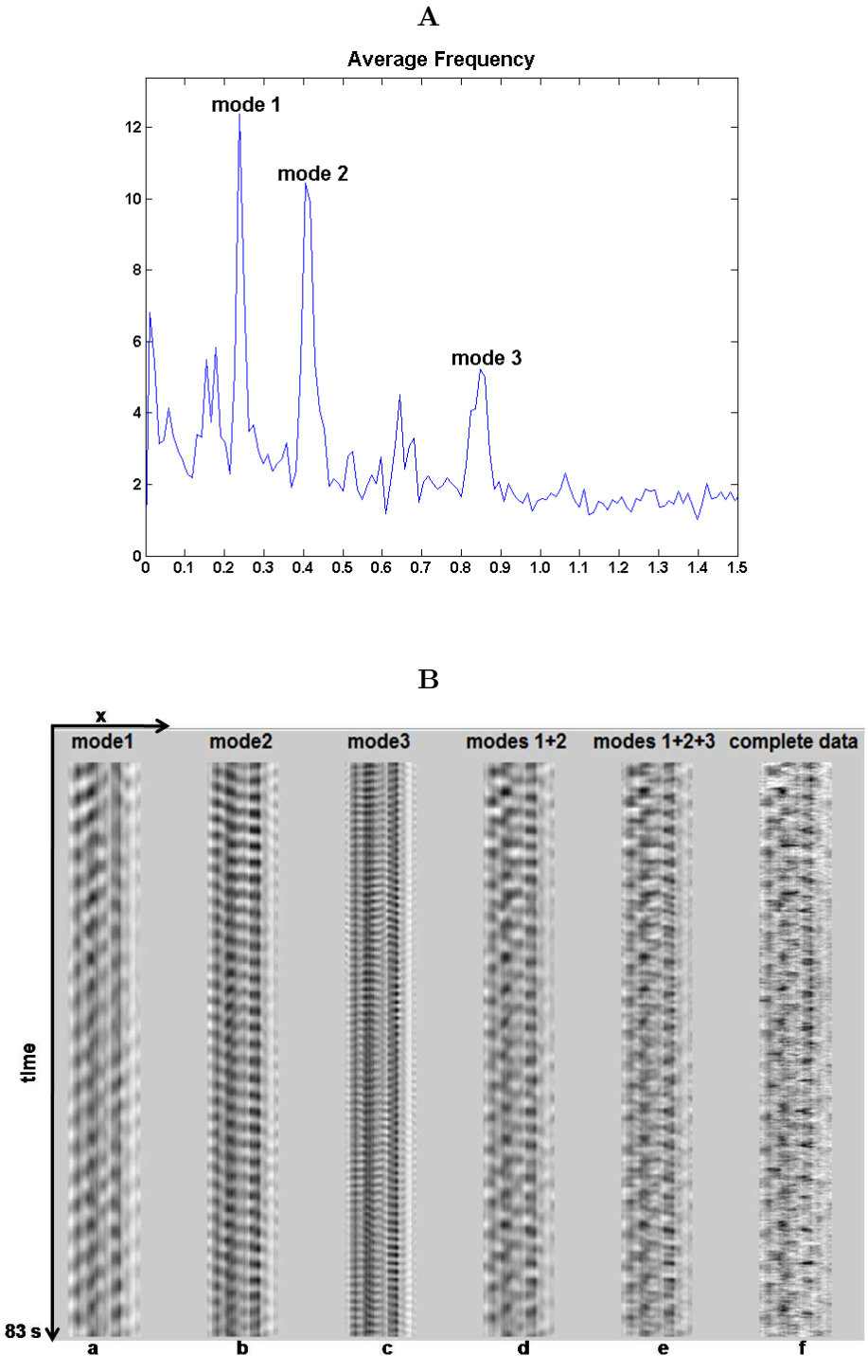

Figure B.7. Fourier analysis of segmental motility: Isoflurane Dataset 5.

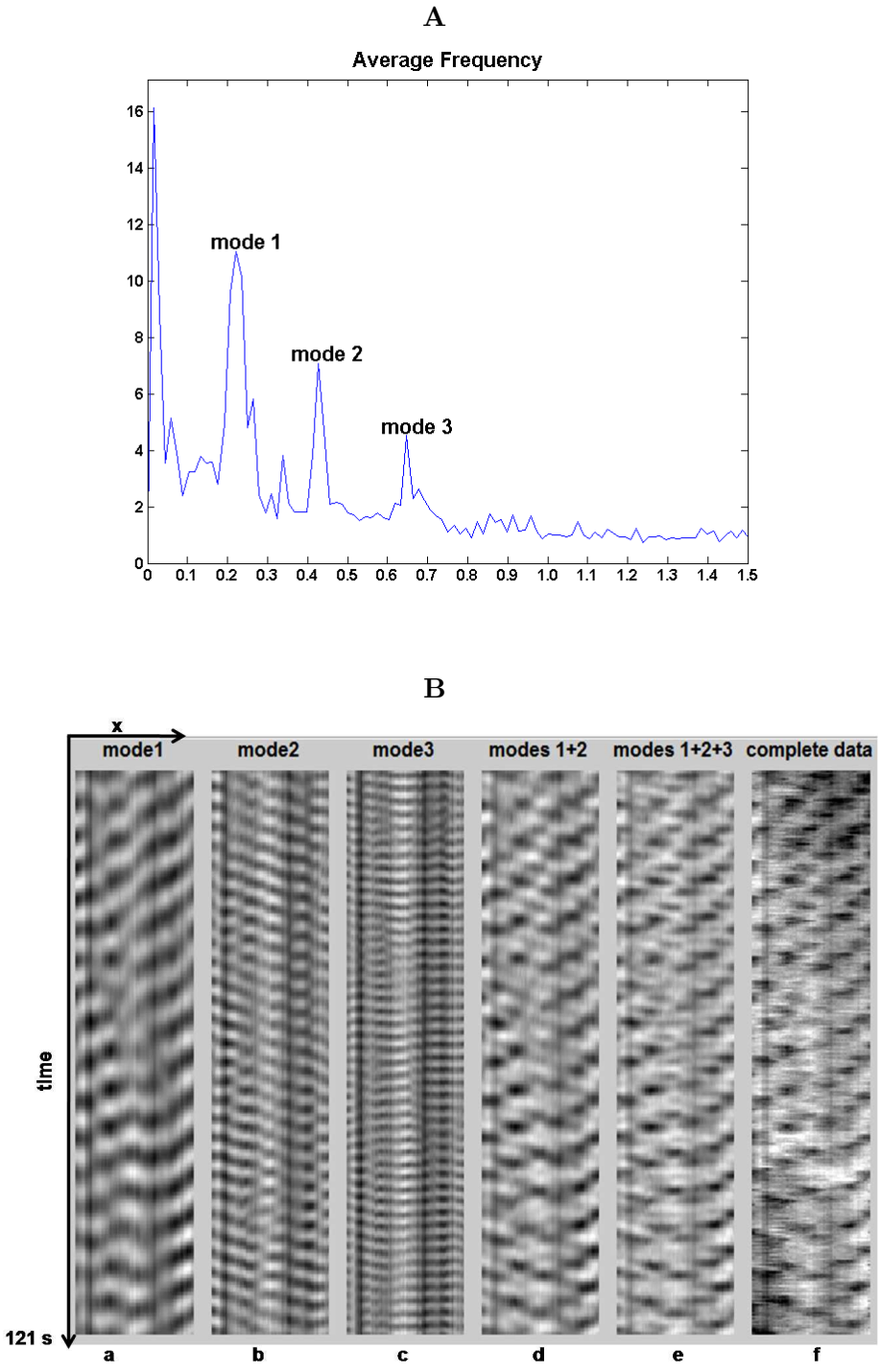

Figure B.8. Fourier analysis of segmental motility: Isoflurane Dataset 6.

Datasets	Mode1 (Hz)
1	0.485
2	0.53
3	0.38
Mean ± SD	0.463 ± 0.076

Table B.3. Frequency modes for peristaltic motion under inactin anesthesia. The values were derived from average frequency response of individual dataset from each animal and then averaged over all the animals (Mean ± SD).

are shown in the bottom row (B). For Figures B.9 and B.10, the reconstructed spatio-temporal maps represent following cases: (a) individual dominant peak (mode1); (b) low frequency components; (c) summation of mode1 and low frequency components (mode1 + low frequency components); and (d) unaltered complete data. The frequency centers were obtained from the average frequency analysis of the corresponding dataset. A third dataset represents a mixed motility pattern, where peristalsis and segmental are observed in the same section of the gut. In this case the peristalsis was short lived and lasted for 13 s (see Figure B.11a). A spatio-temporal map of the dominant mode and complete peristaltic motility is shown in Figures B.11b and c, respectively. The quantitative results of each peristaltic dataset and the average frequency analysis of all the datasets are summarized in Table B.3.

B.2.2 Segmental

The results of each animal (also termed here as dataset) are shown in Figures B.12 to B.19. The average frequency response for the corresponding dataset is shown in the top row (A) and spatio-temporal maps of decomposed modes and other combination of modes are shown in the bottom row (B). For datasets 1, 3, 5 and 6 (see Figures B.12, B.14, B.16 and B.17), the reconstructed spatio-temporal maps represented following cases: (a

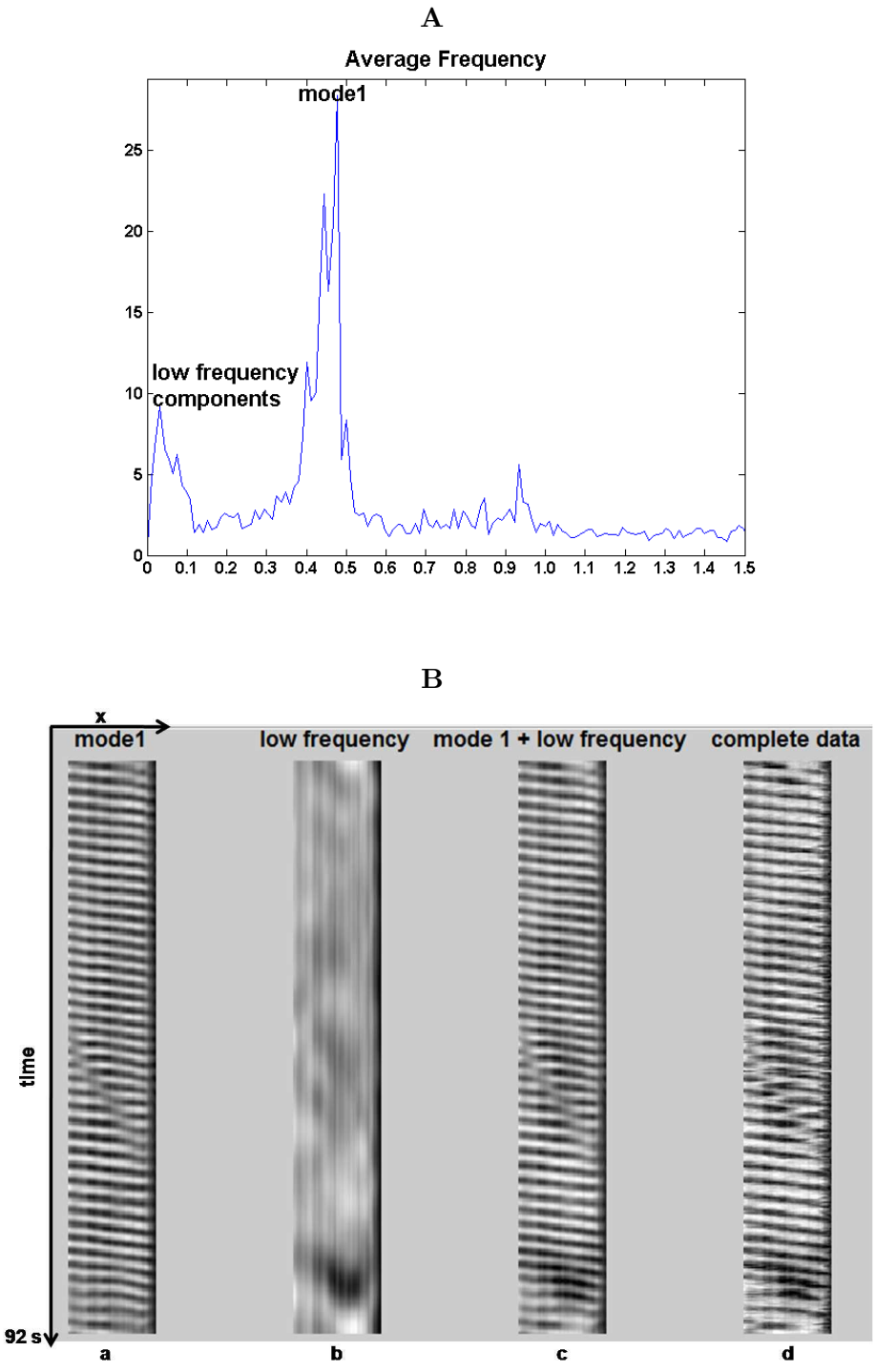

Figure B.9. Fourier analysis of peristaltic motility: Inactin Dataset 1.

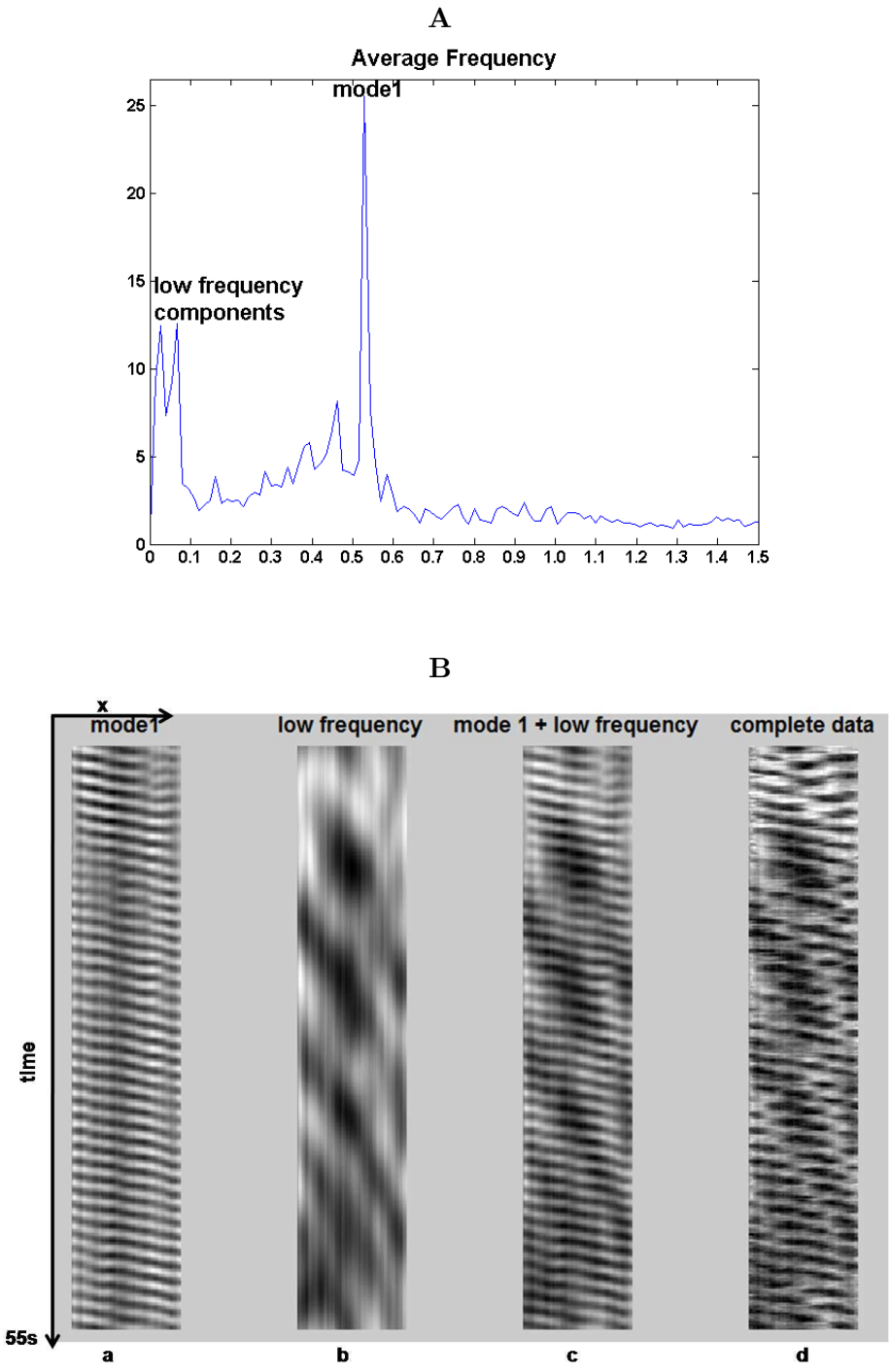

Figure B.10. Fourier analysis of peristaltic motility: Inactin Dataset 2.

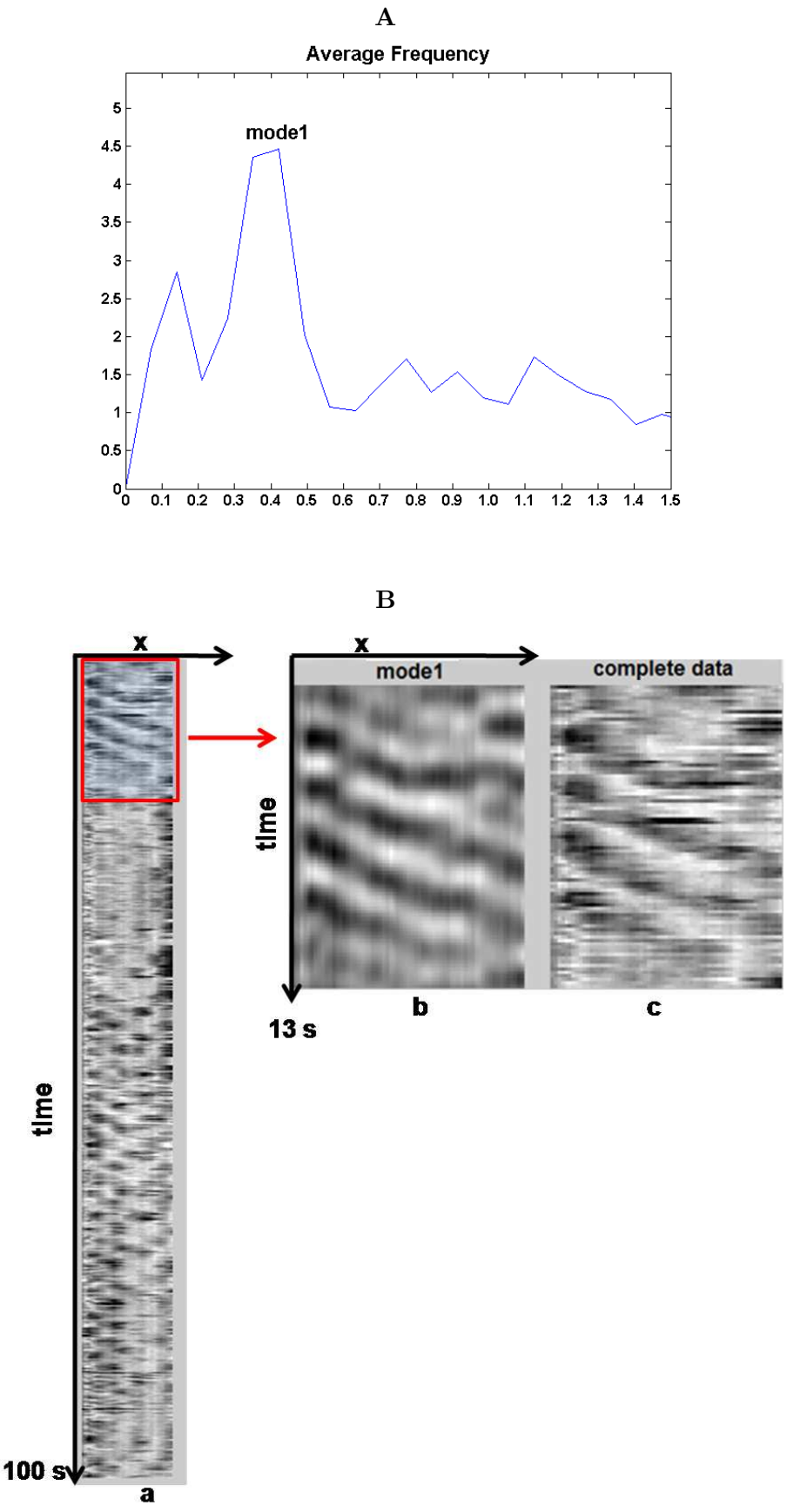

Figure B.11. Fourier analysis of peristaltic motility: Inactin Dataset 3.

Datasets	Mode1 (Hz)	Mode2 (Hz)	Mode3 (Hz)
1	0.45	0.57	1.02
2	0.33	0.56	0.92
3	0.26	0.41	*absent*
4	0.24	0.54	0.8
5	0.43	0.63	1.11
6	0.4	0.47	0.83
7	0.21	0.34	0.60
8	0.25	0.44	0.69
Mean ± SD	0.321 ± 0.095	0.495 ± 0.096	0.853 ± 0.179

Table B.4. Frequency modes for segmental motion under inactin anesthesia. The values were derived from average frequency response of individual dataset from each animal and then averaged over all the animals (Mean ± SD).

to c) individual dominant peaks (mode1, mode2 and mode3); (d) summation of first two peaks (modes 1+2); (e) summation of all three peaks (modes 1+2+3) and (f) unaltered complete data. The frequency centers were obtained from the average frequency analysis of the corresponding dataset. Similarly for datasets 2 and 4 (see Figures B.13 and B.15), the reconstructed spatio-temporal maps represented following cases: (a to b) individual dominant peaks (mode1 and mode2); (c) summation of first two peaks (modes 1+2); and (d) unaltered complete data. The frequency centers were obtained from the average frequency analysis of the corresponding dataset. The quantitative results of each segmental dataset and the average frequency analysis of all the datasets are summarized in Table B.4.

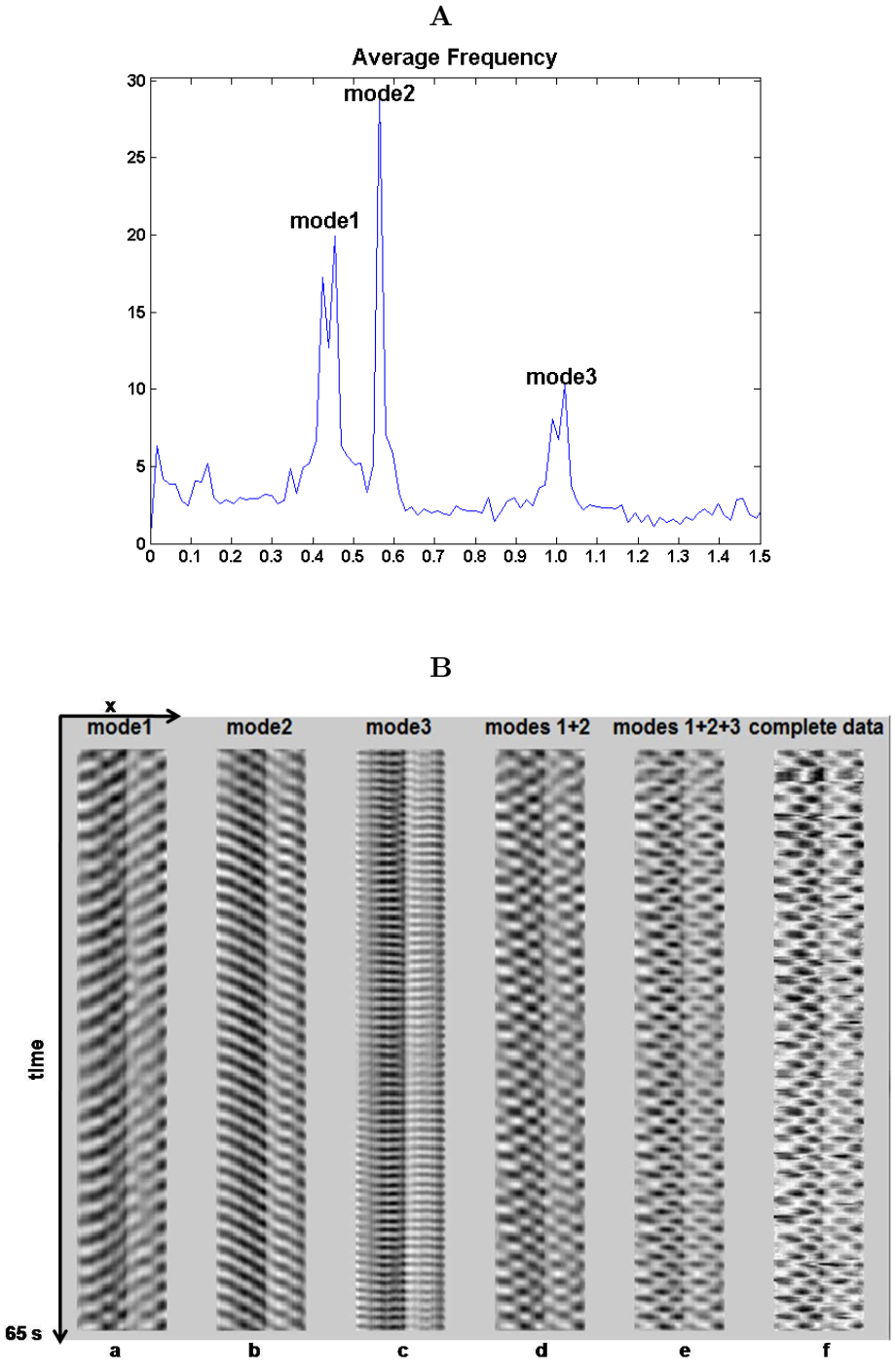

Figure B.12. Fourier analysis of segmental motility: Inactin Dataset 1.

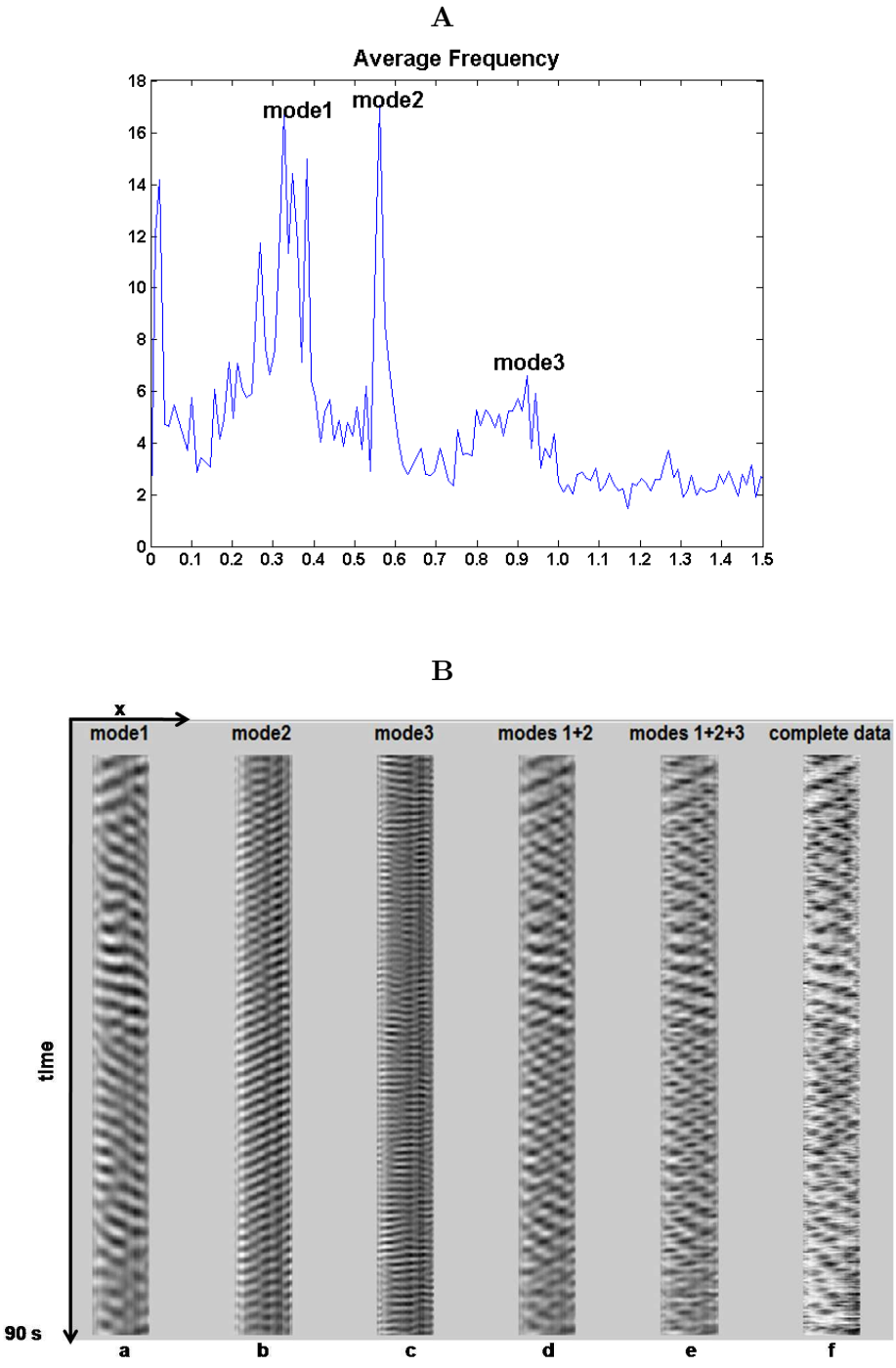

Figure B.13. Fourier analysis of segmental motility: Inactin Dataset 2.

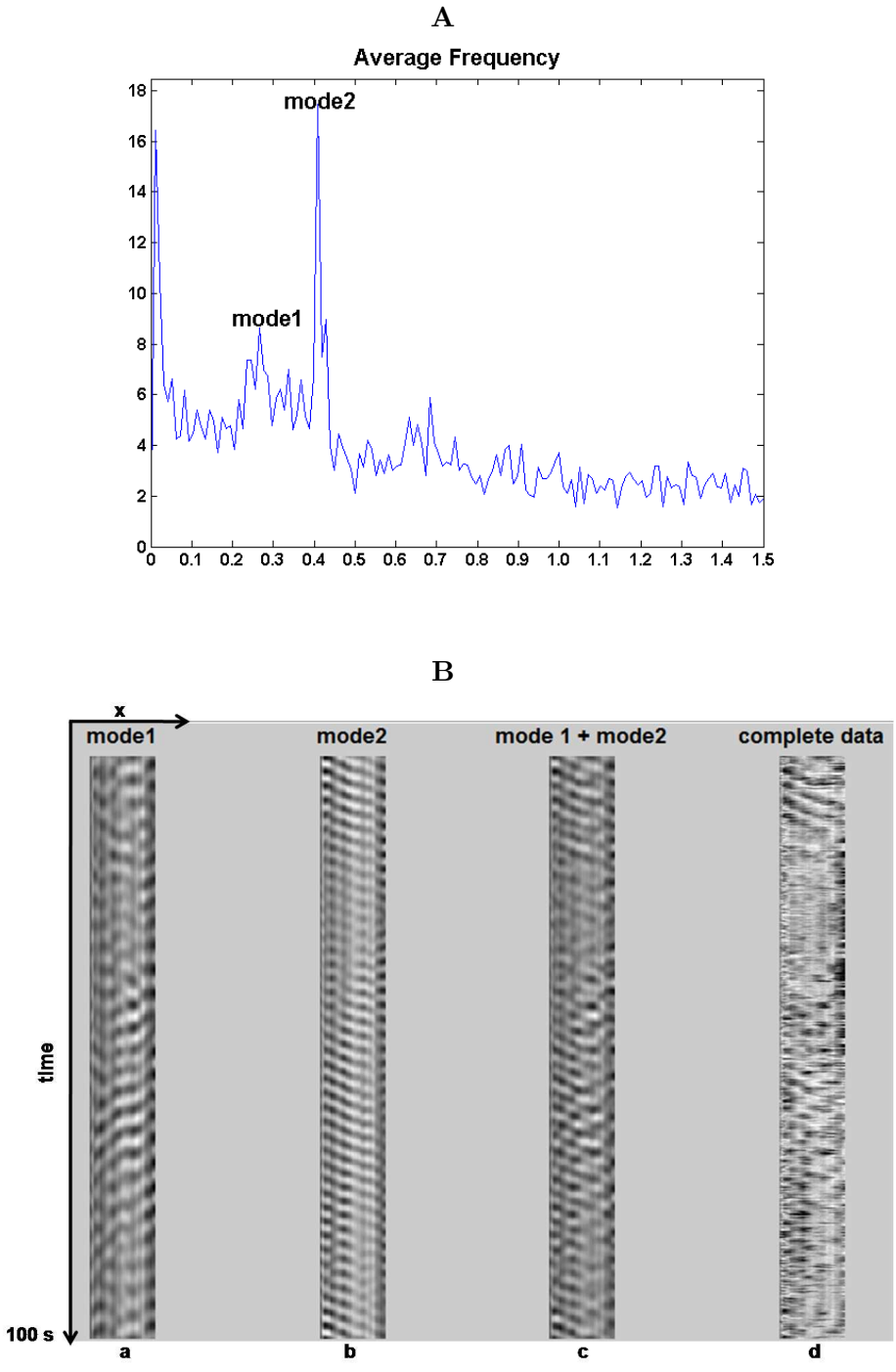

Figure B.14. Fourier analysis of segmental motility: Inactin Dataset 3.

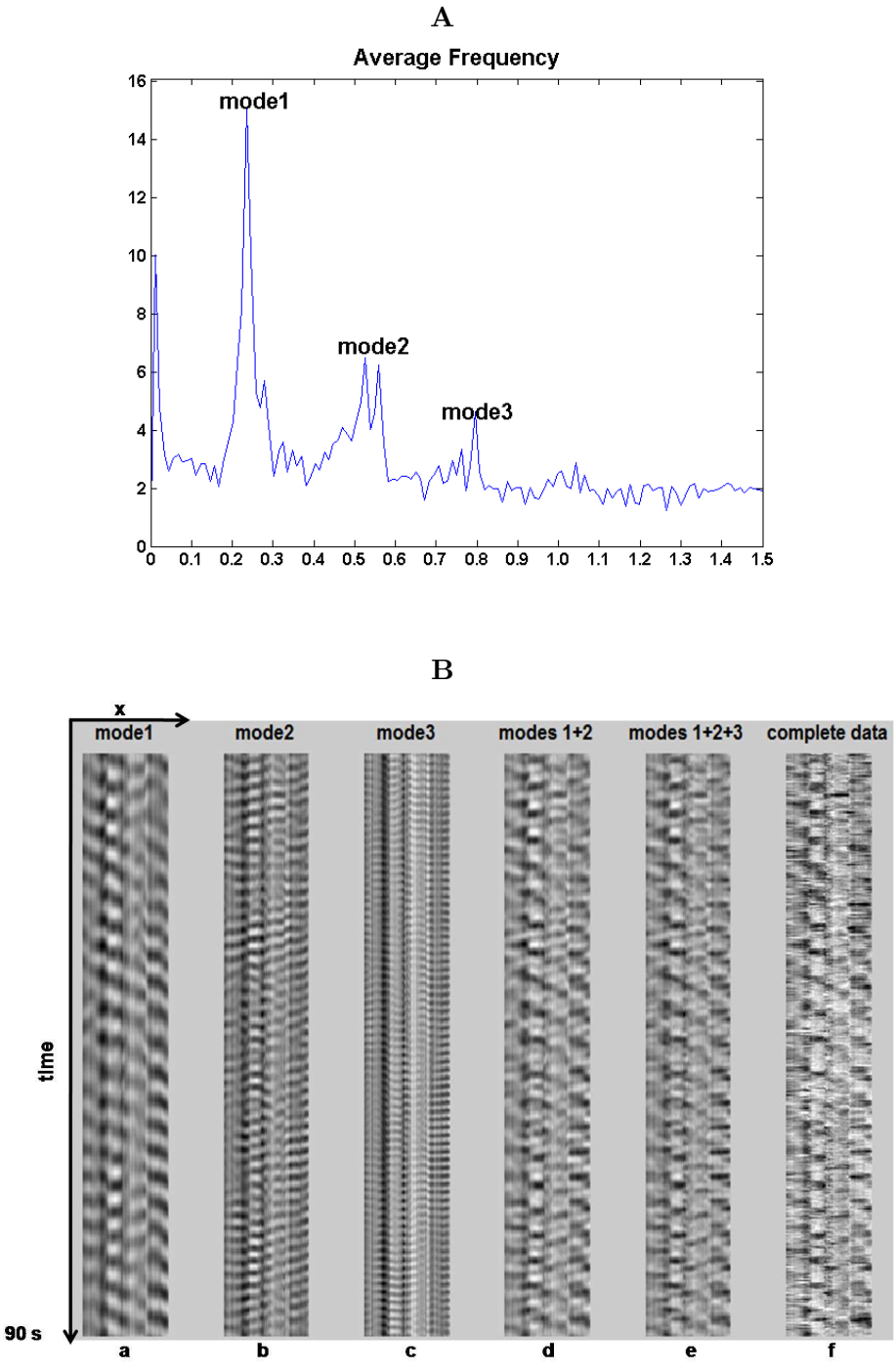

Figure B.15. Fourier analysis of segmental motility: Inactin Dataset 4.

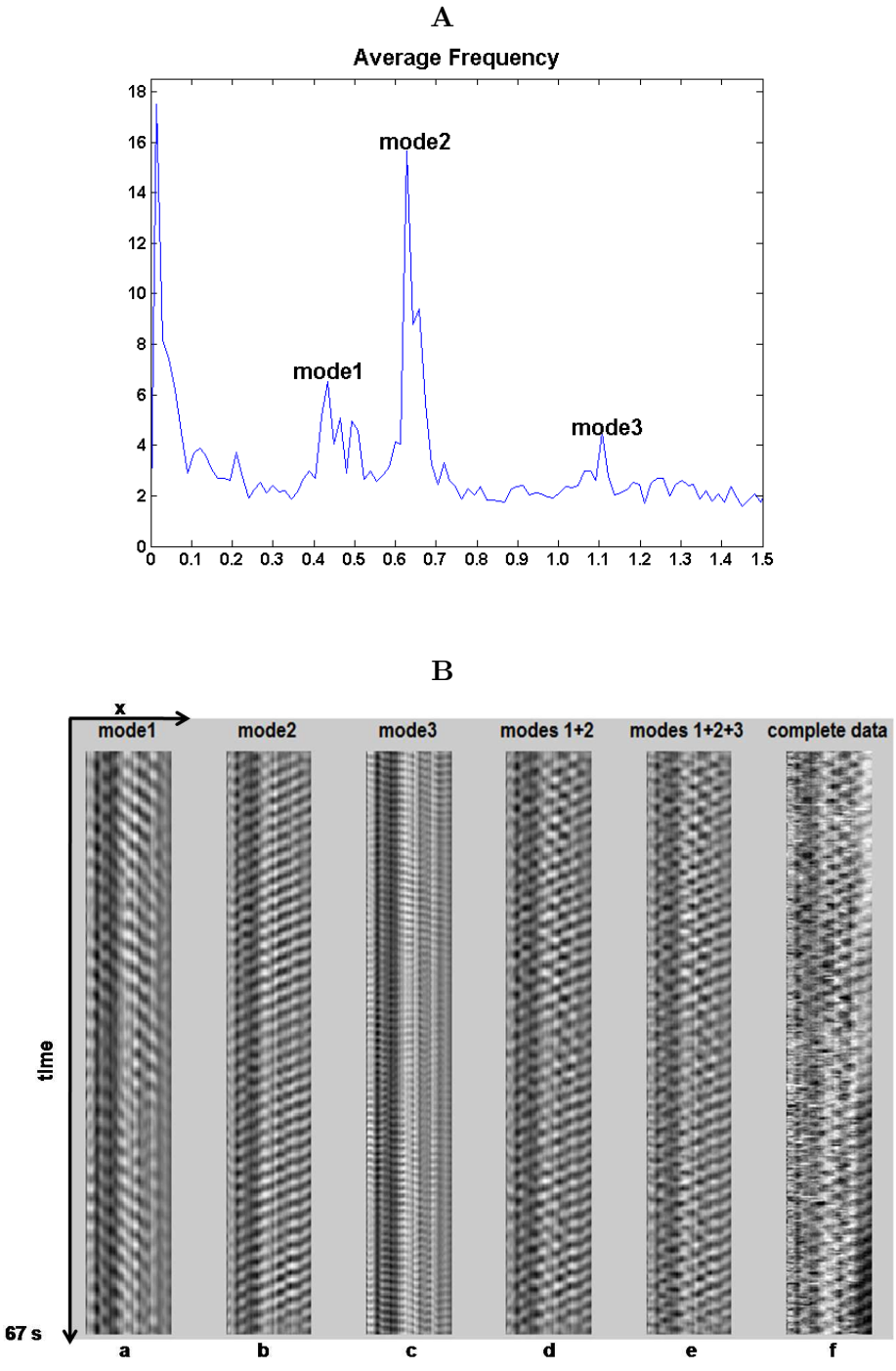

Figure B.16. Fourier analysis of segmental motility: Inactin Dataset 5.

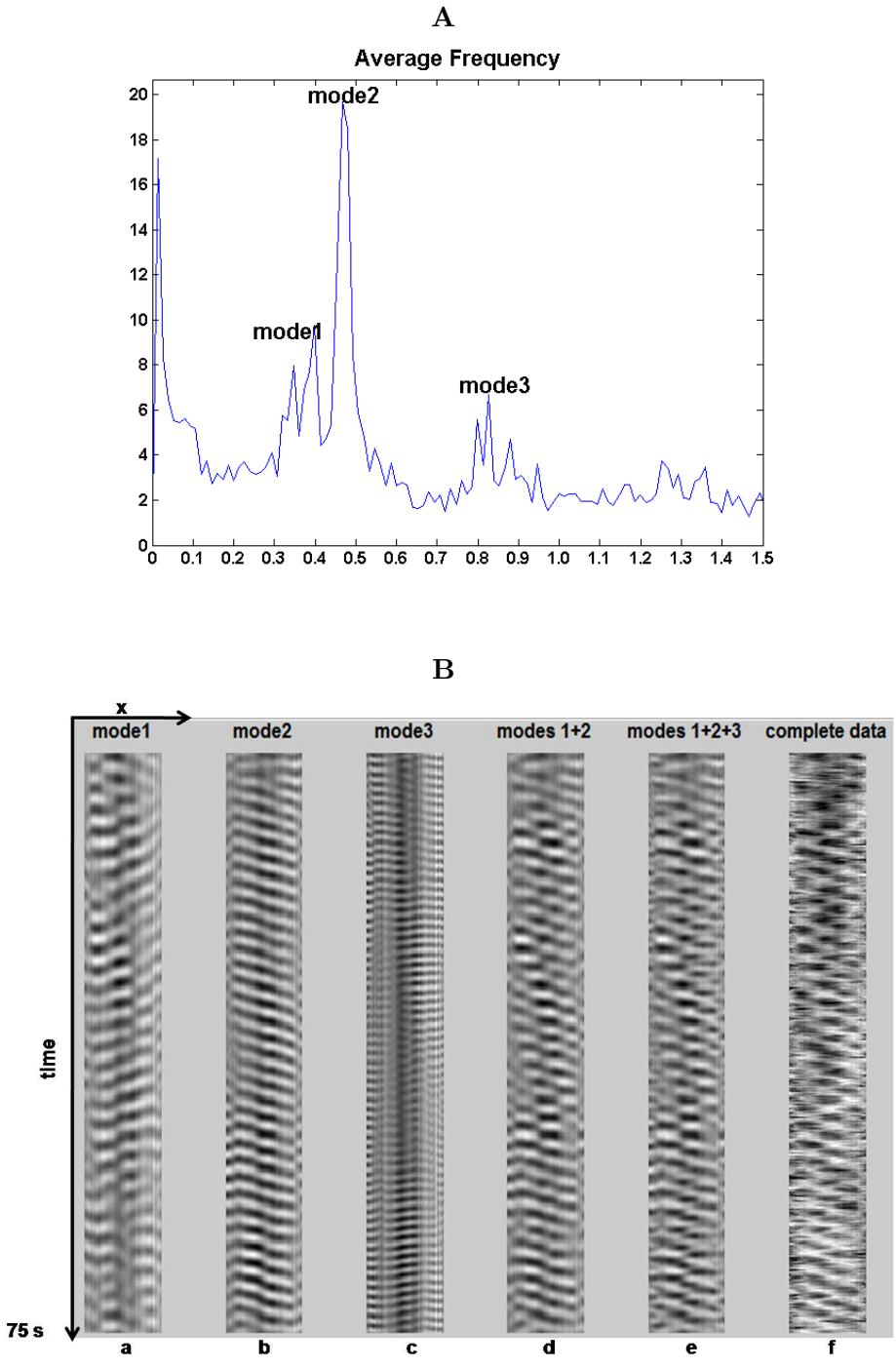

Figure B.17. Fourier analysis of segmental motility: Inactin Dataset 6.

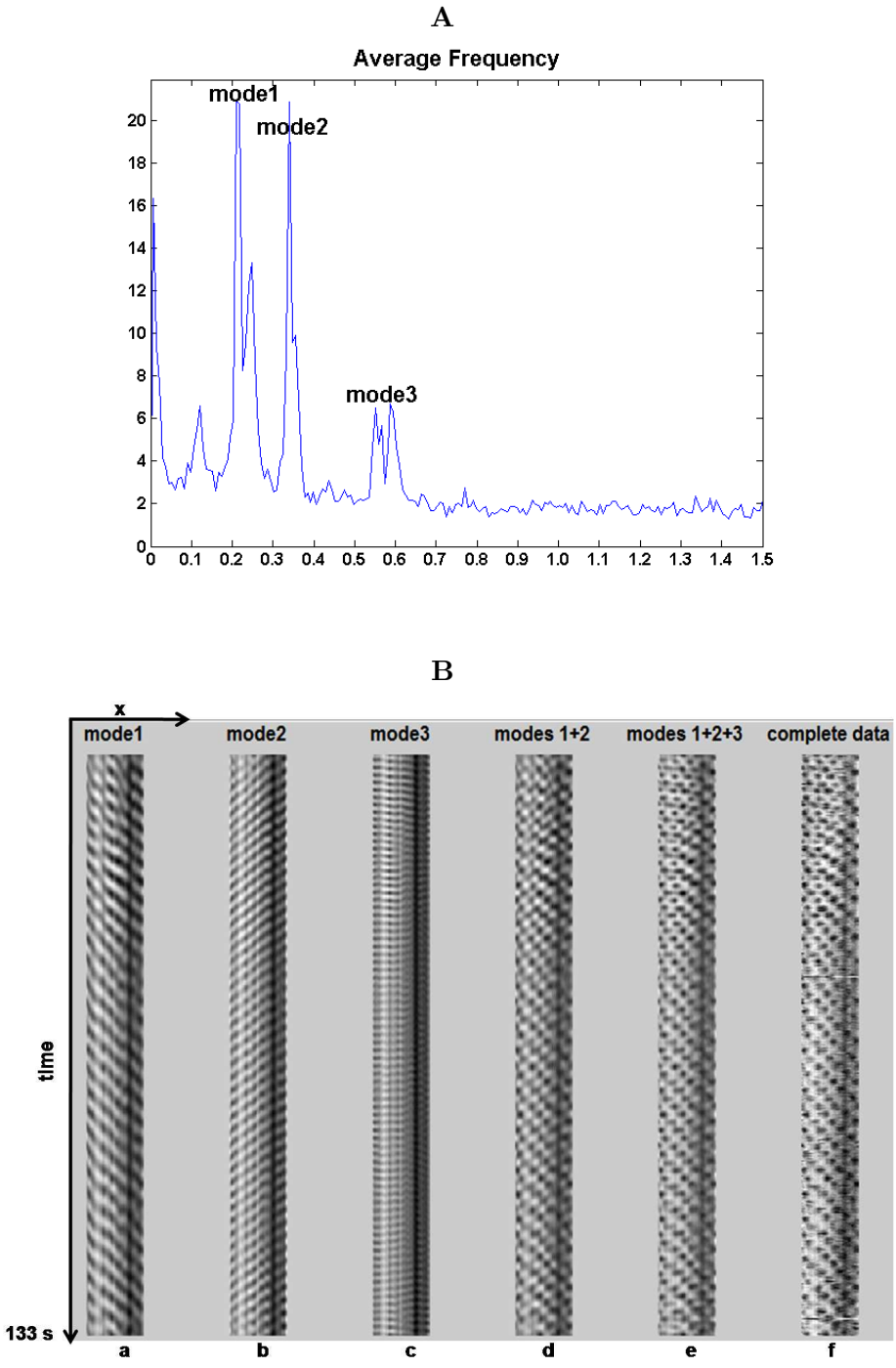

Figure B.18. Fourier analysis of segmental motility: Inactin Dataset 7.

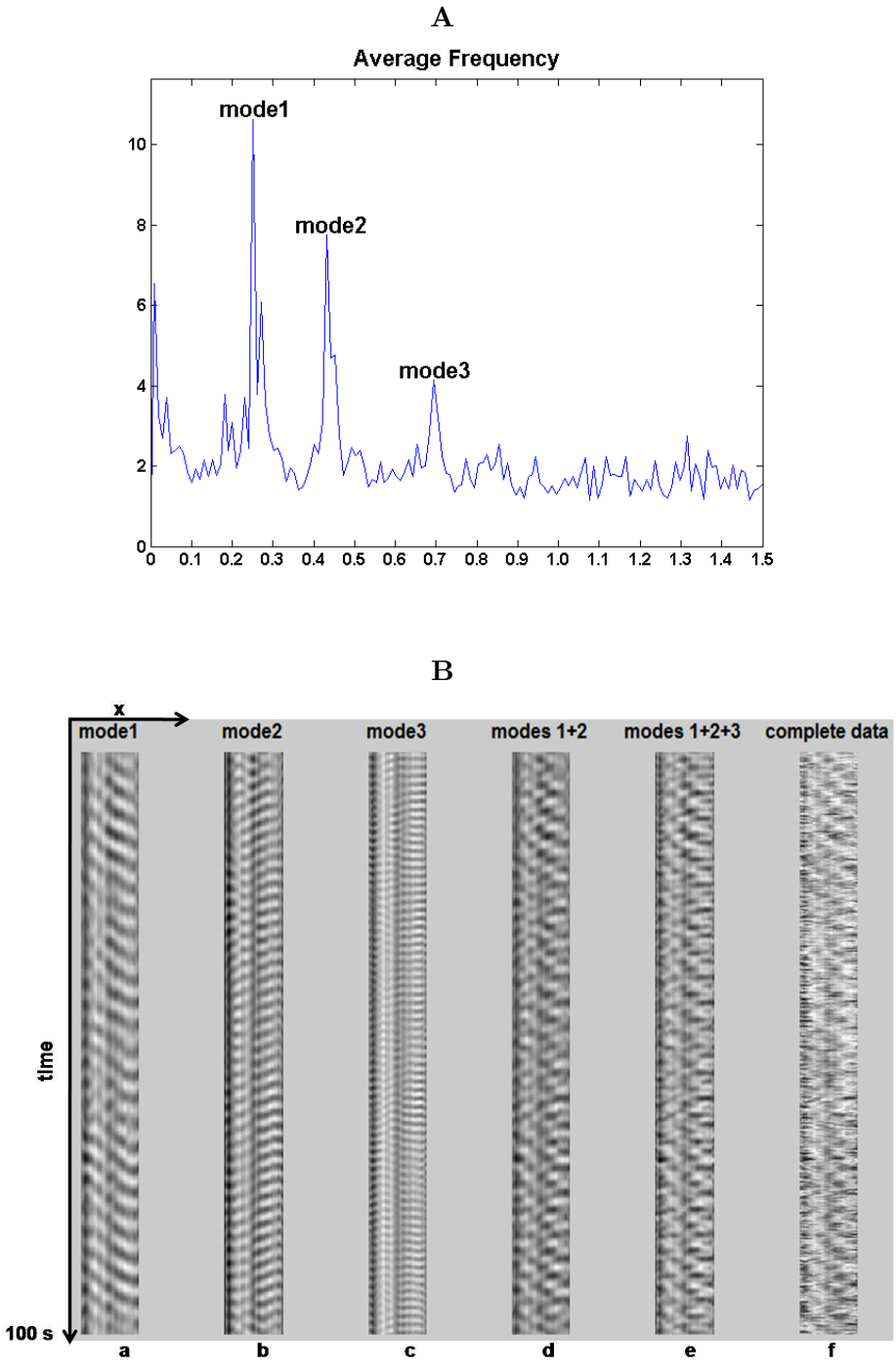

Figure B.19. Fourier analysis of segmental motility: Inactin Dataset 8.

References

[1] E. M. M. Quigley and R. F. Pfeiffer, *Neuro-Gastroenterology.* Butterworth-Heinemann, Elsevier, Inc., 2004.

[2] W. B. Cannon, "Peristalsis, segmentation, and the myenteric reflex," *Am J Physiol.*, vol. 30, pp. 114–128, Apr 1912.

[3] H. J. Ehrlein, M. Schemann, and M. L. Siegle, "Motor patterns of small intestine determined by closely spaced extraluminal transducers and videofluoroscopy," *Am. J. Physiol.*, vol. 253, pp. G259–267, Sep 1987.

[4] I. S. Fox, *Human Physiology.* The McGraw-Hill Companies, Inc., 1999.

[5] R. L. Schiller and M. Feldman, *Gastroenterology and Hepatology: The Comprehensive Visual Reference.* Current Medicine, Inc., 1997.

[6] B. W. Anderson, A. S. Levine, D. G. Levitt, J. M. Kneip, and M. D. Levitt, "Physiological measurement of luminal stirring in perfused rat jejunum," *Am. J. Physiol.*, vol. 254, pp. G843–848, Jun 1988.

[7] A. Malcolm and J. E. Kellow, "Small bowel motility," *Curr. Opin. Gastroenterol.*, vol. 18, pp. 187–191, Mar 2002.

[8] M. K. Herbert, R. Weis, P. Holzer, and N. Roewer, "Peristalsis in the Guinea pig small intestine in vitro is impaired by acetaminophen but not aspirin and dipyrone," *Anesth. Analg.*, vol. 100, pp. 120–127, Jan 2005.

[9] N. Rawal, "Combined regional and general anaesthesia," *Curr Opin Anaesthesiol*, vol. 13, pp. 531–537, Oct 2000.

[10] M. K. Ahlijanian and A. E. Takemori, "Effects of (-)-N6-(R-phenylisopropyl)-adenosine (PIA) and caffeine on nociception and morphine-induced analgesia, tolerance and dependence in mice," *Eur. J. Pharmacol.*, vol. 112, pp. 171–179, Jun 1985.

[11] Y. Mizuta, S. Shikuwa, H. Isomoto, R. Mishima, Y. Akazawa, J. Masuda, K. Omagari, F. Takeshima, and S. Kohno, "Recent insights into digestive motility in functional dyspepsia," *J. Gastroenterol.*, vol. 41, pp. 1025–1040, Nov 2006.

[12] T. Benard, M. Bouchoucha, M. Dupres, and P. H. Cugnenc, "In vitro analysis of rat intestinal wall movements at rest and during propagated contraction: a new method," *Am. J. Physiol.*, vol. 273, pp. G776–784, Oct 1997.

[13] M. Bouchoucha, T. Benard, and M. Dupres, "Temporal and spatial rhythmicity of jejunal wall motion in rats," *Neurogastroenterol. Motil.*, vol. 11, pp. 339–346, Oct 1999.

[14] R. M. Gwynne and J. C. Bornstein, "Mechanisms underlying nutrient-induced segmentation in isolated guinea pig small intestine," *Am. J. Physiol. Gastrointest. Liver Physiol.*, vol. 292, pp. G1162–1172, Apr 2007.

[15] R. M. Gwynne, E. A. Thomas, S. M. Goh, H. Sjvall, and J. C. Bornstein, "Segmentation induced by intraluminal fatty acid in isolated guinea-pig duodenum and jejunum," *J. Physiol. (Lond.)*, vol. 556, pp. 557–569, Apr 2004.

[16] G. W. Hennig, M. Costa, B. N. Chen, and S. J. Brookes, "Quantitative analysis of peristalsis in the guinea-pig small intestine using spatio-temporal maps," *J. Physiol. (Lond.)*, vol. 517 (Pt 2), pp. 575–590, Jun 1999.

[17] D. M. Ferens, E. C. Chang, G. Bogeski, A. D. Shafton, P. D. Kitchener, and J. B. Furness, "Motor patterns and propulsion in the rat intestine in vivo recorded by spatio-temporal maps," *Neurogastroenterol. Motil.*, vol. 17, pp. 714–720, Oct 2005.

[18] G. Bogeski, A. D. Shafton, P. D. Kitchener, D. M. Ferens, and J. B. Furness, "A quantitative approach to recording peristaltic activity from segments of rat small intestine in vivo," *Neurogastroenterol. Motil.*, vol. 17, pp. 262–272, Apr 2005.

[19] J. Schnoor, S. Bartz, B. Klosterhalfen, W. Kuepper, R. Rossaint, and J. K. Unger, "A long-term porcine model for measurement of gastrointestinal motility," *Lab. Anim.*, vol. 37, pp. 145–154, Apr 2003.

[20] A. Huge, M. E. Kreis, E. C. Jehle, H. J. Ehrlein, M. Starlinger, H. D. Becker, and T. T. Zittel, "A model to investigate postoperative ileus with strain gauge transducers in awake rats," *J. Surg. Res.*, vol. 74, pp. 112–118, Feb 1998.

[21] H. J. Ehrlein, "A new technique for simultaneous radiography and recording of gastrointestinal motility in unanesthetized dogs," *Lab. Anim. Sci.*, vol. 30, pp. 879–884, Oct 1980.

[22] A. Webb, *Introduction to biomedical imaging*. John Wiley and Sons, 2003.

[23] J. M. Froehlich, M. A. Patak, C. von Weymarn, C. F. Juli, C. L. Zollikofer, and K. U. Wentz, "Small bowel motility assessment with magnetic resonance imaging," *J Magn Reson Imaging*, vol. 21, pp. 370–375, Apr 2005.

[24] J. B. Frkjaer, E. Larsen, E. Steffensen, A. H. Nielsen, and A. M. Drewes, "Magnetic resonance imaging of the small bowel in Crohn's disease," *Scand. J. Gastroenterol.*, vol. 40, pp. 832–842, Jul 2005.

[25] D. R. Martin, T. Lauenstein, and S. V. Sitaraman, "Utility of magnetic resonance imaging in small bowel Crohn's disease," *Gastroenterology*, vol. 133, pp. 385–390, Aug 2007.

[26] V. A. Pupillo, E. Di Cesare, G. Frieri, N. Limbucci, M. Tanga, and C. Masciocchi, "Assessment of inflammatory activity in Crohn's disease by means of dynamic contrast-enhanced MRI," *Radiol Med*, vol. 112, pp. 798–809, Sep 2007.

[27] C. L. Hoad, L. Marciani, S. Foley, J. J. Totman, J. Wright, D. Bush, E. F. Cox, E. Campbell, R. C. Spiller, and P. A. Gowland, "Non-invasive quantification of small bowel water content by MRI: a validation study," *Phys Med Biol*, vol. 52, pp. 6909–6922, Dec 2007.

[28] A. Laghi, P. Paolantonio, F. Iafrate, O. Borrelli, L. Dito, E. Tomei, S. Cucchiara, and R. Passariello, "MR of the small bowel with a biphasic oral contrast agent (polyethylene glycol): technical aspects and findings in patients affected by Crohn's disease," *Radiol Med*, vol. 106, pp. 18–27, 2003.

[29] A. Laghi, P. Paolantonio, F. Iafrate, F. Altomari, C. Miglio, and R. Passariello, "Oral contrast agents for magnetic resonance imaging of the bowel," *Top Magn Reson Imaging*, vol. 13, pp. 389–396, Dec 2002.

[30] A. S. Borthne, M. Abdelnoor, J. C. Hellund, J. T. Geitung, T. Storaas, K. I. Gjesdal, and N. E. Klw, "MR imaging of the small bowel with increasing concentrations of an oral osmotic agent," *Eur Radiol*, vol. 15, pp. 666–671, Apr 2005.

[31] A. S. Borthne, M. Abdelnoor, J. Rugtveit, G. Perminow, T. Reiseter, and N. E. Klw, "Bowel magnetic resonance imaging of pediatric patients with oral mannitol MRI compared to endoscopy and intestinal ultrasound," *Eur Radiol*, vol. 16, pp. 207–214, Jan 2006.

[32] W. Ajaj, S. C. Goehde, H. Schneemann, S. G. Ruehm, J. F. Debatin, and T. C. Lauenstein, "Oral contrast agents for small bowel MRI: comparison of different additives to optimize bowel distension," *Eur Radiol*, vol. 14, pp. 458–464, Mar 2004.

[33] G. E. Wesbey, R. C. Brasch, B. L. Engelstad, A. A. Moss, L. E. Crooks, and A. C. Brito, "Nuclear magnetic resonance contrast enhancement study of the gastrointestinal tract of rats and a human volunteer using nontoxic oral iron solutions," *Radiology*, vol. 149, pp. 175–180, Oct 1983.

[34] P. Saha, B. Chanda, and D. Dutta Majumder, "A single scan boundary removal thinning algorithm for 2-d binary object," *Pattern Recognition Letters*, vol. 14, no. 3, pp. 173 – 9, 1993/03/.

[35] A. P. Kiraly, J. P. Helferty, E. A. Hoffman, G. McLennan, and W. E. Higgins, "Three-dimensional path planning for virtual bronchoscopy," *IEEE Trans Med Imaging*, vol. 23, pp. 1365–1379, Nov 2004.

[36] A. Pal, K. Indireshkumar, W. Schwizer, B. Abrahamsson, M. Fried, and J. G. Brasseur, "Gastric flow and mixing studied using computer simulation," *Proc. Biol. Sci.*, vol. 271, pp. 2587–2594, Dec 2004.

[37] A. Pal, J. G. Brasseur, and B. Abrahamsson, "A stomach road or "Magenstrasse" for gastric emptying," *J Biomech*, vol. 40, pp. 1202–1210, 2007.

[38] K. Schulze, "Imaging and modelling of digestion in the stomach and the duodenum," *Neurogastroenterol. Motil.*, vol. 18, pp. 172–183, Mar 2006.

[39] J. M. DeSesso and C. F. Jacobson, "Anatomical and physiological parameters affecting gastrointestinal absorption in humans and rats," *Food Chem. Toxicol.*, vol. 39, pp. 209–228, Mar 2001.

[40] F. H. Netter, *The Netter Collection of Medical Illustrations, Digestive System Part II; Lower Digestive Tract.* Colorpress. New York, NY, 1962.

[41] W. Snyder and M. Cook, *Report on the Task Group on Reference Man. International Commission on Radiological Protection.* Pergamon, New York, 1975.

[42] R. Hebel and W. Stromberg, *Anatomy and embryology of the laboratory rat.* Worthsee, Germany, 1985.

[43] D. Granger, J. Barrowman, and P. Kvietys, *Clinical Gastrointestinal Physiology.* W. B. Saunders, Philadelphia, 1985.

[44] C. S. Marcus and F. W. Lengemann, "Use of radioyttrium to study food movement in the small intestine of the rat," *J. Nutr.*, vol. 76, pp. 179–182, Feb 1962.

[45] K. E. Barrett, *Gastrointestinal Physiology.* Lange Medical Books.McGraw-Hill., 2006.

[46] W. O. Abbott and E. P. Pendergrass, "Intubation studies of the human small intestine, V. The motor effects of single clinical doses of morphine sulphate in normal subjects," *Am. J. Roentgenol.*, vol. 35, p. 289, 1936.

[47] W. M. "Bayliss and E. H. . Starling, "The movements and innervation of the small intestine," *J. Physiol. (Lond.)*, vol. 24, pp. 99–143, May 1899.

[48] W. M. "Bayliss, "The movements and innervation of the small intestine," *J. Physiol. (Lond.)*, vol. 26, pp. 125–138, Feb 1901.

[49] W. Cannon, "The Movements of the intestines studied by means of the Rntgen Rays," *The American Journal of Physiology*, vol. 6, pp. 251–277, 1902.

[50] A. Strocchi and M. D. Levitt, "A reappraisal of the magnitude and implications of the intestinal unstirred layer," *Gastroenterology*, vol. 101, pp. 843–847, Sep 1991.

[51] F. A. Wilson and J. M. Dietschy, "Characterization of bile acid absorption across the unstirred water layer and brush border of the rat jejunum," *J. Clin. Invest.*, vol. 51, pp. 3015–3025, Dec 1972.

[52] V. L. Sallee and J. M. Dietschy, "Determinants of intestinal mucosal uptake of short- and medium-chain fatty acids and alcohols," *J. Lipid Res.*, vol. 14, pp. 475–484, Jul 1973.

[53] B. Borgstrom, A. Dahlqvist, G. Lundh, and J. Sjovall, "Studies of intestinal digestion and absorption in the human," *J. Clin. Invest.*, vol. 36, pp. 1521–1536, Oct 1957.

[54] H. Shay, C. J. Gershon, S. Fels, L. Munro, and H. Siplet, "The absrption and dilution of glucose solutions in the human stomach and duodenum," *Am. J. Dig. Dis.*, vol. 36, pp. 535–544, 1939-1940.

[55] M. D. Levitt, J. K. Furne, A. Strocchi, B. W. Anderson, and D. G. Levitt, "Physiological measurements of luminal stirring in the dog and human small bowel," *J. Clin. Invest.*, vol. 86, pp. 1540–1547, Nov 1990.

[56] W. J. Lammers, A. M. Lammers-van den Berg, J. F. Morrison, G. A. Petroianu, and P. Trendelenburg, "Translating Trendelenburg; back to the future," *Naunyn Schmiedebergs Arch. Pharmacol.*, vol. 373, pp. 134–138, May 2006.

[57] K. Schulze-Delrieu, "Intrinsic differences in the filling response of the guinea pig duodenum and ileum," *J. Lab. Clin. Med.*, vol. 117, pp. 44–50, Jan 1991.

[58] Schulze., "Visual parameters define the phase and the load of contractions in isolated guinea pig ileum," *Am. J. Physiol.*, vol. 276, pp. G1417–1424, Jun 1999.

[59] G. W. Hennig, M. Costa, B. N. Chen, and S. J. Brookes, "Quantitative analysis of peristalsis in the guinea-pig small intestine using spatio-temporal maps," *J. Physiol. (Lond.)*, vol. 517 (Pt 2), pp. 575–590, Jun 1999.

[60] F. J. Ingelfinger and W. O. Abbott, "Intubation studies of the human small intestine, XX. The diagnostic significance of motor disturbances." *Am. J. Digest. Dis.*, vol. 7, pp. 468–474, Nov 1940.

[61] H. J. Ehrlein and E. Hiesinger, "Computer analysis of mechanical activity of gastroduodenal junction in unanaesthetized dogs," *Q J Exp Physiol*, vol. 67, pp. 17–29, Jan 1982.

[62] M. A. Patak, J. M. Froehlich, C. von Weymarn, M. A. Ritz, C. L. Zollikofer, and K. Wentz, "Non-invasive distension of the small bowel for magnetic-resonance imaging," *Lancet*, vol. 358, pp. 987–988, Sep 2001.

[63] M. Iida, M. Ikeda, M. Kishimoto, T. Tsujino, H. Kaneto, M. Matsuhisa, Y. Kajimoto, T. Watarai, Y. Yamasaki, and M. Hori, "Evaluation of gut motility in type II diabetes by the radiopaque marker method," *J. Gastroenterol. Hepatol.*, vol. 15, pp. 381–385, Apr 2000.

[64] P. Gimondo, A. La Bella, P. Mirk, and A. Torsoli, "Duplex-Doppler evaluation of intestinal peristalsis in patients with bowel obstruction," *Abdom Imaging*, vol. 20, pp. 33–36, 1995.

[65] Y. J. An, H. Lee, D. Chang, Y. Lee, J. K. Sung, M. Choi, and J. Yoon, "Application of pulsed Doppler ultrasound for the evaluation of small intestinal motility in dogs," *J. Vet. Sci.*, vol. 2, pp. 71–74, Apr 2001.

[66] T. C. Lauenstein, H. Schneemann, F. M. Vogt, C. U. Herborn, S. G. Ruhm, and J. F. Debatin, "Optimization of oral contrast agents for MR imaging of the small bowel," *Radiology*, vol. 228, pp. 279–283, Jul 2003.

[67] W. Schwizer, R. Fraser, J. Borovicka, G. Crelier, P. Boesiger, and M. Fried, "Measurement of gastric emptying and gastric motility by magnetic resonance imaging (MRI)," *Dig. Dis. Sci.*, vol. 39, pp. 101S–103S, Dec 1994.

[68] A. Laghi, P. Paolantonio, and R. Passariello, "Small bowel," *Magn Reson Imaging Clin N Am*, vol. 13, pp. 331–348, May 2005.

[69] J. Borovicka, R. Lehmann, P. Kunz, R. Fraser, C. Kreiss, G. Crelier, P. Boesiger, G. A. Spinas, M. Fried, and W. Schwizer, "Evaluation of gastric emptying and motility in diabetic gastroparesis with magnetic resonance imaging: effects of cisapride," *Am. J. Gastroenterol.*, vol. 94, pp. 2866–2873, Oct 1999.

[70] R. F. Thoeni and R. G. Gould, "Enteroclysis and small bowel series: comparison of radiation dose and examination time," *Radiology*, vol. 178, pp. 659–662, Mar 1991.

[71] J. B. Kneeland and J. S. Hyde, "High-resolution MR imaging with local coils," *Radiology*, vol. 171, pp. 1–7, Apr 1989.

[72] P. Lauterbur, "Image formation by induced local interactions: Examples employing nuclear magnetic resonance," *Nature*, vol. 242, pp. 190–191, March 1973.

[73] D. L. Pham, C. Xu, and J. L. Prince, "Current methods in medical image segmentation," *Annu Rev Biomed Eng*, vol. 2, pp. 315–337, 2000.

[74] W. E. Higgins, N. Chung, and E. L. Ritman, "Extraction of left-ventricular chamber from 3-D CT images of the heart," *IEEE Trans Med Imaging*, vol. 9, pp. 384–395, 1990.

[75] W. E. "Higgins, N. Chung, and E. L. . Ritman, "LV chamber extraction from 3-D CT images–accuracy and precision," *Comput Med Imaging Graph*, vol. 16, pp. 17–26, 1992.

[76] L. Lemieux, G. Hagemann, K. Krakow, and F. G. Woermann, "Fast, accurate, and reproducible automatic segmentation of the brain in T1-weighted volume MRI data," *Magn Reson Med*, vol. 42, pp. 127–135, Jul 1999.

[77] L. Liang, K. Rehm, R. P. Woods, and D. A. Rottenberg, "Automatic segmentation of left and right cerebral hemispheres from MRI brain volumes using the graph cuts algorithm," *Neuroimage*, vol. 34, pp. 1160–1170, Feb 2007.

[78] A. Souza, J. K. Udupa, G. Grevera, Y. Sun, D. Odhner, N. Suri, and M. D. Schnall, "Iterative live wire and live snake: new user-steered 3d image segmentation paradigms," vol. 6144, no. 1. SPIE, 2006, p. 61443N.

[79] M. Kass, A. Witkin, and D. Terzopoulos, "Snakes: active contour models," *International Journal of Computer Vision*, vol. 1, no. 4, pp. 321 – 31, 1987//.

[80] T. Cootes, A. Hill, C. Taylor, and J. Haslam, "Use of active shape models for locating structures in medical images," *Image and Vision Computing*, vol. 12, no. 6, pp. 355 – 65, 1994/07/.

[81] E. N. Mortensen and W. A. Barrett, "Interactive segmentation with intelligent scissors," *Graphical Models and Image Processing*, vol. 60, no. 5, pp. 349 – 384, 1998.

[82] A. Falcao, J. Udupa, S. Samarasekera, S. Sharma, B. Hirsch, and R. de a Lotufo, "User-steered image segmentation paradigms: live wire and live lane," *Graphical Models and Image Processing*, vol. 60, no. 4, pp. 233 – 60, 1998/07/.

[83] A. X. Falco and J. K. Udupa, "A 3D generalization of user-steered live-wire segmentation," *Med Image Anal*, vol. 4, pp. 389–402, Dec 2000.

[84] G. Hamarneh, J. Yang, C. McIntosh, and M. Langille, "3d live-wire-based semi-automatic segmentation of medical images," vol. 5747, no. 1, USA, 2005//, pp. 1597 – 603.

[85] C. Xu and J. L. Prince, "Generalized gradient vector flow external forces for active contours," *Signal Processing*, vol. 71, no. 2, pp. 131 – 139, 1998.

[86] C. "Xu and J. L. . Prince, "Snakes, shapes, and gradient vector flow," *IEEE Trans Image Process*, vol. 7, pp. 359–369, 1998.

[87] J. Cheng and S. W. Foo, "Dynamic directional gradient vector flow for snakes," *IEEE Trans Image Process*, vol. 15, pp. 1563–1571, Jun 2006.

[88] K. Lu and W. E. Higgins., "Interactive segmentation based on the live wire for 3D CT chest image analysis," *International Journal of Computer Assisted Radiology and Surgery*, vol. 2, no. 3, pp. 151–167, 2007.

[89] S. P. Raya and J. K. Udupa, "Shape-based interpolation of multidimensional objects," *IEEE Trans Med Imaging*, vol. 9, pp. 32–42, 1990.

[90] J. Liang, T. McInerney, and D. Terzopoulos, "United snakes," *Med Image Anal*, vol. 10, pp. 215–233, Apr 2006.

[91] T. Cootes, C. Taylor, D. Cooper, and J. Graham, "Active shape models-their training and application," *Computer Vision and Image Understanding*, vol. 61, no. 1, pp. 38 – 59, 1995/01/.

[92] K. W and W. R, "Peristalsis in the isolated guinea-pig ileum during opiate withdrawal," *N-S Arch Pharm.*, vol. 314, pp. 191–193, 1980.

[93] M. Rukebusch and J. Fioramonti, "Electrical spiking activity and propulsion in small intestine in fed and fasted rats," *Gastroenterology*, vol. 68, pp. 1500–1508, Jun 1975.

[94] L. D. Scott and R. W. Summers, "Correlation of contractions and transit in rat small intestine," *Am. J. Physiol.*, vol. 230, pp. 132–137, Jan 1976.

[95] R. J. Sheldon, M. E. Malarchik, D. A. Fox, T. F. Burks, and F. Porreca, "Pharmacological characterization of neural mechanisms regulating mucosal ion transport in mouse jejunum," *J. Pharmacol. Exp. Ther.*, vol. 249, pp. 572–582, May 1989.

[96] P. Bercik, D. Armstrong, R. Fraser, P. Dutoit, C. Emde, M. P. Primi, A. L. Blum, and P. Kucera, "Origins of motility patterns in isolated arterially perfused rat intestine," *Gastroenterology*, vol. 106, pp. 649–657, Mar 1994.

[97] M. L. Siegle, S. Bhner, M. Schemann, H. R. Schmid, and H. J. Ehrlein, "Propagation velocities and frequencies of contractions along canine small intestine," *Am. J. Physiol.*, vol. 258, pp. G738–744, May 1990.

[98] K. Hipper and H. J. Ehrlein, "Motility of the large intestine and flow of digesta in pigs," *Res. Vet. Sci.*, vol. 71, pp. 93–100, Oct 2001.

[99] M. C. Torjman, J. I. Joseph, C. Munsick, M. Morishita, and Z. Grunwald, "Effects of isoflurane on gastrointestinal motility after brief exposure in rats," *Int J Pharm*, vol. 294, pp. 65–71, Apr 2005.

[100] S. K. Ghosh, P. Janiak, W. Schwizer, G. S. Hebbard, and J. G. Brasseur, "Physiology of the esophageal pressure transition zone: separate contraction waves above and below," *Am. J. Physiol. Gastrointest. Liver Physiol.*, vol. 290, pp. G568–576, Mar 2006.

[101] S. K. Ghosh, P. Janiak, M. Fox, W. Schwizer, G. S. Hebbard, and J. G. Brasseur, "Physiology of the oesophageal transition zone in the presence of chronic bolus retention: studies using concurrent high resolution manometry and digital fluoroscopy," *Neurogastroenterol. Motil.*, vol. 20, pp. 750–759, Jul 2008.

[102] W. J. Lammers and J. R. Slack, "Of slow waves and spike patches," *News Physiol. Sci.*, vol. 16, pp. 138–144, Jun 2001.

[103] W. J. Lammers, "Propagation of individual spikes as "patches" of activation in isolated feline duodenum," *Am. J. Physiol. Gastrointest. Liver Physiol.*, vol. 278, pp. 297–307, Feb 2000.

[104] W. J. Lammers, L. Ver Donck, J. A. Schuurkes, and B. Stephen, "Peripheral pacemakers and patterns of slow wave propagation in the canine small intestine in vivo," *Can. J. Physiol. Pharmacol.*, vol. 83, pp. 1031–1043, Nov 2005.

[105] J. D. Huizinga, L. Thuneberg, M. Klppel, J. Malysz, H. B. Mikkelsen, and A. Bernstein, "W/kit gene required for interstitial cells of Cajal and for intestinal pacemaker activity," *Nature*, vol. 373, pp. 347–349, Jan 1995.

[106] K. M. Sanders, "A case for interstitial cells of Cajal as pacemakers and mediators of neurotransmission in the gastrointestinal tract," *Gastroenterology*, vol. 111, pp. 492–515, Aug 1996.

[107] V. M. Lukasik and R. J. Gillies, "Animal anaesthesia for in vivo magnetic resonance," *NMR Biomed*, vol. 16, pp. 459–467, Dec 2003.

[108] J. Buelke-Sam, J. F. Holson, J. J. Bazare, and J. F. Young, "Comparative stability of physiological parameters during sustained anesthesia in rats," *Lab. Anim. Sci.*, vol. 28, pp. 157–162, Apr 1978.

[109] M. Sababi and U. H. Bengtsson, "Enhanced intestinal motility influences absorption in anaesthetized rat," *Acta Physiol. Scand.*, vol. 172, pp. 115–122, Jun 2001.

[110] M. Sababi and O. Nylander, "Comparative study of the effects of nitric oxide synthase and cyclo-oxygenase inhibition on duodenal functions in rats anaesthetized with inactin, urethane or alpha-chloralose," *Acta Physiol. Scand.*, vol. 158, pp. 45–52, Sep 1996.

[111] A. C. Ailiani, T. Neuberger, J. G. Brasseur, G. Banco, Y. Wang, N. B. Smith, and A. G. Webb, "Quantitative analysis of peristaltic and segmental motion in vivo in the rat small intestine using dynamic MRI," *Magn Reson Med*, vol. 62, pp. 116–126, Jul 2009.

[112] L. R. Wiseman and D. Faulds, "Cisapride. An updated review of its pharmacology and therapeutic efficacy as a prokinetic agent in gastrointestinal motility disorders," *Drugs*, vol. 47, pp. 116–152, Jan 1994.

[113] J. A. Barone, L. M. Jessen, J. L. Colaizzi, and R. H. Bierman, "Cisapride: a gastrointestinal prokinetic drug," *Ann Pharmacother*, vol. 28, pp. 488–500, Apr 1994.

[114] A. A. Megens, L. L. Canters, F. H. Awouters, and C. J. Niemegeers, "Is in vivo dissociation between the antipropulsive and antidiarrheal properties of opioids in rats related to gut selectivity," *Arch Int Pharmacodyn Ther*, vol. 298, pp. 220–229, 1989.

Vita

Amit Ailiani

Amit Ailiani received the B.Engg. degree in Biomedical Engineering from TSEC, University of Mumbai, Mumbai, India, in 2001. He received his MS degree in Bioengineering from University of Illinois at Chicago, Chicago, IL, USA. His research interests are in image processing and image analysis for Magnetic Resonance Imaging, Computed Tomography and Ultrasound modalities.